Multi-Proxy Annual Profiles In Narwhal Tusks Reveal Biogeochemical Baseline Restructuring Under Rapid Arctic Change

Shanie Brault Nikolajew

Thesis submitted to the University of Ottawa in partial fulfillment of the requirements for the Master of Sciences degree in Earth Sciences

Department of Earth and Environmental Sciences
Faculty of Science
University of Ottawa

ABSTRACT

The Arctic is undergoing rapid physical and biogeochemical change, yet major gaps remain in our understanding of how these transformations propagate through marine food webs and influence the ecology of long-lived marine mammals. Climate-driven shifts in prey availability, sea-ice dynamics, and habitat structure shape diet, mobility, and contaminant exposure, but the ecological consequences of these interacting pressures remain difficult to disentangle. Similar isotopic and elemental responses can arise from changes in foraging behaviour, movement patterns, or environmental baselines, creating a central interpretive challenge for long-term geochemical records.

This thesis uses incrementally growing narwhal tusks as natural archives to disentangle ecological change from climate-driven restructuring of baseline conditions. Multi-proxy geochemical profiles were measured along annual growth layer groups in two narwhal tusks from contrasting Canadian Arctic regions, Baffin Bay and Hudson Bay, spanning the late 1990s to early 2020s. Stable isotopes ($\delta^{13}C$ and $\delta^{15}N$ in collagen; $\delta^{13}C$ and $\delta^{18}O$ in carbonate), isotopic spacing between carbonate and collagen ($\Delta^{13}C_{carb\text{-}coll}$), mercury concentrations, lead isotope ratios ($^{206}Pb/^{204}Pb$, $^{208}Pb/^{206}Pb$, $^{206}Pb/^{207}Pb$), and selected elemental ratios (Pb:Ca, Cd:Ca, As:Ca) were integrated with regional time series of sea-ice extent, coastal ocean temperature and salinity, and Arctic climate modes. Additional population-level $\delta^{13}C$ and $\delta^{15}N$ data from Pond Inlet narwhal embedded teeth and Baffin Bay beluga teeth were used to evaluate whether inferred baseline shifts are expressed across individuals, populations, and species.

The dominant isotopic signal was a pronounced decline in $\delta^{15}N_{collagen}$ in the Baffin Bay individual, whereas $\delta^{15}N_{collagen}$ remained comparatively stable in the Hudson Bay individual. Mobility-sensitive tracers showed strong interannual variability but no sustained directional trends, indicating no long-term relocation sufficient to account for the observed $\delta^{15}N$ pattern. In both individuals, Ba:Ca, Sr:Ca, and $\Delta^{13}C_{carb\text{-}coll}$ displayed consistent early-life structure, supporting an ontogenetic transition toward an adult-like feeding regime and changes in macronutrient routing. Bulk collagen isotopes behaved differently: $\delta^{13}C_{collagen}$ covaried with $\delta^{13}C_{CO3}$ in both tusks, indicating a shared sensitivity to baseline carbon-system variability, while the contrasting $\delta^{15}N$ records may reflect population-specific baseline forcing, potentially limiting the use of bulk $\delta^{15}N$ as a long-term trophic indicator. Toxicological proxies showed contrasting trajectories, with

mercury increasing through time in both individuals, consistent with trophic biomagnification combined with climate-sensitive baseline forcing, whereas Pb:Ca, Cd:Ca, and As:Ca declined systematically, consistent with changing exposure pathways driven by sea-ice loss, altered primary production, circulation shifts, and reduced atmospheric inputs. Lead isotope variability further indicated changes in contaminant provenance, particularly in Baffin Bay.

Independent multi-individual datasets revealed coherent shifts toward lower $\delta^{13}C$ and $\delta^{15}N$ beginning around the early 2000s at the population level in narwhals and also in belugas, demonstrating that the signal extends beyond single individuals to multiple populations and species. The concordance of these records is consistent with an ecosystem-scale baseline driver potentially linked to climate-driven loss of sea ice and associated reorganization of carbon and nitrogen cycling at the base of the food web in Baffin Bay. In this region, the population-level decline in $\delta^{15}N$ is interpreted as reflecting increased reliance on regenerated nitrogen and enhanced N_2 fixation under declining sea-ice conditions, processes that would lower baseline $\delta^{15}N$ values in primary producers and propagate upward to apex predators. Concurrent declines in $\delta^{13}C$ are consistent with shifts in dominant carbon sources associated with reduced ice-algal production, enhanced pelagic phytoplankton growth, and changing CO_2 availability, indicating baseline restructuring within the Baffin Bay ecosystem.

Together, these findings establish narwhal tusks as high-resolution archives of both ontogenetic ecology and multi-decadal baseline restructuring. The integration of isotopic and elemental tracers within annual growth layers provides a robust framework for disentangling ecological change from shifting environmental baselines and for improving understanding of how Arctic marine systems and the species inhabiting them respond to changes in primary production, reorganization of biogeochemical cycling, ongoing sea-ice loss, and evolving contaminant pathways.

RÉSUMÉ

L'Arctique subit des transformations rapides sur les plans physique et biogéochimique, mais d'importantes lacunes persistent dans notre compréhension de la manière dont ces changements se propagent à travers les réseaux trophiques marins et influencent l'écologie des mammifères marins longévifs. Les modifications climatiques de la disponibilité des proies, de la dynamique de la glace de mer et de la structure des habitats façonnent l'alimentation, la mobilité et l'exposition aux contaminants, toutefois les conséquences écologiques de ces pressions interactives demeurent difficiles à démêler. Des réponses isotopiques et élémentaires similaires peuvent découler de changements dans les comportements alimentaires, les mouvements migratoires ou les conditions environnementales de base, ce qui constitue un défi central pour l'interprétation des archives géochimiques à long terme.

Cette thèse utilise des défenses de narvals à croissance incrémentielle comme archives naturelles afin de distinguer les changements écologiques de la restructuration climatique des conditions biogéochimiques de base. Des profils géochimiques multi-proxys ont été mesurés le long des groupes annuels de croissance dans deux défenses provenant de régions contrastées de l'Arctique canadien, la baie de Baffin et la baie d'Hudson, couvrant la fin des années 1990 jusqu'au début des années 2020. Les isotopes stables ($\delta^{13}C$ et $\delta^{15}N$ du collagène; $\delta^{13}C$ et $\delta^{18}O$ du carbonate), l'écart isotopique entre carbonate et collagène ($\Delta^{13}C_{carb\text{-}coll}$), les concentrations de mercure, les rapports isotopiques du plomb ($^{206}Pb/^{204}Pb$, $^{208}Pb/^{206}Pb$, $^{206}Pb/^{207}Pb$) ainsi que certains rapports élémentaires (Pb:Ca, Cd:Ca, As:Ca) ont été intégrés à des séries temporelles régionales de l'étendue de la glace de mer, de la température et de la salinité côtières ainsi qu'à des indices de variabilité atlantique à l'échelle du bassin. Des données populationnelles de $\delta^{13}C$ et $\delta^{15}N$ provenant de dents incluses de narvals de Pond Inlet et de dents de bélugas de la baie de Baffin ont également été utilisées afin d'évaluer si les changements de base inférés s'expriment à l'échelle des individus, des populations et des espèces.

Le signal isotopique dominant correspond à une diminution du $\delta^{15}N_{collagen}$ chez l'individu de la baie de Baffin, tandis que le $\delta^{15}N_{collagen}$ demeure relativement stable chez l'individu de la baie d'Hudson. Les traceurs sensibles à la mobilité présentent une forte variabilité interannuelle, sans tendance directionnelle soutenue, ce qui exclut un déplacement durable suffisant pour expliquer le signal observé de $\delta^{15}N$. Chez les deux individus, les rapports Ba:Ca, Sr:Ca et $\Delta^{13}C_{carb\text{-}coll}$ montrent

une structure cohérente en début de vie chez les deux individus, appuyant une transition ontogénétique vers un régime alimentaire adulte et des changements dans la répartition métabolique des macronutriments. Les isotopes du collagène se comportent différemment; $\delta^{13}C_{collagen}$ covarie avec $\delta^{13}C_{CO3}$ dans les deux défenses, indiquant une sensibilité partagée à la variabilité du régime de base de carbone, tandis que les contrastes observés pour $\delta^{15}N$ pourraient refléter un forçage de base propre à chaque population, ce qui pourrait limiter l'utilisation de $\delta^{15}N$ comme indicateur trophique à long terme. Les traceurs toxicologiques présentent des trajectoires contrastées; les concentrations de mercure augmentent chez les deux individus, ce qui reflète une biomagnification trophique combinée à un forçage de base sensible au climat, alors que les rapports Pb:Ca, Cd:Ca et As:Ca diminuent systématiquement, en accord avec une modification des voies d'exposition associée à la perte de glace de mer, à des changements dans la production primaire, à l'évolution de la circulation océanique et à la diminution des apports atmosphériques. La variabilité isotopique du plomb indique en outre des changements dans la provenance des contaminants, particulièrement dans la baie de Baffin.

Des ensembles de données indépendants à l'échelle de plusieurs individus révèlent des diminutions cohérentes de $\delta^{13}C$ et $\delta^{15}N$ à partir du début des années 2000 chez les populations de narvals ainsi que chez les bélugas, démontrant que ce signal se manifeste au-delà des profils individuels pour s'exprimer à l'échelle de multiples populations et espèces. La concordance de ces enregistrements appuie l'existence d'un forçage de base à l'échelle de l'écosystème, potentiellement lié à la perte de glace de mer induite par le climat et à la réorganisation associée des cycles du carbone et de l'azote à la base du réseau trophique dans la baie de Baffin. Dans cette région, la diminution populationnelle du $\delta^{15}N$ est interprétée comme reflétant une dépendance accrue envers l'azote régénéré ainsi qu'une intensification de la fixation du N_2 sous des conditions de glace de mer en déclin, des processus susceptibles d'abaisser les valeurs de référence du $\delta^{15}N$ chez les producteurs primaires et de se propager vers les niveaux trophiques supérieurs. Les diminutions concomitantes du $\delta^{13}C$ sont compatibles avec des changements dans les sources de carbone associés à une réduction de la production algale liée à la glace de mer, à une intensification de la production phytoplanctonique pélagique et à une modification de la disponibilité de CO_2, indiquant une restructuration des conditions de base au sein de l'écosystème de la baie de Baffin.

Dans l'ensemble, ces résultats établissent les défenses de narvals comme des archives à haute résolution des processus ontogénétiques et des restructurations de base à l'échelle

pluridécennale. L'intégration de traceurs isotopiques et élémentaires dans des couches de croissance annuelles fournit un cadre robuste pour dissocier les changements écologiques des modifications des conditions environnementales de base et pour améliorer la compréhension de la manière dont les systèmes marins arctiques et les espèces qui les habitent réagissent aux changements de la production primaire, à la réorganisation des cycles biogéochimiques, à la perte continue de glace de mer et à l'évolution des voies de contamination.

ACKNOWLEDGEMENTS

I would first like to acknowledge that the University of Ottawa is located on the traditional unceded territory of the Algonquin Anishnaabeg People. I am grateful for the opportunity to learn and conduct research on this land. I would also like to acknowledge the communities of Arctic Bay and Naujaat, from which the samples used in this thesis originate. This research was funded by the Regional Partnerships and Research Program of Crown-Indigenous Relations and Northern Affairs Canada (CIRNAC).

I am profoundly grateful to my supervisor, Dr. Clément Bataille, for his continuous support, guidance, and mentorship throughout this project. Since my honours project in 2022, he has consistently encouraged my scientific growth, always making time for meetings, discussions, and thoughtful feedback. His expertise, availability, and dedication to teaching greatly shaped this thesis and my development as a scientist.

I would like to thank Dr. Cortney Watt and Justine Hudson from the Department of Fisheries and Oceans Canada for providing the narwhal tusks and for their invaluable help with sampling. I am especially grateful for their warm welcome in Winnipeg and for the meaningful professional relationships that continue beyond this project.

I would like to thank Dr. Danielle Fraser from the Canadian Museum of Nature, with whom my narwhal research journey began in 2022, for her help with the tusks, sampling strategy, and insightful meetings. I am also grateful to Dr. Peter Crockford at Carleton University for his guidance and help with sample preparation, valuable discussions, and insights, and to Dr. Petrus Le Roux from the University of Cape Town for his help with isotope results and interpretation. I also thank Dr. Jonathan O'Neil for agreeing to serve as my co-supervisor, and Dr. Oliver Warr and Dr. Peter Crockford for their support and for accepting to be part of my thesis defence committee.

I extend my sincere thanks to Dr. Nimal De Silva and Smitarani Mohanty for their long-standing support in the laboratory, particularly with trace metal and major element analyses. Their patience, explanations, and guidance were essential throughout the years. I am also grateful to Paul Middlestead, Erin Gomes-Reissmann, Wendy Abdi, and Elim Herx, at the Jan Veizer Laboratory at the University of Ottawa for their technical assistance and support. I also thank Laura Motta at the Woods Hole Oceanographic Institution for her assistance with mercury analyses. Special thanks to Maggie for her help with collagen preparation and sample weighing.

I am very thankful for my SAIVE Lab colleagues and friends, Eve, Zoe, Brent, Isabella, Megan, Auguste, and Lea, for their help in the lab, encouragement, shared laughter, and for building friendships that grew well beyond the walls of academia.

To my partner, Alex Kreimes, thank you for your unwavering love, patience, and support throughout the years. Thank you for always believing in me and for being by my side through both the highs and the lows. I also want to thank my furry friend, Leo, whose loyal presence, gentle interruptions, and unconditional affection provided daily reminders to pause, breathe, and keep going.

Finally, I owe my deepest gratitude to my family, my mom Sylvie Brault, my dad Taras Nikolajew, and my sister Vikie Brault Nikolajew, for their constant encouragement, kind words, and unconditional support. Your belief in me has meant everything. I also thank my friends Juliette, Shawna, Marylène, Vanessa, Nele, and Sophie, for their friendship, encouragement, and for reminding me to enjoy life beyond my thesis.

TABLE OF CONTENTS

LIST OF FIGURES

CHAPTER 1: INTRODUCTION

The Arctic is undergoing rapid transformation as a direct result of anthropogenically-mediated climate change, which is reshaping marine ecosystems that have remained relatively stable for millennia. These changes have global consequences by influencing ocean circulation, carbon cycling, contaminant transport, and climate feedbacks, while also affecting food security, commercial fisheries, and Indigenous communities. As sea-ice declines and physical and biogeochemical regimes reorganize, understanding how these changes propagate through marine food webs has become essential for predicting the future structure, function, and resilience of Arctic ecosystems. Marine mammals occupy a pivotal position in this effort. As long-lived, wide-ranging, upper-trophic-level consumers, they integrate environmental conditions across extended intervals of space and time. Their foraging ecology, migratory behavior, and contaminant exposure are tightly linked to sea-ice dynamics, making them powerful ecological sentinels of Arctic change. Importantly, sea-ice does not only regulate habitat and prey fields; it also mediates biogeochemical coupling and contaminant delivery through seasonal storage and release. Consequently, sea-ice decline may produce not only gradual ecological trends, but also threshold-like shifts in exposure pathways and baseline chemistry that can be recorded directly in the tissues of long-lived consumers.

1.1. Rapid Environmental Change in the Arctic

The Arctic is warming at a rate far exceeding the global average (Rantanen et al., 2022), a phenomenon known as Arctic amplification. Over the past 50 years, Arctic temperatures have risen three to four times faster than the global mean (Hoegh-Guldberg & Bruno, 2010; Rantanen et al., 2022). This intensifying warming has triggered sweeping physical changes in the ocean and cryosphere, including unprecedented reductions in sea-ice extent and thickness, earlier melt onset, delayed freeze-up, and altered seasonal ice dynamics (Dietz et al., 2021; Heide-Jørgensen & Laidre, 2004; Hoegh-Guldberg & Bruno, 2010; Reed et al., 2021). These physical transformations carry far-reaching implications for marine ecosystems. Declines in sea-ice modify surface albedo, ocean-atmosphere heat exchange, freshwater inputs, and upper-ocean stratification (Garcia-Soto et al., 2021; Polyakov et al., 2017). They restructure nutrient delivery, primary-production regimes,

and seasonal food-web dynamics (Chambault et al., 2020; Findlay et al., 2015; Kędra et al., 2015; Lewis et al., 2020; Lind et al., 2018; Macdonald et al., 2015; Markus et al., 2009; Parmentier et al., 2017; Polyakov et al., 2017; Post et al., 2013; Reed et al., 2021; Solan et al., 2021; Stroeve & Notz, 2018; Yunda-Guarin et al., 2020). As warming progresses, the Arctic is transitioning from an ecosystem historically defined by strong cryospheric control to one increasingly dominated by open-water processes, which all have increasingly severe, cascading effects on biological communities, biogeochemical pathways, and contaminant cycling.

1.1.1. Physical and Biogeochemical Changes

Satellite and field observations over the past four decades reveal substantial declines in both the extent and thickness of Arctic sea-ice. Summer sea-ice extent has decreased at approximately 13% per decade, while winter ice has declined by about 2.5% per decade (Figure 1; Fetterer et al., 2017, 2025; Garcia-Soto et al., 2021; Perovich et al., 2020). These reductions are accompanied by earlier melt onset, later freeze-up, and a shift toward thinner, more mobile first-year ice. Such physical changes fundamentally reshape the Arctic Ocean's structure and seasonal energy balance. Loss of ice cover lowers surface albedo, increases ocean-atmosphere heat exchange, and enhances wind-driven mixing in newly open-water regions (Garcia-Soto et al., 2021; Reed et al., 2021). Variability in ice formation and melt also alters the distribution of polynyas (i.e., recurring open-water areas within the pack ice) which serve as critical foraging habitats for numerous species of marine mammals (Heide-Jørgensen et al., 2013). Earlier and longer open-water periods modify the seasonal progression of primary production by shifting the timing and duration of phytoplankton blooms (Buchanan et al., 2022; Feng et al., 2018; Lewis et al., 2020; Markus et al., 2009; Post et al., 2013). These physical transformations cascade throughout the marine ecosystem, influencing prey availability, predator-prey interactions, and the spatial organization of habitats used by top predators.

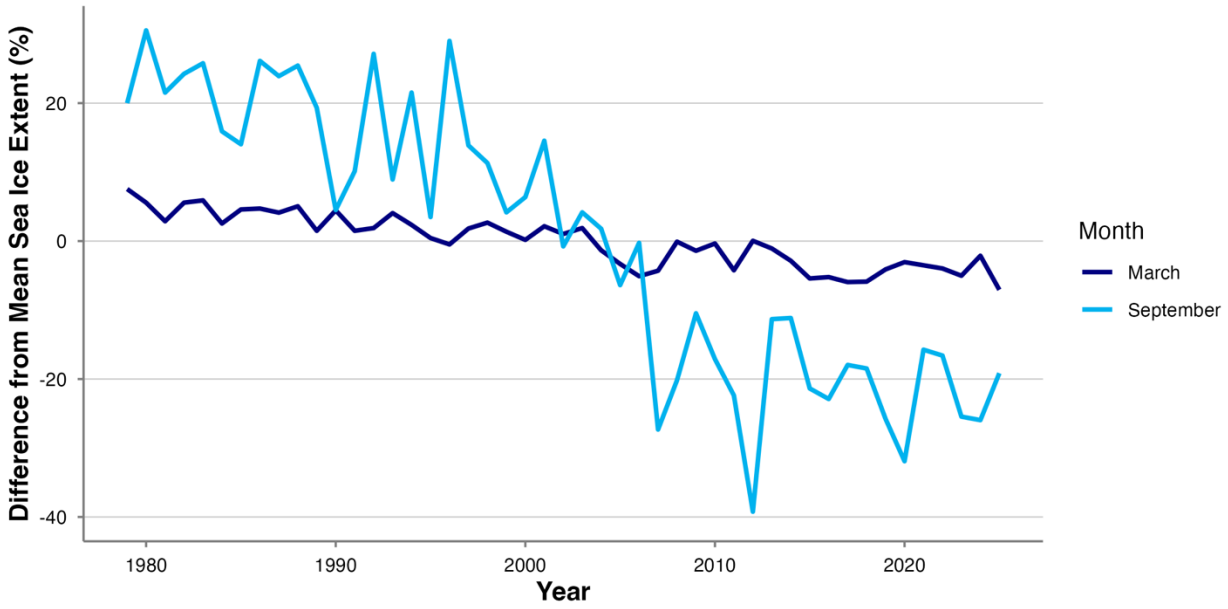

Figure 1. Percent difference from mean Arctic sea-ice extent in March (dark blue, winter maximum) and September (light blue, summer minimum) from 1979 to 2025. Values expressed as anomalies relative to the 1979-2025 mean. The steep decline in September highlights the strong loss of summer sea-ice. Data was obtained from the *Sea-ice Index, Version 4* (Fetterer et al., 2025).

1.1.2. Changes in Biogeochemical Cycles

The biogeochemical structure of the Arctic Ocean is being reorganized alongside physical changes in sea-ice and ocean circulation. Freshwater from melting sea-ice strengthens upper-ocean stratification, limiting vertical nutrient replenishment and altering the spatial and seasonal distribution of primary production (Assmy et al., 2017; Lewis et al., 2020; Lind et al., 2018; Macdonald et al., 2015; Parmentier et al., 2017; Polyakov et al., 2017; Reed et al., 2021; Solan et al., 2021; Stroeve & Notz, 2018). Reduced prevalence of ice-associated algal communities diminishes an early-season sympagic (ice-associated) carbon pathway, favoring pelagic phytoplankton blooms that peak later in spring and are more sensitive to light and stratification conditions (Assmy et al., 2017; Buchanan et al., 2022; Feng et al., 2018; Post et al., 2013; Von Friesen et al., 2025). Simultaneously, diminished ice cover promotes increased exchange with sub-Arctic waters, introducing distinct nutrient regimes, warmer Atlantic inflows, and temperate species that can alter food-web structure (Laidre et al., 2008; Macdonald et al., 2015; Shuert et al., 2022; Stevenson & Abbott, 2019). These shifts influence zooplankton community composition, carbon transfer efficiency, and ultimately the prey base available to Arctic marine mammals.

Biogeochemical pathways of contaminants are also changing. Sea-ice has historically acted as a reservoir for metals and organic pollutants, concentrating contaminants through deposition and scavenging processes. As the ice cover diminishes, changes in melt timing, microbial activity, and redox conditions may modify contaminant release and transformation, including mercury methylation dynamics (Heimbürger et al., 2015; Kirk et al., 2012; Krabbenhoft & Sunderland, 2013; Stern et al., 2012; Zhang et al., 2020). These shifts alter both the distribution and bioavailability of contaminants across marine food webs. Together, these biogeochemical transformations reshape the energy pathways, nutrient dynamics, and contaminant exposure landscapes that underpin the ecology of Arctic marine mammals, influencing their diet, habitat use, and physiological stressors.

1.2. Effects of Arctic Environmental Change on Marine Mammals

Marine mammals occupy upper trophic levels in Arctic food webs and are tightly coupled to the distribution, timing, and productivity of sea-ice-dependent ecosystems. As long-lived and wide-ranging predators, they integrate environmental variability across broad spatial and temporal scales. Consequently, shifts in sea-ice dynamics, primary productivity, prey availability, and contaminant pathways often have immediate and often measurable impacts on their foraging behavior, migratory patterns, habitat selection, and ecological exposure.

For many species, sea-ice is not merely habitat but a structuring force that governs access to prey, facilitates predator avoidance, and mediates energy balance. Alterations to the seasonal timing of ice formation and breakup, the availability of polynyas, and the spatial extent of coastal and offshore ice habitats have already influenced the ecological habits of polar bears, seals, walruses, beluga whales, and narwhals (Derocher, 2005; Ferguson et al., 2005; Huntington, 2009; Kovacs et al., 2012; Laidre et al., 2008, 2015; Moore & Huntington, 2008). These ecological responses vary by species and region, but collectively they reflect a system undergoing rapid restructuring.

Climate-driven environmental change influences marine mammals through three principal pathways. First, as apex predators, they may adjust their diet and foraging strategies in response to shifting prey availability and food-web restructuring. Second, as highly mobile species, they can modify their movement patterns and migration routes to track suitable habitats or prey

distributions. Third, environmental change can alter the physical and biogeochemical characteristics of their habitats, including sea-ice conditions, nutrient dynamics, and contaminant pathways, thereby reshaping the ecological baselines to which these mammals are exposed.

1.2.1. Changes in Diet and Foraging Ecology

Sea-ice loss is restructuring Arctic food webs, influencing the composition and availability of prey for marine mammals. Many upper-trophic-level species depend heavily on ice-associated zooplankton and fishes, particularly *Calanus glacialis*, an Arctic copepod, and Arctic cod (*Boreogadus saida*), two key species that dominate the energy pathway in ice-covered regions (Bouchard & Fortier, 2020; Søreide et al., 2010). With sea-ice loss, the timing of primary production is shifting, creating seasonal mismatches between prey availability and marine mammal foraging demands (Chambault et al., 2020; Leu et al., 2011; Markus et al., 2009; Post et al., 2013; Søreide et al., 2010; Yunda-Guarin et al., 2020). Documented dietary changes across multiple species reflect these broader ecological transitions. In regions where ice-associated prey have declined, predators that occupy higher trophic levels, such as ringed seals (*Pusa hispida*) and beluga whales (*Delphinapterus leucas*), have become increasingly reliant on sub-Arctic or pelagic prey, such as capelin (*Mallotus villosus*) (Hop & Gjøsæter, 2013; Yurkowski et al., 2018). Evidence from stable isotopes, including declines in carbon ($\delta^{13}C$) and shifts in nitrogen isotopes ($\delta^{15}N$), support these transitions towards more pelagic feeding strategies (Brown et al., 2017; De La Vega et al., 2019; Dietz et al., 2021; Hobson et al., 2002; Newsome et al., 2009, 2010).

1.2.2. Changes in Mobility and Migration

Marine mammal migration routes, timing, and energetic cost are largely shaped by sea-ice dynamics (Pagano & Williams, 2021). As sea-ice declines, becomes thinner, or shifts spatially, marine mammals are adjusting their migratory corridors, timing, and habitat use to accommodate the new physical landscape. Telemetry studies provide evidence for these shifts. Several species including belugas, narwhals (*Monodon monoceros*), bowhead whales (*Balaena mysticetus*) and ringed seals have changed their migration corridors and timing in response to declining ice cover (Citta et al., 2018; Shuert et al., 2022; Watt et al., 2017). For example, ringed seals appear to have

adjusted their haul-out timing and diving behaviors to accommodate altered ice conditions, with potential consequences for energy expenditure and reproductive success (Crawford et al., 2019; Lydersen et al., 2017).

1.2.3. Habitats and Changes in Biogeochemical Cycles

Environmental changes associated with sea-ice loss extend beyond prey availability and migration routes. They also reshape the underlying physical and biogeochemical characteristics of marine mammal habitats. Altered stratification, shifts in primary production regimes, and changes in nutrient delivery can modify the distribution, quality, and seasonal timing of prey across Arctic ecosystems. For example, the transition from sympagic to pelagic production in many regions may change the energy pathways supporting zooplankton and fish communities, thereby influencing the energetic efficiency of marine food webs (Chambault et al., 2020; Dietz et al., 2021; Laidre et al., 2008; McLeish, 2013; Michel et al., 2012).

1.3. Contaminants and Climate-Driven Changes in Exposure in Arctic Marine Mammals

Arctic marine mammals are also being affected by climate-driven shifts in contaminant pathways. Contaminants such as mercury (Hg), lead (Pb), cadmium (Cd), and arsenic (As) are transported to the Arctic through atmospheric circulation, riverine discharge, and oceanic inflow from sub-Arctic regions (Berner et al., 2016; De Vera et al., 2021a; Stern et al., 2012). Once introduced into high-latitude systems, these contaminants undergo a range of biogeochemical transformations that influence their mobility, chemical form, and bioavailability.

Marine mammals are particularly vulnerable to the effects of these changes. Their long lifespans, high trophic positions, and reliance on predictable foraging grounds increase exposure to contaminants that biomagnify through food webs (Borgå et al., 2022; De María et al., 2021; Dietz et al., 2009, 2013, 2021; Huntington, 2009). The uptake of those contaminants has traditionally been interpreted through dietary and habitat preferences; however, their environmental baselines are likely being reshaped by climate-driven changes in sea-ice cover and biogeochemical cycles (Pradel et al., 2025; Pućko et al., 2015). As a result, climate-driven changes

in sea-ice cover, stratification, and water-mass structure may alter contaminant uptake independently of dietary or behavioral change.

To understand how contaminant exposure is evolving, it is therefore necessary to consider both ecological processes, such as diet and mobility, and the changing environmental context that shapes contaminant pathways in the Arctic. The following subsections outline the sources and transformations of key contaminants, and how climate-driven ecological and biogeochemical changes influence exposure levels in marine mammals.

1.3.1. Sources and Pathways of Contaminants

Arctic ecosystems receive contaminants from a combination of long-range atmospheric transport, riverine inputs, and oceanic inflow from sub-Arctic and industrialized regions (Stern et al., 2012). Metals such as Hg, Pb, Cd and As can be deposited onto snow and sea-ice, scavenged from the atmosphere, or delivered through major river systems. Once introduced into the Arctic Ocean, these contaminants circulate through distinct water masses and undergo transformations that determine their chemical form and biological availability (Berner et al., 2016; De Vera et al., 2021a).

Among these contaminants, Hg is of particular concern. Inorganic Hg deposited from the atmosphere can be microbially converted into methylmercury (MeHg), a highly toxic and bioaccumulative compound (AMAP, 2018; Desforges et al., 2016; Rohonczy et al., 2024; Stern et al., 2012; Thévenod & Lee, 2013). The rate of methylation depends on environmental variables such as redox conditions, microbial communities and primary productivity. Because these processes are influenced by sea-ice cover and ocean stratification, climate-driven changes can directly alter the pathways through which Hg becomes bioavailable (Krabbenhoft & Sunderland, 2013; Zhang et al., 2020). Some populations of belugas, narwhals, ringed seals, and polar bears show rising burdens of total Hg and MeHg accumulated in their tissues from the 1980s through the 2010s, reflecting enhanced methylation in a changing Arctic, shifts in diet and prey composition, and alterations to sea-ice-driven food-web pathways (AMAP, 2018; Dietz et al., 2013, 2021).

Other metals, such Pb, Cd, and As enter marine food webs through uptake by phytoplankton and other primary producers. Their concentrations in biota are shaped by factors

such as temperature, salinity gradients, water-mass origin, or nutrient levels (Azizur Rahman et al., 2012; Barkay et al., 1997; Campbell et al., 2005; Stern et al., 2012; Von Friesen et al., 2025). As these contaminants move through the food web, biomagnification leads to high concentrations of those metals in marine mammals (AMAP, 2018; Dietz et al., 2021). These pathways highlight the tight coupling between environmental conditions, biogeochemical processes, and contaminant exposure in Arctic marine ecosystems, underscoring why climate-driven changes may significantly alter contaminant burdens in marine mammals.

1.3.2. Influence of Diet and Contaminant Exposure

Because contaminants such as Hg, Pb, Cd, and As move through marine food webs, the foraging ecology of marine mammals plays a central role in determining their exposure levels. Dietary shifts induced by sea-ice loss can alter contaminant exposure. For example, a switch from ice-associated prey to more pelagic and/or benthic prey can modify the intake of contaminants because different prey usually differ in their contaminant loads (Azizur Rahman et al., 2012; Braune et al., 2015; Dehn et al., 2006, 2006; Rohonczy et al., 2024).

Contaminant dynamics also vary by trophic pathways. Many of these metals biomagnify, resulting in higher concentrations in prey from higher trophic levels (Borgå et al., 2022; De María et al., 2021; Dietz et al., 2009, 2013, 2021; Huntington, 2009). In contrast, other metals may exhibit biodilution in certain Arctic food webs, particularly where pelagic species excrete them efficiently or sequester them in tissues that are not commonly consumed by predators (Campbell et al., 2005; Rohonczy et al., 2024). This means that shifts in prey type, feeding depth, or the balance between pelagic and benthic foraging can produce distinct contaminant signatures across individuals and populations. As Arctic warming continues to reshape prey communities, the chemical exposure landscape experienced by marine mammals will reflect not only environmental baselines but also changes in species-specific feeding strategies. Understanding these dietary influences is therefore essential for interpreting how contaminant burdens respond to both ecological and climatic pressures.

1.3.3. Influence of Mobility and Migration

Migration and habitat use play a significant role in shaping contaminant exposure in Arctic marine mammals. Because contaminant concentrations vary across oceanographic regions, water masses, and prey communities, animals that move across large spatial scales experience heterogeneous chemical environments. As a result, individuals or populations that shift their migratory routes or seasonal habitats may accumulate contaminants at different rates or in different forms, even if their trophic level remains unchanged (De Vera et al., 2021a; Outridge et al., 2005).

Climate-driven changes in sea-ice distribution can further modify these exposure pathways. As ice retreats or shifts spatially, marine mammals may be redirected into new foraging areas where prey species have distinct contaminant loads or where biogeochemical conditions favor higher rates of metal uptake (Chambault et al., 2020; Dietz et al., 2021). For example, movement into regions with enhanced mercury methylation or elevated riverine inputs could increase contaminant exposure independently of dietary change.

Species with long-distance migrations, such as narwhals, belugas, and bowhead whales, integrate contaminant signals from multiple regions over annual cycles. In contrast, species with more localized habitat use behaviours may reflect finer-scale environmental variability. These spatial differences underscore how mobility interacts with climate-driven environmental change to shape contaminant burdens in Arctic marine mammals.

1.3.4. Sea-Ice Decline and Contaminant Cycling

Sea-ice plays a central role in regulating contaminant dynamics in the Arctic, acting both as a reservoir and as a mediator of chemical transformations. Metals and other pollutants can accumulate within snow and sea-ice through atmospheric deposition, snow scavenging, and incorporation into ice-associated particulates and microbial communities (Berner et al., 2016; De Vera et al., 2021a; Kirk et al., 2012). Multi-year ice often contains elevated concentrations of these contaminants, reflecting prolonged deposition and storage (Beattie et al., 2014). During spring melt, contaminants stored in the seasonal snowpack and sea-ice are released into surface waters, producing short-lived but ecologically important pulses that can propagate throughout the food

web during periods of high biological activity (Jensen et al., 2021; Krabbenhoft & Sunderland, 2013).

Sea-ice decline can weaken this seasonal concentrating mechanism by reducing the number of contaminants stored in snow/ice and shortening the duration of storage. As a result, exposure to metals that are efficiently scavenged from the atmosphere and concentrated in snow and ice (e.g., Pb, Cd, As) may decrease even if atmospheric deposition rates remain similar, because the spring melt pulse becomes smaller or less distinct. In contrast, mercury (Hg) is additionally shaped by in situ biogeochemical processing, particularly the microbial conversion of inorganic Hg into MeHg, a highly bioaccumulative form (Krabbenhoft & Sunderland, 2013; Zhang et al., 2020). As sea-ice thins and retreats, changes in stratification, redox gradients, microbial communities, and the location of methylation "hotspots" may alter MeHg production and availability (Kirk et al., 2012; Zhang et al., 2020). When sea-ice is reduced, a major temporary reservoir of contaminants disappears. Without seasonal trapping, metals may instead remain more widely dispersed through the water column and have distinct speciation making them bioavailable to different component of the food web (Kirk et al., 2012; Stern et al., 2012). Consequently, Hg concentrations in marine food webs may remain stable or increase even as exposure to other atmospherically scavenged metals declines. Together, these mechanisms imply that climate-driven sea-ice loss can decouple contaminant trends among elements, producing contrasting trajectories that reflect environmental reorganization rather than trophic change alone.

1.4. Knowledge Gaps and Research Opportunities

Despite substantial progress in documenting Arctic physical and biogeochemical change, major gaps remain in our understanding of how these transformations propagate through marine food webs and affect the ecology of long-lived marine mammals. Diet, mobility, habitat use, and contaminant exposure are all shaped by climate-driven changes in prey availability, sea-ice dynamics, and habitat structure, yet the ecological consequences of these interacting pressures remain difficult to disentangle.

A central challenge arises from the fact that the responses of marine mammal to environmental change are multi-dimensional. Shifts in $\delta^{13}C$ or $\delta^{15}N$, for example, may indicate changes in prey composition, but they may also reflect altered habitat use or evolving baseline

isotopic conditions associated with changing primary production. Similarly, contaminants may increase due to dietary transitions, migration into new water masses, or environmentally driven changes in methylation and metal cycling. Because these ecological processes occur simultaneously, it is difficult to determine the relative contributions of diet, migration, and habitat change to observed patterns across populations and regions.

Another key limitation is temporal. Many Arctic marine mammals live for several decades, and their ecological histories integrate long-term environmental variability. However, most ecological observations such as satellite telemetry, diet studies, or contaminant monitoring span only a few years. These short-term datasets provide valuable snapshots but offer limited insight into how individuals or populations experience cumulative environmental change over their lifetimes or across generational timescales.

Finally, because ecological and biogeochemical baselines are potentially shifting at the same time as marine mammal behavior, distinguishing cause from consequence remains challenging. For instance, is a shift in $\delta^{15}N$ driven by a true dietary change, by movement into a new habitat, or by a transformation of baseline nitrogen cycling? Similarly, increases in Hg may reflect changes in methylation rates rather than an alteration in foraging behavior. Without frameworks that can separate these overlapping influences, it remains difficult to attribute ecological change to specific climate-driven mechanisms.

Together, these gaps highlight the need for approaches that can integrate dietary, spatial, and environmental information over the timescales relevant to Arctic marine mammals. Such approaches must be capable of capturing long-term ecological trajectories, distinguishing among competing drivers of change, and linking individual behavior with broader ecosystem transformations.

1.5. Marine Mammal Biomineralized Tissues as Natural Archives

The biological structures of marine mammals themselves provide an exceptional resource for reconstructing long-term ecological and environmental histories. Many Arctic marine mammals including narwhals, belugas, walruses, and several seal species produce teeth or tusks that grow incrementally throughout their lives. These tissues form annual to sub-annual growth

layers that are deposited sequentially and remain chemically stable over time, creating a chronological archive analogous to tree rings.

Within these layers, a wide range of geochemical markers are incorporated through diet, water intake, habitat use, and exposure to contaminants. As a result, teeth and tusks preserve multi-decadal records that include information relevant to diet, migration, habitat use, and contaminant exposure across the entire lifespan of an individual (Clark et al., 2020, 2021; Dietz et al., 2021; Feddern et al., 2021; Jaouen et al., 2016; Matthews et al., 2016; Rey-Iglesia et al., 2023; Walker & Macko, 1999). For long-lived species, this allows ecological and environmental signals to be evaluated over the same temporal scales at which Arctic ecosystems have undergone their most rapid transformation.

Because these structures record information at fine temporal resolution, they offer a unique opportunity to examine how environmental change influences the ecology of marine mammal on seasonal to annual timescales. Dietary shifts, altered migration routes, and changes in habitat characteristics or contaminant pathways can all leave distinct chemical signals in these biomineralized tissues. Thus, teeth and tusks provide a rare integrative archive that can capture direct indicators of ecological behavior (i.e., diet, habitat use, movement), reflect environmental baselines (i.e., biogeochemical and contaminant conditions), and span the multi-decadal interval during which changes in Arctic ecosystems have accelerated most rapidly. Together, these properties make them ideally suited for disentangling the combined effects of ecological behavior and environmental change in Arctic marine mammals.

1.6. Disentangle Shifts in Diet, Mobility, Biogeochemical Cycle Shifts, and Contaminant Exposure in Marine Mammal Teeth

Interpreting geochemical records preserved in the teeth and tusks of long-lived marine mammals is inherently challenging because multiple ecological and environmental processes are recorded simultaneously within the same tissues. In narwhals and other Arctic cetaceans, changes in diet, migration routes, and habitat use occur alongside rapidly shifting biogeochemical baselines and evolving contaminant regimes. Consequently, temporal trends in isotopic and trace-element composition may reflect a combination of altered prey community structure, changes in spatial

habitat use, and climate-driven reorganization of primary production and nutrient cycling, rather than a single ecological response.

Addressing this complexity requires a clear understanding of the strengths and limitations of individual geochemical proxies and an integrated framework that combines complementary tracers to separate ecological behavior from changing environmental baselines. The following sections review the most informative geochemical tools for reconstructing marine mammal ecology and environment, with emphasis on their ability to resolve (i) long-term mobility and habitat use, (ii) shifts in diet and trophic position, (iii) exposure to toxic metals, and (iv) the interaction between ecological behavior and changing biogeochemical baselines.

1.6.1. Tracing Mobility of Marine Mammals

Migration is a key challenge in isotope interpretation: if animals move across isotopically distinct water masses, isotopic variability in their tissues may reflect geographic shifts rather than dietary change. Intrinsic tracers preserved in biomineralized tissues, such as dentin and enamel, offer a rare opportunity to track individuals across their lifetimes because they archive environmental and physiological signals that accumulate annually (Dietz et al., 2021; Newsome et al., 2010). However, effective use of these records to infer mobility requires proxies that respond predictably to spatial differences in water-mass properties while being minimally affected by internal physiological processes. Such proxies are essential for distinguishing true behavioral change from baseline or trophic variability.

1.6.1.1. $\delta^{18}O$ in Bioapatite

Oxygen isotopes ($\delta^{18}O$) in bioapatite are used to reconstruct habitat use and water-mass characteristics because the $\delta^{18}O$ of body water reflects the isotopic composition of ambient seawater. In marine mammals, $\delta^{18}O$ values in enamel and dentin record the isotopic composition of the seawater that the animal experienced during tissue formation (Ciner et al., 2016; Daniel Bryant et al., 1996; Matthews et al., 2016; Newsome et al., 2010).

In the Arctic, seawater $\delta^{18}O$ shows strong spatial gradients because Atlantic-derived waters are relatively ^{18}O-enriched, while regions heavily influenced by sea-ice melt, glacial melt, and

river discharge are ^{18}O-depleted (Kopec et al., 2024). In Baffin Bay, this typically corresponds to enriched (i.e., less negative) $\delta^{18}O$ on the Greenland/eastern side, where waters are strongly influenced by Atlantic-derived input from the West Greenland Current (surface Atlantic Water average around -0.3‰, with values reaching +0.7‰; Kopec et al., 2024). In contrast, $\delta^{18}O$ values are depleted (i.e., more negative) toward the Canadian side and near outflows from the Canadian Arctic Archipelago, where freshwater influence is stronger (surface mixed/coastal waters in their Baffin Bay/Canadian Arctic Archipelago-influenced groupings are around -1‰ to -2‰; Kopec et al., 2024). These pronounced gradients make $\delta^{18}O$ a powerful tracer of mobility, and sequential measurements along tusk growth axes can improve our understanding of seasonal and interannual movements of animals between isotopically distinct habitats, including coastal, fjord, shelf, and offshore basins. Therefore, temporal changes in $\delta^{18}O$ may theoretically reflect shifts in migratory corridors, changes in habitat preference, and variation in freshwater influence linked to climate-driven changes in ice melt or runoff.

1.6.2. Untangling Diet from Biogeochemical Cycle Shifts

Interpreting dietary signals in marine mammal tissues is complicated by the fact that many geochemical tracers respond simultaneously to both ecological processes and underlying environmental variability. Bulk stable carbon and nitrogen isotopes ($\delta^{13}C$ and $\delta^{15}N$) remain central to reconstructing trophic ecology, yet their values are also shaped by changes in primary production, nutrient cycling, freshwater influence, and spatial movement across isotopically heterogeneous water masses. As Arctic ecosystems undergo rapid physical and biogeochemical transformation, distinguishing true shifts in prey composition from baseline-driven variability becomes increasingly challenging. This section examines the limitations of traditional isotopic proxies and introduces complementary elemental and isotopic tools that can help disentangle dietary change from broader environmental influences.

1.6.2.1. Challenges with $\delta^{13}C$ and $\delta^{15}N$ as dietary proxies

$\delta^{13}C$ and $\delta^{15}N$ are among the most widely used tracers for reconstructing the ecology of marine mammals and are routinely applied to infer diet, trophic position, and habitat use across a

broad range of species and ocean basins (Ben-David & Flaherty, 2012; Hobson & Welch, 1992; Newsome et al., 2010). In Arctic marine food webs, $\delta^{13}C$ has traditionally been interpreted as an indicator of carbon source and foraging habitat, for example differentiating between sympagic (ice-associated) and pelagic primary production or between coastal and offshore feeding grounds, whereas $\delta^{15}N$ is generally used to estimate relative trophic position (Dalerum & Angerbjörn, 2005; Dietz et al., 2021; Newsome et al., 2010).

However, in a rapidly changing Arctic, environmental shifts can modify baseline isotopic values at the base of the food web, through its effects on primary production, nutrient sources, and carbon cycling, while at the same time reshaping prey communities and migratory behavior of higher-trophic-level consumers (De La Vega et al., 2019; Kortsch et al., 2015; Ruiz-Cooley et al., 2014; Wassmann et al., 2011). In addition to these broad-scale drivers, finer-scale processes, such as freshwater inputs, stratification, bloom timing, and altered nitrogen recycling, can generate substantial intra-regional variability in both $\delta^{13}C$ and $\delta^{15}N$ (Buchanan et al., 2022; De La Vega et al., 2019; Leu et al., 2020; Westbrook et al., 2024). As a result, temporal trends in $\delta^{13}C$ and $\delta^{15}N$ recorded in the tissues of long-lived marine mammals may reflect an unknown combination of baseline shifts, dietary change, and movement among isotopically distinct water masses. Disentangling these overlapping influences is essential for using bulk $\delta^{13}C$ and $\delta^{15}N$ to reconstruct ecological histories and for distinguishing true changes in diet or trophic ecology from signals that primarily reflect physical and biogeochemical change.

Mapping $\delta^{13}C$ variations at the base of the food chain across the Arctic could provide some insights into spatial variations. $\delta^{13}C$ in marine mammals derives from the isotopic composition of dissolved inorganic carbon (DIC) and particulate organic carbon (POC) at the base of the food web. In the Arctic, DIC and POC $\delta^{13}C$ values vary with sea-ice cover, freshwater inputs, primary production, and atmospheric CO_2 uptake, all of which have changed markedly over recent decades (De La Vega et al., 2019; Fox & Walker, 2022). Additionally, long-term and spatially resolved measurements of DIC and POC are sparse, and such datasets remain limited in the Arctic, particularly at temporal resolutions comparable to growth records in mammal tissues. Without these baselines, $\delta^{13}C$ variations in marine mammal tissues cannot be confidently attributed to dietary or habitat changes alone, underscoring the need for complementary proxies and independent constraints on biogeochemical variability.

Baseline variability similarly complicates the interpretation of bulk $\delta^{15}N$ values in Arctic marine mammals. $\delta^{15}N$ at the base of the food web is strongly influenced by nitrogen sources and cycling processes, including nitrate availability, regeneration versus new production, denitrification, and nitrogen fixation, all of which can vary spatially and temporally in response to sea-ice cover, stratification, and primary productivity (Ruiz-Cooley et al., 2014; Von Friesen et al., 2025; Westbrook et al., 2024). In the Arctic, reduced sea-ice extent and enhanced stratification can alter nutrient supply pathways and favor recycled nitrogen, potentially increasing or reducing baseline $\delta^{15}N$ values independently of trophic structure (Westbrook et al., 2024). As a result, temporal changes in $\delta^{15}N$ recorded in marine mammal tissues may reflect shifts in baseline nitrogen cycling rather than changes in trophic position alone. This baseline sensitivity is particularly problematic for long-lived, mobile species that integrate nitrogen signals across multiple regions and water masses with distinct nitrogen biogeochemistry.

Mobility further complicates the interpretation of $\delta^{13}C$ and $\delta^{15}N$ in highly mobile marine mammals. Individuals move across isotopically heterogeneous water masses and inevitably integrate multiple baseline signals through time, independent of any dietary change. For example, $\delta^{13}C$ in teeth can reflect water-mass-specific carbon sources and primary production regimes, such that even modest shifts in horizontal or vertical habitat use may register in the isotopic record (Pomerleau et al., 2016). Similarly, $\delta^{15}N$ may track regional differences in nitrogen cycling, nitrate availability, or prey community composition, a pattern observed in several migratory marine predators that traverse broad biogeochemical gradients (Ruiz-Cooley et al., 2014). As a result, apparent isotopic changes in consumer tissues may arise simply from changes in the isotopic landscapes animals encounter, rather than from shifts in trophic behavior.

In summary, bulk $\delta^{13}C$ and $\delta^{15}N$ integrate composite signals that encode intertwined information on diet, habitat, movement, and environmental change. Interpreting them requires additional tracers to deconvolve these multiple influences.

1.6.2.2. Ba:Ca and Sr:Ca

Elemental ratios in bioapatite, particularly barium-to-calcium (Ba:Ca) and strontium-to-calcium (Sr:Ca), provide additional insight into diet and habitat use in marine mammals (Peek & Clementz, 2012). Because Ba and Sr substitute for Ca during mineralization, their incorporation

into bioapatite is closely linked to dietary intake and physiological discrimination during assimilation. In marine systems, both elements exhibit relatively stable concentrations compared to terrestrial environments, making their ratios particularly well suited for trophic applications. Importantly, Sr:Ca and Ba:Ca ratios decrease with increasing trophic position, a pattern known as biopurification. This effect arises because non-essential elements such as Sr and Ba are preferentially excluded relative to Ca during intestinal absorption and metabolic processing (Balter, 2004; Botta et al., 2015; Peek & Clementz, 2012). As a result, higher-trophic-level consumers consistently display lower Ba:Ca and Sr:Ca ratios relative to their prey (Botta et al., 2015; Peek & Clementz, 2012).

In the open ocean, Sr:Ca ratios are largely homogeneous, reflecting the long residence time of Sr in seawater. As a result, Sr:Ca in marine mammal bioapatite predominantly reflects dietary composition and trophic position rather than environmental variability (Albuquerque et al., 2012; Botta et al., 2015; Dorval et al., 2005). Ba:Ca ratios are similarly stable in offshore marine environments, though they can be modestly influenced in coastal or estuarine settings where freshwater inputs elevate Ba availability (Botta et al., 2015; Coffey et al., 1997). In Arctic marine systems dominated by shelf and open-ocean habitats, however, these environmental effects are expected to be secondary relative to trophic controls. When interpreted alongside $\delta^{13}C$ and $\delta^{15}N$, Sr:Ca and Ba:Ca therefore provide independent, physiologically grounded constraints on trophic position, strengthening the ability to distinguish dietary change from shifts driven by mobility or biogeochemical baseline variability.

1.6.2.3. $\Delta^{13}C_{carb\text{-}coll}$ as a Metabolic-Dietary Proxy

The isotopic spacing between carbonate and collagen $\delta^{13}C$ values within biomineralized tissues ($\Delta^{13}C_{carb\text{-}coll} = \delta^{13}C_{CO3} - \delta^{13}C_{collagen}$) provides a powerful proxy for reconstructing dietary composition, macronutrient routing, and metabolic organization in mammals. A broad consensus in stable isotope ecology holds that $\delta^{13}C_{collagen}$ primarily reflects the protein component of the diet, whereas $\delta^{13}C_{CO3}$ reflects the whole diet, integrating protein, carbohydrates, and lipids (Ambrose et al., 1997; DeSantis et al., 2022). Consequently, the $\Delta^{13}C_{carb\text{-}coll}$ between these two tissue pools captures how different macronutrients are routed during tissue synthesis and varies systematically with feeding strategy and trophic ecology.

Across terrestrial mammals, $\Delta^{13}C_{carb\text{-}coll}$ exhibits strong dietary structure. Carnivores display the lowest values (typically ~4.3-4.8‰), whereas herbivores show higher values (~6.8-7.6‰), with intermediate values in omnivores (Clementz et al., 2009; DeSantis et al., 2022; Lee-Thorp et al., 1989). Lower $\Delta^{13}C_{carb\text{-}coll}$ values are associated with diets richer in meat and lipid-derived carbon, whereas higher values indicate greater reliance on carbohydrate-rich resources. $\Delta^{13}C_{carb\text{-}coll}$ has therefore been widely applied as an indicator of trophic category and relative contributions of dietary macronutrients in both modern and fossil mammals (Clementz et al., 2009; DeSantis et al., 2022; Lee-Thorp et al., 1989).

Although comparable reference ranges have not yet been systematically established for marine mammals, the physiological mechanisms underlying carbonate and collagen carbon incorporation are conserved across mammals, supporting the application of $\Delta^{13}C_{carb\text{-}coll}$ as a relative tracer of trophic and metabolic structure in marine systems. Recent work further demonstrates that $\Delta_{carb\text{-}coll}$ is not a fixed constant but responds sensitively to diet composition, digestive physiology, and tissue type (Eastham & Feranec, 2025). In particular, diet-driven variation in $\Delta^{13}C_{carb\text{-}coll}$ has been shown to follow consistent ecological patterns across feeding strategies, while values derived from teeth are often higher and more variable than those from bone, reflecting differences in tissue formation and metabolic routing (Eastham & Feranec, 2025). These findings highlight $\Delta^{13}C_{carb\text{-}coll}$ as a dynamic tracer of dietary-metabolic structure rather than a static trophic index.

In incrementally growing tissues, $\Delta^{13}C_{carb\text{-}coll}$ therefore provides a unique window into ontogenetic transitions in feeding ecology and metabolic organization. When evaluated alongside trophic indicators such as Ba:Ca and Sr:Ca, coherent shifts in $\Delta^{13}C_{carb\text{-}coll}$ can be interpreted as evidence for fundamental changes in diet and physiological state rather than short-term environmental variability. This makes $\Delta^{13}C_{carb\text{-}coll}$ a critical complementary proxy for disentangling dietary and metabolic change from baseline or habitat effects in long-lived Arctic marine mammals.

1.6.2.4. Compound Specific Nitrogen Isotopes of Amino Acids

$\delta^{15}N$ in individual amino acids offers a powerful, baseline-corrected approach for reconstructing trophic relationships. Compound-specific nitrogen isotope analysis of amino acids (CSIA-AA) distinguishes between source amino acids (e.g., phenylalanine), which largely retain

the $\delta^{15}N$ of primary producers and records baseline nitrogen processes, and trophic amino acids (e.g., glutamic acid), which show strong, predictable enrichment with each trophic transfer (Chikaraishi et al., 2009; Germain et al., 2013; Lorrain et al., 2009; McMahon & McCarthy, 2016; Whiteman et al., 2019). The isotopic offset between trophic and source amino acids (e.g., $\delta^{15}N$-Glu - $\delta^{15}N$-Phe) provides a robust estimate of trophic position that is largely independent of baseline variability, a critical advantage in the rapidly changing Arctic, where sea-ice decline is altering nutrient dynamics, nitrogen sources, and primary production pathways. When applied to incrementally growing tissues such as dentine, CSIA-AA allows simultaneous reconstruction of long-term trends in both trophic ecology and baseline nitrogen cycling at annual to sub-annual resolution.

CSIA-AA therefore represents a powerful complement to bulk isotope analyses by providing independent constraints on trophic position and allowing ecological changes to be disentangled from shifting nitrogen baselines. This capability is particularly valuable in the Arctic, where rapid environmental change complicates interpretation of bulk $\delta^{15}N$. However, despite its promise, CSIA-AA remains analytically demanding, sample-intensive, and has been sparsely applied to incrementally growing tissues in marine mammals, which currently limits its routine use in long-term ecological reconstructions.

1.6.3. Tracing Toxic Metals and Exposure Pathways

Toxic metals preserved in marine mammal tissues provide direct evidence of exposure to both natural and anthropogenic contaminants and offer insight into how climate-driven environmental change reshapes contaminant pathways in the Arctic. In contrast to stable isotopes that primarily reflect ecological processes such as diet and movement, trace metals record the combined influence of food-web transfer, habitat use, and changing biogeochemical conditions that regulate metal mobilization, transformation, and bioavailability. In long-lived Arctic cetaceans, incrementally growing tissues such as tusks provide an opportunity to examine how contaminant exposure has evolved over decadal timescales coincident with rapid sea-ice loss, particularly where sea-ice acts as a major seasonal mediator of atmospheric metal deposition, storage, and release.

1.6.3.1. Mercury Concentrations

As outlined in Section 1.3, reductions in sea-ice cover can alter water-column stratification and redox conditions, restructure ice-associated microbial communities, modify light exposure beneath thinning ice, and redistribute Hg methylation zones from under-ice and marginal ice environments to the open water column, shelf sediments, or estuarine settings (Heimbürger et al., 2015; Krabbenhoft & Sunderland, 2013; Stern et al., 2012; Zhang et al., 2020). These processes can change both the magnitude and spatial distribution of MeHg production and, consequently, the baseline exposure of marine food webs. Importantly, this climate sensitivity distinguishes Hg from many other toxic metals in Arctic systems. Whereas the exposure to toxic metals is strongly influenced by atmospheric scavenging and seasonal storage in snow and sea-ice, Hg bioavailability is governed by in situ biogeochemical processing. As a result, Hg concentrations in marine mammal tissues may remain stable or increase even as sea-ice loss reduces exposure to other atmospheric-derived metals.

1.6.3.2. Non-Essential Toxic Heavy Metals (Pb, Cd, As)

Toxic non-essential elements such as Pb, Cd, and As accumulate in tissues and primarily reflect environmental exposure rather than physiological regulation (Dietz et al., 2013; Outridge et al., 2005). In the Arctic, a substantial fraction of Pb, Cd, and As enters marine ecosystems through direct atmospheric deposition onto snow and sea-ice, where these metals are efficiently scavenged and seasonally concentrated. During spring melt, contaminants stored in snowpacks and sea-ice are released into surface waters, producing short-lived but biologically important exposure pulses that coincide with periods of intense feeding by marine mammals. As sea-ice cover diminishes, this seasonal trapping and pulsed release mechanism weakens, potentially reducing bioavailable metal exposure even if total atmospheric deposition remains unchanged (AMAP, 2018; De Vera et al., 2021a; Macdonald et al., 2005; Stern et al., 2012).

In addition to those seasonal exposure fluctuations, these metals have distinct spatial patterns in the Arctic. Surface Pb concentrations in the Arctic Ocean are generally lower than in Atlantic-derived waters, reflecting reduced contemporary emissions and scavenging during long-range transport (De Vera et al., 2021b; Rogalla et al., 2025). However, Atlantic inflow can introduce higher Pb concentrations and distinct isotopic signatures, while coastal and shelf waters

influenced by river discharge and sediment resuspension often show locally elevated Pb levels (Colombo et al., 2019; De Vera et al., 2021b; Rogalla et al., 2025). Cd and As display nutrient-like behavior in the ocean, with relatively low concentrations in surface waters due to biological uptake and higher concentrations at depth (Azizur Rahman et al., 2012; Gerringa et al., 2021; Sunda, 2012). In the Arctic, enhanced Cd and As concentrations are frequently observed in shelf and near-coastal regions influenced by freshwater input, benthic fluxes, and sediment-water interactions (Gerringa et al., 2021; Perryman et al., 2020). As sea-ice loss alters stratification, productivity, and shelf-basin exchange, the distribution and bioavailability of these metals may shift independently of trophic changes.

In marine mammals, Pb, Cd, and As concentrations primarily reflect environmental exposure integrated through diet and habitat use rather than physiological regulation. In incrementally growing tissues such as tusks, these metals record changes in exposure associated with movement across water masses, shifts in foraging regions, or climate-driven reorganization of contaminant delivery to Arctic marine ecosystems (De María et al., 2021; Dietz et al., 2021; Evans et al., 1995; Hobson & Sease, 1998; Outridge & Stewart, 1999).

1.6.3.3. Pb Isotopes as a Tracer of Contaminant Sources

Lead isotopes ($^{206}Pb/^{204}Pb$, $^{208}Pb/^{206}Pb$, $^{206}Pb/^{207}Pb$) add a source-diagnostic dimension to Pb concentration data. Distinct isotopic signatures characterize natural crustal material, riverine inputs, and anthropogenic emissions, allowing Pb isotopes to trace contaminant provenance (De Vera et al., 2021b; Maccali et al., 2018; Olivelli et al., 2025). In the Arctic, Pb inputs arise from both oceanic transport and direct atmospheric deposition. Atlantic-derived waters generally carry higher Pb concentrations and more radiogenic isotopic compositions than Arctic surface waters, reflecting historical industrial emissions transported from lower latitudes via ocean circulation (Colombo et al., 2019; De Vera et al., 2021b; Rogalla et al., 2025). However, recent work has shown that atmospheric deposition remains a major pathway for Pb delivery to the Arctic, with aerosols and snowfall introducing isotopically distinct anthropogenic Pb directly to sea-ice, snowpacks, and surface waters, independent of oceanic mixing (De Vera et al., 2021b).

In regions with extensive seasonal ice cover, this atmospheric pathway may dominate Pb delivery to surface waters, further decoupling Pb isotopic signatures from ocean circulation alone.

As a result, Pb isotopic compositions in marine mammals integrate multiple exposure pathways. Changes in migratory behavior or increased use of Atlantic-influenced waters can shift Pb isotope ratios through altered water-mass exposure, while changes in atmospheric deposition intensity or source regions can modify isotopic signatures without any change in habitat use. In narwhals, Pb isotopes preserved in tusk dentin therefore record an integrated signal of contaminant provenance, atmospheric inputs, and spatial exposure. When combined with independent mobility proxies such as $\delta^{18}O$, Pb isotopes can help disentangle migration-driven exposure from changes driven primarily by atmospheric deposition or shifts in contaminant source regions.

1.7. Narwhals as Model Species

In this thesis, narwhals (*Monodon monoceros*) are used as a model to evaluate how rapid sea-ice decline is reshaping Arctic marine ecosystems and contaminant exposure. Narwhals are especially informative for this purpose because their ecology is tightly constrained by sea-ice, their annual movements are highly predictable and uniquely structured in accordance with their respective population, and they occupy a high trophic position throughout the duration of their multi-decade lifespan. These characteristics make narwhals particularly sensitive to the physical and biogeochemical transitions described in Sections 1.1-1.3 and provide a clear ecological context for testing whether long-term chemical trends reflect (i) changes in diet and mobility or (ii) broader baseline reorganization of Arctic biogeochemistry.

Narwhals differ from many Arctic marine mammals in four key ways that directly align with the objectives of this thesis: 1) Strong dependence on sea-ice which links their habitat use, prey access, and exposure pathways to ice dynamics (Laidre et al., 2008, 2015), 2) high site fidelity and well-defined migratory corridors, which provide testable expectations in interpreting long-term habitat changes (Chambault et al., 2020; Shuert et al., 2022), 3) high trophic position and long lifespan, which integrates environmental and toxicological signals over decades (Dietz et al., 2021), and 4) a unique continuously growing tusk, which provide a chronological record for evaluating how ecological behavior, contaminant exposure and sea-ice covary through time and through history (Dietz et al., 2021; Nweeia et al., 2014).

1.7.1. Population Structure and Migratory Patterns

Narwhals have a circumpolar Arctic distribution, occurring primarily in Canadian and Greenlandic waters (COSEWIC, 2004; Lowry et al., 2017). Their seasonal distribution is structured into populations with strong fidelity to specific summering areas and consistent seasonal migrations between coastal habitats and offshore wintering grounds (COSEWIC, 2004; Heide-Jørgensen et al., 2003; Laidre et al., 2008). This predictable seasonal range is important for this thesis because it provides a clear ecological framework for testing whether long-term chemical trends arise from changes in where narwhals spend time (i.e., water-mass exposure) versus changes occurring within the ecosystem itself (i.e., baseline shifts).

Three main narwhal populations are recognized based on their summering distributions: the Baffin Bay population, the Hudson Bay population, and the East Greenland population (COSEWIC, 2004). Each population returns annually to the same coastal summering fjords and inlets during summer and uses relatively consistent migratory corridors in spring and autumn (COSEWIC, 2004; Heide-Jørgensen et al., 2003; Laidre et al., 2008). During winter, they occupy deep offshore waters beneath dense pack ice, surfacing only at leads for breathing, and migrate to coastal summer habitats in spring (Chambault et al., 2020).

In the Baffin Bay region, narwhals aggregate in deep coastal inlets and archipelago channels in the Canadian High Arctic (Finley, 1976; Read & Stephansson, 1976; Richard et al., 1994), migrating between High Arctic summering areas and wintering grounds in Baffin Bay and Davis Strait (COSEWIC, 2004). The Hudson Bay population summers in northwest Hudson Bay and Foxe Basin, and winters primarily in eastern Hudson Strait (COSEWIC, 2004; Gaston & Ouellet, 1997; Gonzalez, 2001; Richard, 1991). The East Greenland population remains largely restricted to Greenlandic waters (COSEWIC, 2004).

Sea-ice dynamics is the primary driver of narwhal migration timing and corridor use. Delayed autumn freeze-up has been associated with later fall migrations, consistent with narwhals tracking the shifting ice edge and adjusting movements to seasonal freeze-up and melt (Laidre & Heide-Jørgensen, 2011; Laidre et al., 2015; Shuert et al., 2022). This strong spatial fidelity represents long-term adaptation to Arctic seasonality but may also increase their vulnerability as ice regimes, vessel traffic, and industrial activity change along the same corridors narwhals repeatedly use

(Blackwell et al., 2018; Heide-Jørgensen et al., 2013, 2015; Heide-Jørgensen, 2018; Laidre et al., 2008, 2015; Reeves et al., 2014; Watt et al., 2013).

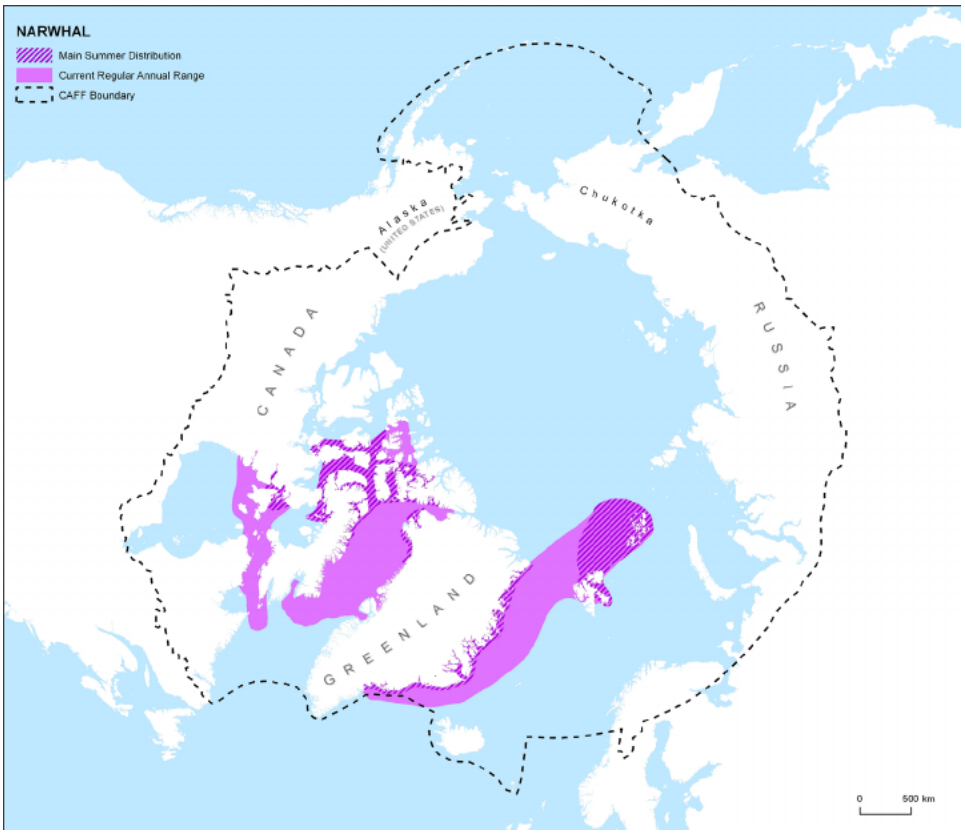

Figure 2. Circumpolar distribution of narwhal populations, annual ranges, and main summering areas. Figure used from Reeves et al. (2014).

1.7.2. Foraging Ecology and Diet

Narwhals are deep-diving predators whose foraging ecology is strongly shaped by seasonal movements, sea-ice conditions, and access to deep-water prey. Their diet is often described as relatively selective, with heavy reliance on a narrow suite of prey species that varies seasonally and by region (Heide-Jørgensen et al., 2013; Heide-Jørgensen, 2018; Laidre et al., 2008; Neve, 1995; Watt et al., 2013, 2017).

Seasonal feeding patterns reflect reproductive timing and habitat accessibility. During summer, feeding activity is often reduced and individuals may rely more on energy reserves while prioritizing calving and use of coastal habitats (Finley & Gibb, 1982; Heide-Jørgensen, 2018; Laidre & Heide-Jorgensen, 2005; Mansfield et al., 1975; Marcoux et al., 2012). Summer diets

consist primarily of Arctic cod (*Boreogadus saida*), capelin (*Mallotus villosus*), polar cod (*Arctogadus glacialis*), squid (*Gonatus sp.*), and shrimp (*Pandalus sp.*), consistent with prey availability in those coastal habitats (Blackwell et al., 2018; Heide-Jørgensen et al., 2014; Watt et al., 2013). The low foraging intensity during summer is supported by stomach content and stable isotope analyses showing reduced prey diversity compared to winter months (Finley & Gibb, 1982; Laidre et al., 2004; Laidre & Heide-Jørgensen, 2005; Mansfield et al., 1975; Watt et al., 2013, 2017).

During the spring and fall, narwhals exhibit transitional foraging when moving along migratory routes, targeting Arctic cod and polar cod (Laidre & Heide-Jorgensen, 2005; Marcoux et al., 2012). In fall, feeding activity increases with the consumption of shrimp, *Gonatus* squid, Arctic cod, and polar cod (Heide-Jørgensen, 2018; Laidre et al., 2003, 2004; Laidre & Heide-Jørgensen, 2005; Marcoux et al., 2012).

Feeding typically intensifies in autumn and winter. During winter, narwhals perform repeated deep dives (>1000 m) to forage on deep benthic and mesopelagic prey, particularly Greenland halibut (*Reinhardtius hippoglossoides*), with squid contributing in some regions (Dietz et al., 2021; Heide-Jørgensen et al., 2002; Laidre et al., 2003, 2004, 2008; Laidre & Heide-Jørgensen, 2005; Watt et al., 2017). Regional differences are apparent: narwhals in northern Hudson Bay primarily target benthic prey and individuals in Baffin Bay preferentially consume higher-trophic-level prey like Greenland halibut (Heide-Jørgensen, 2018). These seasonal and regional contrasts provide an ecological basis for comparing Baffin Bay and Hudson Bay individuals under the same multi-decadal sea-ice decline interval.

1.7.3. Tusk of the Narwhal

The narwhal tusk represents one of the defining morphological features of the species and is best understood in biological terms as a highly modified tooth that grows continuously throughout the life of the animal. The tusk originates from the elongated left maxillary canine and may exceed 3 m in length (COSEWIC, 2004; Heide-Jørgensen, 2018; Nweeia et al., 2012, 2014). Tusk development is strongly sexually dimorphic: males typically possess an erupted left tusk and an embedded right tusk, whereas females typically retain two embedded tusks, although exceptions occur (COSEWIC, 2004; Heide-Jørgensen, 2018; Nweeia et al., 2012).

Tusk eruption begins when narwhals reach approximately 2.5 m body length and continues gradually through life (Heide-Jørgensen, 2018). Growth occurs by incremental deposition of dentin, so the tusk provides a chronological record in which earlier growth is preserved toward the distal end and later growth nearer the base (Dietz et al., 2021). Beyond its role in social and sexual selection, the tusk has been proposed to function as a sensory structure, with dentinal tubules and innervation potentially allowing detection of environmental conditions, such as water temperature, salinity and pressure (Berkovitz, 2013; Dietz et al., 2021; Nweeia et al., 2014). Tusks provide a rare, life-long sequence of growth that can be sampled through time to evaluate how narwhal exposure and ecology track the rapid loss of sea-ice.

1.7.4. Chemical Incorporation: Stable Isotopes, Trace Elements, and Metals

Traditional approaches such as satellite telemetry, genetics, and stomach content analysis have established the seasonal ecology and population structure of narwhals, but they are limited in duration and provide only partial insight into multi-decadal trajectories of diet, habitat use, and contaminant exposure at the individual level. In contrast, the continuously growing narwhal tusk preserves a sequential, time-ordered record of chemical incorporation that can be used to reconstruct ecological and environmental histories across decades. Because tooth dentin is deposited incrementally and remains chemically stable over time, the tusk provides a chronological framework in which multiple tracers can be measured at annual to sub-annual resolution within the same individual (Dietz et al., 2021; Garde et al., 2012; Heide-Jørgensen, 2018).

In this thesis, tusk chemistry is used to test competing explanations for long-term change in Arctic marine ecosystems. Narwhals migrate between distinct seasonal habitats, forage across coastal and offshore prey fields, and experience strong seasonal coupling to sea-ice. These characteristics create clear testable predictions when using a combination of independent proxies. Conversely, if major chemical shifts occur without corresponding evidence for large changes in movement or trophic structure, then those shifts more plausibly reflect reorganization of baseline biogeochemistry and contaminant pathways associated with sea-ice decline. The tusk therefore provides an integrated archive for distinguishing ecological plasticity (diet and mobility) from climate-driven environmental restructuring (baseline and exposure change) within the same animals.

1.8. Objectives and Hypotheses

This thesis aims to determine whether chemical variability preserved in narwhal tusks primarily reflects inherent ecological flexibility, such as in mobility behaviour, diet, and trophic level, or whether these records instead capture a broader restructuring of Arctic marine biogeochemical cycles during a period of rapid sea-ice decline.

To test these competing explanations, this study integrates multiple geochemical proxies and compares two narwhals of similar age from two oceanographically distinct populations (Baffin Bay and Hudson Bay) spanning the same ~25-year interval marked by major reductions in sea-ice cover. By employing annual sampling resolution, this thesis evaluates whether mobility, diet, and contaminant exposure changed in predictable ways, or whether shifts in $\delta^{13}C$ and $\delta^{15}N$ isotopes are better explained by ecosystem-wide baseline changes.

1.8.1. Objective 1: Constrain Mobility and Water-Mass Use

Hypothesis 1: Oxygen isotope ratios ($\delta^{18}O$) recorded in narwhal tusk dentin will reflect interannual use of distinct water masses consistent with known, population-specific migratory corridors. Because Baffin Bay and Hudson Bay differ markedly in freshwater influence and oceanographic structure, we expect systematic differences in mean $\delta^{18}O$ values between individuals from these populations. However, directional long-term changes in mobility proxies through time are expected to be modest, reflecting strong site fidelity and relatively stable migratory behavior despite sea-ice decline. If long-term trends in bulk $\delta^{13}C$ and $\delta^{15}N$ were primarily driven by changes in migration or habitat use, then these isotopic shifts should covary with independent indicators of water-mass and spatial use, such as $\delta^{18}O$ and Pb isotopes.

Testable prediction: If temporal trends in $\delta^{13}C$ and $\delta^{15}N$ do not covary with $\delta^{18}O$ or Pb isotopes, then changes in migration or water-mass use cannot account for the observed long-term isotopic shifts.

1.8.2. Objective 2: Evaluate Long-Term Dietary Shifts

Hypothesis 2: Elemental ratios sensitive to trophic position, particularly Ba:Ca and Sr:Ca, together with $\Delta^{13}C_{carb\text{-}coll}$, will record both ontogenetic and ecological variation in narwhal diet. Ontogenetically, younger narwhals are expected to occupy lower trophic positions and consume smaller prey, whereas older individuals progressively target larger, higher-trophic-level prey. This life-history progression should be expressed as gradual, age-related decreases in Ba:Ca and Sr:Ca through early to mid-life, reflecting increasing trophic position, accompanied by systematic changes in $\Delta^{13}C_{carb\text{-}coll}$ reflecting shifts in dietary composition and macronutrient routing.

Superimposed on this ontogenetic signal, population-specific dietary differences may be present between Baffin Bay and Hudson Bay individuals due to regional prey availability and foraging habitats. However, because Ba:Ca, Sr:Ca, and $\Delta^{13}C_{carb\text{-}coll}$ are largely governed by trophic and physiological processes and are relatively insensitive to large-scale baseline biogeochemical change, we predict that neither ontogenetic dietary shifts nor regional dietary differences alone will explain major, coherent directional trends in bulk $\delta^{13}C$ and $\delta^{15}N$ through time. If long-term $\delta^{13}C$ and $\delta^{15}N$ trends primarily reflect changes in ecosystem baselines associated with sea-ice loss, then they should decouple from trophic indicators once ontogenetic effects are accounted for.

Testable prediction: If dietary change is the dominant driver of isotopic variation, then $\delta^{13}C$ and $\delta^{15}N$ should covary with Ba:Ca, Sr:Ca and $\Delta^{13}C_{carb\text{-}coll}$ after accounting for age-related (ontogenetic) trends. A lack of covariance, particularly during periods of rapid sea-ice decline, would indicate that baseline biogeochemical restructuring, rather than diet alone, governs the observed isotopic shifts.

1.8.3. Objective 3: Determine Changes in Contaminant Exposure

Hypothesis 3: Trace-metal profiles in narwhal tusks will primarily reflect long-term changes in exposure pathways driven by sea-ice decline, rather than large, sustained shifts in diet or migration. Specifically, the loss of seasonal sea-ice is expected to weaken the atmospheric “scavenging-storage-melt pulse” mechanism that concentrates many metals in snow and ice and releases them to surface waters during spring melt. If this mechanism diminishes, exposure to non-essential

metals that are efficiently scavenged and seasonally stored (e.g., Pb, Cd, As) should decline through time, even if trophic position remains relatively stable. In contrast, Hg may remain stable or increase because its bioavailability is strongly influenced by in situ methylation and redox-driven biogeochemical processing that can intensify or shift location as sea-ice conditions and stratification change.

Testable prediction:

- If declining sea-ice reduces seasonal metal pulsing, Pb:Ca, Cd:Ca, and As:Ca should show a coherent long-term decrease that is not mirrored by dietary proxies (Ba:Ca, Sr:Ca, $\Delta^{13}C_{carb\text{-}coll}$) or indicators of mobility and water-mass exposure ($\delta^{18}O$, Pb isotopes).
- If Hg is governed by changes in methylation and MeHg availability rather than atmospheric scavenging and storage, Hg may diverge from Pb, Cd, and As trends (stable or increasing when other metals decline).
- A systematic decoupling between non-essential metal trends and trophic/mobility indicators would support an exposure-pathway shift consistent with climate-driven reorganization of sea-ice-mediated contaminant cycling.

1.8.4. Objective 4: Test the Role of Arctic Biogeochemical Restructuring

Central Hypothesis of the Thesis:

When all proxies are integrated, long-term trends in bulk $\delta^{13}C$ and $\delta^{15}N$ cannot be fully explained by changes in mobility or diet alone. Instead, these isotopic records are hypothesized to reflect a systematic shift in baseline biogeochemical conditions associated with Arctic-wide restructuring of nutrient and contaminant pathways during sea-ice decline.

Under this framework, the dominant long-term isotopic signal preserved in narwhal tusks is expected to emerge from environmental change rather than solely from ecological plasticity. If supported, the tusk record would document a fundamental reorganization of Arctic marine biogeochemistry over the last ~25 years, coincident with the rapid loss of seasonal sea-ice.

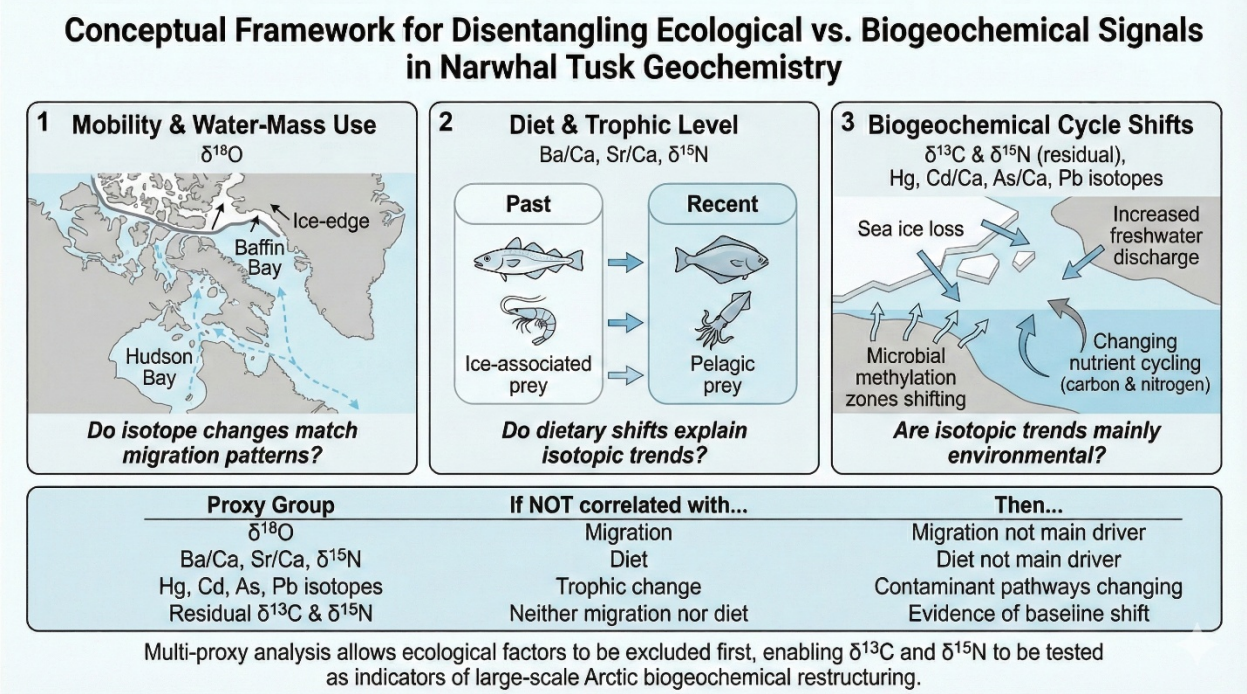

Figure 3. Conceptual framework illustrating how narwhal tusks record ecological and biogeochemical signals through time. Together, these proxies allow narwhal tusks to disentangle ecological behaviour from environmental change. Figure created using Google Gemini.

1.9. Overview of Thesis Structure

This thesis therefore uses the narwhal tusk as a natural archive to test whether long-term geochemical variation in Arctic marine mammals primarily reflects ecological flexibility, or whether it records a broader, climate-driven restructuring of Arctic marine biogeochemical cycles. By combining a multi-proxy framework with high-resolution, intra-individual sampling from two distinct populations encompassing the temporal period of rapid sea-ice decline, this study provides a rare opportunity to isolate and independently assess the roles of mobility, diet, contaminant exposure, and environmental baseline change. Through this approach, the tusk becomes not only a record of individual life history, but a means to evaluate whether Arctic ecosystems have already undergone substantial ecological and biogeochemical restructuring. The following chapter describes the analytical strategy developed to test these hypotheses.

This thesis is organized into five chapters. Chapter 1 synthesizes current knowledge on rapid environmental change in the Arctic and its impacts on sea-ice, biogeochemical cycles, food webs, contaminant pathways, and marine mammals, introduces narwhals as a model species for

studying these changes, highlights key knowledge gaps, and presents the research objectives, hypotheses, and predictions guiding this work. Chapter 2 details the materials and methods, including specimen selection, GLG sampling, analytical techniques for stable isotopes, trace metals, and major elements, and statistical approaches. Chapter 3 presents the results, focusing on temporal trends and time series of isotopic and elemental variables, principal component analyses and correlation matrices, statistical assessments of relationships among geochemical proxies and environmental variables, and isotopic niche comparisons. Chapter 4 offers a comprehensive discussion of narwhal diet and migration strategies, contaminant exposure, and population-level baseline shifts, with particular emphasis on disentangling ecological processes from climate-driven biogeochemical restructuring in Baffin Bay. Finally, Chapter 5 synthesizes the main findings, outlines the broader ecological implications for Arctic marine ecosystems, and identifies key directions for future research.

CHAPTER 2: MATERIALS AND METHODS

The flowchart in Figure 4 summarizes the sampling and analytical workflow for isotopic and elemental analyses of narwhal tusks, illustrating the sequential steps involved in sample collection, preparation and laboratory analyses for trace metals, major elements, and isotopic components.

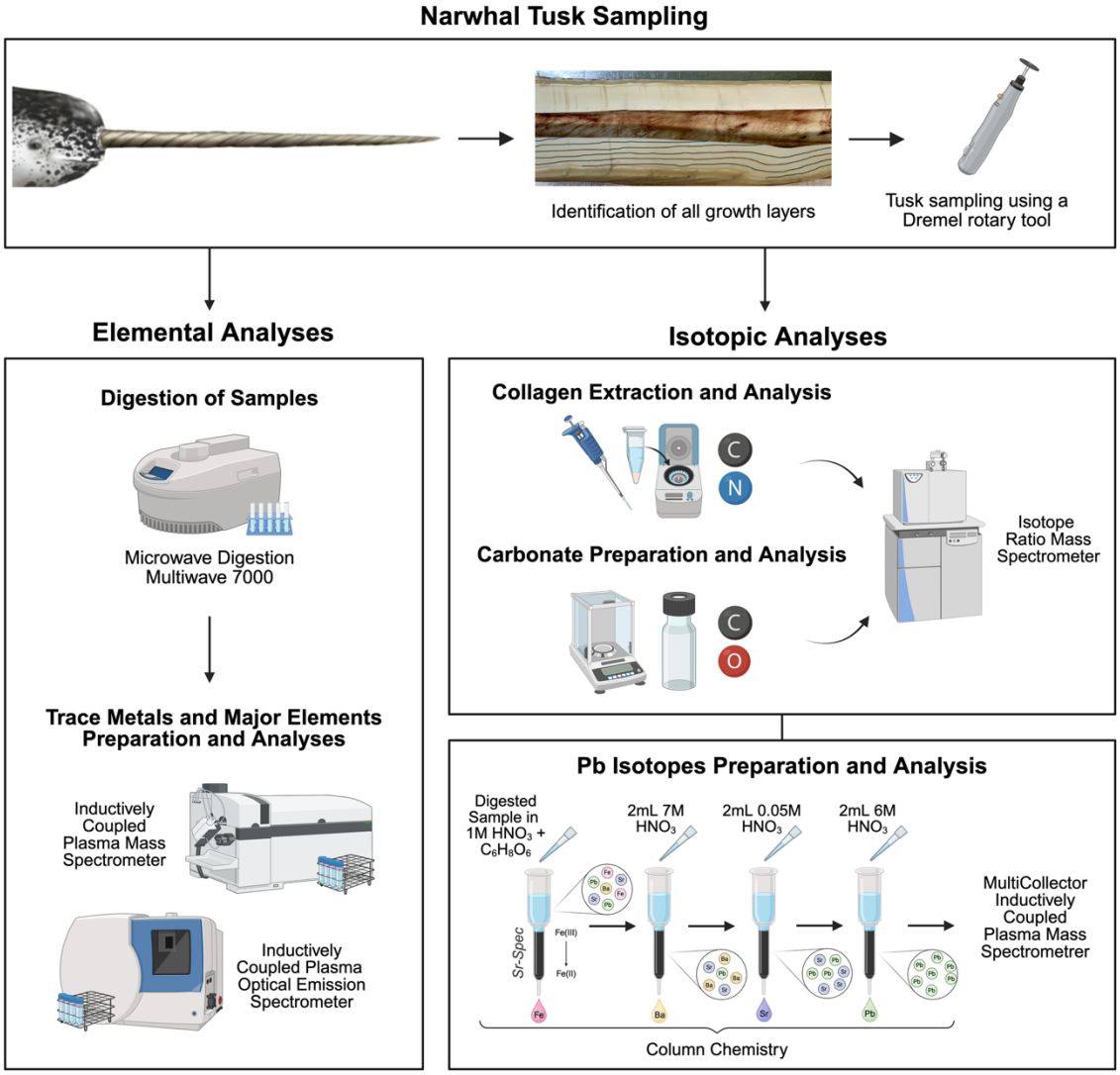

Figure 4. Overview of the sampling and analytical workflow for isotopic and elemental analyses of narwhal tusks. The flowchart illustrates the sequential steps for sample collection, preparation, and laboratory analyses for trace metals, major elements, and isotopic components. The figure was created with BioRender.com and the narwhal illustration was adapted from Britannica Editors (2025).

2.1. Specimen Overview

To develop the isotope tools to trace the mobility, diet and environmental exposure of narwhals, we selected two tusks archived from the Department of Fisheries and Ocean (DFO). Those tusks were selected because they are approximately the same length and they represent individuals that lived approximately to the same age (~25 years) around the same time (date of collection was similar). Most importantly, these two individuals belonged to two distinct but well-studied populations with different mobility and dietary habits with plenty of modern data serving as a reference for developing geolocation or dietary inferences from isotopes.

The Baffin Bay tusk (Tusk 1) was collected in 2020 in Arctic Bay by a local hunter. The tusk measures 180 cm in length, with an intact tip, and is curated at the DFO facility in Winnipeg, Manitoba (ID AI-2020-244-S). The hunter reported that the specimen belonged to the Baffin Bay population and was potentially a female. Genetic analyses were conducted, but the results were inconclusive and therefore could not support the hunter's statement.

The Hudson Bay tusk (Tusk 2) was collected in 2021 in Naujaat, also known as Repulse Bay. The tusk measures 187.4 cm, the tip is intact, and it is also curated at the DFO facility in Winnipeg (ID NHB-2021-068-A). The specimen was reported by the hunter to originate from the Hudson Bay population and was confirmed to be albino through genetic and eye analyses, according to DFO.

Figure 5. Photographs of the two narwhal tusks analyzed in this study. (**A**) AI-2020-244-S (Tusk 1; Baffin Bay) shown on the left, and (**B**) NHB-2021-068-A (Tusk 2; Hudson Bay) shown on the right. At the time the photographs were taken, Tusk 1 had been cut into two segments (with a third segment to be prepared subsequently), whereas Tusk 2 had already been divided into three segments.

2.2. Annual Sampling

To test whether isotopes could uncover distinct mobility and dietary habits with climate, ontogeny and population of origin of each individual, we needed high resolution sampling at annual resolution. Annual sampling would allow for comparison of the long-term life history of individuals within distinct ontogenetic stages and population in a changing climate.

To facilitate sampling, the tusks were longitudinally bisected at DFO. The central cavities were cleaned with brushing and water to remove all residual tissue and blood, after which the tusks were disinfected with ethanol. To enhance the visibility of growth layer groups (GLGs) and minimize interference from surface contaminants, the exposed surfaces were sanded with an orbital sander and subsequently with waterproof sandpaper under water.

GLGs were identified by carefully tracing each growth band to the next. They were first outlined with pencil markings, then incised along these marks using an X-Acto knife. The pencil traces were later removed with ethanol. In total, 24 GLGs were identified and counted in each tusk, likely representing approximately 24 years of individual life history.

All samples were collected using a 7760 4.0V Max High-Performance Wireless LITE Dremel rotary tool equipped with a 1/8-inch tungsten carbide bit. The Dremel head was placed at the center of each GLG and run laterally along a GLG band. As GLG widths were approximately ¾ the size of the drill head, the entire GLG width was sampled, and care was taken to avoid drilling deeper than 1mm to avoid mixing underlying GLG. This approach ensures that "annual samples" represented approximately a year based on the presumed duration of GLG. The drill was used to produce homogeneous powdered samples, which were collected on weighing paper and transferred into pre-labeled and pre-weighed centrifuge tubes. Between each sampling, a duster was used to remove residual powder from the tusk surface, the tool and bit, and from hands to prevent cross-contamination between layers. In total, 24 annual samples were collected from each tusk, resulting in 48 samples ranging from 100 to 250 mg. Samples from Tusk 1 were labeled BB-01 to BB-24, and those from Tusk 2 were labeled HB-01 to HB-24, with numbering progressing from the tip (01) to the base (24).

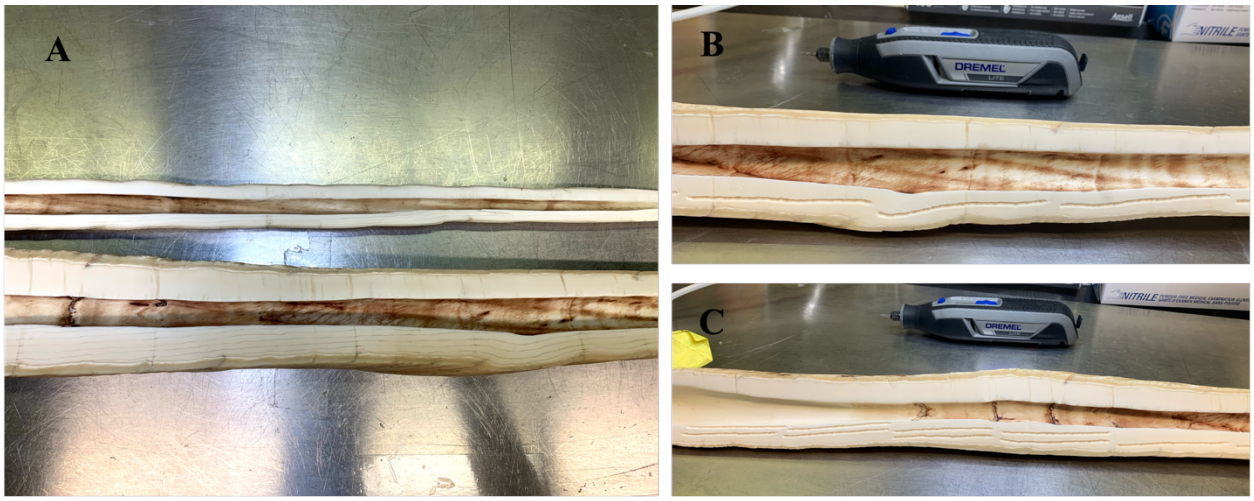

Figure 6. Photographs illustrating the identification and sampling of growth layer groups (GLGs) in narwhal Tusk 1 (Baffin Bay). (**A**) Identification of annual GLGs along the tusk's longitudinal section. (**B**) Annual sampling marks following each GLG in the middle portion of the tusk, (**C**) Annual sampling marks on the end segment of the tusk, corresponding to the last GLGs.

2.3. Collagen Extraction and Analysis

As a pre-requisite to carbon and nitrogen isotope analysis, collagen extraction was carried out on all 48 annual powdered tusk samples. Approximately 10 mg of material from each sample was weighed and transferred into pre-labeled plastic microcentrifuge tubes. To initiate decalcification, 1.5 mL of 0.1 M HCl was added to each tube, and the contents were briefly homogenized with a vortex mixer. The microcentrifuge tubes were left open and covered with aluminum foil to allow degassing before being stored at 4 °C for 30 minutes. Following decalcification, samples were centrifuged at 7,000 RPM for 7 minutes. The supernatant acid solution was removed by aspiration using plastic pipettes assigned to each sample, leaving the collagen fraction at the bottom of the tube. To rinse the collagen, 1.5 mL of distilled water was added to each tube, which were then vortexed and centrifuged again at 7,000 RPM for 7 minutes. The rinse water was subsequently removed by aspiration. This rinsing step was repeated five times in total. Afterward, the collagen residues were freeze-dried overnight and stored in a desiccator until analysis.

For isotopic analysis, approximately 1 mg of collagen from each sample and 0.5 mg of standards were weighed into tin capsules. These were analyzed for $\delta^{13}C$ and $\delta^{15}N$ values using an elemental analyzer (Vario EL Cube, Elementar, Germany) coupled via a Conflo IV interface (Thermo Finnigan, Germany) to an isotope ratio mass spectrometer (IRMS; Delta XP, Thermo Finnigan, Germany) at the Ján Veizer Stable Isotope Laboratory, Ottawa. Samples underwent flash combustion (Dumas method) at 1800°C, and the resulting gases were carried by helium through oxidation and reduction columns optimized for CO_2 and N_2 separation. The products were then purified using a purge-and-trap adsorption column before entering the IRMS interface for isotopic measurement.

Isotope ratios are expressed using the standard δ notation:

$$\delta = \left(\frac{R_{sample} - R_{standard}}{R_{standard}}\right) \times 1000$$

where R is the ratio of the abundance of the heavy to the light isotope. Collagen $\delta^{13}C$ ($\delta^{13}C_{collagen}$) values are reported in ‰ relative to the Vienna Pee Dee Belemnite (VPDB) standard

and are normalized to internal standards calibrated to international standards: IAEA-CH-6 (-10.45±0.03‰; Coplen et al., 2006), NBS-22 (-29.91±0.04‰; Coplen et al., 2006), USGS-40 (-26.24±0.042‰; Qi et al., 2003), and USGS-41 (37.76±0.049‰; Qi et al., 2003). Collagen $\delta^{15}N$ ($\delta^{15}N_{collagen}$) values are reported in ‰ relative to air (AIR) and are normalized to internal standards calibrated to international standards: IAEA-N1 (+0.4±0.07‰; Kendall & Grim, 1990), IAEA-N2 (+20.3±0.12‰; Kendall & Grim, 1990), USGS-40 (-4.52±0.1‰; Qi et al., 2003), and USGS-41 (47.57±0.2‰; Qi et al., 2003).

Internal laboratory standards included C-51 nicotinamide ($\delta^{15}N$ = 0.07±0.2‰, $\delta^{13}C$ = -22.95±0.2‰,), C-52 (ammonium sulphate + sucrose; $\delta^{15}N$ = 16.58±0.2‰, $\delta^{13}C$ = -11.94±0.2‰), and C-54 caffeine ($\delta^{15}N$ = -16.61±0.2‰, $\delta^{13}C$ = -34.46±0.2‰). C-55, a blind standard of L-glutamic acid, was analyzed alongside samples for both isotopes and percent elemental composition. Across seven replicate analyses, C-55 produced values of $\delta^{13}C$ = -28.53±0.08‰ and $\delta^{15}N$ = -3.98±0.23‰, which fall within the expected values of $\delta^{13}C$ = -28.52‰±0.16‰ (n = 3,687) and $\delta^{15}N$ = -3.90±0.19‰ (n = 3,548). Elemental composition of C-55 was 40.88±0.39% C and 9.47±0.37% N, consistent with expected values of 40.82% C and 9.52% N.

Percent elemental composition for samples was determined from IRMS signal areas at mass 44 for carbon and mass 28 for nitrogen, with calibration against C-51 nicotinamide (59.01% C, 22.94% N) and C-54 caffeine.

2.4. Carbonate Preparation and Analysis

Carbonate isotope analyses ($\delta^{13}C_{CO3}$ and $\delta^{18}O_{CO3}$) were performed on both annual and seasonal tusk samples. Approximately 5 mg of powdered material from each sample, along with 0.5-1 mg of reference standards, were weighed into 12 mL glass vials (Exetainer). For each sample, 0.3 mL of previously prepared 100% phosphoric acid (H_3PO_4, specific gravity of 1.91) was added to the shoulder of the horizontally positioned vial. The vials were then capped and helium-flushed for four minutes at a flow rate of 60 to 70 mL per minute, verified with a flowmeter (ADM 1000, Agilent Technologies, USA).

Following helium flushing, vials were placed upright and reacted at 70°C for 24 hours. The resulting CO_2 was extracted in a continuous helium flow using a GasBench II (Thermo Finnigan, Germany) connected to a Conflo IV interface (Thermo Finnigan, Germany). Isotopic compositions

were measured on a Delta XP isotope ratio mass spectrometer (Thermo Finnigan, Germany). Six peaks were recorded per analysis and averaged to generate final values. Analytical precision was ±0.1‰ (2σ).

$\delta^{13}C_{CO3}$ measurements were calibrated against two international standards: NBS-19 (C-35; +1.95‰; Ghosh et al., 2005) and NBS-18 (C-36; 5.01±0.035‰; Verkouteren & Klinedinst, 2003). $\delta^{18}O_{CO3}$ were calibrated to the same two international standards: NBS-19 (C-35; -2.20‰; Friedman et al., 1982) and NBS-18 (C-36; -23.00±0.1‰, Verkouteren & Klinedinst, 2003).

During analysis, a capillary within the GasBench partially snapped prior to sample HB-24 through sample HB-34. These correspond to the last annual sample (HB-24) and the then seasonal samples (HB-25 to HB-34) collected from Tusk 2. This caused irregular gas flows and incomplete peak shapes, rendering the affected measurements unreliable. The capillary was replaced, and the entire tray was re-analyzed, including the first set of standards and samples HB-24 through HB-34. Re-run data for all standards were consistent with expected values, and duplicate analyses of samples confirmed that the integrity of the carbonate gases in the vials was unaffected.

For samples BB-01 to BB-34 and HB-01 to HB-23, 4 replicates of the internal blind standard C-44 Lalime were analyzed ($\delta^{13}C$ = -1.9±0.09‰, $\delta^{18}O$ = -21.8±0.09‰). For samples HB-25 to HB-34, 4 replicates of the internal standard C-44 Lalime were analyzed ($\delta^{13}C$ = -1.8±0.1‰, $\delta^{18}O$ = -21.8±0.05‰). All replicates of the blind standard match the expected values of $\delta^{13}C$ = -1.84±0.37‰ (n = 11,332) and $\delta^{18}O$ = -21.97±0.35‰ (n = 10,819). $\delta^{18}O$ values were corrected using the phosphoric acid fractionation factor for calcite at 70 °C (α = 1.008692), as reported by Sharma et al. (2002) and recommended by IUPAC guidelines (Kim et al., 2015).

To facilitate comparison with oceanographic datasets, $\delta^{18}O_{CO3}$ values were converted from the VPDB to the VSMOW scale using the IUPAC-recommended relationship (Kim et al., 2015):

$$\delta^{18}O_{VSMOW} = 1.0309 \times \delta^{18}O_{VPDB} + 30.92$$

Both VPDB and VSMOW values are reported in Tables 10 and 22, although only VSMOW-converted values are used in comparisons with ocean water data.

2.5. Correction for $\delta^{13}C$ values

To account for the decline in oceanic $\delta^{13}C$ values caused by the anthropogenic addition of isotopically light CO_2 (known as the Suess effect), all measured $\delta^{13}C$ values were corrected following the exponential model originally proposed by Hilton et al. (2006) and later adopted in Clark et al. (2021). The Suess effect correction factor was calculated as:

$$\text{Suess Effect Correction Factor} = -0.011 \times e^{(b \times 0.027)}$$

where *b* is the number of years since 1850, representing the onset of the industrial revolution, and *e* is the base of the natural logarithm (2.71828). The coefficient -0.011 represents the rate of decline in $\delta^{13}C$ per year, derived from Dietz et al. (2021) and supported by De La Vega et al. (2019), who quantified similar trends in Arctic marine systems. The exponential parameter 0.027 was obtained by Hilton et al. (2006) after fitting a curve to global surface ocean $\delta^{13}C$ data from Gruber et al. (1999), spanning 1945-1997. This model describes the temporal decrease in $\delta^{13}C$ of dissolved inorganic carbon due to the progressive incorporation of anthropogenic CO_2 into the oceans. Corrected $\delta^{13}C$ values were then calculated as:

$$\delta^{13}C_{\text{Suess Effect}-\text{Corrected}} = \delta^{13}C_{\text{Measured}} - \text{Suess Effect Correction Factor}$$

This correction allows for temporal comparability among samples collected across different decades by normalizing $\delta^{13}C$ values to pre-industrial baselines unaffected by fossil fuel emissions.

2.6. Trace Metals Preparation and Analysis

Prior to trace metal analysis, all samples were digested. All handling and digestion steps were conducted in a clean laboratory environment to minimize contamination. Acid-cleaned PTFE digestion vials were prepared with concentrated TraceMetal™ Grade HNO_3 (Fisher Chemical, Mississauga, ON, Canada). Between 50 mg and 250 mg of powdered tusk material was weighed into each vial using a precision analytical balance. The reference material NIST SRM 1486 (bone

meal**)** was included and processed in parallel with the tusk samples following the same digestion and analytical procedures.

1 mL of concentrated nitric acid (HNO_3) was added to each digestion vial, which was placed in a Teflon liner containing 150 mL of deionized water and 5 mL of concentrated HNO_3. Samples were digested using a Multiwave 7000 microwave system (Anton Paar, Austria), ramping from ambient temperature to 250°C over 20 minutes, and held at 250°C for 15 minutes under pressure. The digests were then transferred into pre-cleaned Teflon containers and rinsed twice with Milli-Q water to recover any remaining material. The samples were evaporated on a hotplate at 80°C overnight until dry, leaving a white residue. Each residue was re-dissolved in 2% v/v HNO_3 and reheated at 80°C for 24 hours to ensure complete dissolution.

An 0.1 mL aliquot of each digestate was pipetted into a 15 mL acid-cleaned centrifuge tube and diluted into 2% TMG (Trace Metal Grade) HNO_3 containing indium (In) as an internal standard. Calibration standards were prepared from certified single-element stock solutions (SCP Science Inc., Montreal, QC, Canada). Two multi-element mixes (Mix A and Mix B) were prepared at 100, 50, 25, 12.5, 6.25, and 3.125 ppb, along with three check standards at 12.5 ppb for quality assurance. All standards and samples were spiked with indium to correct for instrumental drift and matrix effects. Standards were diluted from 10 ppm stock solutions using 2% v/v HNO_3 + In, following rigorous pipette-rinsing and acid-cleaning procedures to minimize cross-contamination.

The trace metal analyses were performed using inductively coupled plasma mass spectrometry (ICP-MS; Agilent 8800 Triple Quadrupole ICP-MS Spectrometer, Agilent Technologies Inc., Santa Clara, CA, USA) at the Department of Earth and Environmental Sciences, University of Ottawa. Two distinct ICP-MS analytical runs were conducted. Run 1 included samples BB-16 to BB-20 and HB-11 to HB-15, with approximately 50 mg of sample material per digestion. Run 2 included all remaining samples, with sample masses ranging between approximately 50 mg and 250 mg. The run 2 was analyzed at a slightly higher dilution factor to limit calcium (Ca) concentrations.

A total of 20 elements were analyzed in each annual sample: Al, K, Ca, Sc, Ti, V, Cr, Mn, Fe, Co, Ni, Cu, Zn, As, Sr, Mo, Cd, In, Ba, and Pb. Calibration curves were generated for each element, and procedural blanks were analyzed throughout each run to monitor contamination. Following data acquisition, all ICP-MS results were processed by applying blank corrections, standard-curve calibration, and indium-based drift correction. Concentrations were recalculated

according to the appropriate dilution factor and expressed as element concentrations within the tusk. Based on detection limits, only calcium (Ca) manganese (Mn; Run 1 RSD = 2.49%; Run 2 RSD = 6.33%), iron (Fe; Run 1 RSD = 3.78%; Run 2 RSD = 12.53%), arsenic (As; Run 1 RSD = 5.38%; Run 2 RSD = 14.56%), cadmium (Cd; Run 1 RSD = 5.38%; Run 2 RSD = 14.74%), and lead (Pb; Run 1 RSD = 3.10%; Run 2 RSD = 16.02%) were above quantification thresholds and retained for interpretation. All RSD values were based on four replicate quality-control standards analyzed for each run at 12.5 ppb (n = 4). RSD values were not reported for Ca because Ca concentrations in the control standards are ~4 orders of magnitude lower than Ca concentrations in the analyzed samples. The high Ca concentrations lead to blank values to reach magnitude similar to the control standard. As a result, the reported QC RSD values are not representative of the actual precision at the high Ca concentrations measured in the samples.

2.7. Alkaline-Earth Metals and Major Elements Preparation and Analysis

Alkaline-Earth Metals (Ba, Sr and Ca) along with other key elements (Al, B, Co, Cr, Cu, Fe, K, Mg, Mn, Na, Ni, P, S, Sc, Si, Ti, V, and Zn) were also analyzed by inductively coupled plasma optical emission spectrometry (ICP-OES; Agilent 5110 Synchronous Dual View ICP Emission Spectrometer, Agilent Technologies Inc., Santa Clara, CA, USA) at the Department of Earth and Environmental Sciences, University of Ottawa.

An aliquot from the supernatant was pipetted in an acid-clean 15 mL centrifuge tube and diluted by adding 2% TMG HNO_3. Calibration standards were prepared from certified single-element stock solutions (SCP Science Inc., Montreal, QC, Canada). Two multi-element standard mixes (Mix A and Mix B) and a Ca series were prepared for calibration. The Ca standards were prepared at concentrations of 100, 50, 25, and 12.5 ppm, while Mix A and B standards were prepared at 10, 5, 2.5, 1.25, and 0.625 ppm, along with three check standards at 1.25 ppm for quality assurance. All standards were diluted in 2% v/v HNO_3.

Analyses were performed in two runs: Run 1 included samples BB-16 to BB-20 and HB-11 to HB-15, while Run 2 included all remaining samples. The same sample masses were used for digestion, and all samples were diluted twice to achieve a final dilution factor (DF) of approximately 2000 prior to analysis. The certified reference material NIST SRM 1486 (bone

meal) was analyzed alongside the samples to verify calibration accuracy and analytical reproducibility.

Calibration standards were prepared from certified single-element stock solutions (SCP Science Inc., Montreal, QC, Canada). Two multi-element standard mixes (Mix A and Mix B) and a Ca series were prepared for calibration. The Ca standards were prepared at concentrations of 100, 50, 25, and 12.5 ppm, while Mix A and B standards were prepared at 10, 5, 2.5, 1.25, and 0.625 ppm, along with three check standards at 1.25 ppm for quality assurance. All standards were diluted in 2% v/v HNO_3 + indium (In) to monitor instrumental drift, and all pipetting and rinsing steps followed strict acid-cleaning protocols to minimize contamination.

Samples and standards were analyzed on the Agilent 5110 ICP-OES under standard operating conditions. Analytical wavelengths were selected to minimize inter-element interference and optimize signal stability. Calibration curves were constructed for each element using the prepared standards, and procedural blanks were analyzed periodically to monitor background contamination.

Following data acquisition, results were corrected for blanks and calibrated using external standard curves. Instrumental drift was assessed using the mean standard deviation of all quality control standards, which were measured repeatedly throughout each analytical run. Since indium was not selected as an internal standard during analysis, drift correction was based on the stability and reproducibility of these quality control standards rather than internal normalization. Concentrations were recalculated according to the final dilution factor and expressed as elemental concentrations within the tusk material.

After data screening and quality control, only magnesium (Mg; Run 1 RSD = 0.35%; Run 2 RSD = 0.19%), chromium (Cr; Run 1 RSD = 0.06%; Run 2 RSD = 0.32%), cobalt (Co; Run 1 RSD = 0.029%; Run 2 RSD = 0.32%), zinc (Zn; Run 1 RSD = 0.39%; Run 2 RSD = 0.40%), calcium (Ca; Run 1 RSD = 0.21%; Run 2 RSD = 0.57%)**,** strontium (Sr; Run 1 RSD = 0.44%; Run 2 RSD = 0.42%), and barium (Ba; Run 1 RSD = 0.54%; Run 2 RSD = 0.25%) were above detection limits and retained for interpretation. All RSD values were based on four replicate quality-control standards analyzed per run (n = 4).

2.8. Hg Concentrations

Narwhal samples (5-20 mg) were analyzed for mercury (Hg) concentrations using a NIC MA-series mercury analyzer (Nippon Instruments Corporation, Japan) via combustion coupled with vapor atomic absorption, following the mineral protocol (sample heating to 850°C for 8 minutes), at the Motta Lab within the Woods Hole Oceanographic Institution. Analytical accuracy and precision were monitored using NRC TORT-3 lobster hepatopancreas (certified value 0.292±0.022 µg/g; Willie et al., 2013) and NIST SRM 1646a Estuarine Sediment (non-certified reference value ≈ 0.04 mg/kg; May & Rumble, 2004). TORT-3 analyzed under the organic protocol yielded a mean of 0.287±0.006 µg/g (n = 11), while 1646a analyzed under the mineral protocol returned 0.0295±0.0012 µg/g (n = 7). The TORT-3 results were within 2% of the certified value, and 1646a was comparable to its reported reference value, confirming analytical consistency throughout the sequence. Instrument calibration was performed with a reference Hg-cysteine solution, producing an R^2 value of 0.999.

2.9. Pb Isotopes Preparation and Analysis

Lead (Pb) elemental separation and isotope analyses were conducted at the MC-ICP-MS Facility of the Department of Geological Sciences, University of Cape Town, South Africa.

Lead was separated from the sample matrix using column chemistry following the procedures of Pin et al. (2014). These methods enable the rapid and simultaneous elemental separation of Sr, Pb, and Nd from complex matrices prior to isotope ratio determination by mass spectrometry. All resin columns and acids were prepared and calibrated under clean-lab conditions to minimize contamination, and procedural blanks were monitored throughout.

Purified Pb fractions were analyzed on a Nu Instruments Plasma3 MC-ICP-MS coupled to an Aridus 3 desolvating sample introduction system. Measurements were conducted using 10^{12} Ω resistors on Faraday detectors to enhance signal precision for low-concentration samples (~5 ppb Pb and lower).

Each analytical session was bracketed with measurements of the NIST SRM981 lead isotopic reference material and all data reported are normalised to accepted values of $^{208}Pb/^{204}Pb$ = 36.7219±0.0044**,** $^{207}Pb/^{204}Pb$ = 15.4963±0.0016, and $^{206}Pb/^{204}Pb$ = 16.9405±0.0015 (Galer &

Abouchami, 1998). NIST SRM997 was added to all sampled and standards to yield Pb:Tl ratios of ±10, with instrumental mass fractionation then corrected using the exponential law and a $^{205}Tl/^{203}Tl$ ratio of 2.3889 following Galer & Abouchami (1998).

Internal precision (2σ) for individual measurements typically ranged from ±0.0005 to ±0.0100, depending on isotopic ratio and signal intensity. Blanks were negligible compared to the total Pb signal. The resulting isotope ratios were expressed as $^{206}Pb/^{204}Pb$, $^{207}Pb/^{204}Pb$, $^{208}Pb/^{204}Pb$, $^{207}Pb/^{206}Pb$, and $^{208}Pb/^{206}Pb$, and data quality was verified using repeated analyses of SRM981 and internal consistency checks among standards and procedural duplicates.

2.10. Statistical Analysis

All statistical analyses were performed in R (v.4.5.1; packages readxl, dplyr, broom, purrr, writexl, factoextra, corrplot, and ggplot2). Analyses were restricted to annual growth layers for both tusks, with data examined separately for each tusk and for both combined when relevant. A significance threshold of $\alpha = 0.05$ was used, with $p \leq 0.05$ considered significant and $p \leq 0.01$ highly significant.

To assess whether variables followed a normal distribution, Shapiro-Wilk tests were conducted on all isotope ratios ($\delta^{13}C_{collagen}$, $\delta^{15}N_{collagen}$, $\delta^{13}C_{CO3}$, and $\delta^{18}O_{CO3}$), Hg concentrations, Pb isotope ratios ($^{206}Pb/^{204}Pb$, $^{208}Pb/^{206}Pb$, $^{206}Pb/^{207}Pb$), major elements normalized to calcium (Mg:Ca, Cr:Ca, Co:Ca, Zn:Ca, Sr:Ca, Ba:Ca), and trace metals normalized to calcium (Mn:Ca, Fe:Ca, As:Ca, Cd:Ca, Pb:Ca), with all element-to-calcium ratios normalized using Ca concentrations measured on the ICP-OES. The results were used to guide the choice of correlation analyses.

Pairwise relationships among isotopic and elemental variables were examined using Spearman's rank correlation coefficients (ρ), as most variables deviated from normality (Supplemental Material Tables 2 and 3). For isotope-only comparisons between tusks, Pearson correlations were applied when both variables were normally distributed, while Spearman correlations were used otherwise. Each correlation test returned both the correlation coefficient and associated *p*-value. Correlation matrices were constructed and visualized for each tusk.

To assess temporal trends**,** ordinary least-squares (OLS) linear regressions were fitted for each tusk separately, relating each isotopic or elemental variable (*Y*) to the yearly growth-layer group (*X*) according to the model:

$$Y = a + bX + \varepsilon$$

where *a* is the intercept, *b* is the slope (rate of change through time), and ε represents residual error. To determine whether the two tusks followed statistically similar temporal trends, models including an interaction term between yearly GLG and tusk were fitted using the equation:

$$\text{Value} \sim \text{GLG}_{\text{Year}} \times \text{Tusk}$$

where the interaction term tests for significant differences in slope between tusks. All outputs were exported to Excel for reporting and interpretation.

Principal Component Analyses (PCA) were conducted on isotopic and elemental data to identify major axes of covariation and visualize relationships among variables. Separate PCAs were performed for Tusk 1, Tusk 2, and the combined dataset. The proportion of variance explained by each principal component and variable loadings were used to interpret multivariate structure.

Isotopic niche overlap between tusks was estimated using a robust Monte Carlo approach based on $\delta^{13}C_{collagen}$ and $\delta^{15}N_{collagen}$ values. Ellipses representing 95% confidence regions were constructed for each tusk, and overlap was expressed as a Jaccard percentage, representing the proportion of shared isotopic niche space. All statistical outputs were exported to Excel for reporting and interpretation.

To assess relationships between environmental conditions and geochemical variations in narwhal tusks, non-parametric correlation analyses were conducted in R (v.4.5.1; packages readxl, dplyr, tidyr, purrr, readr, stringr, and writexl). Analyses were restricted to annual growth layers and performed separately for each tusk, using the same significance threshold of $\alpha = 0.05$, with $p \leq 0.05$ considered significant and $p \leq 0.01$ highly significant. Spearman's rank correlation coefficients (ρ) were used to evaluate associations between geochemical proxies and environmental parameters to maintain consistency with other correlation analyses performed in this study.

For Tusk 1 (Baffin Bay), annual geochemical proxies were compared with mean annual sea ice extent in Baffin Bay, as well as with mean annual sea surface temperature (SST) and salinity from Arctic Bay (85.1480° W, 73.0376° N) for the years 1997-2020. For Tusk 2 (Hudson Bay), proxies were compared with mean annual sea ice extent in Hudson Bay and with SST and salinity from Naujaat (86.2361° W, 66.5253° N) for the years 1998-2021.

Sea ice extent data were obtained from the National Centers for Environmental Information (NCEI) Regional Sea Ice database for Baffin Bay and Hudson Bay (*Baffin Bay Sea Ice Extent*, n.d.; *Hudson Bay Sea Ice Extent*, n.d.). Oceanographic variables (SST and salinity) were derived from the EN4.2.2 dataset (Good et al., 2013), which includes the .g10 correction described by Gouretski & Reseghetti (2010). As per requested, the EN.4.2.2 data were obtained from https://www.metoffice.gov.uk/hadobs/en4/ and are © British Crown Copyright, Met Office, 2013, provided under a Non-Commercial Government Licence http://www.nationalarchives.gov.uk/doc/non-commercial-government-licence/version/2/.

Environmental datasets were merged by year with corresponding tusk geochemical records, and pairwise Spearman correlations were computed between each environmental parameter and all geochemical variables, including isotopic ratios ($\delta^{13}C_{collagen}$, $\delta^{15}N_{collagen}$, $\delta^{13}C_{CO3}$, $\delta^{18}O_{CO3}$), Hg concentrations, Pb isotope ratios ($^{206}Pb/^{204}Pb$, $^{208}Pb/^{206}Pb$, $^{206}Pb/^{207}Pb$), major elements normalized to calcium (Mg:Ca, Cr:Ca, Co:Ca, Zn:Ca, Sr:Ca, Ba:Ca), and trace metals normalized to calcium (Mn:Ca, Fe:Ca, As:Ca, Cd:Ca, Pb:Ca). Benjamini-Hochberg false discovery rate (FDR) corrections were applied to account for multiple testing across all correlations and within each environmental dataset. Each test returned the correlation coefficient (ρ) and associated *p*-value. All correlation outputs were compiled and exported to Excel for reporting and interpretation.

To examine whether large-scale Atlantic circulation variability influenced long-term geochemical patterns recorded in narwhal tusks, correlations were also performed between tusk geochemical proxies and annual Atlantic circulation anomalies. Monthly circulation indices spanning 1870-2020 were obtained from the Climate Data Guide maintained by the National Center for Atmospheric Research (Trenberth & Zhang, 2025). Monthly values were averaged to produce annual anomalies, and only years overlapping with tusk records were retained for statistical analyses. For Tusk 1 (Baffin Bay), correlations were restricted to 1997-2020, whereas for Tusk 2 (Hudson Bay), analyses were limited to 1998-2020 due to the absence of data for 2021.

Pairwise Spearman rank correlations (ρ) were calculated between annual circulation anomalies and all tusk geochemical variables (Supplemental Material Tables 35 and 36), including isotopic ratios ($\delta^{13}C_{collagen}$, $\delta^{15}N_{collagen}$, $\delta^{13}C_{CO3}$, and $\delta^{18}O_{CO3}$), Hg concentrations, Pb isotope ratios ($^{206}Pb/^{204}Pb$, $^{208}Pb/^{206}Pb$, $^{206}Pb/^{207}Pb$), major elements normalized to calcium (Mg:Ca, Cr:Ca, Co:Ca, Zn:Ca, Sr:Ca, Ba:Ca), and trace metals normalized to calcium (Mn:Ca, Fe:Ca, As:Ca, Cd:Ca, Pb:Ca). Benjamini-Hochberg false-discovery-rate corrections were applied to account for multiple testing.

Long-term linear trends in Atlantic circulation anomalies were assessed using ordinary least-squares regression for both the full 1870-2020 record and the subset overlapping tusk growth (1997-2020), with slope and *p*-value (Supplemental Material Table 32).

CHAPTER 3: RESULTS

3.1. Potential Mobility Indicators Recorded in Narwhal Tusks

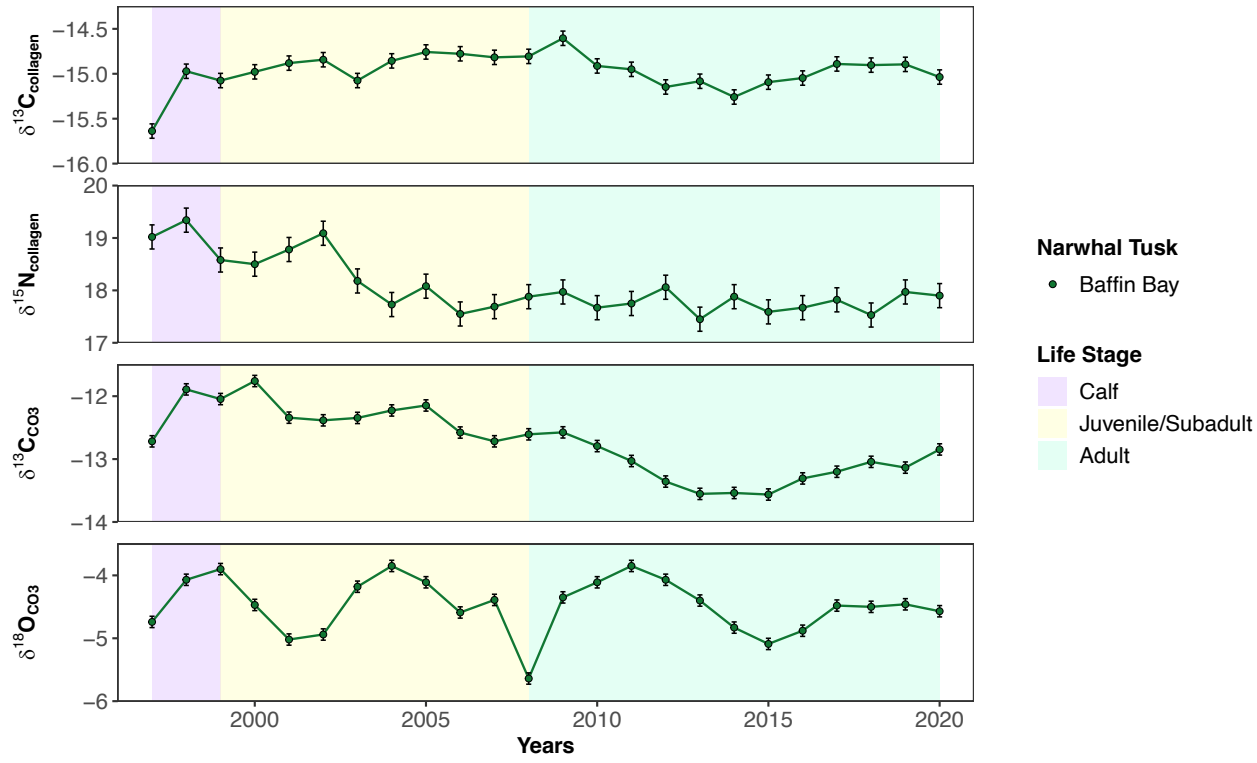

Figure 7. Time series of isotopic compositions ($\delta^{13}C_{collagen}$, $\delta^{15}N_{collagen}$, $\delta^{13}C_{CO3}$, $\delta^{18}O_{CO3}$; ‰) of Baffin Bay narwhal tusk (Tusk 1) spanning 1997-2020. Points represent annual mean isotopic values with associated analytical uncertainty (±1 SD, based on replicate measurements of laboratory standards; ‰). Shaded background bands indicate estimated life stages: calf in purple, juvenile/subadult in yellow, and adult in green (Garde et al., 2007, 2015; Heide-Jørgensen, 2018; Kingsley, 1989; Zhao et al., 2021). $\delta^{13}C_{collagen}$ and $\delta^{13}C_{CO3}$ values were corrected for the Suess effect to account for long-term atmospheric ^{13}C depletion caused by fossil fuel emissions (Clark et al., 2021; De La Vega et al., 2019; Dietz et al., 2021; Gruber et al., 1999; Hilton et al., 2006).

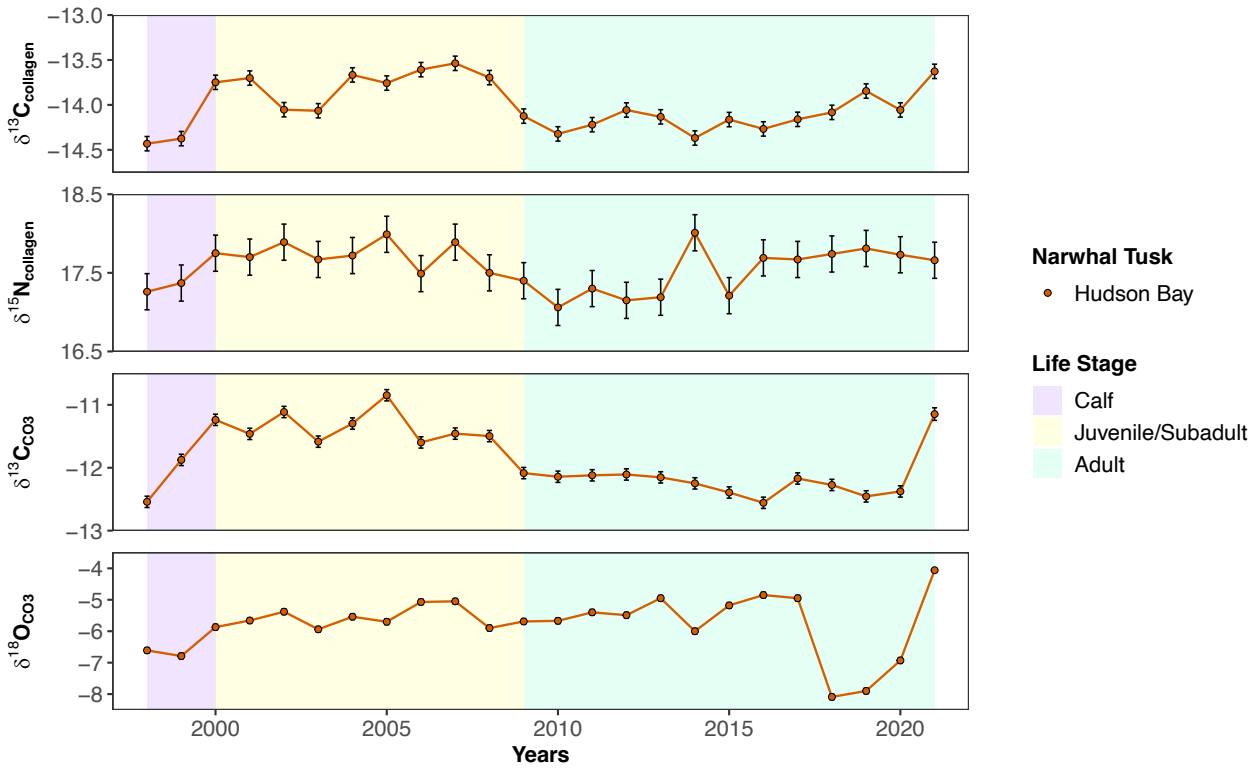

Figure 8. Time series of isotopic compositions ($\delta^{13}C_{collagen}$, $\delta^{15}N_{collagen}$, $\delta^{13}C_{CO3}$, $\delta^{18}O_{CO3}$; ‰) of Hudson Bay narwhal tusk (Tusk 2) spanning 1998-2021. Points represent annual mean isotopic values with associated analytical uncertainty (±1 SD, based on replicate measurements of laboratory standards; ‰). Shaded background bands indicate estimated life stages: calf in purple, juvenile/subadult in yellow, and adult in green (Garde et al., 2007, 2015; Heide-Jørgensen, 2018; Kingsley, 1989; Zhao et al., 2021). $\delta^{13}C_{collagen}$ and $\delta^{13}C_{CO3}$ values were corrected for the Suess effect to account for long-term atmospheric ^{13}C depletion caused by fossil fuel emissions (Clark et al., 2021; De La Vega et al., 2019; Dietz et al., 2021; Gruber et al., 1999; Hilton et al., 2006).

3.1.1. Isotope Profiles in Collagen: $\delta^{13}C_{collagen}$ and $\delta^{15}N_{collagen}$

In Figures 7 and 8, collagen $\delta^{13}C$ ($\delta^{13}C_{collagen}$) values in Tusk 1 (Baffin Bay) range from a minimum of -15.64‰ (1997) to a maximum of -14.60‰ (2009). In Tusk 2 (Hudson Bay), values range from -14.43‰ (1998) to -13.54‰ (2007). Error bars represent ±1 standard deviation (SD) of ±0.08‰ for both tusks.

Both tusks show a sharp increase in $\delta^{13}C_{collagen}$ values of similar magnitude (~0.7‰) during the early (calf) life stage, rising from -15.64‰ (1997) to -14.97‰ (1998) for Tusk 1 and from -14.43‰ (1998) to -13.75‰ (2000) for Tusk 2. In Tusk 1, values continue to rise gradually through juvenile/subadult stage, from -14.97‰ (1998) to -14.60‰ (2009), apart from a dip to -15.08‰ in 2003. In adulthood, $\delta^{13}C_{collagen}$ values then decrease to -15.26‰ (2014), rise again to -14.89‰ in 2017, and subsequently stabilize before declining slightly to a final value of -15.04‰ in 2020.

For Tusk 2, values remain relatively stable during the juvenile/subadult stage (2000-2007), except for dips in 2002 (-14.05‰) and 2003 (-14.07‰). Between 2007 and 2010, values decrease to -14.32‰. During adulthood (after 2010), values fluctuate but overall increase to reach a final value of -13.63‰ in 2021. Although both records exhibit phases of stability, decline, and increase, they do not follow the same trajectory in time. The two datasets show a consistent baseline shift, with Tusk 2 enriched in $\delta^{13}C_{collagen}$ relative to Tusk 1 (~0.5-1.2‰).

Cyclical variation is observable in both records, with three or four cycles present in both tusks (cycle 1:1997-2003, cycle 2: 2004-2010, cycle 3: 2011-2014, and cycle 4: 2015-2021). Cycle 3 is not clearly visible for Tusk 1.

In Figures 7 and 8, collagen $\delta^{15}N$ ($\delta^{15}N_{collagen}$) in Tusk 1 shows a statistically significant decreasing trend of -0.055‰ per year ($p < 0.001$; Supplemental Material Table 1). In contrast, Tusk 2 exhibits a non-significant increasing trend of +0.001‰ per year ($p = 0.862$). In Tusk 1, values range from a minimum of 17.45‰ (2013) to a maximum of 19.34‰ (1998). In Tusk 2, values range from 17.06‰ (2010) to 18.01‰ (2014). Error bars represent ±1 standard deviation (SD) of ±0.23‰ for both tusks.

In Tusk 1, $\delta^{15}N_{collagen}$ values are elevated early in life and decline progressively through the juvenile/subadult stage, decreasing from 19.02‰ (1997) to 17.55‰ (2006). From 2007 to the end of the record, $\delta^{15}N_{collagen}$ values remain relatively stable, fluctuating around 17.77‰, with a sharp drop between 2012 and 2013 (from 18.06‰ to 17.45‰). In Tusk 2, $\delta^{15}N_{collagen}$ values increase

between the calf to the juvenile/subadult life stage, rising from 17.26‰ (1998) to 17.75‰ (2000), then remain stable between 2000 and 2007, hovering around 17.76‰. Near and during adulthood, values decrease from 2008 to 2014, followed by an abrupt increase from 17.19‰ (2013) to 18.01‰ (2014). In 2015, $\delta^{15}N_{collagen}$ values decrease sharply to 17.21‰, increase in 2016 to 17.69‰, and subsequently stabilize until 2021, fluctuating around 17.72‰.

Both tusks exhibit comparable short-term increases and decreases in 2005, 2006, and 2010, as well as during the period from 2013 to 2015. Cyclical variation is present in both records, with three cycles in each tusk. For Tusk 1, these occur from 1997 to 2006, 2007 to 2013, and 2014 to 2020. For Tusk 2, the cycles occur from 1998 to 2010, 2011 to 2015, and 2016 to 2021.

3.1.2. Isotope Profiles in Dentine Carbonate: $\delta^{13}C_{CO3}$ and $\delta^{18}O_{CO3}$

In Figures 7 and 8, carbonate $\delta^{13}C$ ($\delta^{13}C_{CO3}$) values in both tusks show statistically significant decreasing trends over time, with Tusk 1 (Baffin Bay) declining at -0.060‰ per year ($p < 0.001$) and Tusk 2 (Hudson Bay) declining at -0.034‰ per year ($p = 0.022$; Supplemental Material Table 1). In Tusk 1, $\delta^{13}C_{CO3}$ values range from a minimum of -13.56‰ (2015) to a maximum of -11.76‰ (2000). In Tusk 2, values range from -12.56‰ (2016) to -10.85‰ (2005). Error bars represent ±1 standard deviation (SD), equal to 0.09‰ for both tusks except for sample HB-24, which has an SD of 0.10‰.

In both tusks, $\delta^{13}C_{CO3}$ values increase sharply during the early (calf) life, by ~0.8‰ in Tusk 1 (1997-1998) and ~1.3‰ in Tusk 2 (1997-1999). During the juvenile/subadult stage, values continue to rise from -12.72‰ (1997) to -11.76‰ (2000) in Tusk 1, and from -12.54‰ (1998) to -10.85‰ (2005) in Tusk 2, with additional short-term fluctuations after 2000. Thereafter, Tusk 1 decreases by ~1.7‰ from 2000 (-11.76‰) to 2015 (-13.56‰), and Tusk 2 decreases by ~1.8‰ from 2005 (-10.85‰) to 2016
(-12.56‰). After 2015, $\delta^{13}C_{CO3}$ values in Tusk 1 gradually increase, reaching -12.85‰ in 2020. Tusk 2 shows fluctuations from 2016 to 2020 and then increases sharply in 2021 to -11.15‰.

Throughout the records, Tusk 2 consistently shows higher $\delta^{13}C_{CO3}$ values than Tusk 1 (~0.5-1.3‰), reflecting a baseline shift between the two datasets. Cyclical variation is apparent in both records. For Tusk 1, three cycles occur from 1997 to 2007, from 2008 to 2015, and from 2016

to 2021. For Tusk 2, cycles occur from 1998 to 2009 and from 2010 to 2020, followed by a distinctly different value in 2021 that may indicate the start of a new cycle.

In Figures 7 and 8, carbonate $\delta^{18}O$ ($\delta^{18}O_{CO3}$) values in both tusks show non-statistically significant decreasing trends over time, with a slope of -0.009‰ per year ($p = 0.480$) for Tusk 1 and a slope of -0.001‰ per year ($p = 0.974$; Supplemental Material Table 1) for Tusk 2. In Tusk 1, $\delta^{18}O_{CO3}$ values range from a minimum of -5.64‰ (2008) to a maximum of -3.85‰ (2004 and 2011). In Tusk 2, values range from -8.09‰ (2018) to -4.06‰ (2021). Error bars represent ±1 standard deviation (SD), equal to 0.09‰ for both tusks except for sample HB-24, which has an SD of 0.05‰.

In Tusk 1, two cycles occur during the calf and juvenile/subadult life stages (1997-2001 and 2002-2008), followed by a pronounced drop in 2008 to -5.64‰. Two additional cycles are evident during adulthood, from 2009 to 2015 and from 2016 to 2020. In Tusk 2, two cycles also occur during calf and juvenile/subadult life stages (1998-2003 and 2004-2008), with a concurrent drop in 2008 to -5.90‰. During adulthood, additional sharp declines are observed from -4.95‰ (2013) to -6.00‰ (2014) and from -4.95‰ (2017) to -8.09‰ (2018). $\delta^{18}O_{CO3}$ values then increase markedly from 2018 to 2021, reaching -4.06‰ in 2021. Additional cycles are apparent between 2009 and 2014, 2015 and 2018, and between 2019 and 2021.

Across the record, $\delta^{18}O_{CO3}$ values in Tusk 2 are generally more negative than those in Tusk 1, with differences ranging from less than 1‰ to more than 3‰ depending on the year.

3.2. Potential Dietary Indicators Recorded in Narwhal Tusks

3.2.1. Potential Dietary Proxies in Tusk 1

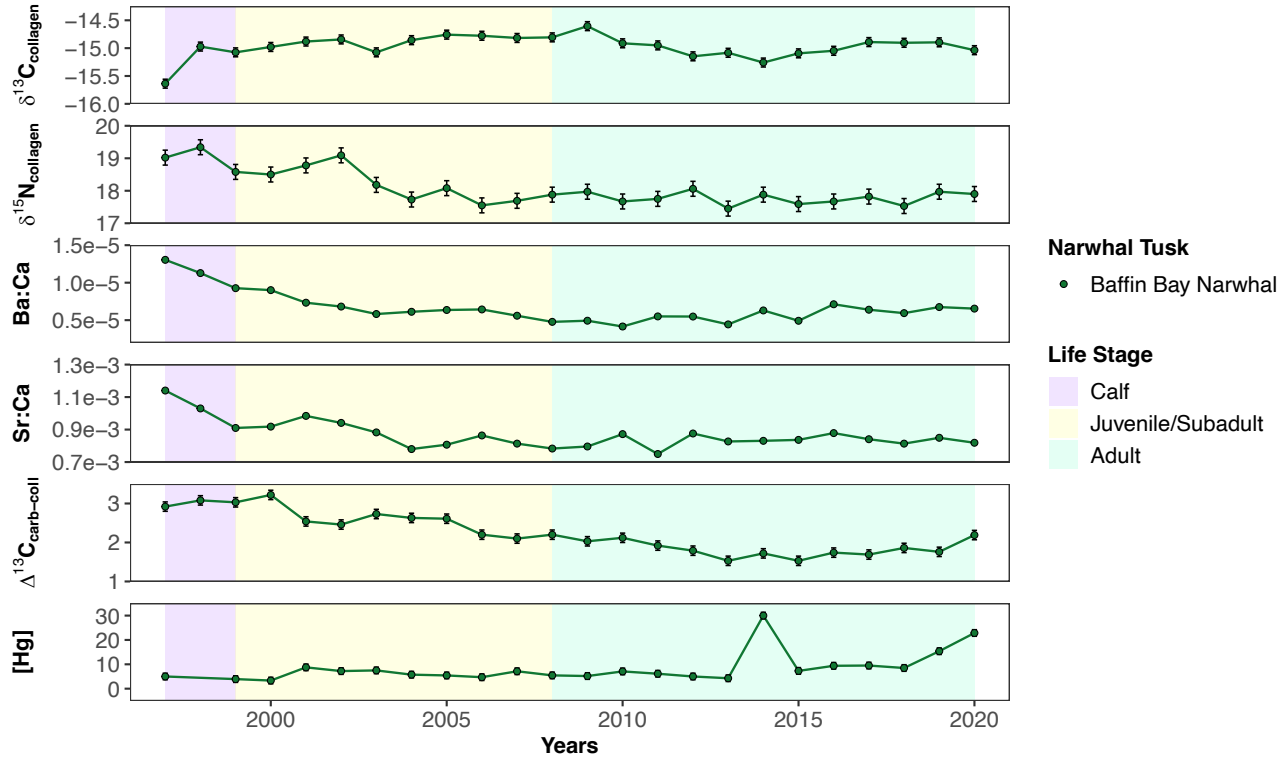

Figure 9. Time series of potential dietary proxy indicators in Baffin Bay narwhal tusk (Tusk 1) spanning 1997-2020, including $\delta^{13}C_{collagen}$ (‰), $\delta^{15}N_{collagen}$ (‰), Ba:Ca, Sr:Ca, $\Delta^{13}C_{carb\text{-}coll}$ (‰), and Hg concentrations (µg/g). Points represent annual mean isotopic values with associated analytical uncertainty (±1 SD, based on replicate measurements of laboratory standards). Shaded background bands indicate estimated life stages: calf in purple, juvenile/subadult in yellow, and adult in green (Garde et al., 2007, 2015; Heide-Jørgensen, 2018; Kingsley, 1989; Zhao et al., 2021). $\delta^{13}C_{collagen}$ values were corrected for the Suess effect to account for long-term atmospheric ^{13}C depletion caused by fossil fuel emissions (Clark et al., 2021; De La Vega et al., 2019; Dietz et al., 2021; Gruber et al., 1999; Hilton et al., 2006).

Figure 9 presents annual time series of $\delta^{13}C_{collagen}$, $\delta^{15}N_{collagen}$, Ba:Ca, Sr:Ca, $\Delta^{13}C_{carb\text{-}coll}$, and Hg concentrations for Tusk 1 between 1997 and 2020. The temporal patterns of $\delta^{13}C_{collagen}$ and $\delta^{15}N_{collagen}$ are described in detail in Section 3.1.1.

Ba:Ca values show a statistically significant decreasing trend over time with a slope of -1.76×10^{-7} per year ($p = 0.002$; Supplemental Material Table 1). Ba:Ca values are highest at the beginning of the record (1.58×10^{-5} in 1997) and decline through the calf and juvenile/subadult life stages to 4.77×10^{-6} by 2008. Thereafter, Ba:Ca exhibits interannual variability, but values remain overall low and relatively stable through the remainder of the record. Depending on the sample, the standard deviation (±1 SD) ranges from 1.52×10^{-8} to 2.91×10^{-7}.

Sr:Ca values show a statistically significant decreasing trend over time with a slope of -7.54×10^{-6} per year ($p = 0.002$). Sr:Ca follows a similar temporal pattern, with high initial values (1.14×10^{-3} in 1997) that decrease through the calf and juvenile/subadult life stages to 7.83×10^{-4} by 2008. Subsequently, Sr:Ca displays interannual variability but remains overall low and stable. The standard deviation (±1 SD) ranges from 3.27×10^{-7} to 4.36×10^{-6} across samples.

$\Delta^{13}C_{carb\text{-}coll}$ exhibits a pattern comparable to those of Ba:Ca and Sr:Ca, with a statistically significant decreasing trend over time (slope of -0.063‰ per year; $p < 0.001$). Values are highest early in the record and decline through the juvenile/subadult stage into adulthood, decreasing from 2.92‰ in 1997 to 1.53‰ in 2013. After 2013, $\Delta^{13}C_{carb\text{-}coll}$ remains relatively stable through 2020, with interannual variability. Error bars represent ±1 standard deviation (SD) of ±012‰.

Hg concentrations increase significantly over time at a rate of +0.481µg/g per year ($p = 0.010$), ranging from 3.33µg/g in 2000 to 30µg/g in 2014. Error bars represent ±1 standard deviation (SD) of ±1.35µg/g. Hg values show initial decline, followed by an increase reaching 8.75µg/g by 2001. From 2001 to 2013, Hg values remain relatively stable. Between 2015 and 2020, concentrations increase consistently, except for a small drop in 2018 to 8.48µg/g, reaching 22.86µg/g in 2020. No cyclical variations are observed. A value recorded in 1998 was excluded from the graph, as analyses resulted in negative concentrations, indicating concentrations below the detection limits.

3.2.2. Potential Dietary Proxies in Tusk 2

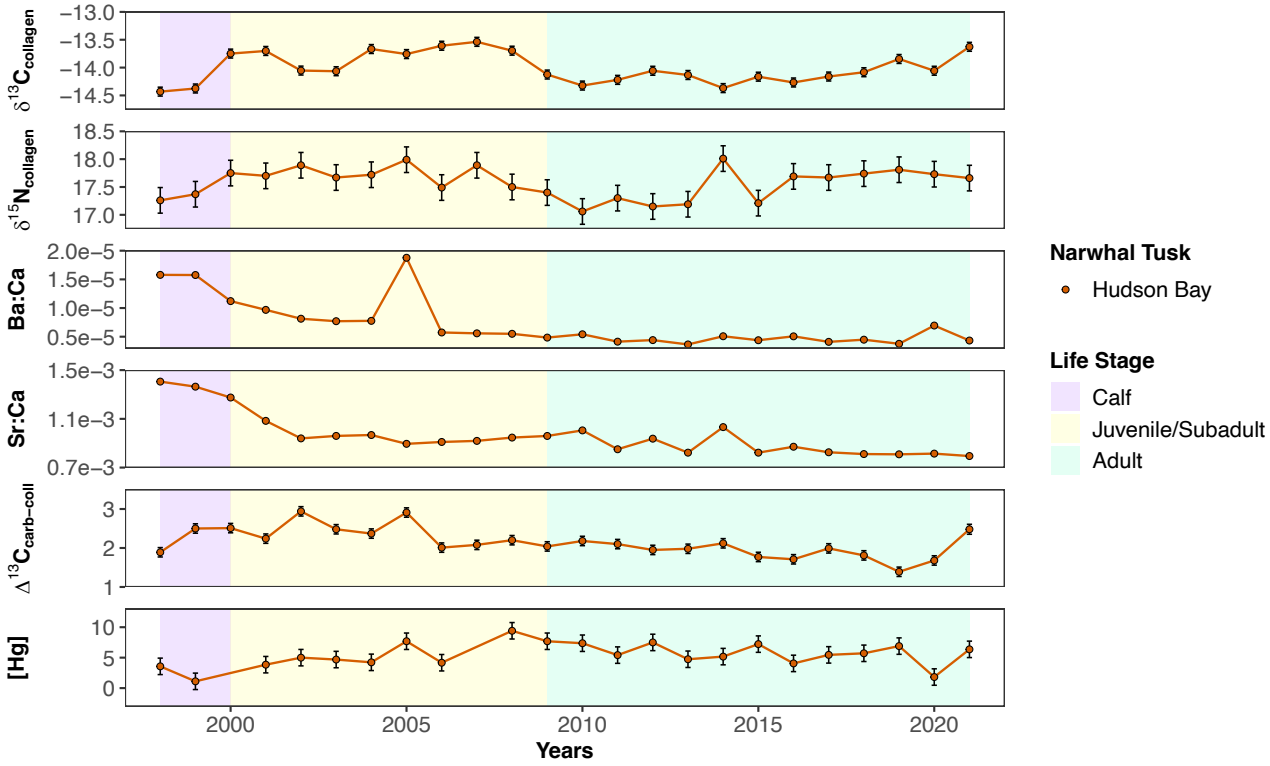

Figure 10. Time series of potential dietary proxy indicators in Hudson Bay narwhal tusk (Tusk 2) spanning 1998-2021, including $\delta^{13}C_{collagen}$ (‰), $\delta^{15}N_{collagen}$ (‰), Ba:Ca, Sr:Ca, $\Delta^{13}C_{carb\text{-}coll}$ (‰), and Hg concentrations (µg/g). Points represent annual mean isotopic values with associated analytical uncertainty (±1 SD, based on replicate measurements of laboratory standards). Shaded background bands indicate estimated life stages: calf in purple, juvenile/subadult in yellow, and adult in green (Garde et al., 2007, 2015; Heide-Jørgensen, 2018; Kingsley, 1989; Zhao et al., 2021). $\delta^{13}C_{collagen}$ values were corrected for the Suess effect to account for long-term atmospheric ^{13}C depletion caused by fossil fuel emissions (Clark et al., 2021; De La Vega et al., 2019; Dietz et al., 2021; Gruber et al., 1999; Hilton et al., 2006).

Figure 10 presents annual time series of $\delta^{13}C_{collagen}$, $\delta^{15}N_{collagen}$, Ba:Ca, Sr:Ca, $\Delta^{13}C_{carb\text{-}coll}$, and Hg concentrations for Tusk 2 between 1998 and 2021. The temporal patterns of $\delta^{13}C_{collagen}$ and $\delta^{15}N_{collagen}$ are described in detail in Section 3.1.1.

Ba:Ca values show a statistically significant decreasing trend over time with a slope of -4.16×10^{-7} per year ($p < 0.001$; Supplemental Material Table 1). Ba:Ca values are highest at the beginning of the record (1.30×10^{-5} in 1998) and decline through the calf and juvenile/subadult life stages to 4.84×10^{-6} by 2009. Thereafter, Ba:Ca exhibits interannual variability, but values remain overall low and relatively stable through the remainder of the record. Depending on the sample, the standard deviation (±1 SD) ranges from 1.27×10^{-8} to 3.25×10^{-8}.

Sr:Ca values show a statistically significant decreasing trend over time with a slope of -1.87×10^{-5} per year ($p < 0.001$). Sr:Ca follows a similar temporal pattern, with high initial values (1.41×10^{-3} in 1998) that decrease through the calf and juvenile/subadult life stages to 8.95×10^{-4} by 2005. Subsequently, Sr:Ca displays interannual variability but remains overall low and stable. The standard deviation (±1 SD) ranges from 3.31×10^{-7} to 4.97×10^{-7} across samples.

$\Delta^{13}C_{carb\text{-}coll}$ shows a statistically significant decreasing trend over time with a slope of -0.031‰ per year; $p < 0.001$). Values increase from the calf stage until the middle of the juvenile subadult stage (1.89‰ in 1998 to 2.91‰ in 2005). Values then decrease and remain relatively stable until 2019. Afterward value increase until the end of the record, reaching 2.48‰ in 2021. Error bars represent ±1 standard deviation (SD) of ±012‰, except for sample HB-24 which has an SD of 0.13‰.

Hg concentrations show an overall increasing trend through time, but this trend is not statistically significant (slope = +0.072µg/g per year, $p = 0.257$). Hg values decrease from 3.57µg/g in 1998 to 1.11µg/g in 1999, then increase to 7.69µg/g by 2005. Hg concentrations subsequently decline to 4.17µg/g in 2006, followed by a sharp increase to 9.41µg/g in 2008. After 2008, Tusk 2 shows a progressive decline to 6.36µg/g by 2021, with a notable drop in 2020 to 1.82µg/g. Error bars represent ±1 standard deviation (SD) of ±1.35 µg g-1. No cyclical variations are observed. Values recorded in 2000 and 2007 were excluded from the graph, as analyses resulted in negative concentrations, indicating concentrations below detection limits.

3.3. Trace Metal Exposure in Narwhal Tusks

3.3.1. Temporal Trends in Metal Exposure and Pb Isotopes in Tusk 1

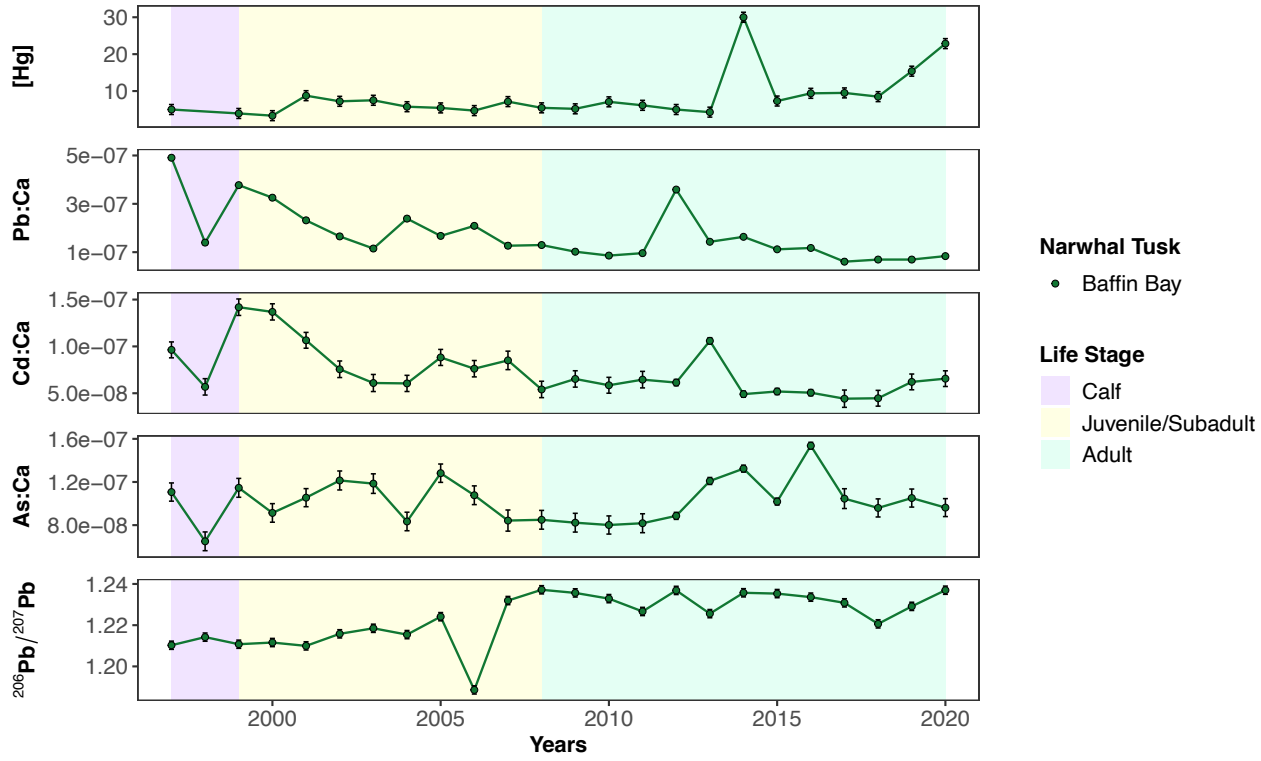

Figure 11. Time series of potential toxicological indicators in Baffin Bay narwhal tusk (Tusk 1) spanning 1997-2020, including Hg concentrations (µg/g), Pb:Ca, Cd:Ca, As:Ca, and $^{206}Pb/^{207}Pb$. Points represent annual mean isotopic values with associated analytical uncertainty (±1 SD, based on replicate measurements of laboratory standards). Shaded background bands indicate estimated life stages: calf in purple, juvenile/subadult in yellow, and adult in green (Garde et al., 2007, 2015; Heide-Jørgensen, 2018; Kingsley, 1989; Zhao et al., 2021).

Figure 11 presents annual time series of Hg concentrations, Pb:Ca, Cd:Ca, As:Ca and $^{206}Pb/^{207}Pb$ for Tusk 1 between 1997 and 2020. The temporal patterns of [Hg] are described in detail in Section 3.2.1.

Pb:Ca values show a statistically significant long-term decline, with a slope of -1.01×10^{-8} per year ($p < 0.001$; Supplemental Material Table 1). Substantial interannual variability is observed, with the highest values recorded during the calf stage (4.91×10^{-7} in 1997). Values decrease through the juvenile/subadult stage, reaching 1.15×10^{-7} in 2003. An abrupt increase occurs in 2012 (3.59×10^{-7}), after which Pb:Ca follows a sustained downward trajectory to the end of the record, reaching 8.37×10^{-8} in 2020. Depending on the sample, the standard deviation (±1 SD) ranges from 1.82×10^{-9} to 1.02×10^{-8}.

Cd:Ca values also exhibit a statistically significant decreasing trend over time, with a slope of -2.26×10^{-9} per year ($p = 0.002$). Values increase during the calf stage from 9.63×10^{-8} (1997) to 1.42×10^{-7} (2000). Following 2000, Cd:Ca values decrease steadily, reaching 6.56×10^{-8} in 2020, with an abrupt increase in 2013 at 1.06×10^{-7}. The standard deviation (±1 SD) ranges from 3.29×10^{-9} to 9.87×10^{-9} across samples.

As:Ca values show a non-statistically significant increasing trend over time, with a slope of $+3.99 \times 10^{-10}$ per year ($p = 0.518$). As:Ca values increase between 1997 and 2005, rising from 1.11×10^{-7} in 1997 to 1.28×10^{-7} in 2005. Values then fluctuate with a slight overall decline, reaching 8.86×10^{-8} in 2012. From 2012 onward, As:Ca values remain relatively stable, with minor variability, and show a slight increase toward the end of the record, reaching 9.63×10^{-8} in 2020. The standard deviation (±1 SD) ranges from 3.17×10^{-9} to 9.81×10^{-9} across samples.

$^{206}Pb/^{207}Pb$ values in Tusk 1 increase significantly over time at a rate of +0.001 per year ($p < 0.001$), ranging from 1.189 in 2006 to 1.237 in 2008 (~0.05 total variation). $^{206}Pb/^{207}Pb$ values fluctuate between 1997 and 2005 but increase overall from 1.210 to 1.224. A sharp decrease occurs in 2006 (1.189), followed by a rapid increase in 2007 (1.232). During adulthood, values continue to vary slightly but remain generally stable, reaching 1.237 in 2020. No cyclical pattern is observed for Tusk 1.

3.3.2. Temporal Trends in Metal Exposure and Pb Isotopes in Tusk 2

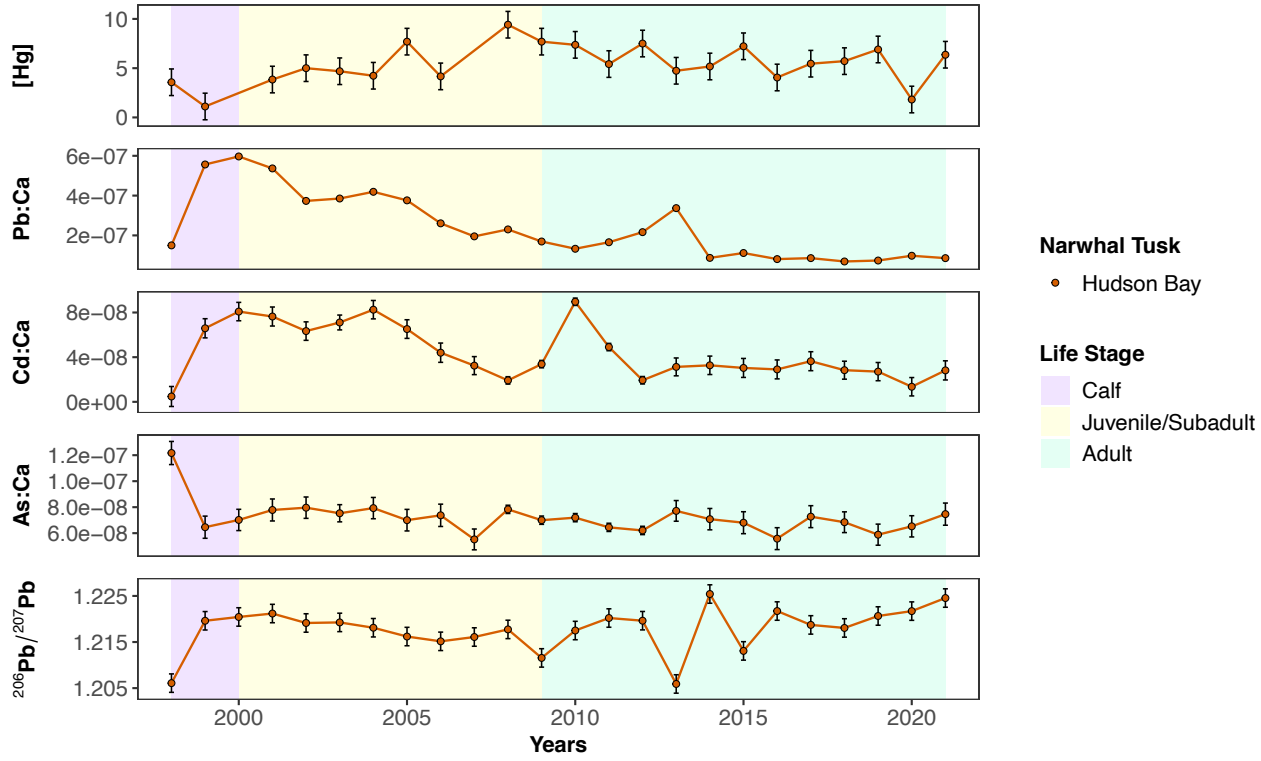

Figure 12. Time series of potential toxicological indicators in Hudson Bay narwhal tusk (Tusk 2) spanning 1998-2021, including Hg concentrations (µg/g), Pb:Ca, Cd:Ca, As:Ca, and $^{206}Pb/^{207}Pb$. Points represent annual mean isotopic values with associated analytical uncertainty (±1 SD, based on replicate measurements of laboratory standards). Shaded background bands indicate estimated life stages: calf in purple, juvenile/subadult in yellow, and adult in green (Garde et al., 2007, 2015; Heide-Jørgensen, 2018; Kingsley, 1989; Zhao et al., 2021).

Figure 12 presents annual time series of Hg concentrations, Pb:Ca, Cd:Ca, As:Ca and $^{206}Pb/^{207}Pb$ for Tusk 2 between 1998 and 2021. The temporal patterns of [Hg] are described in detail in Section 3.2.2.

Pb:Ca values exhibit a statistically significant decreasing trend over time, with a slope of -1.86×10^{-8} per year ($p < 0.001$; Supplemental Material Table 1). Pb:Ca increase sharply during the calf stage, rising from 1.50×10^{-7} (1998) to 5.97×10^{-7} (2000). Thereafter, values decrease to 8.58×10^{-8} (2021), except for a peak in 2014 (8.70×10^{-8}). Depending on the sample, the standard deviation (±1 SD) ranges from 1.81×10^{-9} to 9.29×10^{-9}.

Cd:Ca values show a statistically significant decreasing trend over time, with a slope of -1.84×10^{-9} per year ($p = 0.007$). Cd:Ca increases abruptly during the calf stage, from 4.79×10^{-9} (1998) to 8.08×10^{-8} (2000). Values decrease during the juvenile/subadult stage, reaching 1.92×10^{-8} in 2008. A secondary peak occurs in 2010 (8.96×10^{-8}), followed by a rapid decrease to 1.93×10^{-8} by 2012. For the remainder of the record, Cd:Ca values remain relatively stable. The standard deviation (±1 SD) ranges from 3.28×10^{-9} to 8.95×10^{-9} across samples.

As:Ca values also display a statistically significant decreasing trend over time, with a slope of -8.26×10^{-10} per year ($p < 0.001$). As:Ca declines sharply at the beginning of the record, dropping from 1.22×10^{-7} in 1998 to 6.46×10^{-8} in 1999. Thereafter, values remain relatively stable for most of the record, with two notable drops in 2007 (5.52×10^{-8}) and 2016 (5.58×10^{-8}). The standard deviation (±1 SD) ranges from 3.16×10^{-9} to 8.89×10^{-9} across samples.

$^{206}Pb/^{207}Pb$ values in Tusk 2 show no significant trend, with a slope of $+1.91 \times 10^{-4}$ per year ($p = 0.183$) and ranging from 1.206 in 2013 to 1.225 in 2014 (~0.02 total variation). Error bars represent ±1 standard deviation (SD) of ±0.002. $^{206}Pb/^{207}Pb$ values increase sharply early in life from 1.206 in 1999 to 1.220 in 2000, then remain stable though the juvenile/subadult stage aside from a notable drop in 2009 (1.212). During adulthood, values display pronounced interannual variability, with decreases in 2013 (1.206) and 2015 (1.213) and increases in 2014 (1.225) and 2016 (1.222). From 2016 onwards, values generally increase, reaching 1.225 in 2021. No cyclical pattern is observed.

3.3.3. Comparative Lead Isotope Profiles in Dentine Carbonates of Both Tusks

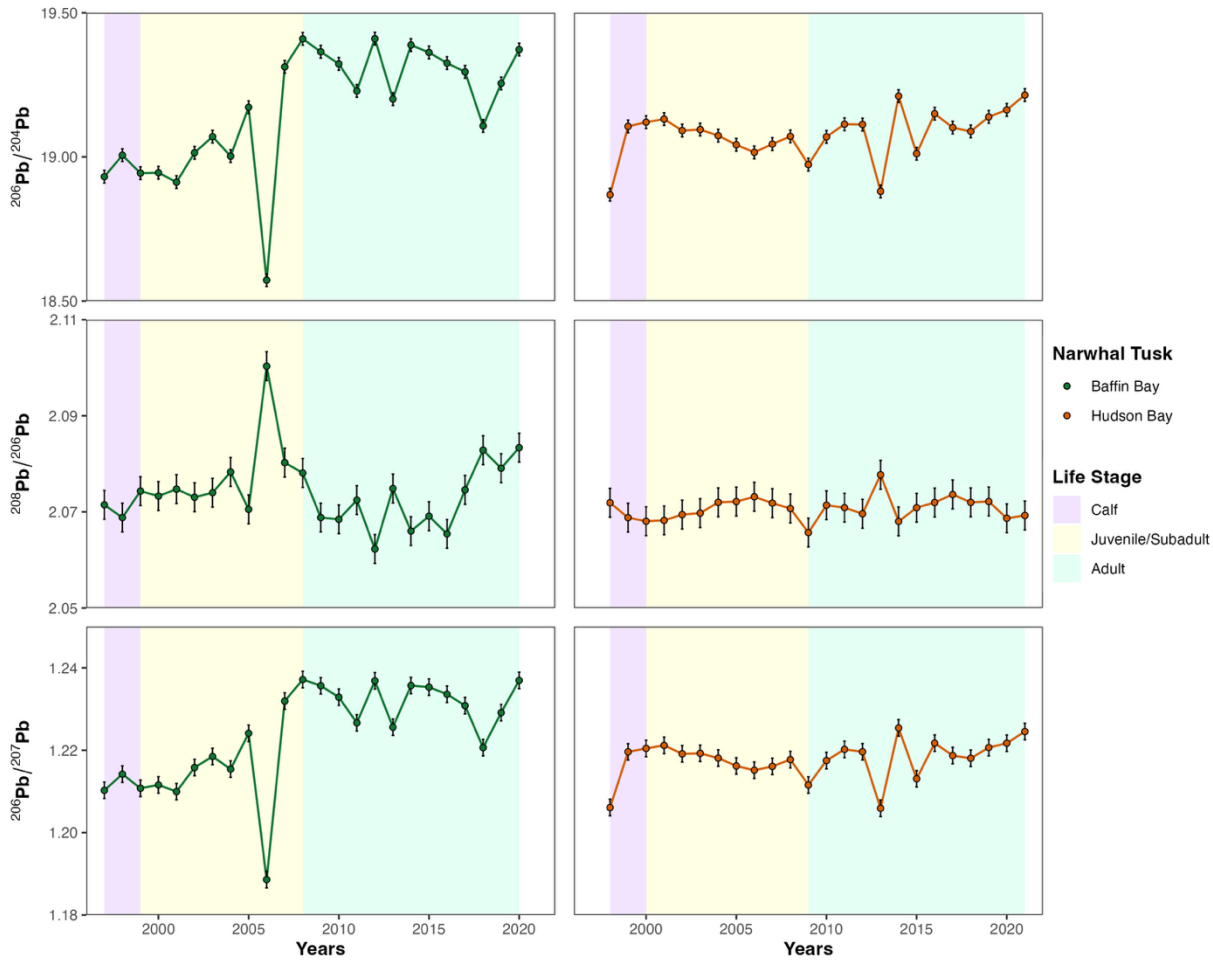

Figure 13. Time series of isotopic compositions ($^{206}Pb/^{204}Pb$, $^{208}Pb/^{206}Pb$, and $^{206}Pb/^{207}Pb$) from narwhal tusks collected in Baffin Bay (Tusk 1; left panels) and Hudson Bay (Tusk 2; right panels). Data span from 1997 to 2021. Points represent annual mean isotopic values with associated analytical uncertainty (±1 SD, based on replicate measurements of laboratory standards). Shaded background bands indicate estimated life stages: calf in purple, juvenile/subadult in yellow, and adult in green (Garde et al., 2007, 2015; Heide-Jørgensen, 2018; Kingsley, 1989; Zhao et al., 2021).

In Figure 13, $^{206}Pb/^{204}Pb$ values in Tusk 1 (Baffin Bay) increase significantly at a rate of +0.020 per year ($p < 0.001$; Supplemental Material Table 1), ranging from 18.572 in 2006 to 19.410 2012 (~0.84 total variation). In Tusk 2 (Hudson Bay), $^{206}Pb/^{204}Pb$ values increase at a slower and non-significant rate of +0.004 per year ($p = 0.079$), ranging from 18.869 in 1998 to 19.214 in 2021 (~0.35 total variation). Error bars represent ±1 standard deviation (SD) of ±0.022 for both tusks.

In Tusk 1, $^{206}Pb/^{204}Pb$ values fluctuate between 1997 and 2005 but increase overall from 18.931 to 19.172. A sharp drop occurs from 2005 (19.172) to 2006 (18.572), followed by a rapid increase to 19.312 in 2007. During adulthood (after 2008), values exhibit minor variability but remain generally stable, reaching 19.372 in 2020. No cyclical pattern is observed for Tusk 1.

In Tusk 2, $^{206}Pb/^{204}Pb$ values rise sharply during the calf stage, from 18.869 in 1998 to 19.106 in 1999, then remain stable throughout the juvenile/subadult stage aside from a notable drop in 2009 (18.973). During adulthood, values display pronounced interannual variability, with sharp decreases in 2013 (18.880) and 2015 (19.011) and increases in 2014 (19.211) and 2016 (19.150). From 2016 onwards, values generally increase, reaching 19.214 in 2021. No cyclical pattern is observed for Tusk 2.

$^{208}Pb/^{206}Pb$ values in Tusk 1 show no significant change over time, with a slope of 5.32×10^{-5} per year ($p = 0.821$; Supplemental Material Table 1) and ranging from 2.062 in 2012 to 2.100 in 2006 (~0.04 total variation). In Tusk 2, $^{208}Pb/^{206}Pb$ values also display no significant trend, with a slope of 6.43×10^{-5} per year ($p = 0.380$) and ranging from 2.066 in 2009 to 2.078 in 2013 (~0.01 total variation). Error bars represent ±1 standard deviation (SD) of ±0.003 for both tusks.

In Tusk 1, $^{208}Pb/^{206}Pb$ values remain relatively stable between 1997 and 2005, followed by a sharp increase in 2006 from 2.071 to 2.100. A gradual decline occurs between 2006 and 2010, reaching 2.068. During adulthood, values fluctuate interannually, with increases in 2011 (2.072), 2013 (2.075), and 2015 (2.069), and decreases in 2012 (2.062), 2014 (2.066), and 2016 (2.065). After 2016, values increase overall, reaching 2.083 in 2020. No cyclical pattern is observed for Tusk 1.

The temporal patterns of $^{206}Pb/^{204}Pb$ are described in detail in Section 3.3.1. for Tusk 1 and in Section 3.3.2. for Tusk 2.

3.3.4. Lead Isotope Niche of Both Narwhals Tusks

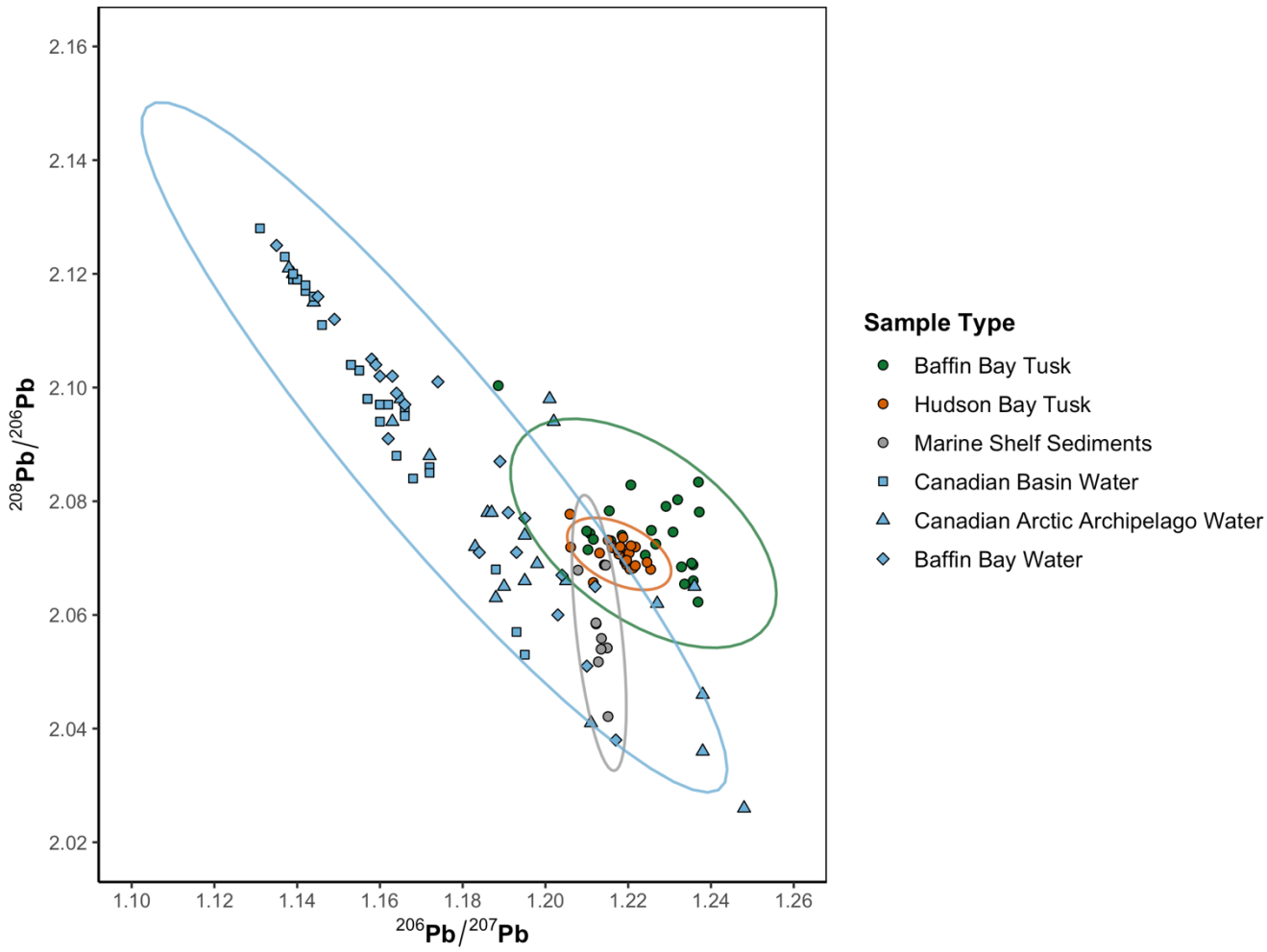

Figure 14. Ratios of $^{206}Pb/^{207}Pb$ and $^{208}Pb/^{206}Pb$ of Baffin Bay (green) and Hudson Bay tusks (orange), compared with marine shelf sediments (grey; Maccali et al., 2018), Canadian Basin water samples (blue squares; De Vera et al., 2021b), Canadian Arctic Archipelago water samples (blue triangles; De Vera, 2020; De Vera et al., 2021b), and Baffin Bay water samples (blue diamonds; De Vera, 2020).

In Figure 14, lead isotope ratios ($^{206}Pb/^{207}Pb$ vs. $^{208}Pb/^{206}Pb$) show distinct distributions between tusks and environmental samples. Data from the Baffin Bay tusk (in green) are more widely distributed along both axes, whereas the Hudson Bay tusk (in orange) displays values clustered closely together. The 95 % confidence ellipses of the two tusks overlap by 17.9% (Supplemental Material Table 31).

Neither tusk overlaps with the Canadian Basin Water samples. The Baffin Bay tusk shows greater overlap with the Canadian Arctic Archipelago Water (16.5%) and Baffin Bay Water (3.8%) compared with the Hudson Bay tusk, which overlaps by 3.6% and 0.3%, respectively. The Hudson Bay tusk shows a higher overlap with Marine Shelf Sediments (11.8%) than the Baffin Bay tusk (6.2%). Canadian Basin Water samples plot toward higher $^{208}Pb/^{206}Pb$ ratios and lower $^{206}Pb/^{207}Pb$ ratios, while both tusks display relatively higher $^{206}Pb/^{207}Pb$ and mid to low range $^{208}Pb/^{206}Pb$ values.

3.4. Multivariate Analysis of Geochemical Profiles for Tusks 1 and 2

3.4.1. PCA and Correlation Matrix for both Tusk 1 and Tusk 2

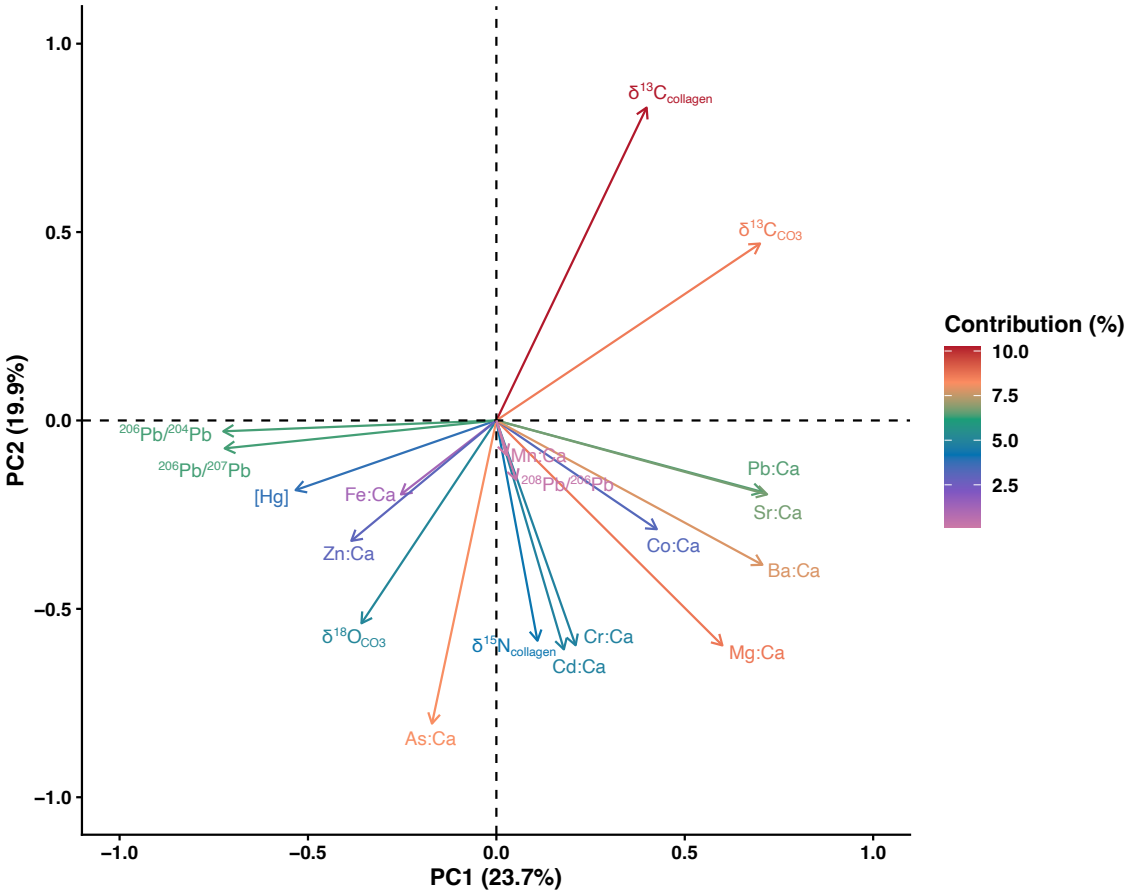

Figure 15. Principal Component Analysis (PCA) of four stable isotopes ($\delta^{13}C_{collagen}$, $\delta^{15}N_{collagen}$, $\delta^{13}C_{CO3}$, $\delta^{18}O_{CO3}$), Hg concentrations, three lead isotope ratios ($^{206}Pb/^{204}Pb$, $^{208}Pb/^{206}Pb$, $^{206}Pb/^{207}Pb$), six major elements normalized to calcium (Mg:Ca, Cr:Ca, Co:Ca, Zn:Ca, Sr:Ca, Ba:Ca), and five trace metals normalized to calcium (Mn:Ca, Fe:Ca, As:Ca, Cd:Ca, Pb:Ca) in annual growth layers of Baffin Bay individual (Tusk 1) and Hudson Bay individual (Tusk 2). The first two principal components (PC1 and PC2) account for 43.6% of the total variance. Variable contributions are represented by both color intensity and vector length.

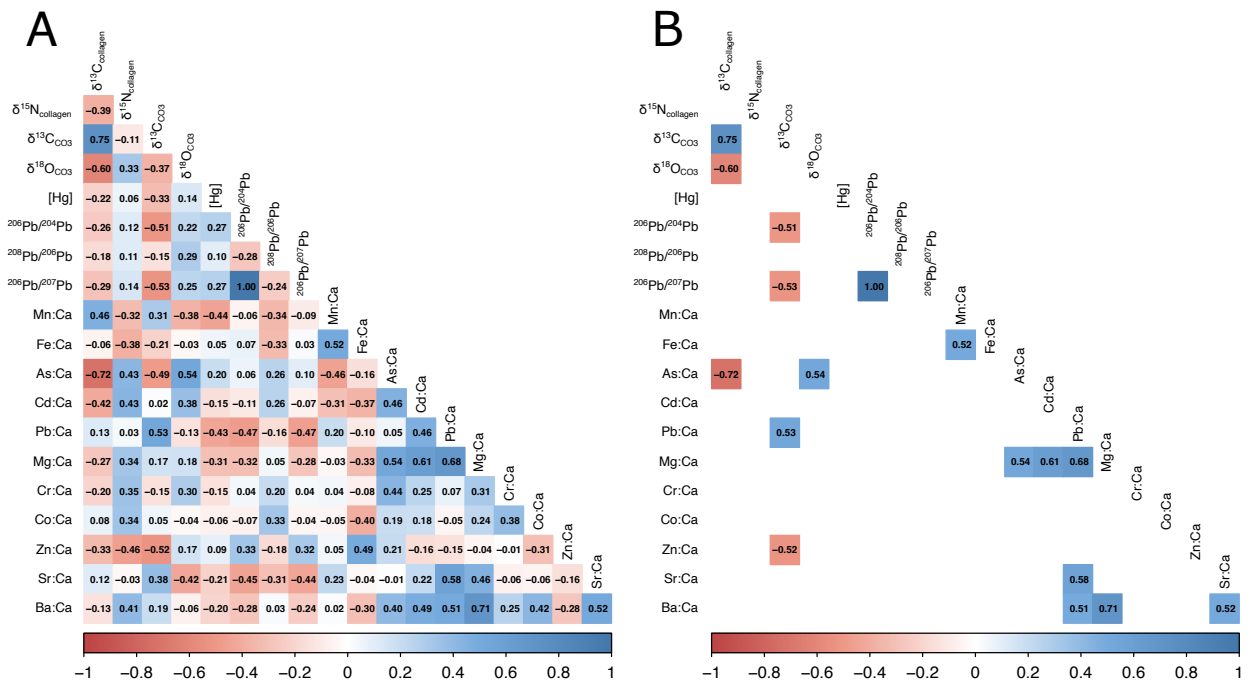

Figure 16. A. Spearman correlation matrix of four stable isotopes ($\delta^{13}C_{collagen}$, $\delta^{15}N_{collagen}$, $\delta^{13}C_{CO3}$, $\delta^{18}O_{CO3}$), Hg concentrations, three lead isotope ratios ($^{206}Pb/^{204}Pb$, $^{208}Pb/^{206}Pb$, $^{206}Pb/^{207}Pb$), six major elements normalized to calcium (Mg:Ca, Cr:Ca, Co:Ca, Zn:Ca, Sr:Ca, Ba:Ca), and five trace metals normalized to calcium (Mn:Ca, Fe:Ca, As:Ca, Cd:Ca, Pb:Ca) in annual growth layers of Baffin Bay individual (Tusk 1) and Hudson Bay individual (Tusk 2). **B.** Same matrix filtered to display only moderate-to-strong correlations ($|\rho| > 0.5$). Color intensity and numeric labels reflect the strength and direction of pairwise correlations, where blue indicates positive and red indicates negative relationships. Missing or low correlations ($|\rho| < 0.5$) are not displayed in panel B.

Figure 15 shows the PCA combining all elemental and isotope data from both individuals and shows clear grouping on a PCA1 and PCA2 axis plot representing close to half of the total variance (43.6%). Covariations are observed between several variables including Sr:Ca, Ba:Ca, Co:Ca, Pb:Ca, and Mg:Ca (Group 1); Hg concentrations, Zn:Ca, Fe:Ca and $\delta^{18}O_{CO3}$ (Group 2); $^{206}Pb/^{204}Pb$ and $^{206}Pb/^{207}Pb$ (Group 3); and Mn:Ca, Cd:Ca, Cr:Ca, $^{208}Pb/^{206}Pb$, and $\delta^{15}N_{collagen}$ (Group 4). Notable negative correlations are also observed, including between $\delta^{13}C_{CO3}$ and Group 2 variables, and between $\delta^{13}C_{collagen}$ and As:Ca.

In Figure 16, $\delta^{13}C_{collagen}$ shows strong correlations with $\delta^{13}C_{CO3}$ ($\rho = 0.75$) and As:Ca ($\rho = -0.72$), and moderate to strong negative correlations with $\delta^{18}O_{CO3}$ ($\rho = -0.60$) and Cd:Ca ($\rho = -0.52$), all with $p \leq 0.005$ (Supplemental Material Table 4). $\delta^{15}N_{collagen}$ shows moderate to strong correlations with As:Ca ($\rho = 0.43$), Cd:Ca ($\rho = 0.43$), Zn:Ca ($\rho = -0.46$), and Ba:Ca ($\rho = 0.41$), all with $p < 0.05$.

$\delta^{13}C_{CO3}$ exhibits moderate to strong correlations with $^{206}Pb/^{204}Pb$ ($\rho = -0.51$), $^{206}Pb/^{207}Pb$ ($\rho = -0.53$), As:Ca ($\rho = -0.49$), Pb:Ca ($\rho = 0.53$), and Zn:Ca ($\rho = -0.52$), all with $p < 0.001$. $\delta^{18}O_{CO3}$ shows strong positive correlations with As:Ca ($\rho = 0.54$, $p < 0.001$), and a moderate negative correlation with Sr:Ca ($\rho = -0.42$, $p = 0.004$).

Hg concentration exhibits moderate negative correlations with Mn:Ca ($\rho = -0.44$, $p = 0.002$) and Pb:Ca ($\rho = -0.43$, $p = 0.003$). Pb isotope ratios ($^{206}Pb/^{204}Pb$ and $^{206}Pb/^{207}Pb$) are perfectly interrelated ($\rho = 1.00$, $p < 0.001$) and show moderate negative correlations with Pb:Ca ($\rho = -0.47$, $p = 0.001$) and Sr:Ca ($\rho = -0.44$ to -0.45, $p \leq 0.003$).

3.4.2. PCA and Correlation Matrix for Tusk 1

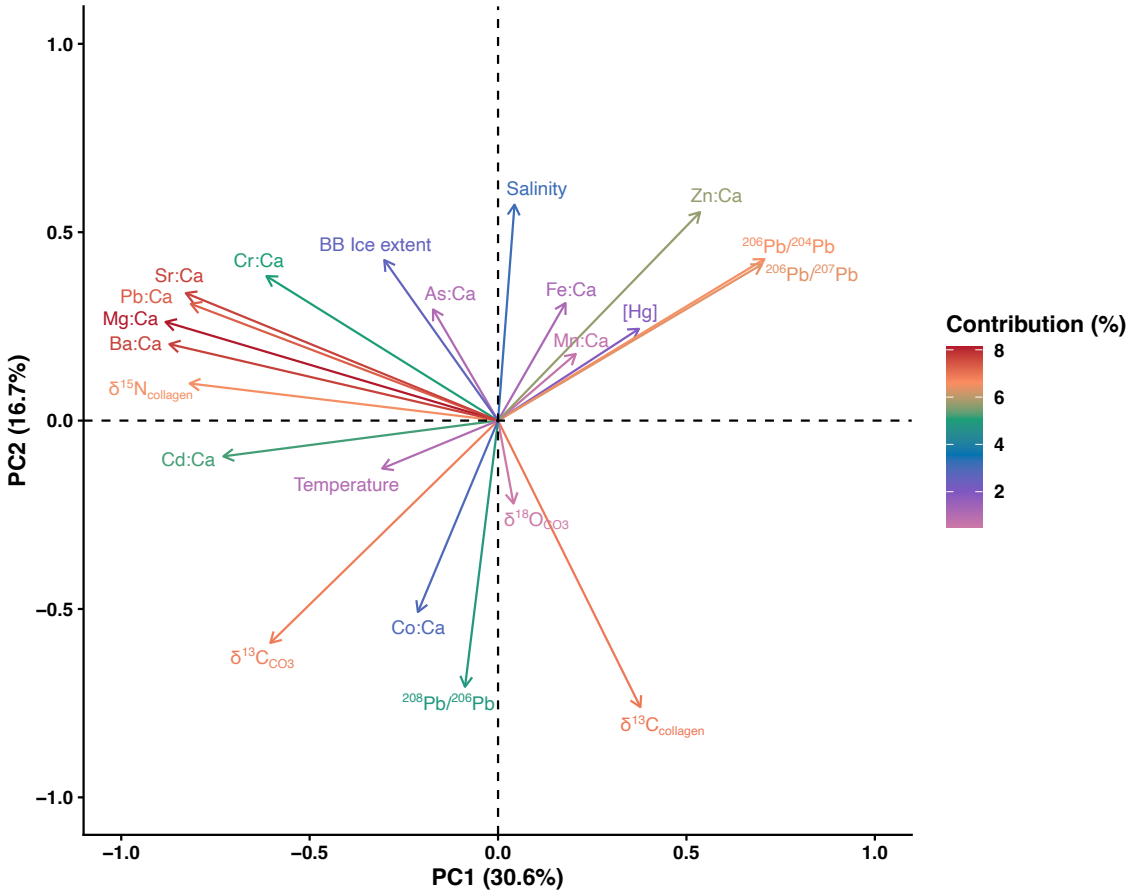

Figure 17. Principal Component Analysis (PCA) of four stable isotopes ($\delta^{13}C_{collagen}$, $\delta^{15}N_{collagen}$, $\delta^{13}C_{CO3}$, $\delta^{18}O_{CO3}$), Hg concentrations, three lead isotope ratios ($^{206}Pb/^{204}Pb$, $^{208}Pb/^{206}Pb$, $^{206}Pb/^{207}Pb$), six major elements normalized to calcium (Mg:Ca, Cr:Ca, Co:Ca, Zn:Ca, Sr:Ca, Ba:Ca), and five trace metals normalized to calcium (Mn:Ca, Fe:Ca, As:Ca, Cd:Ca, Pb:Ca) in annual growth layers of Baffin Bay individual (Tusk 1), and three environmental variables (Arctic Bay water temperature, Arctic Bay salinity, and Baffin Bay ice extent; *Baffin Bay Sea Ice Extent, n.d.; EN4: Quality Controlled Subsurface Ocean Temperature and Salinity Profiles and Objective Analyses, n.d.).* The first two principal components (PC1 and PC2) account for 47.3% of the total variance. Variable contributions are represented by both color intensity and vector length.

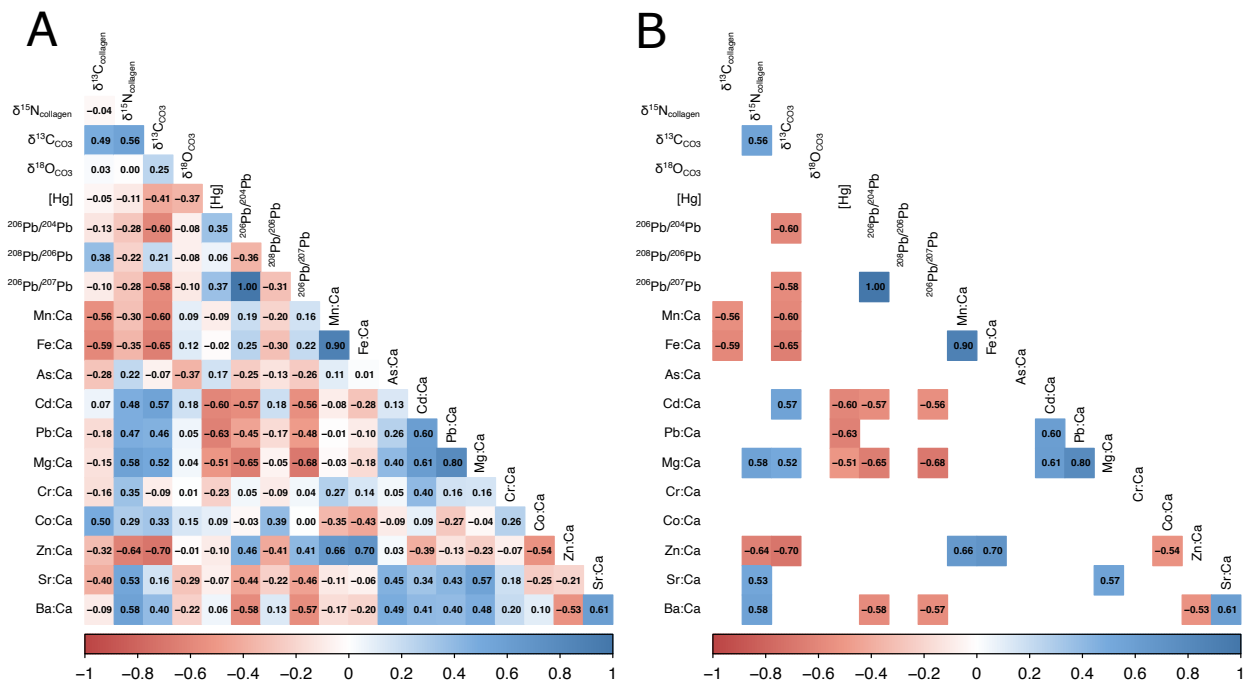

Figure 18. A. Spearman correlation matrix of four stable isotopes ($\delta^{13}C_{collagen}$, $\delta^{15}N_{collagen}$, $\delta^{13}C_{CO3}$, $\delta^{18}O_{CO3}$), Hg concentrations, three lead isotope ratios ($^{206}Pb/^{204}Pb$, $^{208}Pb/^{206}Pb$, $^{206}Pb/^{207}Pb$), six major elements normalized to calcium (Mg:Ca, Cr:Ca, Co:Ca, Zn:Ca, Sr:Ca, Ba:Ca), and five trace metals normalized to calcium (Mn:Ca, Fe:Ca, As:Ca, Cd:Ca, Pb:Ca) in annual growth layers of Baffin Bay individual (Tusk 1). **B.** Same matrix filtered to display only moderate-to-strong correlations ($|\rho| > 0.5$). Color intensity and numeric labels reflect the strength and direction of pairwise correlations, where blue indicates positive and red indicates negative relationships. Missing or low correlations ($|\rho| < 0.5$) are not displayed in panel B.

Figure 17 shows the PCA combining all elemental and isotopic data for Tusk 1 (Baffin Bay), along with environmental variables. The PCA shows clear grouping on a PCA1 and PCA2 axis plot representing almost half of the total variance (47.3%). Covariations are observed among several variables, including Fe:Ca, Zn:Ca, Mn:Ca, Hg concentrations, $^{206}Pb/^{204}Pb$, and $^{206}Pb/^{207}Pb$ (Group 1); $\delta^{18}O_{CO3}$ and $\delta^{13}C_{collagen}$ (Group 2); Co:Ca and $^{208}Pb/^{206}Pb$ (Group 3); Cd:Ca, $\delta^{13}C_{CO3}$ and Baffin Bay sea surface temperature (Group 4); $\delta^{15}N_{collagen}$, Mg:Ca, Ba:Ca, Sr:Ca, Pb:Ca and Cr:Ca (Group 5); and As:Ca and Baffin Bay ice extent (Group 6). Notable negative correlations are observed between Group 1 and Group 4 variables, between Group 2 and Group 6 variables, as well as between Arctic Bay salinity and Group 3 variables.

In Figure 18, $\delta^{13}C_{collagen}$ shows moderate to strong correlations with $\delta^{13}C_{CO3}$ ($\rho = 0.49$, $p = 0.019$), Mn:Ca ($\rho = -0.56$, $p = 0.007$), Fe:Ca ($\rho = -0.59$, $p = 0.003$), Co:Ca ($\rho = 0.50$, $p = 0.017$), and Sr:Ca ($\rho = -0.40$, $p = 0.063$; Supplemental Material Table 5). $\delta^{15}N_{collagen}$ is strongly correlated with Zn:Ca ($\rho = -0.64$, $p = 0.001$), and moderately correlated with $\delta^{13}C_{CO3}$ ($\rho = 0.56$, $p = 0.005$), Cd:Ca ($\rho = 0.48$, $p = 0.021$), Pb:Ca ($\rho = 0.47$, $p = 0.023$), Mg:Ca ($\rho = 0.58$, $p = 0.004$), Sr:Ca ($\rho = 0.53$, $p = 0.009$) and Ba:Ca ($\rho = 0.58$, $p = 0.004$).

$\delta^{13}C_{CO3}$ shows a strong correlation with Zn:Ca ($\rho = -0.70$, $p < 0.001$), Mn:Ca ($\rho = -0.60$, $p = 0.003$), Fe:Ca ($\rho = -0.65$, $p = 0.001$), and $^{206}Pb/^{204}Pb$ ($\rho = -0.60$, $p = 0.003$), along with moderate correlations with $^{206}Pb/^{207}Pb$ ($\rho = -0.58$, $p = 0.004$), Cd:Ca ($\rho = 0.57$, $p = 0.006$), Pb:Ca ($\rho = 0.46$, $p = 0.029$), Mg:Ca ($\rho = 0.52$, $p = 0.013$), and Ba:Ca ($\rho = 0.40$, $p = 0.061$). Hg concentration shows strong negative correlations with Pb:Ca ($\rho = -0.63$), Cd:Ca ($\rho = -0.60$), and Mg:Ca ($\rho = -0.51$), all with $p \leq 0.05$.

Pb isotope ratios ($^{206}Pb/^{204}Pb$ and $^{206}Pb/^{207}Pb$) are perfectly interrelated ($\rho = 1.00$, $p < 0.001$) and show moderate to strong negative correlations with Cd:Ca ($\rho = -0.56$ to -0.57, $p < 0.007$), Mg:Ca ($\rho = -0.65$ to -0.68, $p \leq 0.001$), Pb:Ca ($\rho = -0.45$ to -0.48, $p < 0.05$), Ba:Ca ($\rho = -0.57$ to -0.58, $p \leq 0.05$), Sr:Ca ($\rho = -0.44$ to -0.46, $p < 0.05$). Moderate to strong positive correlations with Zn:Ca are also observed ($\rho = 0.41$ to 0.46, $p \leq 0.052$).

Among the elemental variables, Cd:Ca, Pb:Ca, and Mg:Ca form a tightly intercorrelated cluster, with correlations ranging from strong to very strong ($\rho = 0.60$ to 0.80, $p < 0.05$). Zn:Ca is moderately to strongly positively correlated with Fe:Ca ($\rho = 0.70$) and Mn:Ca ($\rho = 0.66$), both with $p < 0.001$, and moderately negatively correlated with Co:Ca ($\rho = -0.54$, $p = 0.009$) and Ba:Ca ($\rho = -0.53$, $p = 0.01$). Ba:Ca is moderately to strongly positively correlated with As:Ca ($\rho = 0.49$, $p =$

0.019), Cd:Ca ($\rho = 0.41$, $p = 0.054$), Pb:Ca ($\rho = 0.40$, $p = 0.062$), Mg:Ca ($\rho = 0.48$, $p = 0.023$), Pb:Ca ($\rho = 0.40$, $p = 0.062$), and Sr:Ca ($\rho = 0.61$, $p = 0.002$). Sr:Ca is moderately positively correlated with Mg:Ca ($\rho = 0.57$, $p = 0.005$).

3.4.3. PCA and Correlation Matrix for Tusk 2

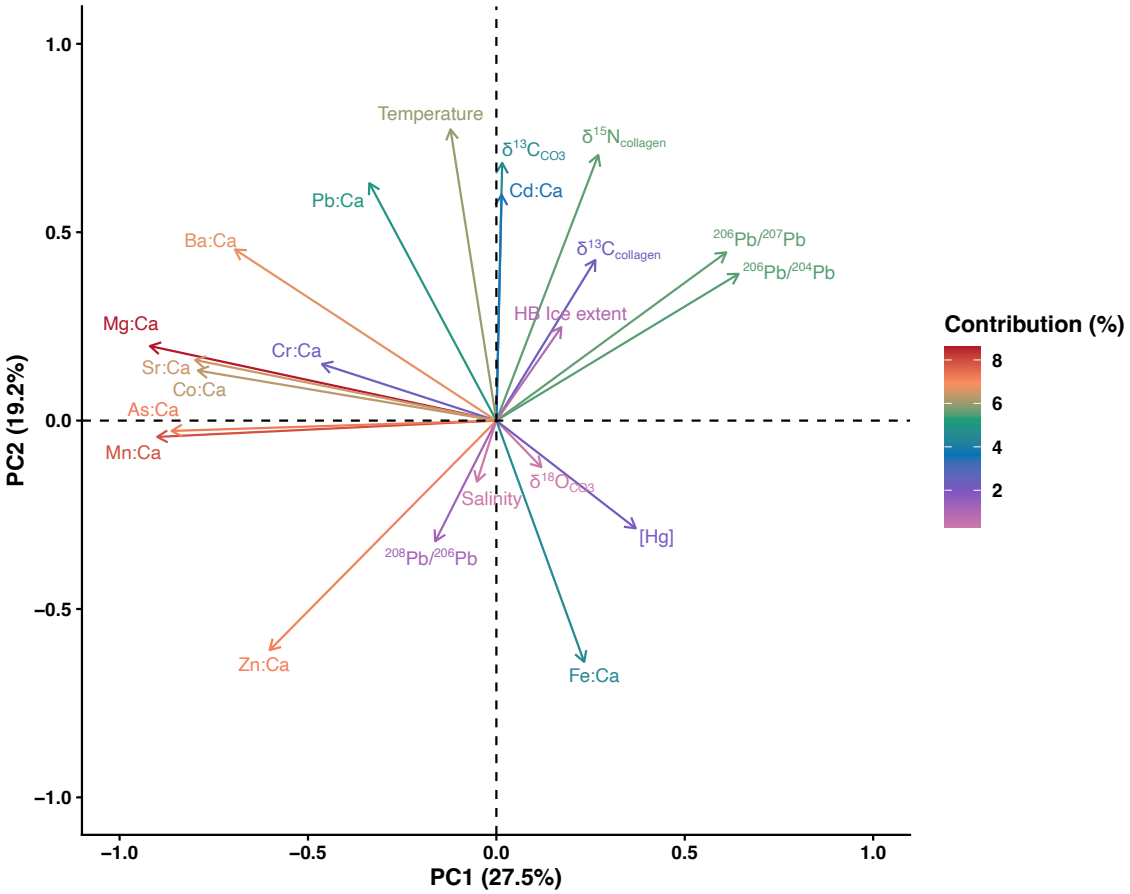

Figure 19. Principal Component Analysis (PCA) of four stable isotopes ($\delta^{13}C_{collagen}$, $\delta^{15}N_{collagen}$, $\delta^{13}C_{CO3}$, $\delta^{18}O_{CO3}$), Hg concentrations, three lead isotope ratios ($^{206}Pb/^{204}Pb$, $^{208}Pb/^{206}Pb$, $^{206}Pb/^{207}Pb$), six major elements normalized to calcium (Mg:Ca, Cr:Ca, Co:Ca, Zn:Ca, Sr:Ca, Ba:Ca), and five trace metals normalized to calcium (Mn:Ca, Fe:Ca, As:Ca, Cd:Ca, Pb:Ca) in annual growth layers of Hudson Bay individual (Tusk 2), and three environmental variables (Naujaat water temperature, Naujaat salinity, and Hudson Bay ice extent; *EN4: Quality Controlled Subsurface Ocean Temperature and Salinity Profiles and Objective Analyses*, n.d.; *Hudson Bay Sea Ice Extent*, n.d.). The first two principal components (PC1 and PC2) account for 46.7% of the total variance. Variable contributions are represented by both color intensity and vector length.

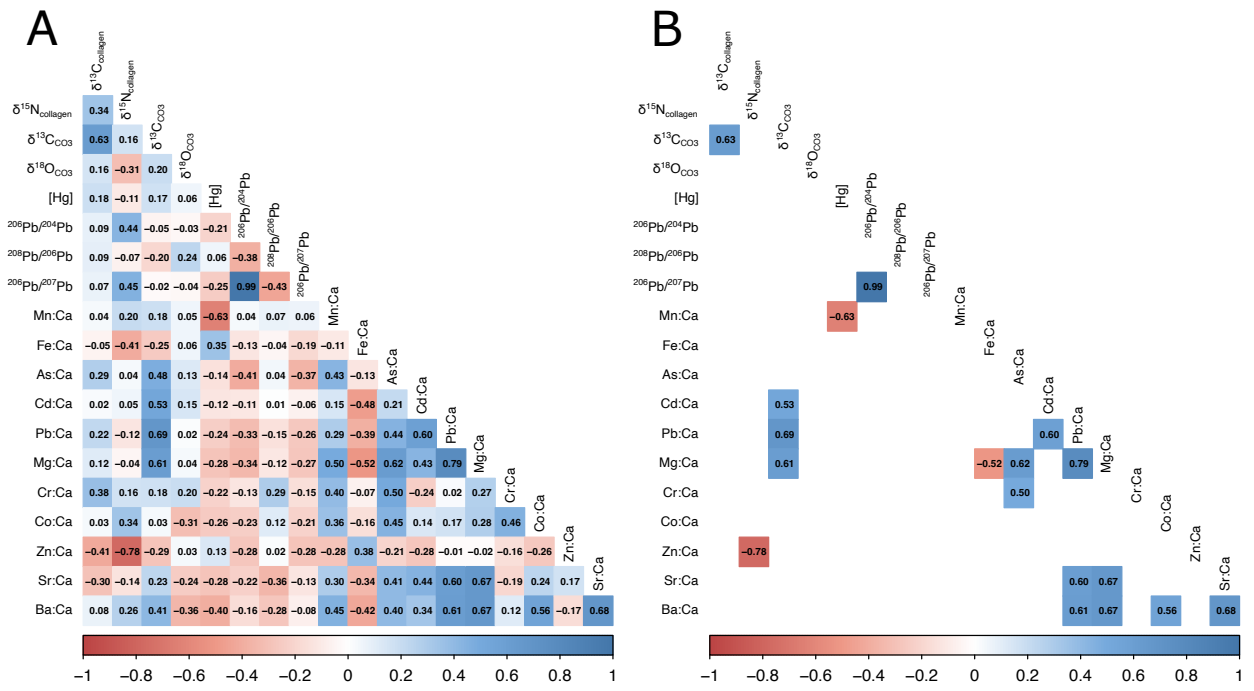

Figure 20. A. Spearman correlation matrix of four stable isotopes ($\delta^{13}C_{collagen}$, $\delta^{15}N_{collagen}$, $\delta^{13}C_{CO3}$, $\delta^{18}O_{CO3}$), Hg concentrations, three lead isotope ratios ($^{206}Pb/^{204}Pb$, $^{208}Pb/^{206}Pb$, $^{206}Pb/^{207}Pb$), six major elements normalized to calcium (Mg:Ca, Cr:Ca, Co:Ca, Zn:Ca, Sr:Ca, Ba:Ca), and five trace metals normalized to calcium (Mn:Ca, Fe:Ca, As:Ca, Cd:Ca, Pb:Ca) in annual growth layers of Hudson Bay individual (Tusk 2). **B.** Same matrix filtered to display only moderate-to-strong correlations ($|\rho| > 0.5$). Color intensity and numeric labels reflect the strength and direction of pairwise correlations, where blue indicates positive and red indicates negative relationships. Missing or low correlations ($|\rho| < 0.5$) are not displayed in panel B.

Figure 19 presents the PCA combining all elemental and isotopic data for Tusk 2, along with environmental variables. The PCA reveals distinct groupings along the PCA1 and PCA2 axes, which together explain almost half of the total variance (46.7%). Covariations are observed among several variables, including $\delta^{13}C_{collagen}$, $\delta^{15}N_{collagen}$, $^{206}Pb/^{204}Pb$ and $^{206}Pb/^{207}Pb$ and Hudson Bay ice extent (Group 1); $\delta^{13}C_{CO3}$ and Cd:Ca (Group 2), Pb:Ca, Ba:Ca and Naujaat sea surface temperature (Group 3); Sr:Ca, Mg:Ca, As:Ca, Co:Ca, Mn:Ca and Cr:Ca (Group 4); Zn:Ca, $^{208}Pb/^{206}Pb$ and Naujaat salinity (Group 5); and Fe:Ca, Hg concentrations and $\delta^{18}O_{CO3}$ (Group 6). Notable negative correlations are observed between Group 1 and Group 5 variables, and between Group 3 and Group 6 variables.

In Figure 20, $\delta^{13}C_{collagen}$ shows a strong positive correlation with $\delta^{13}C_{CO3}$ ($\rho = 0.63$, $p = 0.002$; Supplemental Material Table 6). $\delta^{15}N_{collagen}$ is strongly negatively correlated with Zn:Ca ($\rho = -0.78$, $p < 0.001$) and moderately correlated with Fe:Ca ($\rho = -0.41$, $p = 0.060$).

$\delta^{13}C_{CO3}$ exhibits moderate to strong positive correlations with Ba:Ca ($\rho = 0.41$, $p = 0.058$), As:Ca ($\rho = 0.48$, $p = 0.026$), Cd:Ca ($\rho = 0.53$, $p = 0.012$), Mg:Ca ($\rho = 0.61$, $p = 0.003$), Pb:Ca ($\rho = 0.69$, $p < 0.001$). $\delta^{18}O_{CO3}$ shows no statistically significant correlations above moderate with elemental or isotopic variables. Hg concentration is moderately to strongly negatively correlated with Ba:Ca ($\rho = -0.40$, $p = 0.068$) and Mn:Ca ($\rho = -0.63$, $p = 0.02$).

Pb isotope ratios ($^{206}Pb/^{204}Pb$ and $^{206}Pb/^{207}Pb$) are perfectly interrelated ($\rho = 1.00$, $p < 0.001$). $^{206}Pb/^{204}Pb$ is moderately negatively correlated with As:Ca ($\rho = -0.41$, $p = 0.062$), and $^{208}Pb/^{206}Pb$ is moderately negatively correlated with $^{206}Pb/^{207}Pb$ ($\rho = -0.43$, $p = 0.046$).

Among elemental variables, Mn:Ca is moderately positively correlated with As:Ca ($\rho = 0.43$, $p = 0.046$), Mg:Ca ($\rho = 0.50$, $p = 0.020$), and Cr:Ca ($\rho = 0.40$, $p = 0.067$). Fe:Ca is moderately negatively correlated with Cd:Ca ($\rho = -0.48$, $p = 0.025$), Mg:Ca ($\rho = -0.52$, $p = 0.015$), and Ba:Ca ($\rho = -0.42$, $p = 0.051$). As:Ca, Cd:Ca, Pb:Ca, Mg:Ca, Sr:Ca, and Ba:Ca form a tightly intercorrelated group, with correlations ranging from moderate ($\rho = 0.40$ to 0.44, $p \leq 0.065$) to strong ($\rho = 0.60$ to 0.79, $p < 0.05$).

CHAPTER 4: DISCUSSION

4.1. Do Changes in Mobility and Migration Control Isotopic and Metal Profiles in Tusks?

4.1.1. Key Observation: A Large, Unexpected $\delta^{15}N$ Decline in Tusk 1

The most striking feature of the Baffin Bay tusk record (Tusk 1) is a pronounced, long-term decline in $\delta^{15}N_{collagen}$ (Figure 7). This pattern is unexpected because narwhals generally increase trophic level with age, a process that should drive $\delta^{15}N$ values upward rather than downward. The central question of this thesis therefore becomes whether this decline reflects (1) a change in movement ecology such as altered migration timing or habitat use (2) a change in diet, or (3) a shift in $\delta^{15}N$ baseline conditions within the Baffin Bay system.

A migration-based explanation is plausible because $\delta^{15}N$ baselines vary spatially across the Arctic Ocean as a function of nitrogen sources, trophic structure, and water-mass history, including contrasts between Atlantic- and Pacific-influenced systems. Atlantic-derived nitrate, which strongly influences Baffin Bay, is isotopically lighter than Pacific-derived nitrate by approximately 3‰, reflecting differences in upstream biological processing between the two ocean basins (De La Vega et al., 2021, 2022; Lehmann et al., 2022; Sherwood et al., 2021). Consequently, even modest year-to-year changes in the proportion of time spent in different foraging regions could generate coherent shifts in $\delta^{15}N$ (De La Vega et al., 2021). In Baffin Bay, telemetry studies document strong population structuring, high site fidelity, and repeated use of migration corridors, but also indicate that climate warming and sea-ice loss can modify migration timing in Arctic marine mammals (Cherry et al., 2013; COSEWIC, 2004; Hauser et al., 2017; Heide-Jørgensen et al., 2003; Laidre et al., 2008; Pilfold et al., 2017; Shuert et al., 2022). One scenario consistent with these observations is extended residence in summering grounds under earlier ice breakup and warmer conditions, coupled with reduced time in offshore waters (Shuert et al., 2022). Increased exposure to nearshore food webs or Pacific-influenced water masses under such a scenario could plausibly shift $\delta^{15}N$ toward lower baseline values.

4.1.2. Testable Prediction: Migration Shifts Should Be Accompanied by Coordinated Changes in Mobility Proxies

Narwhals are highly mobile and migrate annually between distinct summering and wintering habitats. Their movements are strongly population structured, with telemetry data showing repeated use of defined corridors and strong fidelity to wintering areas beneath dense pack ice (COSEWIC, 2004; Heide-Jørgensen et al., 2003, 2013, 2015; Laidre et al., 2008). If an individual experienced sustained relocation, a major shift in migration timing, or long-term changes in habitat use such as persistent occupation of different water masses then multiple geochemical tracers preserved in tusk dentine should change coherently. This expectation follows from the strong spatial structure of these proxies and their incorporation into biomineralized tissues (De La Vega et al., 2019, 2021; De Vera et al., 2021b; Matthews et al., 2016; Newsome et al., 2010; Olivelli et al., 2025; Rogalla et al., 2025; Ventresca Miller et al., 2018).

Under a migration-driven hypothesis, the pronounced $\delta^{15}N_{collagen}$ decline should be accompanied by directional shifts in at least one independent mobility indicator most notably $\delta^{18}O_{CO3}$ and Pb isotope ratios and likely also $\delta^{13}C$ (collagen and/or carbonate), reflecting contrasts between offshore pelagic and nearshore or shelf production regimes. Conversely, if migration and habitat use remained broadly stable, $\delta^{15}N_{collagen}$ could change independently of these mobility proxies, implying a stronger role for dietary change or restructuring of baseline isotope conditions.

4.1.3. $\delta^{18}O$, $\delta^{13}C$, and Pb Isotopes as Independent Indicators of Movement: Contrasting Signals from Baffin Bay and Hudson Bay

Across the Arctic and its marginal seas, seawater oxygen isotope ratios exhibit strong spatial structure driven by hydrography, freshwater inputs, and large-scale ocean circulation (Figure 21). Because oxygen incorporated into bioapatite is derived primarily from ingested water, $\delta^{18}O$ values in dentine provide a sensitive record of the physical properties of the water masses an individual occupies, including temperature, salinity, and freshwater influence (Matthews et al., 2016; Newsome et al., 2010; Ventresca Miller et al., 2018). Sustained changes in migration routes, foraging range, or residence time within distinct water masses should therefore produce coherent, directional trends in $\delta^{18}O_{CO3}$.

In the Baffin Bay individual (Tusk 1), $\delta^{18}O_{CO3}$ displays pronounced interannual variability but no significant long-term trend (-0.009‰ per year, $p = 0.480$; Supplementary Material Table 1). Notably, $\delta^{18}O_{CO3}$ is significantly correlated with anomalies in the Atlantic Multidecadal Oscillation (AMO; $\rho = 0.42$, $p = 0.041$; Supplemental Material Table 35), an index of basin-scale North Atlantic sea-surface temperature variability associated with changes in the strength of the Atlantic Meridional Overturning Circulation (AMOC; Delworth & Mann, 2000; Knight et al., 2005; Kushnir, 1994; Latif et al., 2006).

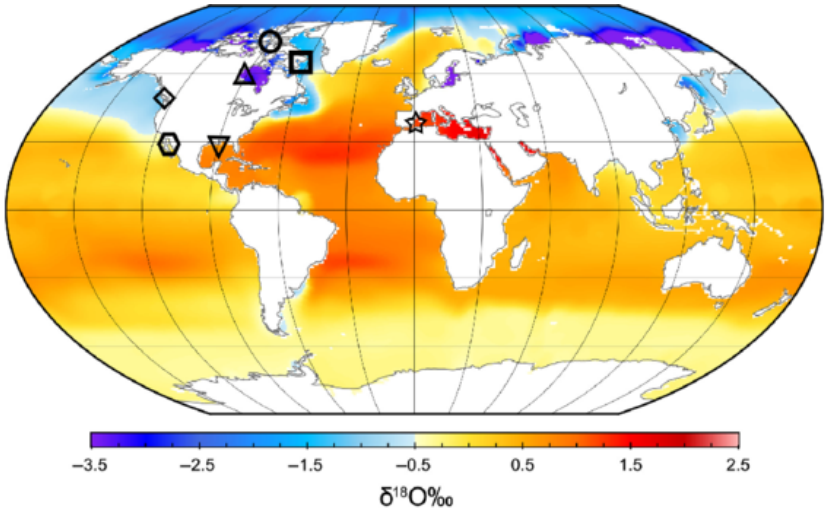

Figure 21. Global distribution of surface seawater $\delta^{18}O$ (‰) values from the Global Seawater Oxygen-18 Database (Schmidt et al., 1999). Figure reused from the open-access article by Matthews et al. (2016).

The Atlantic Multidecadal Oscillation (AMO) describes large-scale, multidecadal fluctuations in North Atlantic sea-surface temperatures (Enfield et al., 2001; Kerr, 2000). Positive AMO phases are characterized by widespread warming across the North Atlantic, particularly in the subpolar region, whereas negative phases reflect basin-scale cooling. These contrasting regimes are apparent in the historical record, with warm phases during the mid-20th century and again since the mid-1990s (Knight et al., 2005; Ruiz-Barradas et al., 2013; Sutton & Hodson, 2005). The AMO exerts broad climatic influence, including modulation of Arctic sea-ice extent (Day et al., 2012; Mahajan et al., 2011; Miles et al., 2014; Yeager et al., 2015; Zhang, 2015), making it particularly relevant for interpreting long-term environmental signals recorded in narwhal tusks.

The significant correlation between $\delta^{18}O_{CO3}$ and the AMO index primarily reflects basin-scale temperature and hydrographic variability rather than changes in individual movement. This relationship suggests that year-to-year fluctuations in $\delta^{18}O_{CO3}$ record climate-driven changes in the thermal and freshwater characteristics of water masses accessible within the animal's established foraging range, without requiring substantial shifts in migration timing or spatial use. If the marked $\delta^{15}N_{collagen}$ decline in Tusk 1 were driven by major changes in migration, such as increased residence in northern summering areas influenced by Pacific-derived waters, $\delta^{18}O_{CO3}$ would be expected to shift in parallel toward lower values characteristic of colder, fresher Arctic and Canadian Archipelago waters (Figure 21). No such coordinated change is observed. Instead, $\delta^{18}O_{CO3}$ variability is effectively decoupled from $\delta^{15}N_{collagen}$ trends, arguing against migration or basin-scale relocation as the dominant driver of the $\delta^{15}N_{collagen}$ decline.

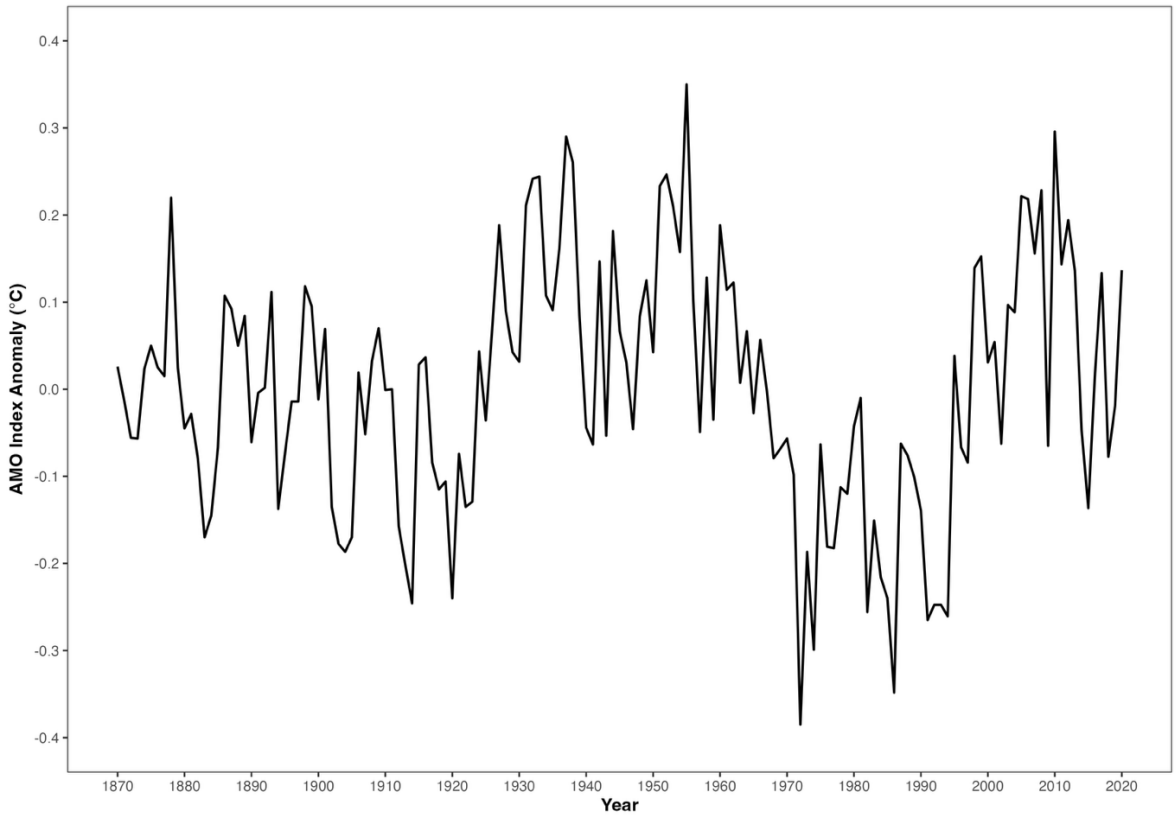

Figure 22. Atlantic Multidecadal Oscillation (AMO) anomalies in °C from the Climate Data Guide: Atlantic Multidecadal Oscillation (AMO) and Atlantic Multidecadal Variability (AMV) (Trenberth & Zhang, 2025).

Carbon isotope patterns provide an additional, independent constraint. In Arctic marine systems, $\delta^{13}C$ values reflect the isotopic composition of dissolved inorganic carbon (DIC) and are sensitive to primary production, air-sea CO_2 exchange, and carbon cycling within distinct water masses, while also exhibiting spatial contrasts between offshore pelagic and nearshore or shelf environments (Figure 23; De La Vega et al., 2019; Dietz et al., 2021; Fox & Walker, 2022; Ocean North Canada, 2014; Post, 2002). If $\delta^{13}C$ trends were driven by shifts in foraging geography, $\delta^{13}C$ and $\delta^{18}O$ would be expected to change coherently as the animal moved between distinct habitats and water masses. In contrast, if $\delta^{13}C$ trends and $\delta^{18}O$ were inversely correlated, this would suggest that carbon isotopes are responding to climate-driven changes in regional carbon cycling and ecosystem structure along a broadly stable foraging range.

In Tusk 1, $\delta^{13}C_{CO3}$ exhibits a pronounced long-term decline (-0.060‰ yr^{-1}, $p < 0.001$; Supplemental Material Table 1), whereas $\delta^{13}C_{collagen}$ shows no significant temporal trend (+0.003‰ yr^{-1}, $p = 0.635$). Despite this difference in secular behavior, the two $\delta^{13}C$ records are moderately and significantly correlated ($\rho = 0.49$, $p = 0.019$; Supplemental Material Table 5), indicating shared sensitivity to an external driver affecting the regional carbon system that is more strongly expressed in the carbonate mineral component of the tusk. Neither $\delta^{13}C_{collagen}$ nor $\delta^{13}C_{CO3}$ is significantly correlated with $\delta^{18}O_{CO3}$, and $\delta^{18}O_{CO3}$ itself shows no significant long-term trend (-0.009‰ yr^{-1}, $p = 0.480$), arguing against large-scale shifts in habitat use as the primary control on $\delta^{13}C$ variability. Collectively, these patterns suggest that $\delta^{13}C$ in the tusk reflects long-term changes in baseline carbon cycling rather than foraging geography.

Pb isotopes offer a further test of the migration hypothesis, as Pb isotope compositions vary geographically across the Arctic owing to contrasts between Atlantic- and Pacific-derived waters, shelf sediment interactions, and atmospheric Pb sources (De Vera et al., 2021b; Olivelli et al., 2025). Sustained changes in water-mass exposure or foraging geography should thus be reflected in corresponding shifts in Pb isotope ratios. In the Baffin Bay individual, neither $\delta^{18}O_{CO3}$ nor Pb isotope ratios exhibit coordinated, directional changes that track the pronounced decline in $\delta^{15}N_{collagen}$. Although $^{206}Pb/^{204}Pb$ and $^{206}Pb/^{207}Pb$ show a shift toward higher values later in life (Figure 13), this change is not significantly correlated with $\delta^{15}N_{collagen}$ ($\rho = -0.28$, p 0.199 and $\rho = -0.28$, p 0.189 respectively; Supplemental Material Table 5). The absence of covariance among $\delta^{15}N_{collagen}$ and these independent mobility indicators indicates that sustained changes in migration timing, foraging range, or basin-scale relocation are unlikely to explain the $\delta^{15}N_{collagen}$ decline.

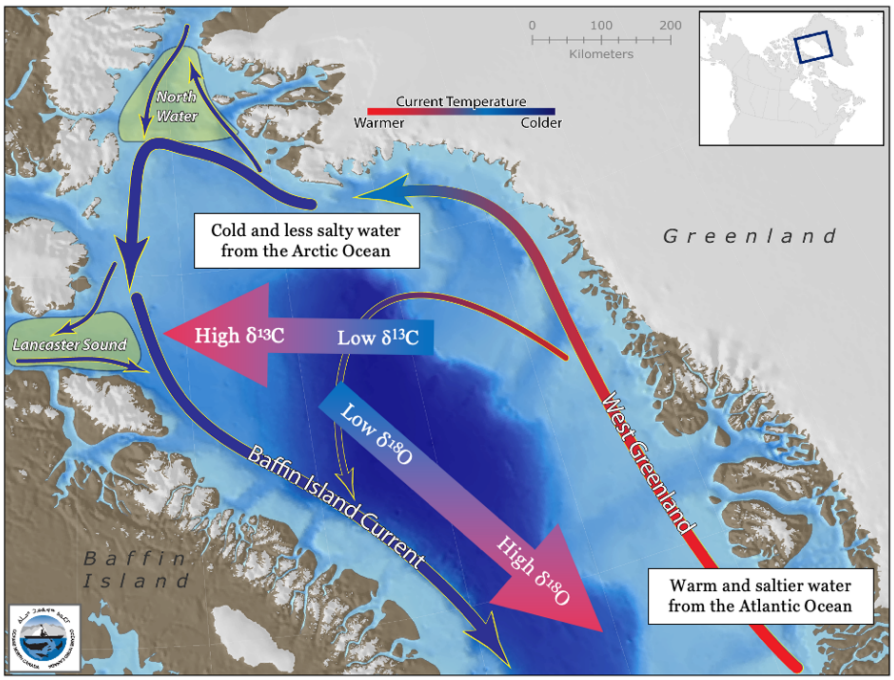

Figure 23. Schematic of major circulation pathways and isotopic gradients in Baffin Bay. Warm, saline Atlantic-derived waters enter via the West Greenland Current, while colder, fresher waters from the Arctic Ocean and Canadian Arctic Archipelago influence the western margin. $\delta^{13}C$ values are generally higher in productive nearshore and shelf environments, and $\delta^{18}O$ values decrease with increasing latitude. Figure reused and modified from Ocean North Canada (2014).

Taken together, the strong $\delta^{18}O_{CO3}$-AMO relationship and the lack of coupling among independent mobility proxies indicate that the Baffin Bay narwhal maintained broadly stable migration patterns. In this context, tusk $\delta^{18}O_{CO3}$ primarily records climate-driven variability in ambient water properties rather than behavioral change.

The Hudson Bay individual (Tusk 2) provides a contrasting but complementary test of the migration hypothesis. As expected, $\delta^{18}O_{CO3}$ values in Tusk 2 are consistently more negative than those in Tusk 1 (Figures 7 and 8), reflecting the strong freshwater influence, low salinity (Figure 24) and low seawater $\delta^{18}O_{CO3}$ values characteristic of Hudson Bay (Figure 21). Throughout most of the individual's life, $\delta^{18}O_{CO3}$ values remain remarkably stable, with no significant long-term trend (-9.26×10^{-4}‰ yr^{-1}, $p = 0.974$; Supplementary Material Table 1), indicating persistent use of a similar hydrographic environment over multiple decades.

Unlike Baffin Bay, the relationship between $\delta^{18}O_{CO3}$ and basin-scale circulation indices such as the AMO is weaker and non-significant in Hudson Bay ($\rho = 0.08$, $p = 0.708$; Supplemental Material Table 36). This is expected given the bay's shallow bathymetry and restricted circulation,

where water temperature and isotopic composition are more strongly controlled by local freshwater inputs (river discharge and sea-ice melt) and regional atmospheric forcing than by open-ocean circulation modes. Accordingly, $\delta^{18}O_{CO3}$ in Tusk 2 does not correlate significantly with Hudson Bay sea-ice extent or Naujaat sea surface temperature ($\rho = -0.16$, $p = 0.441$ and $\rho = -0.16$, $p = 0.444$ respectively; Supplemental Material Table 34), but does show a significant positive correlation with local salinity ($\rho = 0.42$, $p = 0.043$; Supplemental Material Table 34), highlighting the dominant role of freshwater mixing in governing oxygen isotope variability.

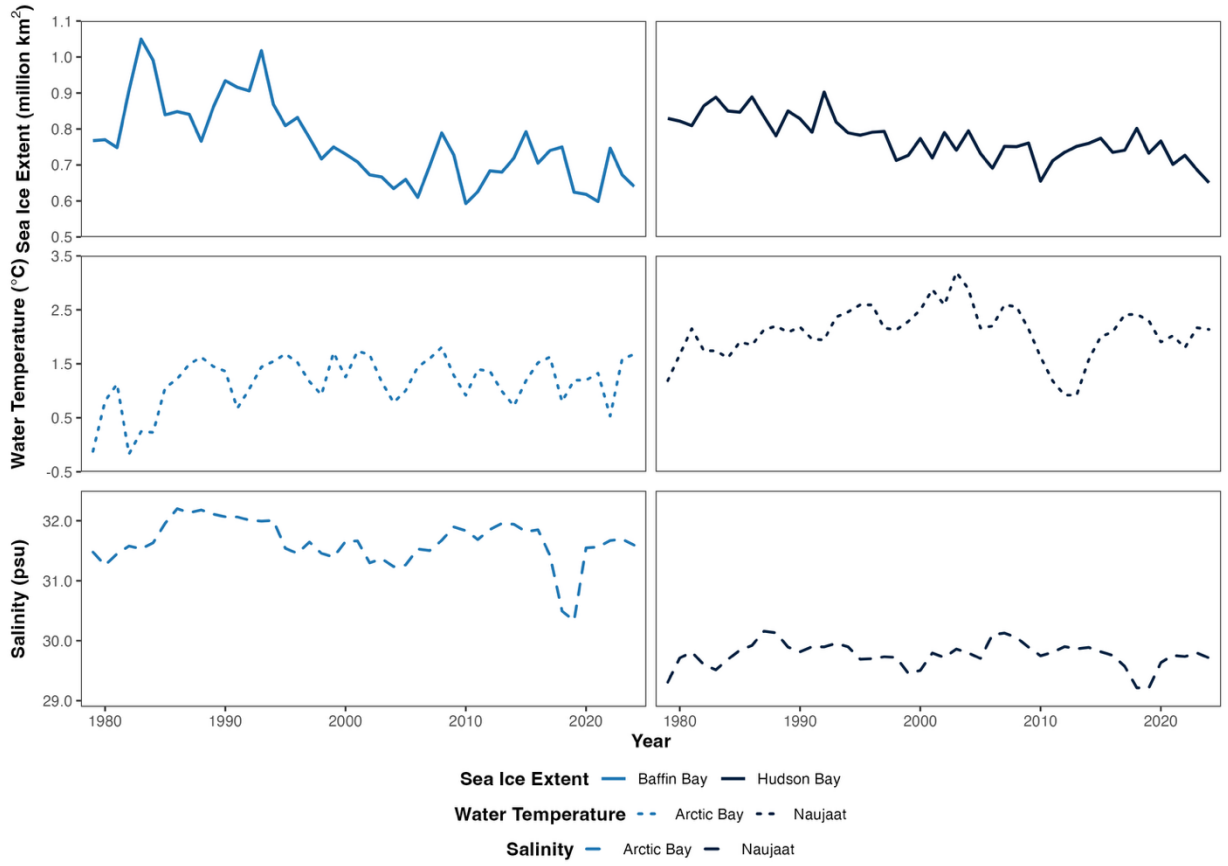

Figure 24. Annual sea-ice extent and coastal water temperature and salinity time series for Baffin Bay and Hudson Bay between 1979 and 2024. Sea-ice extent is shown for Baffin Bay and Hudson Bay (annual mean extent; million km^2), coastal water temperature is shown for Arctic Bay (Baffin Bay region) and Naujaat (Hudson Bay region; annual mean; °C), and salinity is shown for Arctic Bay and Naujaat (annual mean; psu). Sea-ice extent data were obtained from *Baffin Bay Sea Ice Extent* (n.d.) and *Hudson Bay Sea Ice Extent* (n.d.). Temperature and salinity data were obtained from *EN4: Quality Controlled Subsurface Ocean Temperature and Salinity Profiles and Objective Analyses* (n.d.).

Carbon isotope values in the Hudson Bay individual are consistently higher than those in Tusk 1 (Figures 7 and 8), reflecting the strong influence of nearshore and shelf productivity characteristic of Hudson Bay (Figure 23). Variability in $\delta^{13}C$ is significantly correlated with local sea surface temperature ($\delta^{13}C_{collagen}$: $\rho = 0.51$, $p = 0.010$; $\delta^{13}C_{CO3}$: $\rho = 0.48$, $p = 0.017$; Supplementary Material Table 34) but not with $\delta^{18}O_{CO3}$ ($\delta^{13}C_{collagen}$: $\rho = 0.16$, $p = 0.479$; $\delta^{13}C_{CO3}$: $\rho = 0.20$, $p = 0.381$; Supplementary Material Table 6) or Pb isotopes ($^{206}Pb/^{204}Pb$: $\rho = -0.03$, $p = 0.893$; $^{208}Pb/^{206}Pb$: $\rho = 0.24$, $p = 0.288$; $^{206}Pb/^{207}Pb$: $\rho = -0.04$, $p = 0.867$; Supplementary Material Table 6), indicating sensitivity to local ecosystem dynamics rather than changes in foraging geography. Pb isotope ratios remain relatively stable throughout the individual's life (Figure 13), consistent with stable exposure pathways and the absence of sustained shifts in water-mass provenance.

Finally, $\delta^{15}N_{collagen}$ in Tusk 2 shows no pronounced long-term directional trend (+0.001‰ yr^{-1}, $p = 0.862$), despite the individual experiencing the same broad climatic changes affecting the Arctic during the twentieth century. If large-scale migration shifts were a dominant driver of $\delta^{15}N$ variability in narwhals, similar patterns would be expected in both individuals. Instead, the stability of $\delta^{15}N_{collagen}$ in Tusk 2, together with conservative $\delta^{18}O_{CO3}$, $\delta^{13}C_{collagen}$, $\delta^{13}C_{CO3}$, and Pb isotopic signals, indicates that migration patterns remained broadly stable and that $\delta^{15}N$ variability is not systematically linked to changes in movement ecology.

4.2. Diet/Trophic Ecology: Evidence from Elemental and Isotopic Proxies

Having shown in Section 4.1 that long-term changes in mobility and migration cannot explain the divergent $\delta^{15}N$ trajectories, this section evaluates whether differences in diet and trophic ecology provide a more parsimonious explanation.

4.2.1. Ba:Ca and Sr:Ca: Consistent Ontogenetic Trophic Change in Both Tusks

Both tusks show the same first-order pattern in elemental trophic proxies: Ba:Ca and Sr:Ca are elevated early in life, decline over approximately the first 5-7 years, and then stabilize at lower values subsequently (Figures 9 and 10). This shared ontogenetic structure is difficult to explain as a purely environmental signal, as it occurs in individuals inhabiting markedly different

oceanographic regimes. Instead, it is consistent with a physiological and ecological transition early in development followed by the establishment of a stable adult-like foraging mode.

The directionality of these trends in both tusks provides a strong biological and physiological framework for interpretation through the process of biopurification, in which Ba and Sr, non-essential analogs of Ca, are progressively discriminated against relative Ca with increasing trophic position and through physiological filtering during assimilation and tissue formation (Balter, 2004; Botta et al., 2015; Peek & Clementz, 2012). Under this framework, declining Ba:Ca and Sr:Ca during early life reflect increasing trophic position and/or shifts toward larger and higher-trophic prey as foraging competence develops. This trophic interpretation has been widely documented in vertebrates and mineralized tissues and provides a coherent mechanistic basis for linking the observed early-life declines in Ba:Ca and Sr:Ca to ontogenetic changes, feeding ecology, and habitat use (Botta et al., 2015; Clark et al., 2020, 2021).

The fact that both Tusk 1 and Tusk 2 display similar ontogenetic decline followed by long-term stability indicates that both individual likely underwent a broadly similar trophic transition early in life, despite belonging to different populations and oceanographic settings. This interpretation is consistent with independent ecological evidence indicating that narwhals are relatively specialized predators and that juveniles differ from adults in prey size and foraging competence, with adults relying heavily on energy-rich prey such as Greenland halibut in key seasons and in specific regions (Heide-Jørgensen, 2018; Laidre et al., 2003; Laidre & Heide-Jørgensen, 2005; Watt et al., 2017). Importantly, although $\delta^{15}N_{collagen}$ exhibits divergent long-term behavior between the two individuals, the near-identical ontogenetic structure of Ba:Ca and Sr:Ca in both tusks provides compelling independent evidence for a real trophic transition early in life. This demonstrates that ontogenetic change in feeding ecology is expressed in these elemental proxies even when $\delta^{15}N_{collagen}$ does not directly reflect this changing diet.

4.2.2. $\Delta^{13}C_{carb\text{-}coll}$: Parallel Early-Life Decline Supports a Shared Metabolic-Dietary Transition

The carbonate-collagen carbon spacing ($\Delta^{13}C_{carb\text{-}coll}$) exhibit a similar "early decline followed by stabilization" pattern for the Baffin Bay individual (Tusk 1), closely paralleling the trends observed in Ba:Ca and Sr:Ca (Figure 9). Specifically, $\Delta^{13}C_{carb\text{-}coll}$ shows significant

moderate positive correlations with both Ba:Ca ($\rho = 0.48$, $p = 0.019$; Supplemental Material Table 5). For the Hudson Bay individual (Tusk 2), $\Delta^{13}C_{carb\text{-}coll}$ is also moderately positively correlated with Ba:Ca ($\rho = 0.52$, $p = 0.013$; Supplemental Material Table 6) and Sr:Ca ($\rho = 0.46$, $p = 0.03$) but follows a distinct ontogenetic trajectory (Figure 10). Values increase during the calf stage, reach higher levels in the early juvenile/subadult stage, and subsequently decline and stabilize during the later juvenile/subadult stage into adulthood.

Despite these differences in early-life structure, both tusks exhibit a significant long-term decrease in $\Delta^{13}C_{carb\text{-}coll}$ across their records (Tusk 1: -0.063‰ per year, $p < 0.001$; Tusk 2: -0.031‰ per year, $p < 0.002$; Supplementary Material Table 1). Taken together, these patterns are consistent with the elemental proxies and suggest that major and persistent shifts in feeding ecology occur early in life, followed by stabilization into an adult-like regime.

Although $\Delta^{13}C_{carb\text{-}coll}$ can integrate multiple physiological and ecological processes, including diet composition, macronutrient routing, and physiological state (DeSantis et al., 2022; Eastham & Feranec, 2025), the key observation is its internal coherence with the elemental proxies: $\Delta^{13}C_{carb\text{-}coll}$ changes within the same developmental window as Ba:Ca and Sr:Ca and remains comparatively stable following the early-life transition. This congruence supports interpretation of the observed pattern as a coherent ontogenetic transition rather than as a response to environmental variability alone.

The early-life decline in $\Delta^{13}C_{carb\text{-}coll}$ observed in both individuals is consistent with a major reorganization of dietary composition and metabolic routing during ontogeny. As outlined in Section 1.6.2.3., lower $\Delta^{13}C_{carb\text{-}coll}$ values are associated with increased reliance on lipid- and protein-rich resources and reduced contribution of carbohydrate-derived carbon. In narwhals, this pattern likely reflects the transition from milk-based nutrition and juvenile foraging strategies toward an adult feeding regime dominated by high-energy prey such as Arctic cod, Arctic char, and Greenland halibut. This transition coincides with increasing dive capacity, expanding foraging range, and rapidly growing energetic demands, all of which require metabolic processes optimized for lipid-based energy production and deep, prolonged dives. The parallel decline in $\Delta^{13}C_{carb\text{-}coll}$ therefore provides direct geochemical evidence for the establishment of adult-like metabolic organization early in life.

The strong temporal coherence between $\Delta^{13}C_{carb\text{-}coll}$, Ba:Ca, and Sr:Ca further supports this interpretation. Ba:Ca and Sr:Ca ratios in marine mammal dentin are widely interpreted as

indicators of trophic structure and prey composition, with declining values reflecting shifts toward higher trophic level prey. The fact that all three proxies exhibit synchronous early-life declines followed by long-term stabilization indicates that the observed pattern is not driven by transient environmental variability but instead represents a persistent ontogenetic restructuring of feeding ecology and physiology independent of population and geography.

4.2.3. Hg Concentrations: Trophic Biomagnification Signal

In both tusks, Hg concentrations are inversely related to Ba:Ca and Sr:Ca, although the strength of these relationships varies between individuals (Ba:Ca: $\rho = -0.06$, $p = 0.790$ for Tusk 1; $\rho = -0.40$, $p = 0.068$ for Tusk 2; Sr:Ca: $\rho = -0.07$, $p = 0.745$ for Tusk 1; $\rho = -0.28$, $p = 0.203$ for Tusk 2; Supplementary Material Tables 5 and 6). Consistent with the relationships, Hg concentrations increase as Ba:Ca and Sr:Ca decrease (Figures 9 and 10).

Hg exhibit a significant increasing trend through time in Tusk 1 (+0.480µg/g per year, $p = 0.010$; Supplementary Material Table 1) and a weaker, though positive, trend in Tusk 2 (+0.072µg/g per year, $p = 0.257$). This directionality aligns with the current understanding that Hg, particularly methylmercury (MeHg), biomagnifies strongly through marine food webs (Kirk et al., 2012; Krabbenhoft & Sunderland, 2013; Zhang et al., 2020).

The consistency between Hg concentrations and elemental trophic proxies across individuals strengthens the inference that declining Ba:Ca and Sr:Ca reflect increasing trophic exposure and/or increasing reliance on higher-trophic prey as the animal matures, with correspondingly greater biomagnification potential. Moreover, even if $\delta^{15}N_{collagen}$ does not behave as a simple trophic proxy, Hg provides an independent validation of and early-life trophic transition in both individuals. This interpretation is further supported by narwhal-specific work using tusk growth layers, which has demonstrated that tusks record multi-decadal Hg exposure and feeding ecology signals, reinforcing the use of tusk chemistry as a chronological archive for trophic-contaminant coupling (Dietz et al., 2021).

4.2.4. Decoupling $\delta^{15}N_{collagen}$ from Trophic Structure

In contrast to the consistent trophic signals provided by Ba:Ca, Sr:Ca, $\Delta^{13}C_{carb\text{-}coll}$, and Hg concentrations, $\delta^{15}N_{collagen}$ displays a divergent long-term trajectory between the two individuals that cannot be readily reconciled with changes in diet or trophic position. If $\delta^{15}N_{collagen}$ values in the tusks were primarily recording trophic position, then $\delta^{15}N_{collagen}$ would be expected to exhibit the same life-history pattern observed in Ba:Ca, Sr:Ca, and $\Delta^{13}C_{carb\text{-}coll}$: an early-life transition followed by long-term stabilization, and, importantly, similar structure in both individuals. Instead, $\delta^{15}N_{collagen}$ behaves fundamentally differently; it declines significantly over time in Tusk 1 (-0.055‰ per year, $p < 0.001$; Supplementary Material Table 1) but remains relatively stable in Tusk 2 (+0.001‰ per year, $p = 0.862$) despite similar ontogenetic patterns in Ba:Ca, Sr:Ca, and $\Delta^{13}C_{carb\text{-}coll}$, as well as trophically consistent Hg signal in both tusks.

This decoupling suggests that $\delta^{15}N_{collagen}$ is being strongly modulated by other factors than migration and diet. Sea-ice dynamics, stratification, and nitrogen recycling can substantially alter $\delta^{15}N_{collagen}$ baseline independently of food-web structure (Westbrook et al., 2024). These baseline shifts can propagate through the food-web, influencing the isotopic composition of higher trophic levels regardless of changes in diet.

4.3. Biogeochemical Baseline Restructuring and Divergent $\delta^{15}N_{collagen}$ Profiles

4.3.1. Baseline Sensitivity of $\delta^{15}N$ in Arctic Marine Ecosystems

Arctic $\delta^{15}N$ baselines are particularly sensitive to shifts in nutrient sources, nitrogen recycling, and physical controls on primary production, including changes in stratification, light availability, and freshwater input. Increasing freshwater discharge is expected to alter the sources and availability of nitrogen in Arctic marine ecosystems, particularly in coastal regions directly influenced by riverine input from thawing permafrost and glacially fed rivers (Westbrook et al., 2024). Enhanced inputs of dissolved organic nitrogen (DON) into surface waters, especially in

regions that are naturally nitrogen-limited, can stimulate phytoplankton production and modify the magnitude and timing of blooms (Lewis et al., 2020; Westbrook et al., 2024).

Critically, sea-ice decline can further reorganize primary production and the importance of sympagic (sea-ice algae) versus pelagic phytoplankton, alter vertical mixing, modify nutrient inventories, and ultimately reshape nitrogen recycling pathways (Benkort et al., 2020; Kohlbach et al., 2016; Lewis et al., 2020; Matthes et al., 2021; Westbrook et al., 2024). Recent research on nitrogen cycling in the Eastern Canadian Archipelago and Baffin Bay demonstrates spatially structured nitrogen sources and cycling and supports the plausibility of $\delta^{15}N$ baseline shifts over ecological timescales (Westbrook et al., 2024).

4.3.2. Tusk 1 (Baffin Bay): Progressive $\delta^{15}N_{collagen}$ Decline as a Baseline Shift

In Tusk 1, $\delta^{15}N_{collagen}$ exhibits a pronounced multi-year decline that is not mirrored by mobility tracers and is not consistent with the shared ontogenetic trophic patterns inferred from Ba:Ca, Sr:Ca, and $\Delta^{13}C_{carb\text{-}coll}$ (Figure 9).

In Baffin Bay, the physical and biological consequences of sea-ice decline provide a plausible mechanism for progressive restructuring of nitrogen isotopic baselines. Major reductions in sea-ice extent occurred during the period captured by the tusk record (-0.0058 million km^2 per year; $p < 0.001$; Supplemental Material Table 32), with particularly pronounced losses between the mid-1980s and late 2000s and more stable conditions since then (Figure 24). Sea-ice decline alters stratification, bloom phenology, nutrient delivery, and nitrogen recycling pathways, all of which can modify the $\delta^{15}N$ signature of organic matter at the base of the food web (Tamelander et al., 2009). This interpretation is further supported by regional nitrogen cycling studies that document substantial variability in nitrogen sources and transformations, consistent with the notion that $\delta^{15}N$ baselines in Baffin Bay shift over decadal intervals (Fox & Walker, 2022; Westbrook et al., 2024).

The timing of the $\delta^{15}N_{collagen}$ decline in Tusk 1 is consistent with this framework. Values decrease from the beginning of the record (19.34‰ in 1998) through the late juvenile/subadult stage (17.55‰ in 2006), spanning approximately the first decade of life but remained relatively stable after that. Rather than representing a direct response to specific sea-ice loss events, the

gradual decline likely reflects integration of longer-term changes in the nitrogen baseline associated with evolving ice conditions.

Under ontogenetic expectations, $\delta^{15}N_{collagen}$ would be predicted to increase with age as narwhals transition toward larger, higher-trophic-level prey (Louis et al., 2021). The observed long-term decrease therefore runs counter to a trophic explanation, particularly given that independent trophic proxies (Ba:Ca, Sr:Ca, $\Delta^{13}C_{carb\text{-}coll}$) record an early-life trophic transition followed by stabilization. The fact that $\delta^{15}N_{collagen}$ declines in opposition to these proxies strongly suggests that nitrogen baseline dynamics are sufficiently strong to modulate, and in this case reverse, the expected trophic enrichment signal.

Independent isotope studies of marine mammals support this interpretation. A study on Arctic seals demonstrate that bulk $\delta^{15}N$ variability is strongly governed by baseline nitrogen dynamics, as shown by the tight coupling between predator $\delta^{15}N$ and baseline $\delta^{15}N$ indicators, and the weak relationship between $\delta^{15}N$ and trophic position (De La Vega et al., 2021). Similarly, compound-specific $\delta^{15}N$ records from harp seal teeth in the Barents Sea reveal a multi-decadal decline in $\delta^{15}N$ baseline driven by changes in ocean circulation, nutrient supply, and primary production, independent of trophic restructuring (De La Vega et al., 2022). Together, these studies demonstrate that climate-driven baseline reorganization can dominate long-term $\delta^{15}N$ trends in apex marine predators, consistent with the pattern observed in the Baffin Bay narwhal tusk.

4.3.3. Tusk 2 (Hudson Bay): Stable $\delta^{15}N_{collagen}$ in a Freshwater-Influenced System

In Tusk 2, $\delta^{15}N_{collagen}$ values are lower than in the early portion of the Baffin Bay tusk and remain comparatively stable through time (Figure 8), despite clear evidence for ontogenetic transitions recorded by Ba:Ca, Sr:Ca, $\Delta^{13}C_{carb\text{-}coll}$, and Hg. This decoupling suggests that, as observed in Baffin Bay individual, $\delta^{15}N_{collagen}$ may not function as a simple trophic proxy in Tusk 2, potentially reflecting differences in how baseline processes interact with trophic signals.

Hudson Bay is characterized by strong freshwater influence, substantial river discharge, persistent stratification, and local nitrogen recycling, all of which exert strong control on $\delta^{15}N$ baselines (Amiraux et al., 2023; Westbrook et al., 2024). In such systems, high primary productivity and reliance on regenerated nitrogen can lead to isotopically lighter organic matter at

the base of the food web, resulting in lower $\delta^{15}N$ values. Years with reduced sea-ice cover are associated with enhanced phytoplankton production, which tends to lower $\delta^{15}N$ values in organic nitrogen through increased isotopic fractionation during uptake (Tamelander et al., 2009). As a result, trophic enrichment signals in bulk $\delta^{15}N$ can be dampened or effectively counterbalanced by baseline forcing.

Differences in sea-ice extent between regions may further contribute to this contrast. The magnitude of sea-ice decline in Hudson Bay is smaller than in Baffin Bay (Figure 24; -0.0034 million km^2 per year, $p < 0.001$; Supplemental Material Table 32), representing approximately 40% less reduction over the observational period. This more moderate decline may have limited the extent of ice-driven restructuring of nitrogen cycling relative to Baffin Bay. Moreover, under ontogenetic expectations, $\delta^{15}N_{collagen}$ would be predicted to increase with age as predators incorporate higher-trophic-level prey. The absence of such an increase in Tusk 2, despite independent evidence for trophic development, suggests that baseline nitrogen dynamics in Hudson Bay are sufficiently strong to dampen the expected trophic enrichment signal.

One possibility is that baseline restructuring in Hudson Bay and surrounding waters occurred earlier than the observed in Baffin Bay, and the Tusk 2 record captures a post-transition low-sea-ice state rather than a baseline active shift. Alternatively, the combined effects of freshwater inputs, sea-ice melt dilution, sustained pelagic primary production, and inflow of isotopically lighter Atlantic waters may buffer nitrogen cycling, maintaining a persistently low and relatively invariant $\delta^{15}N$ baseline, even in the presence of ^{15}N-enriched Pacific-derived nitrate (Carmack et al., 2016; De La Vega et al., 2021; J. Lee et al., 2023; Westbrook et al., 2024). A further possibility is that, although the elemental proxies clearly record ontogenetic trophic development, the magnitude of trophic enrichment expected in bulk $\delta^{15}N$ is small relative to the strength of baseline nitrogen forcing in Hudson Bay. Under such conditions, baseline processes may suppress or mask trophic signals in $\delta^{15}N$, even when trophic position increases.

Distinguishing among these mechanisms will require additional baseline constraints, including $\delta^{15}N$ measurements of prey and primary producers across regions and time, as well as tusk records from older Hudson Bay individuals that extend further back in time. Nevertheless, the Hudson Bay tusk demonstrates that ontogenetic trophic and habitat transitions can be recorded by multiple independent proxies without corresponding increases in bulk $\delta^{15}N$, highlighting the dominant role of baseline nitrogen dynamics in shaping $\delta^{15}N$ signals in Arctic marine predators.

4.4. Toxicology: Linking Trophic Processes with Baseline Environmental Change

4.4.1. Hg: Trophic Biomagnification and Climate-Sensitive Baseline Forcing

The increase in Hg concentrations (Tusk 1: +0.481 µg/g per year, $p = 0.010$; Tusk 2: +0.072 µg/g per year, $p = 0.257$; Supplementary Material Table 1) combined with the decrease in Ba:Ca (Tusk 1: -1.76×10^{-7} per year, $p = 0.002$; Tusk 2: -4.16×10^{-7} per year, $p < 0.001$) and Sr:Ca (Tusk 1: -7.54×10^{-6} per year, $p = 0.002$; Tusk 2: -1.87×10^{-5} per year, $p < 0.001$) across both tusks indicates a trophic biomagnification component, consistent with established syntheses of Arctic contaminant cycling and mercury exposure pathways (AMAP, 2018; Kirk et al., 2012). This pattern supports the interpretation that increasing reliance on higher-trophic prey during ontogeny is accompanied by enhanced Hg accumulation in both individuals.

However, Hg exposure is not controlled solely by trophic position; Hg availability is also sensitive to where and when methylmercury (MeHg) is produced within the environment. There is compelling evidence that MeHg production can be enhanced or redistributed within the marginal ice zone under changing sea-ice regimes. Recent work has shown that MeHg is produced directly in the marginal sea-ice zone of the central Arctic Ocean under specific biological and physicochemical conditions, linking MeHg production to ice-edge organic matter dynamics and microbial activity (Heimbürger et al., 2015). These processes can shift rapidly as sea-ice extent and seasonality change, providing a climate-sensitive source of MeHg that contributes to baseline Hg availability independently of trophic transfer. Furthermore, recent studies indicate that Hg and MeHg cycling in the Arctic are influenced by multiple sources and transformation pathways, including atmospheric deposition, riverine inputs, and local production and recycling. Physical stratification, organic matter availability, and redox gradients regulate methylation and demethylation rates, indicating that MeHg baseline availability can vary regionally and temporally in response to climatic and hydrological change without corresponding changes in trophic structure (Soerensen et al., 2016).

These dual controls on Hg are potentially reflected in the tusk records. In the Baffin Bay individual (Tusk 1), Hg concentrations increase significantly through life in parallel with declining

Ba:Ca and Sr:Ca (Figure 9), consistent with ontogenetic trophic biomagnification, while continuing to rise as the animal matures, suggesting additional influence from changing baseline Hg availability associated with evolving sea-ice and marginal ice-zone processes. The Hudson Bay individual (Tusk 2) also exhibits an increase in Hg while Ba:Ca and Sr:Ca decrease (Figure 10), supporting trophic biomagnification, but Hg variability remains more tightly constrained and closely aligned with trophic proxies, consistent with a more stable and locally buffered baseline Hg regime in the coastal, freshwater-influenced Hudson Bay system. These patterns indicate that Hg recorded in narwhal tusks integrates both feeding ecology and region-specific, climate-sensitive changes in contaminant cycling.

4.4.2. Pb, Cd, and As: Sea-Ice and Baseline Controls on Exposure Pathways

In contrast to Hg, whose accumulation in marine predators is likely dominated by trophic biomagnification, the behavior of Pb, Cd, and As in Arctic marine systems is governed primarily by exposure pathways and baseline biogeochemical processes (Kirk et al., 2012; Rohonczy et al., 2024; Stern et al., 2012). These metals exhibit pronounced early-life declines that parallel the ontogenetic transitions recorded by Ba:Ca, Sr:Ca, and $\Delta^{13}C_{carb\text{-}coll}$ (Figures 9 and 10), but diverge thereafter (Figures 11 and 12). Pb:Ca and Cd:Ca exhibit significant long-term declines ($p \leq 0.002$), indicating a systematic reduction in exposure to these non-essential metals over the lifetime of each individual. In the Baffin Bay tusk (Tusk 1), Pb:Ca and Cd:Ca decrease through time (Pb:Ca = -1.01 10^{-8} yr^{-1}; Cd:Ca = -2.26×10^{-9} yr^{-1}; Supplemental Material Table 1), while similar declines are observed in the Hudson Bay tusk (Tusk 2) for all three metals (Pb:Ca = -1.86×10^{-8} yr^{-1}; Cd:Ca = -1.84×10^{-9} yr^{-1}; As:Ca = -8.26×10^{-10} yr^{-1}). If these metals were governed primarily by trophic biomagnification, their concentrations would be expected to remain stable or increase with age, broadly tracking the ontogenetic rise in Hg. Instead, their decline indicates that they are controlled primarily by shifts in exposure pathways and baseline environmental availability rather than by trophic position alone.

Pb, Cd, and As enter Arctic marine ecosystems through a combination of long-range atmospheric transport, riverine discharge, and sedimentary and coastal inputs (Stern et al., 2012). Once introduced into surface waters, all three elements are highly particle-reactive and are efficiently scavenged onto suspended particles and organic matter, which strongly regulates their

distribution and bioavailability. Atmospheric deposition onto snow and sea ice further enhances this particle-associated behavior, as trace metals are scavenged from the atmosphere and incorporated into seasonal snowpacks and sea ice, where they become concentrated within ice-associated particulates and microbial communities (Berner et al., 2016; De Vera et al., 2021a; Kirk et al., 2012; Stern et al., 2012). During spring melt, metals stored in snow and sea ice are released into surface waters, generating short-lived but ecologically important exposure pulses that coincide with periods of high biological productivity (Jensen et al., 2021; Krabbenhoft & Sunderland, 2013), thereby concentrating metals within the pelagic Arctic food chain. As Arctic sea ice thins and retreats, this seasonal concentrating-and-release mechanism is altered.

Reduced ice cover weakens the coherence and magnitude of these exposure pulses and redistributes particle-reactive metals more diffusely through the water column including in the benthic zone. Because Pb, Cd, and As are strongly controlled by particle scavenging, stratification, and organic matter cycling, their environmental availability and exposure pathways are therefore highly sensitive to climate-driven changes in sea-ice extent, freshwater input, vertical mixing, and particulate dynamics (Evans & Nishioka, 2019; Kirk et al., 2012; Stern et al., 2012).

The timing of the Pb:Ca decline is consistent with the global phase-out of leaded gasoline. While Pb emissions in North America and Europe began declining in the 1970s and were largely eliminated from on-road fuel by the 1990s, the final phase-out of major remaining global sources around the turn of the 2000s further reduced atmospheric Pb inputs to the Arctic (S. Lee et al., 2023). The marked decrease in Pb:Ca observed in both tusks around ~2000 may therefore reflect the cumulative effect of decades of declining emissions combined with the final removal of major global sources, resulting in a further reduction of atmospheric Pb delivery to the Arctic.

Differences in large-scale water mass sourcing may further contribute to the observed Pb trends. Pacific-derived waters are characterized by lower dissolved Pb (dPb) concentrations, whereas Atlantic-derived waters generally carry higher dPb and distinct isotopic signatures (Colombo et al., 2019; Olivelli et al., 2025). However, ongoing Arctic freshening associated with sea-ice loss can generate negative salinity anomalies in the North Atlantic, which may suppress deep-water formation and influence the strength and structure of overturning circulation (Dickson et al., 2002; Jensen et al., 2021). Such circulation changes have the potential to modulate the delivery of Atlantic-derived dPb to Arctic surface waters, and in this context, declining Pb:Ca may

reflect not only reduced atmospheric inputs but also climate-driven reorganization of ocean circulation and baseline metal supply pathways.

For Cd and As, which display nutrient-like behavior in the ocean, declining concentrations are further reinforced by enhanced biological uptake in surface waters, meltwater dilution, and stronger stratification under reduced ice cover. Although Cd is not considered an essential nutrient, it is actively assimilated by certain phytoplankton taxa, particularly diatoms, in which Cd can substitute for Zn or be incorporated via Cd-specific enzymes (Zhang et al., 2019). In the case of As, uptake by phytoplankton is accompanied by extensive biological transformation into organic As compounds, further reducing the pool of bioavailable inorganic As in surface waters (Azizur Rahman et al., 2012). Together, these processes promote sustained depletion of Cd and As in the surface ocean by increasing primary productivity and limiting surface metal availability despite elevated inventories at depth (Azizur Rahman et al., 2012; Evans & Nishioka, 2019; Gerringa et al., 2021; Jensen et al., 2021; Zhang et al., 2019).

In addition, regional variability in metal sources likely contributes to early-life declines, as juveniles may experience greater exposure in coastal, shelf, or sediment-influenced environments where Pb, Cd, and As are locally enriched, whereas later-life shifts toward offshore or pelagic habitats reduce exposure without requiring a change in trophic position. These ontogenetic shifts in feeding ecology likely contribute to the observed correlations between Pb:Ca, Cd:Ca and As:Ca with Ba:Ca and Sr:Ca, while long-term declines in metal concentrations reflect broader baseline environmental change.

4.4.3. Pb Isotopes as Tracers of Baseline Pb Sources and Exposure Pathways

Pb isotope ratios provide critical constraints on contaminant source pathways because, unlike concentrations, they are insensitive to trophic biomagnification and biological fractionation. Variability in Pb isotope ratios therefore reflects changes in the relative contributions of distinct Pb sources, including atmospheric aerosols, riverine inputs, sedimentary reservoirs, and advected ocean waters (Colombo et al., 2019; De Vera et al., 2021b). When interpreted alongside Pb:Ca ratios, Pb isotopes allow exposure magnitude to be disentangled from source provenance.

The two narwhal tusks exhibit fundamentally different Pb isotope patterns despite both showing long-term declines in Pb:Ca, demonstrating that changes in Pb exposure and Pb source

are not necessarily coupled. In the Hudson Bay individual (Tusk 2), Pb isotope ratios remain tightly clustered through time across all measured ratios ($^{206}Pb/^{204}Pb$, $^{208}Pb/^{206}Pb$, $^{206}Pb/^{207}Pb$; Figure 13). This isotopic stability persists from juvenile stages through adulthood, even as Pb:Ca declines significantly over the individual's life (Figure 12). The lack of directional isotopic change indicates that Pb exposure declined without a corresponding shift in source composition.

The isotopic field occupied by Tusk 2 overlaps most strongly with anthropogenically contaminated shelf sediments and nearshore sources rather than with open-ocean Pb isotopic signatures. This pattern is consistent with a shallow, coastal, freshwater-influenced system in which Pb inputs are dominated by locally recycled sedimentary and river-associated sources. Sediment records from Hudson Bay indicate that anthropogenic Pb has accumulated in shelf deposits and is efficiently retained and recycled within the system rather than being rapidly exported, resulting in a persistent signal even where total Pb fluxes are low (Thibodeau et al., 2017). Within such a framework, Pb incorporated into the food web likely reflects remobilization of historically deposited anthropogenic Pb from sediments and riverine inputs, rather than solely contemporary atmospheric delivery. The continued dominance of anthropogenic Pb in Hudson Bay trophic pathways is therefore consistent with long-term regional contamination combined with strong coastal trapping and proximity to North American emission sources.

In contrast, the Baffin Bay individual (Tusk 1) exhibits pronounced and systematic changes in Pb isotope ratios through time (Figure 13). All three isotope ratios show a coherent shift toward more radiogenic compositions beginning in the early 2000s, coincident with continued declines in Pb:Ca (Figure 11). This pattern indicates that not only did Pb exposure decrease, but that the relative contribution of Pb sources was restructured. The progressive increase in $^{206}Pb/^{207}Pb$ is consistent with a declining influence of isotopically light anthropogenic aerosol Pb historically delivered to the Arctic via long-range atmospheric transport, particularly from North America leaded gasoline and industrial emissions (Nakano, 2016). As these sources diminished, the Pb entering the Baffin Bay system became increasingly dominated by more radiogenic natural inputs, including Atlantic-derived waters and regional geological sources (Colombo et al., 2019; De Vera et al., 2021b; Rogalla et al., 2025).

The timing of this Pb isotope reorganization broadly coincides with the onset of the pronounced decline in $\delta^{15}N_{collagen}$ observed in the same individual (Figures 7 and 13). While Pb isotopes and nitrogen isotopes reflect different biogeochemical processes, their contemporaneous

shifts suggest a common sensitivity to large-scale baseline environmental change rather than independent, unrelated drivers. In particular, the early-2000s transition corresponds to a period of rapid summer sea-ice loss in Baffin Bay (Figure 24) and increased influence of Atlantic-derived waters documented in the region (Ballinger et al., 2022). Reduced sea-ice cover enhances ocean-atmosphere exchange, alters stratification and mixing, and facilitates greater advection of Atlantic waters into Baffin Bay, processes that can simultaneously modify Pb source contributions and nitrogen cycling at the base of the food web.

Importantly, the isotopic shift in Tusk 1 occurs alongside declining Pb:Ca, demonstrating that reduced exposure from anthropogenic lead was accompanied by a change in Pb provenance rather than a uniform reduction across all sources. The broader isotopic range occupied by Tusk 1 relative to Tusk 2 (Figure 14) further reflects the open, circulation-influenced nature of Baffin Bay, where Pb inputs integrate multiple upstream reservoirs whose relative importance can change as atmospheric pathways, sea-ice dynamics, and ocean circulation evolve. Together, these patterns indicate that Pb isotopes in the Baffin Bay tusk record a climate-driven reorganization of baseline source pathways occurring contemporaneously with broader biogeochemical changes also expressed in nitrogen isotope records.

4.5. Population-Level Baseline Shifts

4.5.1. Step-Like Isotopic Transition Recorded in High-Resolution Individual Tusks

High-resolution records preserved in narwhal tusks provide a unique opportunity to constrain the timing and direction of ecosystem change at annual to near-annual resolution. In the Baffin Bay individual (Tusk 1), $\delta^{15}N_{collagen}$ exhibits a pronounced long-term decline that begins around the early 2000s, following an earlier interval of relative stability (Figure 7). This shift is striking because narwhals are expected to increase trophic level with age, which would typically drive $\delta^{15}N$ upward rather than downward. In parallel, carbon-system proxies (particularly $\delta^{13}C_{CO3}$) show directional change consistent with broader reorganization of the carbon environment through time. Importantly, earlier sections demonstrate that the $\delta^{15}N_{collagen}$ decline is not accompanied by

coordinated directional shifts in mobility indicators ($\delta^{18}O_{CO3}$ and Pb isotopes), arguing against migration or sustained habitat relocation as the dominant cause of the nitrogen isotope trend.

This individual-scale evidence raises a critical question: Is the isotopic transition observed in Tusk 1 an individual-specific anomaly, or does it reflect a broader population-level shift in baseline carbon and nitrogen cycling in Baffin Bay? Addressing this requires moving from individual records to population-wide datasets that integrate multiple individuals, cohorts, and decades.

4.5.2. Direction and Timing of Population-Level Change

A compilation of population-level data reveals a clear, coherent, and temporally constrained shift in both $\delta^{13}C_{collagen}$ and $\delta^{15}N_{collagen}$. From the early 1980s through the late 1990s, both isotopes remain remarkably stable, forming a tight isotopic cluster with no directional trend. Beginning in the early 2000s, both $\delta^{13}C_{collagen}$ and $\delta^{15}N_{collagen}$ shift systematically toward lower values, producing a new isotopic cluster that persists through the most recent samples. The transition is step-like rather than gradual, with partial overlap between pre-2000 and post-2000 values, particularly for $\delta^{15}N_{collagen}$ (Figure 25). Crucially, this pattern is expressed at the population scale, not solely within a single individual, and therefore cannot be attributed to individual ontogeny, selective sampling, or atypical behavior.

The timing of a similar isotopic shift in beluga collagen closely matches that observed in narwhal embedded teeth, with stable values prior to ~2000 followed by a coherent decline thereafter. Because belugas and narwhals differ in foraging strategy, prey range, and habitat use (Laidre et al., 2008; Reeves et al., 2014; Watt et al., 2013), the expression of comparable directional change in both species supports a shared environmental driver acting at the base of the food web rather than a species-specific ecological change. Together, the individual tusk archive (Tusk 1) and the population-level embedded tooth dataset converge on the same conclusion: a major isotopic transition occurred around the turn of the millennium across the Baffin Bay ecosystem, and it propagated into multiple apex predators. The next step is to evaluate whether this shift could plausibly be explained by systematic changes in diet, trophic position, or migration, or whether it instead requires baseline restructuring.

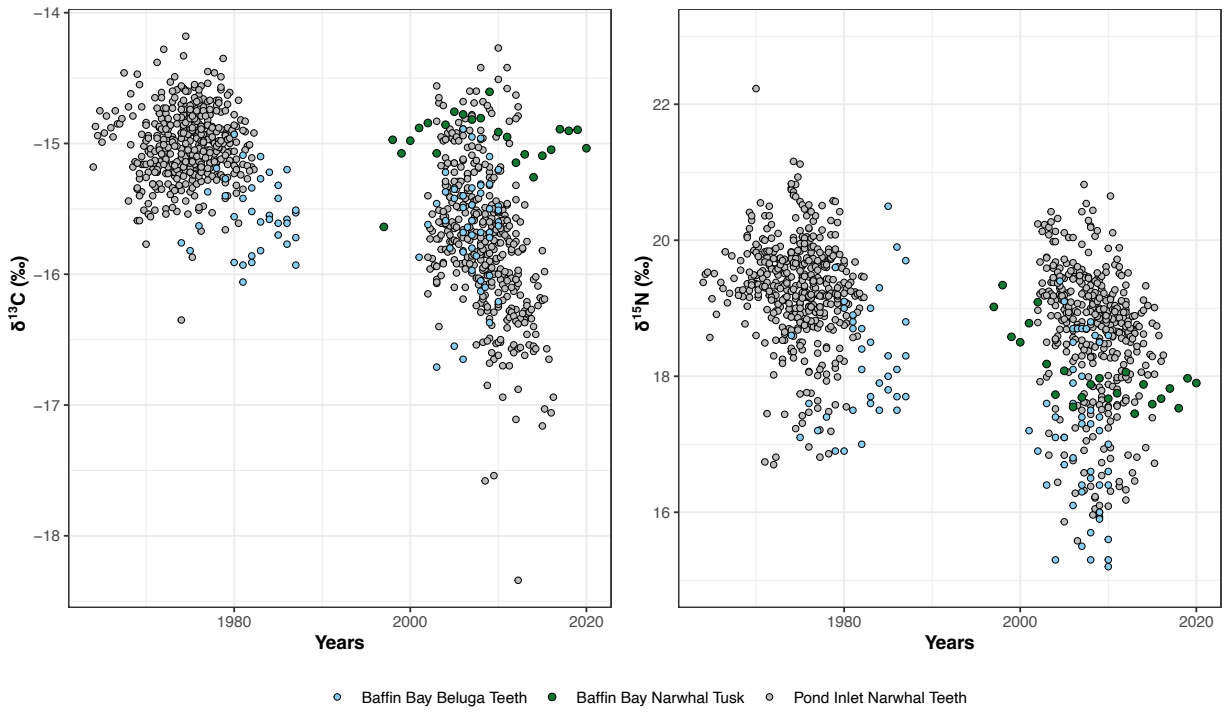

Figure 25. Comparison of $\delta^{13}C_{collagen}$ (left panel) and $\delta^{15}N_{collagen}$ (right panel) trends in narwhals and belugas from Baffin Bay. Grey points show collagen isotope data from embedded narwhal teeth collected at Pond Inlet, spanning pre- and post-2000 periods (Zhao et al., 2025). Calendar years for embedded-tooth samples were assigned using an approximate age model based on the estimated age at harvest, the number of growth layer groups (GLGs) represented in each tooth, the number of samples per GLG, and the year of collection. Because not all annual GLGs are preserved in embedded teeth, some years may be missing and assigned ages should be considered approximate. Green points represent annual growth-layer values from Tusk 1 (Baffin Bay individual) from 1998 to 2020. Light blue points show annual collagen isotope values from beluga teeth collected in Baffin Bay between 1974 and 2016 (Matthews & Ferguson, 2015).

4.5.3. Why this Shift Cannot be Explained by Diet or Trophic Change

A population-wide decline in $\delta^{13}C_{collagen}$ and $\delta^{15}N_{collagen}$ could, in principle, reflect a systematic change in trophic level or prey choice across the Baffin Bay narwhal population. However, multiple lines of evidence strongly argue against this interpretation.

First, narwhals are highly specialized predators with a relatively narrow prey spectrum dominated by Arctic cod and Greenland halibut (Laidre & Heide-Jørgensen, 2005), and there is no evidence for a population-wide shift toward substantially lower trophic-level prey beginning in the early 2000s. Telemetry, stomach content, fatty-acid, and stable-isotope studies consistently indicate broad continuity in foraging ecology across decades, even as environmental conditions

have changed (Dietz et al., 2021; Finley & Gibb, 1982; Heide-Jørgensen et al., 2014; Hornby et al., 2025; Laidre et al., 2004; Laidre & Heide-Jørgensen, 2005; Watt et al., 2013; Watt & Ferguson, 2015).

Second, a trophic explanation would require a coordinated and sustained reduction in trophic position across multiple age classes and cohorts, which is ecologically implausible without major restructuring of the entire food web. Such restructuring would be expected to manifest in independent evidence for broad changes in prey availability, predator condition, or biomagnifying contaminant patterns at the ecosystem scale. While climate-associated shifts in prey composition and habitat use have been documented in Arctic marine systems (Watt & Ferguson, 2015), no reported changes match the magnitude and coherence needed to explain the step-like, population-wide isotopic transition observed here.

Third, the concurrent decline in both $\delta^{13}C_{collagen}$ and $\delta^{15}N_{collagen}$ points away from a trophic interpretation and toward a baseline driver. Changes in trophic position typically produce opposing or non-parallel shifts in $\delta^{13}C$ and $\delta^{15}N$ depending on diet composition and routing, whereas a simultaneous directional decline in both isotopes is more consistent with change at the base of the food web.

Fourth, high-resolution analyses of narwhal embedded teeth reveal pronounced seasonal $\delta^{13}C_{collagen}$ and $\delta^{15}N_{collagen}$ oscillations linked to seasonal feeding, migration, and physiology, but these oscillations are non-directional through time and are insufficient in magnitude to account for the persistent, multi-decadal, population-level shift (Zhao et al., 2025). Moreover, baseline isotopic differences between summer and winter habitats in Baffin Bay are too small to explain the long-term, step-like change, indicating that migration-driven habitat switching alone cannot account for the trend (Zhao et al., 2025). This is consistent with the individual tusk evidence presented earlier, where mobility proxies ($\delta^{18}O_{CO3}$ and Pb isotopes) do not exhibit coordinated directional changes that track the nitrogen isotope shift.

Finally, the beluga record strengthens this inference. Belugas occupy a broadly comparable trophic position to narwhals but differ substantially in prey range and habitat use; they are more opportunistic generalists exploiting coastal, shelf, and estuarine habitats, whereas narwhals are more specialized deep-diving predators, particularly in winter (Laidre et al., 2008; Reeves et al., 2014; Watt et al., 2013). The presence of similar long-term declines in $\delta^{13}C$ and $\delta^{15}N$ in belugas despite these ecological differences argues strongly against a species-specific trophic driver and

instead supports a shared environmental forcing affecting baseline isotope values in Baffin Bay (Matthews & Ferguson, 2015).

Together, these lines of evidence indicate that the population-level decline in $\delta^{13}C_{collagen}$ and $\delta^{15}N_{collagen}$ is not driven primarily by diet, trophic position, or migration. Instead, it points to a coherent and temporally constrained reorganization of $\delta^{13}C$ and $\delta^{15}N$ baseline values at the base of the Baffin Bay food web.

4.5.4. Baseline Isotopic Restructuring as the Most Plausible Explanation

The most parsimonious interpretation of the observed population-level isotopic shift is a baseline restructuring in Baffin Bay, coincident with major changes in sea-ice extent (Figure 24), seasonality, and associated biogeochemical conditions beginning in the late 1990s to early 2000s. This period corresponds to well-documented reductions in summer sea-ice extent, earlier breakup, and later freeze-up across Baffin Bay and the eastern Canadian Arctic (Dietz et al., 2021; Fetterer et al., 2017, 2025; Garcia-Soto et al., 2021; Hoegh-Guldberg & Bruno, 2010; Perovich et al., 2020; Reed et al., 2021).

Sea-ice decline fundamentally alters the timing, magnitude, and structure of primary production in Arctic marine ecosystems. Reduced ice cover diminishes the contribution of ice-associated algae, enhances pelagic phytoplankton production, modifies vertical stratification, and shifts the balance between new, nitrate-based production and regenerated, ammonium-based production pathways (Assmy et al., 2017; Buchanan et al., 2022; Feng et al., 2018; Leu et al., 2011; Lewis et al., 2020; Macdonald et al., 2015; Markus et al., 2009; Post et al., 2013; Reed et al., 2021; Stroeve & Notz, 2018; Von Friesen et al., 2025; Westbrook et al., 2024). Each of these processes exerts strong control on $\delta^{13}C$ and $\delta^{15}N$ baseline values of POM, which propagate through the food web to higher trophic levels (De La Vega et al., 2019; Fox & Walker, 2022; Yunda-Guarin et al., 2020).

The decline in $\delta^{13}C_{collagen}$ in the Pond Inlet narwhal embedded teeth and in the beluga teeth (Figure 25) is consistent with a shift in the dominant carbon sources at the base of the food web. Ice-associated primary production and periods of rapid phytoplankton growth typically produce ^{13}C-enriched (more positive) POC, whereas increased CO_2 availability, enhanced pelagic

production, and greater terrestrial carbon inputs yield ^{13}C-depleted (more negative) organic matter (Burkhardt et al., 1999; De La Vega et al., 2019; Keeley & Sandquist, 1992; Rau et al., 1992).

An important consideration when interpreting long-term trends in $\delta^{13}C_{collagen}$ is the anthropogenic decline in atmospheric and oceanic $\delta^{13}C$ associated with fossil fuel CO_2 emissions (the Suess effect). In principle, adjustment for the Suess effect would reduce the magnitude of the observed $\delta^{13}C$ decline through time. However, the $\delta^{13}C$ values for narwhal embedded teeth and beluga teeth presented here are not corrected for the Suess effect because of uncertainty in the absolute calendar-year assignment of growth layer groups (GLGs). While narwhal tusks provide higher temporal resolution, embedded tooth records necessarily integrate broader age ranges, making precise application of a Suess-effect correction uncertain and potentially misleading at the scale of individual layers. Applying reasonable first-order Suess-effect corrections based on published estimates of oceanic $\delta^{13}C$ decline indicates that a downward shift in $\delta^{13}C$ persists across the study interval, although with reduced magnitude. Thus, uncertainty in Suess-effect correction affects the amplitude but not the direction or timing of the observed isotopic transition. The step-like nature of the population-level shift, its coherence across individuals and species, and its temporal alignment with rapid sea-ice loss in the early 2000s all remain intact regardless of whether an approximate Suess correction is applied. Consequently, the $\delta^{13}C$ trends identified here cannot be explained solely by anthropogenic carbon dilution and instead require additional restructuring of baseline carbon sources and fractionation regimes in the Baffin Bay ecosystem.

In parallel, the observed decline in $\delta^{15}N_{collagen}$ in the Pond Inlet narwhal embedded teeth and in the Baffin Bay beluga teeth (Figure 25) is consistent with a fundamental restructuring of nitrogen cycling at the base of the food web under changing sea-ice and productivity regimes. The isotopic composition of organic nitrogen is tightly controlled by the balance between new, nitrate-based production and regenerated, ammonium-based production. During periods of strong nitrate utilization, phytoplankton preferentially assimilate $^{14}NO_3^-$, progressively enriching the remaining nitrate pool in ^{15}N and leading to elevated $\delta^{15}N$ values in newly formed organic matter as blooms mature. In contrast, when ecosystem productivity is increasingly supported by regenerated nitrogen sources such as ammonium, which undergo stronger isotopic fractionation, organic matter becomes isotopically lighter and exhibits lower $\delta^{15}N$ signatures (Fox & Walker, 2022; Hoondert et al., 2021; Tamelander et al., 2009; Westbrook et al., 2024).

Declining sea ice alters stratification, nutrient supply, and bloom dynamics, thereby shifting the balance between new, nitrate-based and regenerated, ammonium-based production. Earlier breakup, enhanced mixing, and prolonged productive periods favor pelagic phytoplankton growth and increase the contribution of isotopically light regenerated nitrogen at the base of the food web (Hoondert et al., 2021; Tamelander et al., 2009). Because primary producers integrate these changes rapidly, climate-driven modification of nitrogen cycling propagates through the food web and produces sustained declines in $\delta^{15}N$ baseline values at higher trophic levels. This provides a coherent mechanistic explanation for the long-term decrease in $\delta^{15}N$ observed in the Baffin Bay population embedded teeth.

Sea-ice loss may additionally lower $\delta^{15}N$ baselines by stimulating biological N_2 fixation, providing an isotopically light source of reactive (i.e., bioavailable) nitrogen to Arctic food webs (Figure 26). Melting sea ice and increasing solar irradiance initiate intense phytoplankton blooms that account for a substantial fraction of Arctic primary productivity (Campbell et al., 2017; Robicheau et al., 2023; Slagstad et al., 2015). Under such conditions, diazotrophs capable of converting atmospheric N_2 ($\delta^{15}N \approx -1‰$; Zhang et al., 2014) into bioavailable nitrogen can contribute to surface nitrogen pools and influence baseline isotopic composition (Lehmann et al., 2022; Sohm et al., 2011; Tang et al., 2019). Recent observations demonstrate that N_2 fixation rates are highest in waters associated with actively melting sea ice, including the marginal ice zone and decaying multiyear ice, and that fixation rates are positively correlated with primary production (Von Friesen et al., 2025). This pattern is consistent with observations from Antarctica, where nitrogen fixation rates are elevated in waters influenced by sea ice relative to open waters (Shiozaki et al., 2020). Such bloom-associated N_2 fixation along the retreating ice edge would supply isotopically light nitrogen into surface waters, reinforcing declines in $\delta^{15}N$ at the base of the food web.

Importantly, the sharp timing of the isotopic shift, characterized by stable conditions prior to ~2000 followed by a persistently lower baseline, thereafter, mirrors the major transition in Arctic sea-ice conditions during this period (Figure 25). Together, these observations strongly support a climate-driven baseline restructuring mechanism as the primary driver of the population-level isotopic change observed in Baffin Bay narwhals.

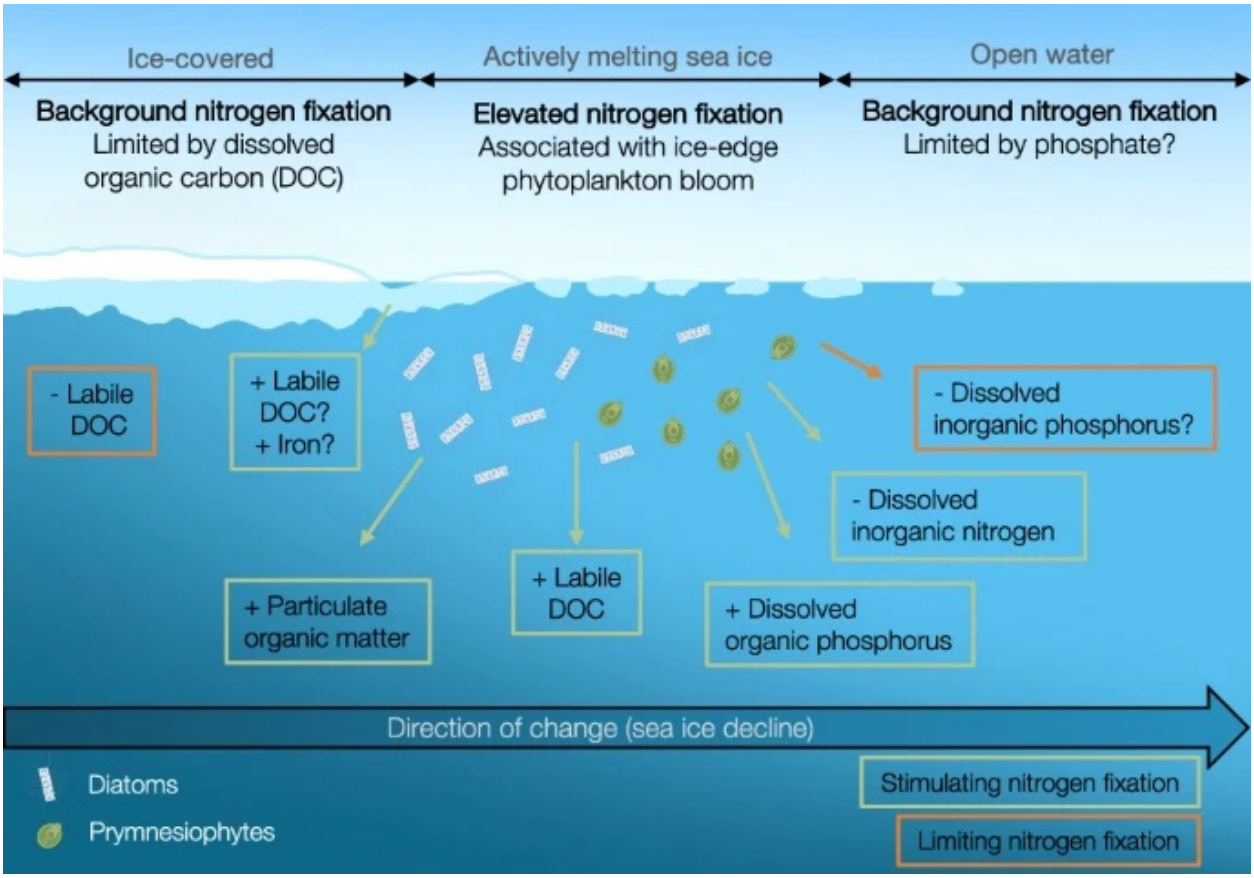

Figure 26. Schematic representation of observed relationships between sea-ice conditions and nitrogen fixation activity in the Arctic. Nitrogen fixation has been reported to be elevated in association with melting sea ice and ice-edge environments relative to consolidated, multi-year ice and open-water regions. Figure reused from the open-access article by Von Friesen et al. (2025).

4.5.5. Linking Population-Level Baseline Shifts to Individual Tusk Records

This population-level signal provides essential context for interpreting the tusk records. The pronounced decline in $\delta^{15}N_{collagen}$ observed in the Baffin Bay tusk (Tusk 1) is not an isolated or individual-specific phenomenon; instead, it reflects integration of a population-wide baseline shift that began around the turn of the millennium. The gradual expression of this transition within the tusk is consistent with the individual progressively incorporating a changing environmental baseline during growth, whereas the broader population dataset captures the contrast between pre- and post-shift conditions at coarser temporal resolution.

Within the individual tusk record, the decline in $\delta^{13}C_{CO3}$ observed in the Baffin Bay Tusk (Tusk 1) directly reflects this baseline shift in the ambient carbon system (Figure 7). The

progressive trend toward more negative $\delta^{13}C_{CO3}$ values indicates reduced reliance on sympagic production and increasing influence of pelagic and terrestrial carbon sources, consistent with the progressive loss of seasonal sea ice in Baffin Bay. In contrast, $\delta^{13}C_{collagen}$ in Tusk 1 remains comparatively stable (Figure 7), indicating that long-term carbon shift is expressed primarily through the environmental carbon system rather than through substantial changes in dietary protein sources. This decoupling reinforces the interpretation that the dominant signal recorded in the tusk reflects environmental baseline change rather than a major reconfiguration of prey choice.

The concurrent decline in $\delta^{15}N_{collagen}$ observed in the Baffin Bay tusk (Figure 7) also reflects large-scale reorganization of nitrogen cycling at the base of the food web. Prolonged pelagic production under reduced ice cover favors increased incorporation of isotopically light regenerated nitrogen into primary producers, while enhanced nitrogen fixation supplies additional isotopically light nitrogen to surface waters, together generating lower $\delta^{15}N$ values that propagate upward through the ecosystem (Hoondert et al., 2021; Tamelander et al., 2009; Von Friesen et al., 2025).

This pattern contrasts with the Hudson Bay tusk record (Tusk 2), where $\delta^{15}N_{collagen}$ remains low and comparatively stable through time despite variability in carbon-system proxies (Figure 8). Rather than indicating stable nitrogen cycling, this pattern suggests that nitrogen isotope signals in Hudson Bay are strongly modulated by baseline processes such as freshwater influence, stratification, and local recycling, which can dampen expected trophic enrichment in bulk $\delta^{15}N$. In contrast, $\delta^{13}C_{CO3}$ in the Hudson Bay tusk exhibits a long-term decline similar to that observed in the Baffin Bay tusk, indicating that baseline carbon cycling responds coherently to large-scale environmental change even where nitrogen isotopic responses differ. It is also possible that major restructuring of the nitrogen baseline in Hudson Bay occurred prior to the interval captured by the tusk record, such that the profile reflects a post-transition state rather than an actively shifting baseline. This decoupling between $\delta^{13}C$ and $\delta^{15}N$ highlights how different baseline processes can propagate through Arctic food webs with unequal sensitivity, producing region-specific isotopic expressions of ecosystem restructuring.

Isotope records from beluga whale teeth provide particularly strong support for this mechanism. In belugas from Hudson Bay and the eastern Canadian Arctic, declining $\delta^{13}C$ trends across dentinal growth layers were attributed primarily to variation in baseline carbon isotope composition, not to trophic-level change, because no corresponding long-term $\delta^{15}N$ trends were

observed (Matthews & Ferguson, 2014). The authors showed that decreases in $\delta^{13}C$ without accompanying declines in $\delta^{15}N$ are inconsistent with trophic shifts and instead reflect changes in baseline carbon sources. They further linked these baseline changes to Arctic sea-ice loss, altered primary production, and declining ice-algal contributions to the food web, demonstrating that sea-ice-driven ecosystem restructuring is directly recorded in marine mammal teeth.

Taken together, the concordant individual and population signals demonstrate that the observed $\delta^{13}C$ and $\delta^{15}N$ trends in Baffin Bay narwhals are best explained by ecosystem-scale biogeochemical reorganization rather than by changes in diet or movement. The agreement between life-history records preserved in tusks and independent population-level isotopic patterns provides strong, independent validation of the baseline-shift hypothesis and highlights the exceptional value of narwhal tissues as long-term archives of Arctic environmental change.

CHAPTER 5: CONCLUSION

5.1. Thesis Overview

This thesis used multi-proxy geochemical profiles measured along annual growth layer groups (GLGs) in two narwhal tusks from contrasting Canadian Arctic regions, Baffin Bay (Tusk 1) and Hudson Bay (Tusk 2), respectively spanning 1997-2020 and 1998-2021. By integrating stable isotopes ($\delta^{13}C_{collagen}$, $\delta^{15}N_{collagen}$, $\delta^{13}C_{CO3}$, $\delta^{18}O_{CO3}$), Hg concentrations, lead isotope ratios ($^{206}Pb/^{204}Pb$, $^{208}Pb/^{206}Pb$, $^{206}Pb/^{207}Pb$), major elements normalized to calcium (Ba:Ca, Sr:Ca), and trace metals normalized to calcium (Pb:Ca, Cd:Ca, As:Ca), this study evaluated whether multi-decadal geochemical variability in narwhal mineralized tissues reflects changes in mobility and trophic ecology or instead records climate-driven restructuring of baseline biogeochemical conditions.

Environmental context was provided by long-term sea-ice extent and coastal ocean temperature and salinity time series for the corresponding regions, as well as basin-scale Atlantic circulation variability quantified using Atlantic Multidecadal Oscillation (AMO) index. In addition, independent population-level $\delta^{13}C$ and $\delta^{15}N$ datasets from Pond Inlet narwhal embedded teeth and Baffin Bay beluga teeth were used to test whether baseline isotopic change inferred from individual tusk profiles is expressed across multiple individuals and taxa.

5.2. Summary of Main Findings

Across both individuals, proxies with strong baseline sensitivity and proxies expected to reflect trophic or physiological processes behaved differently through time, providing a clear basis for disentangling ecological change from environmental baseline forcing.

First, mobility-sensitive tracers were largely conservative through time in both tusks. In Tusk 1 (Baffin Bay), $\delta^{18}O_{CO3}$ exhibited repeated multi-year oscillations but no significant long-term trend and did not covary significantly with $\delta^{13}C_{collagen}$, $\delta^{15}N_{collagen}$, $\delta^{13}C_{CO3}$ and Pb isotope ratios. However, it was significantly correlated with AMO, indicating sensitivity to basin-scale climatic and hydrographic variability. In Tusk 2 (Hudson Bay), $\delta^{18}O_{CO3}$ values were consistently more negative than in Tusk 1, reflecting strong freshwater influence, and remained stable for most of

the record, with increased variability only toward the end of the individual's life. $\delta^{18}O_{CO3}$ values in Tusk 2 likewise showed no significant long-term trend and did not covary with $\delta^{13}C_{collagen}$, $\delta^{15}N_{collagen}$, $\delta^{13}C_{CO3}$, Pb isotope ratios and AMO. Overall, the absence of coherent, directional shifts shared among mobility-sensitive and baseline-sensitive proxies indicates that neither individual underwent a sustained, basin-scale change in water-mass use or long-term relocation sufficient to explain the dominant long-term isotopic trends.

Second, elemental trophic proxies recorded a consistent ontogenetic signal in both individuals. Ba:Ca and Sr:Ca were elevated early in life, declined over approximately the first 5-7 years, and then stabilized at lower values, consistent with an ontogenetic transition toward an adult-like feeding regime. Importantly, the similarity of this early-life structure in two individuals inhabiting very different oceanographic settings argues strongly that these proxies are capturing a shared developmental and trophic transition rather than a purely environmental signal.

Third, $\Delta^{13}C_{carb\text{-}coll}$ exhibited early-life structure consistent with a metabolic-dietary transition and showed coherence with Ba:Ca and Sr:Ca in both individuals, supporting interpretation of a shared ontogenetic reorganization in diet composition and macronutrient routing. In contrast, $\delta^{13}C_{collagen}$ did not exhibit comparable ontogenetic structure and instead appears to track baseline carbon dynamics, supported by its significant correlations with $\delta^{13}C_{CO3}$ in both tusks. Together, these patterns indicate that $\Delta^{13}C_{carb\text{-}coll}$ and elemental proxies more directly capture developmental and physiological transitions, whereas bulk $\delta^{13}C_{collagen}$ is more strongly influenced by environmental carbon baselines.

Fourth, $\delta^{15}N_{collagen}$ did not behave as a simple trophic proxy and instead provided strong evidence for population-specific baseline forcing. In Tusk 1, $\delta^{15}N_{collagen}$ declined significantly through time, contrary to ontogenetic expectations for trophic enrichment, and this decline was not accompanied by coordinated directional changes in mobility tracers. In Tusk 2, $\delta^{15}N_{collagen}$ remained comparatively stable despite clear evidence for ontogenetic change in Ba:Ca, Sr:Ca, $\Delta^{13}C_{carb\text{-}coll}$, and Hg concentrations. This decoupling demonstrates that bulk $\delta^{15}N$ in narwhal biomineralized tissues can be dominated by baseline nitrogen cycling, limiting its reliability as a long-term trophic indicator in rapidly changing Arctic systems.

Fifth, toxicological proxies revealed dual control by trophic and baseline processes, with clear contrasts among elements. Hg concentrations increased through time in both individuals,

with a stronger and significant increase in Tusk 1, consistent with trophic biomagnification superimposed on baseline forcing associated with climate-sensitive methylmercury production and delivery. In contrast, Pb:Ca, Cd:Ca, and As:Ca declined through time, consistent with reductions in baseline exposure pathways rather than trophic biomagnification. Pb isotope ratios provided crucial source constraints: Tusk 2 showed relatively stable Pb isotopic composition consistent with persistent sedimentary and nearshore sources, whereas Tusk 1 showed broader isotopic variability and a shift toward more radiogenic compositions through time, consistent with changing baseline Pb provenance and/or declining influence of isotopically distinct anthropogenic Pb.

Finally, independent population-level datasets confirmed that baseline isotopic change is expressed beyond a single tusk record. $\delta^{13}C$ and $\delta^{15}N$ data from Pond Inlet narwhal embedded teeth and Baffin Bay beluga teeth show a coherent shift toward lower $\delta^{13}C$ and $\delta^{15}N$ values beginning around the early 2000s, forming distinct pre- and post-2000 isotopic clusters. The expression of similar directional change in two ecologically distinct cetaceans strongly supports a shared environmental driver acting at the base of the food web, consistent with climate-driven reorganization of primary production and nitrogen cycling linked to sea-ice decline and changing hydrography.

5.3. Future Research Directions

This work highlights several research priorities that would further strengthen the interpretation of narwhal tusk archives and their sensitivity to Arctic baseline change. First, additional tusks from both Baffin Bay and Hudson Bay populations, including older individuals whose records extend further back in time, would test whether the baseline patterns observed here are consistent and whether Hudson Bay experienced baseline shifts prior to the interval captured by Tusk 2.

Second, direct measurements of $\delta^{13}C$ and $\delta^{15}N$ in primary producers, POM, and key prey species across regions and time would help quantify baseline shifts and separate baseline from trophic effects in apex predators.

Third, compound-specific $\delta^{15}N$ of amino acids in tusk collagen would provide a powerful method to decouple trophic position from baseline nitrogen, directly testing the baseline-driven interpretation advanced here.

Fourth, comparative analyses of albino and non-albino narwhals from the same regions and time periods would help assess whether pigmentation or associated physiological differences influence isotopic and trace element records. Similarly, comparisons between male and female narwhals from the same regions and time periods would help evaluate potential sex-specific differences in foraging behavior, habitat use, and baseline exposure.

Finally, a key priority for future work is the expanded application of seasonal sampling within individual GLGs. Although annual sampling captures long-term baseline trends, seasonal resolution may provide additional insight into intra-annual variation in habitat use, foraging behavior, and baseline exposure that is not resolved at the annual scale. With improved methodological precision, seasonal tusk records could allow clearer differentiation of basin-specific foraging strategies and baseline influences, particularly in regions with strong seasonal contrasts in hydrography and sea-ice dynamics.

5.4. Ethical Statement, Use of Artificial Intelligence and Funding

This thesis is based on biological samples originating from Arctic Bay and Naujaat. The narwhal tusks analyzed in this study were obtained from animals harvested through subsistence hunting by Inuit communities, with ivory was sold to Fisheries and Oceans Canada (DFO) for research purposes. DFO works in collaboration with northern communities to ensure that research conducted using harvested wildlife aligns with community priorities. Communities are kept informed of research objectives and outcomes, and Indigenous knowledge is considered an essential component of understanding Arctic ecosystems and interpreting scientific results.

Artificial intelligence (AI) tools were used in a transparent manner to support writing and editing. Specifically, AI assistance was used to improve clarity, grammar, and organization of text, and to help refine scientific phrasing. All scientific interpretations, analytical decisions, data processing, and conclusions presented in this thesis were developed and verified by the author. The author takes full responsibility for the content of the thesis.

This research was funded by the Regional Partnerships and Research Program of Crown-Indigenous Relations and Northern Affairs Canada (CIRNAC). Additional support, infrastructure, and analytical resources were provided through the author's research group (SAIVE Lab) and institutional facilities.

REFERENCES

Albuquerque, C. Q., Miekeley, N., Muelbert, J. H., Walther, B. D., & Jaureguizar, A. J. (2012). Estuarine dependency in a marine fish evaluated with otolith chemistry. *Marine Biology*, *159*(10), 2229–2239. https://doi.org/10.1007/s00227-012-2007-5

AMAP. (2018). *AMAP assessment 2018: Biological effects of contaminants on Arctic wildlife and fish*. Arctic Monitoring and Assessment Programme (AMAP).

Ambrose, S. H., Butler, B. M., Hanson, D. B., Hunter-Anderson, R. L., & Krueger, H. W. (1997). Stable isotopic analysis of human diet in the Marianas Archipelago, Western Pacific. *American Journal of Physical Anthropology*, *104*(3), 343–361. https://doi.org/10.1002/(SICI)1096-8644(199711)104:3%253C343::AID-AJPA5%253E3.0.CO;2-W

Amiraux, R., Mundy, C. J., Pierrejean, M., Niemi, A., Hedges, K. J., Brown, T. A., Ehn, J. K., Elliott, K. H., Ferguson, S. H., Fisk, A. T., Gilchrist, G., Harris, L. N., Iken, K., Jacobs, K. B., Johnson, K. F., Kuzyk, Z. A., Limoges, A., Loewen, T. N., Love, O. P., … Yurkowski, D. J. (2023). Tracing carbon flow and trophic structure of a coastal Arctic marine food web using highly branched isoprenoids and carbon, nitrogen and sulfur stable isotopes. *Ecological Indicators*, *147*, 109938. https://doi.org/10.1016/j.ecolind.2023.109938

Assmy, P., Fernández-Méndez, M., Duarte, P., Meyer, A., Randelhoff, A., Mundy, C. J., Olsen, L. M., Kauko, H. M., Bailey, A., Chierici, M., Cohen, L., Doulgeris, A. P., Ehn, J. K., Fransson, A., Gerland, S., Hop, H., Hudson, S. R., Hughes, N., Itkin, P., … Granskog, M. A. (2017). Leads in Arctic pack ice enable early phytoplankton blooms below snow-covered sea ice. *Scientific Reports*, *7*(1), 40850. https://doi.org/10.1038/srep40850

Azizur Rahman, M., Hasegawa, H., & Peter Lim, R. (2012). Bioaccumulation, biotransformation and trophic transfer of arsenic in the aquatic food chain. *Environmental Research*, *116*, 118–135. https://doi.org/10.1016/j.envres.2012.03.014

Baffin Bay Sea Ice Extent. (n.d.). [Dataset]. https://www.ncei.noaa.gov/access/monitoring/regional-sea-ice/extent/Baffin/0

Ballinger, T. J., Moore, G. W. K., Garcia-Quintana, Y., Myers, P. G., Imrit, A. A., Topál, D., & Meier, W. N. (2022). Abrupt Northern Baffin Bay Autumn Warming and Sea-Ice Loss Since the Turn of the Twenty-First Century. *Geophysical Research Letters*, *49*(21), e2022GL101472. https://doi.org/10.1029/2022GL101472

Balter, V. (2004). Allometric constraints on Sr/Ca and Ba/Ca partitioning in terrestrial mammalian trophic chains. *Oecologia*, *139*(1), 83–88. https://doi.org/10.1007/s00442-003-1476-0

Barkay, T., Gillman, M., & Turner, R. R. (1997). Effects of dissolved organic carbon and salinity on bioavailability of mercury. *Applied and Environmental Microbiology*, *63*(11), 4267–4271. https://doi.org/10.1128/aem.63.11.4267-4271.1997

Beattie, S. A., Armstrong, D., Chaulk, A., Comte, J., Gosselin, M., & Wang, F. (2014). Total and Methylated Mercury in Arctic Multiyear Sea Ice. *Environmental Science & Technology*, *48*(10), 5575–5582. https://doi.org/10.1021/es5008033

Ben-David, M., & Flaherty, E. A. (2012). Stable isotopes in mammalian research: A beginner's guide. *Journal of Mammalogy*, *93*(2), 312–328. https://doi.org/10.1644/11-MAMM-S-166.1

Benkort, D., Daewel, U., Heath, M., & Schrum, C. (2020). On the Role of Biogeochemical Coupling Between Sympagic and Pelagic Ecosystem Compartments for Primary and Secondary Production in the Barents Sea. *Frontiers in Environmental Science*, *8*, 548013. https://doi.org/10.3389/fenvs.2020.548013

Berkovitz, B. K. B. (2013). Tusks and Ivory. In *Nothing but the Tooth* (pp. 11–33). Elsevier. https://doi.org/10.1016/B978-0-12-397190-6.00002-X

Berner, J., Brubaker, M., Revitch, B., Kreummel, E., Tcheripanoff, M., & Bell, J. (2016). Adaptation in Arctic circumpolar communities: Food and water security in a changing climate. *International Journal of Circumpolar Health*, *75*(1), 33820. https://doi.org/10.3402/ijch.v75.33820

Blackwell, S. B., Tervo, O. M., Conrad, A. S., Sinding, M. H. S., Hansen, R. G., Ditlevsen, S., & Heide-Jørgensen, M. P. (2018). Spatial and temporal patterns of sound production in East Greenland narwhals. *PLOS ONE*, *13*(6), e0198295. https://doi.org/10.1371/journal.pone.0198295

Borgå, K., McKinney, M. A., Routti, H., Fernie, K. J., Giebichenstein, J., Hallanger, I., & Muir, D. C. G. (2022). The influence of global climate change on accumulation and toxicity of persistent organic pollutants and chemicals of emerging concern in Arctic food webs. *Environmental Science: Processes & Impacts*, *24*(1), 1544–1576. https://doi.org/10.1039/D1EM00469G

Botta, S., Albuquerque, C., Hohn, A., Da Silva, V., Santos, M., Meirelles, C., Barbosa, L., Di Beneditto, A., Ramos, R., Bertozzi, C., Cremer, M., Franco-Trecu, V., Miekeley, N., &

Secchi, E. (2015). Ba/Ca ratios in teeth reveal habitat use patterns of dolphins. *Marine Ecology Progress Series*, *521*, 249–263. https://doi.org/10.3354/meps11158

Bouchard, C., & Fortier, L. (2020). The importance of Calanus glacialis for the feeding success of young polar cod: A circumpolar synthesis. *Polar Biology*, *43*(8), 1095–1107. https://doi.org/10.1007/s00300-020-02643-0

Braune, B., Chételat, J., Amyot, M., Brown, T., Clayden, M., Evans, M., Fisk, A., Gaden, A., Girard, C., Hare, A., Kirk, J., Lehnherr, I., Letcher, R., Loseto, L., Macdonald, R., Mann, E., McMeans, B., Muir, D., O'Driscoll, N., … Stern, G. (2015). Mercury in the marine environment of the Canadian Arctic: Review of recent findings. *Science of The Total Environment*, *509–510*, 67–90. https://doi.org/10.1016/j.scitotenv.2014.05.133

Britannica Editors. (2025). Narwhal. In *Encyclopaedia Britannica*. https://www.britannica.com/animal/narwhal

Brown, T. A., Chrystal, E., Ferguson, S. H., Yurkowski, D. J., Watt, C., Hussey, N. E., Kelley, T. C., & Belt, S. T. (2017). Coupled changes between the H-Print biomarker and δ15N indicates a variable sea ice carbon contribution to the diet of Cumberland Sound beluga whales. *Limnology and Oceanography*, *62*(4), 1606–1619. https://doi.org/10.1002/lno.10520

Buchanan, P. J., Tagliabue, A., De La Vega, C., & Mahaffey, C. (2022). Oceanographic and biogeochemical drivers cause divergent trends in the nitrogen isoscape in a changing Arctic Ocean. *Ambio*, *51*(2), 383–397. https://doi.org/10.1007/s13280-021-01635-6

Burkhardt, S., Riebesell, U., & Zondervan, I. (1999). Stable carbon isotope fractionation by marine phytoplankton in response to daylength, growth rate, and CO2 availability. *Marine Ecology Progress Series*, *184*, 31–41. https://doi.org/10.3354/meps184031

Campbell, K., Mundy, C. J., Gosselin, M., Landy, J. C., Delaforge, A., & Rysgaard, S. (2017). Net community production in the bottom of first-year sea ice over the Arctic spring bloom. *Geophysical Research Letters*, *44*(17), 8971–8978. https://doi.org/10.1002/2017GL074602

Campbell, L. M., Norstrom, R. J., Hobson, K. A., Muir, D. C. G., Backus, S., & Fisk, A. T. (2005). Mercury and other trace elements in a pelagic Arctic marine food web (Northwater Polynya, Baffin Bay). *Science of The Total Environment*, *351–352*, 247–263. https://doi.org/10.1016/j.scitotenv.2005.02.043

Carmack, E. C., Yamamoto-Kawai, M., Haine, T. W. N., Bacon, S., Bluhm, B. A., Lique, C., Melling, H., Polyakov, I. V., Straneo, F., Timmermans, M. -L., & Williams, W. J. (2016). Freshwater and its role in the Arctic Marine System: Sources, disposition, storage, export,

and physical and biogeochemical consequences in the Arctic and global oceans. *Journal of Geophysical Research: Biogeosciences*, *121*(3), 675–717. https://doi.org/10.1002/2015JG003140

Chambault, P., Tervo, O. M., Garde, E., Hansen, R. G., Blackwell, S. B., Williams, T. M., Dietz, R., Albertsen, C. M., Laidre, K. L., Nielsen, N. H., Richard, P., Sinding, M. H. S., Schmidt, H. C., & Heide-Jørgensen, M. P. (2020). The impact of rising sea temperatures on an Arctic top predator, the narwhal. *Scientific Reports*, *10*(1), 18678. https://doi.org/10.1038/s41598-020-75658-6

Cherry, S. G., Derocher, A. E., Thiemann, G. W., & Lunn, N. J. (2013). Migration phenology and seasonal fidelity of an Arctic marine predator in relation to sea ice dynamics. *Journal of Animal Ecology*, *82*(4), 912–921. https://doi.org/10.1111/1365-2656.12050

Chikaraishi, Y., Ogawa, N. O., Kashiyama, Y., Takano, Y., Suga, H., Tomitani, A., Miyashita, H., Kitazato, H., & Ohkouchi, N. (2009). Determination of aquatic food-web structure based on compound-specific nitrogen isotopic composition of amino acids. *Limnology and Oceanography: Methods*, *7*(11), 740–750. https://doi.org/10.4319/lom.2009.7.740

Ciner, B., Wang, Y., & Parker, W. (2016). Oxygen isotopic variations in modern cetacean teeth and bones: Implications for ecological, paleoecological, and paleoclimatic studies. *Science Bulletin*, *61*(1), 92–104. https://doi.org/10.1007/s11434-015-0921-x

Citta, J. J., Lowry, L. F., Quakenbush, L. T., Kelly, B. P., Fischbach, A. S., London, J. M., Jay, C. V., Frost, K. J., Crowe, G. O., Crawford, J. A., Boveng, P. L., Cameron, M., Von Duyke, A. L., Nelson, M., Harwood, L. A., Richard, P., Suydam, R., Heide-Jørgensen, M. P., Hobbs, R. C., … Gray, T. (2018). A multi-species synthesis of satellite telemetry data in the Pacific Arctic (1987–2015): Overlap of marine mammal distributions and core use areas. *Deep Sea Research Part II: Topical Studies in Oceanography*, *152*, 132–153. https://doi.org/10.1016/j.dsr2.2018.02.006

Clark, C. T., Cape, M. R., Shapley, M. D., Mueter, F. J., Finney, B. P., & Misarti, N. (2021). SuessR: Regional corrections for the effects of anthropogenic CO2 on δ13C data from marine organisms. *Methods in Ecology and Evolution*, *12*(8), 1508–1520. https://doi.org/10.1111/2041-210X.13622

Clark, C. T., Horstmann, L., & Misarti, N. (2020). Evaluating tooth strontium and barium as indicators of weaning age in Pacific walruses. *Methods in Ecology and Evolution*, *11*(12), 1626–1638. https://doi.org/10.1111/2041-210X.13482

Clark, C. T., Horstmann, L., & Misarti, N. (2021). Walrus teeth as biomonitors of trace elements in Arctic marine ecosystems. *Science of The Total Environment*, *772*, 145500. https://doi.org/10.1016/j.scitotenv.2021.145500

Clementz, M. T., Fox-Dobbs, K., Wheatley, P. V., Koch, P. L., & Doak, D. F. (2009). Revisiting old bones: Coupled carbon isotope analysis of bioapatite and collagen as an ecological and palaeoecological tool. *Geological Journal*, *44*(5), 605–620. https://doi.org/10.1002/gj.1173

Coffey, M., Dehairs, F., Collette, O., Luther, G., Church, T., & Jickells, T. (1997). The Behaviour of Dissolved Barium in Estuaries. *Estuarine, Coastal and Shelf Science*, *45*(1), 113–121. https://doi.org/10.1006/ecss.1996.0157

Colombo, M., Rogalla, B., Myers, P. G., Allen, S. E., & Orians, K. J. (2019). Tracing Dissolved Lead Sources in the Canadian Arctic: Insights from the Canadian GEOTRACES Program. *ACS Earth and Space Chemistry*, *3*(7), 1302–1314. https://doi.org/10.1021/acsearthspacechem.9b00083

Coplen, T. B., Brand, W. A., Gehre, M., Gröning, M., Meijer, H. A. J., Toman, B., & Verkouteren, R. M. (2006). New Guidelines for δ13C Measurements. *Analytical Chemistry*, *78*(7), 2439–2441. https://doi.org/10.1021/ac052027c

COSEWIC. (2004). *COSEWIC assessment and update status report on the narwhal (Monodon monoceros) in Canada. Committee on the Status of Endangered Wildlife in Canada, Ottawa, vii + 50 pp.* https://www.sararegistry.gc.ca/status/status_e.cfm

Crawford, J. A., Frost, K. J., Quakenbush, L. T., & Whiting, A. (2019). Seasonal and diel differences in dive and haul-out behavior of adult and subadult ringed seals (Pusa hispida) in the Bering and Chukchi seas. *Polar Biology*, *42*(1), 65–80. https://doi.org/10.1007/s00300-018-2399-x

Dalerum, F., & Angerbjörn, A. (2005). Resolving temporal variation in vertebrate diets using naturally occurring stable isotopes. *Oecologia*, *144*(4), 647–658. https://doi.org/10.1007/s00442-005-0118-0

Daniel Bryant, J., Koch, P. L., Froelich, P. N., Showers, W. J., & Genna, B. J. (1996). Oxygen isotope partitioning between phosphate and carbonate in mammalian apatite. *Geochimica et Cosmochimica Acta*, *60*(24), 5145–5148. https://doi.org/10.1016/S0016-7037(96)00308-0

Day, J. J., Hargreaves, J. C., Annan, J. D., & Abe-Ouchi, A. (2012). Sources of multi-decadal variability in Arctic sea ice extent. *Environmental Research Letters*, *7*(3), 034011. https://doi.org/10.1088/1748-9326/7/3/034011

De La Vega, C., Buchanan, P. J., Tagliabue, A., Hopkins, J. E., Jeffreys, R. M., Frie, A. K., Biuw, M., Kershaw, J., Grecian, J., Norman, L., Smout, S., Haug, T., & Mahaffey, C. (2022). Multi-decadal environmental change in the Barents Sea recorded by seal teeth. *Global Change Biology*, *28*(9), 3054–3065. https://doi.org/10.1111/gcb.16138

De La Vega, C., Jeffreys, R. M., Tuerena, R., Ganeshram, R., & Mahaffey, C. (2019). Temporal and spatial trends in marine carbon isotopes in the Arctic Ocean and implications for food web studies. *Global Change Biology*, *25*(12), 4116–4130. https://doi.org/10.1111/gcb.14832

De La Vega, C., Mahaffey, C., Tuerena, R. E., Yurkowski, D. J., Ferguson, S. H., Stenson, G. B., Nordøy, E. S., Haug, T., Biuw, M., Smout, S., Hopkins, J., Tagliabue, A., & Jeffreys, R. M. (2021). Arctic seals as tracers of environmental and ecological change. *Limnology and Oceanography Letters*, *6*(1), 24–32. https://doi.org/10.1002/lol2.10176

De María, M., Szteren, D., García-Alonso, J., De Rezende, C. E., Araújo Gonçalves, R., Godoy, J. M., & Barboza, F. R. (2021). Historic variation of trace elements in pinnipeds with spatially segregated trophic habits reveals differences in exposure to pollution. *Science of The Total Environment*, *750*, 141296. https://doi.org/10.1016/j.scitotenv.2020.141296

De Vera, J. (2020). *Tracing the Distribution of Pb and Trace Elements in the Canadian Arctic from the Atmosphere to the Ocean*.

De Vera, J., Chandan, P., Landing, W. M., Stupple, G. W., Steffen, A., & Bergquist, B. A. (2021a). Amount, Sources, and Dissolution of Aerosol Trace Elements in the Canadian Arctic. *ACS Earth and Space Chemistry*, *5*(10), 2686–2699. https://doi.org/10.1021/acsearthspacechem.1c00132

De Vera, J., Chandan, P., Pinedo-González, P., John, S. G., Jackson, S. L., Cullen, J. T., Colombo, M., Orians, K. J., & Bergquist, B. A. (2021b). Anthropogenic lead pervasive in Canadian Arctic seawater. *Proceedings of the National Academy of Sciences*, *118*(24), e2100023118. https://doi.org/10.1073/pnas.2100023118

Dehn, L.-A., Follmann, E. H., Thomas, D. L., Sheffield, G. G., Rosa, C., Duffy, L. K., & O'Hara, T. M. (2006). Trophic relationships in an Arctic food web and implications for trace metal transfer. *Science of The Total Environment*, *362*(1–3), 103–123. https://doi.org/10.1016/j.scitotenv.2005.11.012

Delworth, T. L., & Mann, M. E. (2000). Observed and simulated multidecadal variability in the Northern Hemisphere. *Climate Dynamics*, *16*(9), 661–676. https://doi.org/10.1007/s003820000075

Derocher, A. E. (2005). Population ecology of polar bears at Svalbard, Norway. *Population Ecology*, *47*(3), 267–275. https://doi.org/10.1007/s10144-005-0231-2

DeSantis, L. R. G., Feranec, R. S., Southon, J., Cerling, T. E., Harris, J., Binder, W. J., Cohen, J. E., Farrell, A. B., Lindsey, E. L., Meachen, J., Robin O'Keefe, F., & Takeuchi, G. T. (2022). On the relationship between collagen- and carbonate-derived carbon isotopes with implications for the inference of carnivore dietary behavior. *Frontiers in Ecology and Evolution*, *10*, 1031383. https://doi.org/10.3389/fevo.2022.1031383

Desforges, J.-P. W., Sonne, C., Levin, M., Siebert, U., De Guise, S., & Dietz, R. (2016). Immunotoxic effects of environmental pollutants in marine mammals. *Environment International*, *86*, 126–139. https://doi.org/10.1016/j.envint.2015.10.007

Dickson, B., Yashayaev, I., Meincke, J., Turrell, B., Dye, S., & Holfort, J. (2002). Rapid freshening of the deep North Atlantic Ocean over the past four decades. *Nature*, *416*(6883), 832–837. https://doi.org/10.1038/416832a

Dietz, R., Desforges, J.-P., Rigét, F. F., Aubail, A., Garde, E., Ambus, P., Drimmie, R., Heide-Jørgensen, M. P., & Sonne, C. (2021). Analysis of narwhal tusks reveals lifelong feeding ecology and mercury exposure. *Current Biology*, *31*(9), 2012-2019.e2. https://doi.org/10.1016/j.cub.2021.02.018

Dietz, R., Outridge, P. M., & Hobson, K. A. (2009). Anthropogenic contributions to mercury levels in present-day Arctic animals—A review. *Science of The Total Environment*, *407*(24), 6120–6131. https://doi.org/10.1016/j.scitotenv.2009.08.036

Dietz, R., Sonne, C., Basu, N., Braune, B., O'Hara, T., Letcher, R. J., Scheuhammer, T., Andersen, M., Andreasen, C., Andriashek, D., Asmund, G., Aubail, A., Baagøe, H., Born, E. W., Chan, H. M., Derocher, A. E., Grandjean, P., Knott, K., Kirkegaard, M., … Aars, J. (2013). What are the toxicological effects of mercury in Arctic biota? *Science of The Total Environment*, *443*(15), 775–790. https://doi.org/10.1016/j.scitotenv.2012.11.046

Dorval, E., Jones, C. M., & Hannigan, R. (2005). Chemistry of surface waters: Distinguishing fine-scale differences in sea grass habitats of Chesapeake Bay. *Limnology and Oceanography*, *50*(4), 1073–1083. https://doi.org/10.4319/lo.2005.50.4.1073

Eastham, L. C., & Feranec, R. S. (2025a). Examining potential drivers of variation in the carbonate-collagen stable carbon isotope offset of modern and Late Pleistocene ungulates from C3-dominant ecosystems. *Palaeogeography, Palaeoclimatology, Palaeoecology*, *674*, 113014. https://doi.org/10.1016/j.palaeo.2025.113014

Eastham, L. C., & Feranec, R. S. (2025b). Examining potential drivers of variation in the carbonate-collagen stable carbon isotope offset of modern and Late Pleistocene ungulates

from C3-dominant ecosystems. *Palaeogeography, Palaeoclimatology, Palaeoecology*, *674*, 113014. https://doi.org/10.1016/j.palaeo.2025.113014

EN4: Quality controlled subsurface ocean temperature and salinity profiles and objective analyses. (n.d.). [Dataset]. https://www.metoffice.gov.uk/hadobs/en4/download-en4-2-2.html

Enfield, D. B., Mestas-Nuñez, A. M., & Trimble, P. J. (2001). The Atlantic Multidecadal Oscillation and its relation to rainfall and river flows in the continental U.S. *Geophysical Research Letters*, *28*(10), 2077–2080. https://doi.org/10.1029/2000GL012745

Evans, L. K., & Nishioka, J. (2019). Accumulation processes of trace metals into Arctic sea ice: Distribution of Fe, Mn and Cd associated with ice structure. *Marine Chemistry*, *209*, 36–47. https://doi.org/10.1016/j.marchem.2018.11.011

Evans, R. D., Richner, P., & Outridge, P. M. (1995). Micro-spatial variations of heavy metals in the teeth of walrus as determined by laser ablation ICP-MS: The potential for reconstructing a history of metal exposure. *Archives of Environmental Contamination and Toxicology*, *28*(1), 55–60. https://doi.org/10.1007/BF00213969

Feddern, M. L., Holtgrieve, G. W., & Ward, E. J. (2021). Stable isotope signatures in historic harbor seal bone link food web-assimilated carbon and nitrogen resources to a century of environmental change. *Global Change Biology*, *27*(11), 2328–2342. https://doi.org/10.1111/gcb.15551

Feng, Z., Ji, R., Ashjian, C., Campbell, R., & Zhang, J. (2018). Biogeographic responses of the copepod Calanus glacialis to a changing Arctic marine environment. *Global Change Biology*, *24*(1). https://doi.org/10.1111/gcb.13890

Ferguson, S. H., Stirling, I., & McLoughlin, P. (2005). Climate Change and Ringed Seal (Phoca hispida) Recruitment in Western Hudson Bay. *Marine Mammal Science*, *21*(1), 121–135. https://doi.org/10.1111/j.1748-7692.2005.tb01212.x

Fetterer, F., Knowles, K., Meier, W. N., Savoie, M., Windnagel, A., & Stafford, T. (2025). *Sea Ice Index, Version 4* [Dataset]. National Snow and Ice Data Center. https://doi.org/10.7265/A98X-0F50

Fetterer, F., Knowles, K, Meier, W, Savoie, M, & A, W. (2017). *Sea Ice Index, Version 3* [Dataset]. NSIDC. https://doi.org/10.7265/N5K072F8

Findlay, H. S., Gibson, G., Kędra, M., Morata, N., Orchowska, M., Pavlov, A. K., Reigstad, M., Silyakova, A., Tremblay, J.-É., Walczowski, W., Weydmann, A., & Logvinova, C. (2015). Responses in Arctic marine carbon cycle processes: Conceptual scenarios and

implications for ecosystem function. *Polar Research*, *34*(1), 24252. https://doi.org/10.3402/polar.v34.24252

Finley, K. J. (1976). Studies of the status of marine mammals in the central district of Franklin, N.W.T., June-August, 1975. *LGL Limited, Environmental Research Associates*.

Finley, K. J., & Gibb, E. J. (1982). Summer diet of the narwhal (Monodon monoceros) in Pond Inlet, northern Baffin Island. *Canadian Journal of Zoology*, *60*(12), 3353–3363. https://doi.org/10.1139/z82-424

Fox, A., & Walker, B. D. (2022). Sources and Cycling of Particulate Organic Matter in Baffin Bay: A Multi-Isotope δ13C, δ15N, and Δ14C Approach. *Frontiers in Marine Science*, *9*, 846025. https://doi.org/10.3389/fmars.2022.846025

Friedman, I., O'Neil, J., & Cebula, G. (1982). Two New Carbonate Stable-Isotope Standards. *Geostandards Newsletter*, *6*(1), 11–12. https://doi.org/10.1111/j.1751-908X.1982.tb00340.x

Galer, S. J. G., & Abouchami, W. (1998). Practical Application of Lead Triple Spiking for Correction of Instrumental Mass Discrimination. *Mineralogical Magazine*, *62A*(1), 491–492. https://doi.org/10.1180/minmag.1998.62A.1.260

Garcia-Soto, C., Cheng, L., Caesar, L., Schmidtko, S., Jewett, E. B., Cheripka, A., Rigor, I., Caballero, A., Chiba, S., Báez, J. C., Zielinski, T., & Abraham, J. P. (2021). An Overview of Ocean Climate Change Indicators: Sea Surface Temperature, Ocean Heat Content, Ocean pH, Dissolved Oxygen Concentration, Arctic Sea Ice Extent, Thickness and Volume, Sea Level and Strength of the AMOC (Atlantic Meridional Overturning Circulation). *Frontiers in Marine Science*, *8*, 642372. https://doi.org/10.3389/fmars.2021.642372

Garde, E., Hansen, S. H., Ditlevsen, S., Tvermosegaard, K. B., Hansen, J., Harding, K. C., & Heide-Jørgensen, M. P. (2015). Life history parameters of narwhals (*Monodon monoceros*) from Greenland. *Journal of Mammalogy*, *96*(4), 866–879. https://doi.org/10.1093/jmammal/gyv110

Garde, E., Heide-Jørgensen, M. P., Ditlevsen, S., & Hansen, S. H. (2012). Aspartic acid racemization rate in narwhal (*Monodon monoceros*) eye lens nuclei estimated by counting of growth layers in tusks. *Polar Research*, *31*(1), 15865. https://doi.org/10.3402/polar.v31i0.15865

Garde, E., Heide-Jørgensen, M. P., Hansen, S. H., Nachman, G., & Forchhammer, M. C. (2007). Age-Specific Growth and Remarkable Longevity in Narwhals (*Monodon monoceros*)

from West Greenland as Estimated by Aspartic Acid Racemization. *Journal of Mammalogy*, *88*(1), 49–58. https://doi.org/10.1644/06-MAMM-A-056R.1

Gaston, A. J., & Ouellet, H. (1997). Birds and Mammals of Coats Island, N.W.T. *ARCTIC*, *50*(2), 101–118. https://doi.org/10.14430/arctic1094

Germain, L., Koch, P., Harvey, J., & McCarthy, M. (2013). Nitrogen isotope fractionation in amino acids from harbor seals: Implications for compound-specific trophic position calculations. *Marine Ecology Progress Series*, *482*, 265–277. https://doi.org/10.3354/meps10257

Gerringa, L. J. A., Rijkenberg, M. J. A., Slagter, H. A., Laan, P., Paffrath, R., Bauch, D., Rutgers Van Der Loeff, M., & Middag, R. (2021). Dissolved Cd, Co, Cu, Fe, Mn, Ni, and Zn in the Arctic Ocean. *Journal of Geophysical Research: Oceans*, *126*(9), e2021JC017323. https://doi.org/10.1029/2021JC017323

Ghosh, P., Patecki, M., Rothe, M., & Brand, W. A. (2005). Calcite-CO2 mixed into CO2-free air: A new CO2-in-air stable isotope reference material for the VPDB scale. *Rapid Communications in Mass Spectrometry*, *19*(8), 1097–1119. https://doi.org/10.1002/rcm.1886

Gonzalez, N. (2001). *Inuit traditional ecological knowledge of the Hudson Bay narwhal (Tuugaalik) population.* Report prepared for the Department of Fisheries and Oceans. Iqaluit, Nunavut, Canada.

Good, S. A., Martin, M. J., & Rayner, N. A. (2013). EN4: Quality controlled ocean temperature and salinity profiles and monthly objective analyses with uncertainty estimates. *Journal of Geophysical Research: Oceans*, *118*(12), 6704–6716. https://doi.org/10.1002/2013JC009067

Gouretski, V., & Reseghetti, F. (2010). On depth and temperature biases in bathythermograph data: Development of a new correction scheme based on analysis of a global ocean database. *Deep Sea Research Part I: Oceanographic Research Papers*, *57*(6), 812–833. https://doi.org/10.1016/j.dsr.2010.03.011

Gruber, N., Keeling, C. D., Bacastow, R. B., Guenther, P. R., Lueker, T. J., Wahlen, M., Meijer, H. A. J., Mook, W. G., & Stocker, T. F. (1999). Spatiotemporal patterns of carbon-13 in the global surface oceans and the oceanic suess effect. *Global Biogeochemical Cycles*, *13*(2), 307–335. https://doi.org/10.1029/1999GB900019

Hauser, D. D. W., Laidre, K. L., Stafford, K. M., Stern, H. L., Suydam, R. S., & Richard, P. R. (2017). Decadal shifts in autumn migration timing by Pacific Arctic beluga whales are

related to delayed annual sea ice formation. *Global Change Biology*, *23*(6), 2206–2217. https://doi.org/10.1111/gcb.13564

Heide-Jørgensen, M. P. (2018). Narwhal. In *Encyclopedia of Marine Mammals* (pp. 627–631). Elsevier. https://doi.org/10.1016/B978-0-12-804327-1.00013-3

Heide-Jørgensen, M. P., Dietz, R., Laidre, K. L., Richard, P., Orr, J., & Schmidt, H. C. (2003). The migratory behaviour of narwhals (Monodon monoceros). *Canadian Journal of Zoology*, *81*(8), 1298–1305. https://doi.org/10.1139/z03-117

Heide-Jørgensen, M. P., & Laidre, K. L. (2004). Declining Extent of Open-water Refugia for Top Predators in Baffin Bay and Adjacent Waters. *AMBIO: A Journal of the Human Environment*, *33*(8), 487–494. https://doi.org/10.1579/0044-7447-33.8.487

Heide-Jørgensen, M. P., Nielsen, N. H., Hansen, R. G., & Blackwell, S. B. (2014). Stomach temperature of narwhals (Monodon monoceros) during feeding events. *Animal Biotelemetry*, *2*(1), 9. https://doi.org/10.1186/2050-3385-2-9

Heide-Jørgensen, M. P., Nielsen, N. H., Hansen, R. G., Schmidt, H. C., Blackwell, S. B., & Jørgensen, O. A. (2015). The predictable narwhal: Satellite tracking shows behavioural similarities between isolated subpopulations. *Journal of Zoology*, *297*(1), 54–65. https://doi.org/10.1111/jzo.12257

Heide-Jørgensen, M. P., Richard, P. R., Dietz, R., & Laidre, K. L. (2013). A metapopulation model for Canadian and West Geenland narwhals. *Animal Conservation*, *16*(3), 331–343. https://doi.org/10.1111/acv.12000

Heide-Jørgensen, M. P., Richard, P., Ramsay, M., & Akeeagok, S. (2002). Three recent ice entrapments of Arctic cetaceans in West Greenland and the eastern Canadian High Arctic. *NAMMCO Scientific Publications*, *4*, 143. https://doi.org/10.7557/3.2841

Heimbürger, L.-E., Sonke, J. E., Cossa, D., Point, D., Lagane, C., Laffont, L., Galfond, B. T., Nicolaus, M., Rabe, B., & Van Der Loeff, M. R. (2015). Shallow methylmercury production in the marginal sea ice zone of the central Arctic Ocean. *Scientific Reports*, *5*(1), 10318. https://doi.org/10.1038/srep10318

Hilton, G. M., Thompson, D. R., Sagar, P. M., Cuthbert, R. J., Cherel, Y., & Bury, S. J. (2006). A stable isotopic investigation into the causes of decline in a sub-Antarctic predator, the rockhopper penguin Eudyptes chrysocome. *Global Change Biology*, *12*(4), 611–625. https://doi.org/10.1111/j.1365-2486.2006.01130.x

Hobson, K. A., Fisk, A., Karnovsky, N., Holst, M., Gagnon, J.-M., & Fortier, M. (2002). A stable isotope (δ13C, δ15N) model for the North Water food web: Implications for evaluating

trophodynamics and the flow of energy and contaminants. *Deep Sea Research Part II: Topical Studies in Oceanography*, *49*(22–23), 5131–5150. https://doi.org/10.1016/S0967-0645(02)00182-0

Hobson, K. A., & Sease, J. L. (1998). Stable Isotope Analyses of Tooth Annuli Reveal Temporal Dietary Records: An Example Using Steller Sea Lions. *Marine Mammal Science*, *14*(1), 116–129. https://doi.org/10.1111/j.1748-7692.1998.tb00694.x

Hobson, K., & Welch, H. (1992). Determination of trophic relationships within a high Arctic marine food web using δ13C and δ15N analysis. *Marine Ecology Progress Series*, *84*, 9–18. https://doi.org/10.3354/meps084009

Hoegh-Guldberg, O., & Bruno, J. F. (2010). The Impact of Climate Change on the World's Marine Ecosystems. *Science*, *328*(5985), 1523–1528. https://doi.org/10.1126/science.1189930

Hoondert, R. P. J., Van Den Brink, N. W., Van Den Heuvel-Greve, M. J., Ragas, A. M. J., & Hendriks, A. J. (2021). Variability in nitrogen-derived trophic levels of Arctic marine biota. *Polar Biology*, *44*(1), 119–131. https://doi.org/10.1007/s00300-020-02782-4

Hop, H., & Gjøsæter, H. (2013). Polar cod (*Boreogadus saida*) and capelin (*Mallotus villosus*) as key species in marine food webs of the Arctic and the Barents Sea. *Marine Biology Research*, *9*(9), 878–894. https://doi.org/10.1080/17451000.2013.775458

Hornby, C. A., Togunov, R. R., McClintock, B. T., & Watt, C. A. (2025). Behavioural analysis of multi-year satellite telemetry data provides insight into narwhal (Monodon monoceros) winter prey selection in Baffin Bay. *PLOS One*, *20*(9), e0330928. https://doi.org/10.1371/journal.pone.0330928

Hudson Bay Sea Ice Extent. (n.d.). [Dataset]. https://www.ncei.noaa.gov/access/monitoring/regional-sea-ice/extent/Hudson/0

Huntington, H. P. (2009). A preliminary assessment of threats to arctic marine mammals and their conservation in the coming decades. *Marine Policy*, *33*(1), 77–82. https://doi.org/10.1016/j.marpol.2008.04.003

Jaouen, K., Szpak, P., & Richards, M. P. (2016). Zinc Isotope Ratios as Indicators of Diet and Trophic Level in Arctic Marine Mammals. *PLOS ONE*, *11*(3), e0152299. https://doi.org/10.1371/journal.pone.0152299

Jensen, L. T., Lanning, N. T., Marsay, C. M., Buck, C. S., Aguilar-Islas, A. M., Rember, R., Landing, W. M., Sherrell, R. M., & Fitzsimmons, J. N. (2021). Biogeochemical Cycling

of Colloidal Trace Metals in the Arctic Cryosphere. *Journal of Geophysical Research: Oceans*, *126*(8), e2021JC017394. https://doi.org/10.1029/2021JC017394

Kędra, M., Moritz, C., Choy, E. S., David, C., Degen, R., Duerksen, S., Ellingsen, I., Górska, B., Grebmeier, J. M., Kirievskaya, D., Van Oevelen, D., Piwosz, K., Samuelsen, A., & Węsławski, J. M. (2015). Status and trends in the structure of Arctic benthic food webs. *Polar Research*, *34*(1), 23775. https://doi.org/10.3402/polar.v34.23775

Keeley, J. E., & Sandquist, D. R. (1992). Carbon: Freshwater plants. *Plant, Cell & Environment*, *15*(9), 1021–1035. https://doi.org/10.1111/j.1365-3040.1992.tb01653.x

Kendall, Carol., & Grim, Elizabeth. (1990). Combustion tube method for measurement of nitrogen isotope ratios using calcium oxide for total removal of carbon dioxide and water. *Analytical Chemistry*, *62*(5), 526–529. https://doi.org/10.1021/ac00204a019

Kerr, R. A. (2000). A North Atlantic Climate Pacemaker for the Centuries. *Science*, *288*(5473), 1984–1985. https://doi.org/10.1126/science.288.5473.1984

Kim, S.-T., Coplen, T. B., & Horita, J. (2015). Normalization of stable isotope data for carbonate minerals: Implementation of IUPAC guidelines. *Geochimica et Cosmochimica Acta*, *158*, 276–289. https://doi.org/10.1016/j.gca.2015.02.011

Kingsley, M. (1989). Population dynamics of the narwhal Monodon monoceros: An initial assessement (Odontoceti: Monodontidae). *Journal of Zoology*, *219*(2), 201–208. https://doi.org/10.1111/j.1469-7998.1989.tb02576.x

Kirk, J. L., Lehnherr, I., Andersson, M., Braune, B. M., Chan, L., Dastoor, A. P., Durnford, D., Gleason, A. L., Loseto, L. L., Steffen, A., & St. Louis, V. L. (2012). Mercury in Arctic marine ecosystems: Sources, pathways and exposure. *Environmental Research*, *119*, 64–87. https://doi.org/10.1016/j.envres.2012.08.012

Knight, J. R., Allan, R. J., Folland, C. K., Vellinga, M., & Mann, M. E. (2005). A signature of persistent natural thermohaline circulation cycles in observed climate. *Geophysical Research Letters*, *32*(20), 2005GL024233. https://doi.org/10.1029/2005GL024233

Kohlbach, D., Graeve, M., A. Lange, B., David, C., Peeken, I., & Flores, H. (2016). The importance of ice algae-produced carbon in the central Arctic Ocean ecosystem: Food web relationships revealed by lipid and stable isotope analyses: Ice algal carbon in Arctic food web. *Limnology and Oceanography*, *61*(6), 2027–2044. https://doi.org/10.1002/lno.10351

Kopec, B. G., Klein, E. S., Feldman, G. C., Pedron, S. A., Bailey, H., Causey, D., Hubbard, A., Marttila, H., & Welker, J. M. (2024). Arctic Freshwater Sources and Ocean Mixing

Relationships Revealed With Seawater Isotopic Tracing. *Journal of Geophysical Research: Oceans*, *129*(7), e2023JC020583. https://doi.org/10.1029/2023JC020583

Kortsch, S., Primicerio, R., Fossheim, M., Dolgov, A. V., & Aschan, M. (2015). Climate change alters the structure of arctic marine food webs due to poleward shifts of boreal generalists. *Proceedings of the Royal Society B: Biological Sciences*, *282*(1814), 20151546. https://doi.org/10.1098/rspb.2015.1546

Kovacs, K. M., Aguilar, A., Aurioles, D., Burkanov, V., Campagna, C., Gales, N., Gelatt, T., Goldsworthy, S. D., Goodman, S. J., Hofmeyr, G. J. G., Härkönen, T., Lowry, L., Lydersen, C., Schipper, J., Sipilä, T., Southwell, C., Stuart, S., Thompson, D., & Trillmich, F. (2012). Global threats to pinnipeds. *Marine Mammal Science*, *28*(2), 414–436. https://doi.org/10.1111/j.1748-7692.2011.00479.x

Krabbenhoft, D. P., & Sunderland, E. M. (2013). Global Change and Mercury. *Science*, *341*(6153), 1457–1458. https://doi.org/10.1126/science.1242838

Kushnir, Y. (1994). Interdecadal Variations in North Atlantic Sea Surface Temperature and Associated Atmospheric Conditions. *Journal of Climate*, *7*(1), 141–157. https://doi.org/10.1175/1520-0442(1994)007%253C0141:IVINAS%253E2.0.CO;2

Laidre, K. L., & Heide-Jørgensen, M. P. (2005). Winter Feeding Intensity of Narwhals (Monodon Monoceros). *Marine Mammal Science*, *21*(1), 45–57. https://doi.org/10.1111/j.1748-7692.2005.tb01207.x

Laidre, K. L., & Heide-Jørgensen, M. P. (2011). Life in the lead: Extreme densities of narwhals Monodon monoceros in the offshore pack ice. *Marine Ecology Progress Series*, *423*, 269–278. https://doi.org/10.3354/meps08941

Laidre, K. L., Heide-Jørgensen, M. P., Dietz, R., Hobbs, R., & Jørgensen, O. (2003). Deep-diving by narwhals Monodon monoceros: Differences in foraging behavior between wintering areas? *Marine Ecology Progress Series*, *261*, 269–281. https://doi.org/10.3354/meps261269

Laidre, K. L., Heide-Jørgensen, M. P., Jørgensen, O. A., & Treble, M. A. (2004). Deep-ocean predation by a high Arctic cetacean. *ICES Journal of Marine Science*, *61*(3), 430–440. https://doi.org/10.1016/j.icesjms.2004.02.002

Laidre, K. L., Stern, H., Kovacs, Lowry, L., Moore, S. E., Regehr, E. V., Ferguson, S. H., Wiig, Ø., Boveng, P., Angliss, R. P., Born, E. W., Litovka, D., Quakenbush, L., Lydersen, C., Vongraven, D., & Ugarte, F. (2015). Arctic marine mammal population status, sea ice habitat loss, and conservation recommendations for the 21st century: Arctic Marine

Mammal Conservation. *Conservation Biology*, *29*(3), 724–737. https://doi.org/10.1111/cobi.12474

Laidre, K. L., Stirling, I., Lowry, L. F., Wiig, Ø., Heide-Jørgensen, M. P., & Ferguson, S. H. (2008). Quantifying the Sensitivity of Arctic Marine Mammals to Climate-Induced Habitat Change. *Ecological Applications*, *18*(sp2), S97–S125. https://doi.org/10.1890/06-0546.1

Latif, M., Collins, M., Pohlmann, H., & Keenlyside, N. (2006). A Review of Predictability Studies of Atlantic Sector Climate on Decadal Time Scales. *Journal of Climate*, *19*(23), 5971–5987. https://doi.org/10.1175/JCLI3945.1

Lee, J., Tefs, A., Galindo, V., Stadnyk, T., Gosselin, M., & Tremblay, J.-É. (2023). Nutrient inputs from subarctic rivers into Hudson Bay. *Elem Sci Anth*, *11*(1), 00085. https://doi.org/10.1525/elementa.2021.00085

Lee, S., Lee, K., Han, C., Han, Y., Hong, S.-B., Hur, S. D., Lee, S., Chang, C., Jung, H., Moon, J., Boutron, C. F., & Hong, S. (2023). Recent decline in atmospheric Pb deposition and isotopic constraints on changes in source contributions in snow from northwestern Greenland. *Chemosphere*, *345*, 140441. https://doi.org/10.1016/j.chemosphere.2023.140441

Lee-Thorp, J. A., Sealy, J. C., & Van Der Merwe, N. J. (1989). Stable carbon isotope ratio differences between bone collagen and bone apatite, and their relationship to diet. *Journal of Archaeological Science*, *16*(6), 585–599. https://doi.org/10.1016/0305-4403(89)90024-1

Lehmann, N., Kienast, M., Granger, J., & Tremblay, J. -É. (2022). Physical and Biogeochemical Influences on Nutrients Through the Canadian Arctic Archipelago: Insights From Nitrate Isotope Ratios. *Journal of Geophysical Research: Oceans*, *127*(3), e2021JC018179. https://doi.org/10.1029/2021JC018179

Leu, E., Brown, T. A., Graeve, M., Wiktor, J., Hoppe, C. J. M., Chierici, M., Fransson, A., Verbiest, S., Kvernvik, A. C., & Greenacre, M. J. (2020). Spatial and Temporal Variability of Ice Algal Trophic Markers—With Recommendations about Their Application. *Journal of Marine Science and Engineering*, *8*(9), 676. https://doi.org/10.3390/jmse8090676

Leu, E., Søreide, J. E., Hessen, D. O., Falk-Petersen, S., & Berge, J. (2011). Consequences of changing sea-ice cover for primary and secondary producers in the European Arctic shelf seas: Timing, quantity, and quality. *Progress in Oceanography*, *90*(1–4), 18–32. https://doi.org/10.1016/j.pocean.2011.02.004

Lewis, K. M., Van Dijken, G. L., & Arrigo, K. R. (2020). Changes in phytoplankton concentration now drive increased Arctic Ocean primary production. *Science*, *369*(6500), 198–202. https://doi.org/10.1126/science.aay8380

Lind, S., Ingvaldsen, R. B., & Furevik, T. (2018). Arctic warming hotspot in the northern Barents Sea linked to declining sea-ice import. *Nature Climate Change*, *8*(7), 634–639. https://doi.org/10.1038/s41558-018-0205-y

Lorrain, A., Graham, B., Ménard, F., Popp, B., Bouillon, S., Van Breugel, P., & Cherel, Y. (2009). Nitrogen and carbon isotope values of individual amino acids: A tool to study foraging ecology of penguins in the Southern Ocean. *Marine Ecology Progress Series*, *391*, 293–306. https://doi.org/10.3354/meps08215

Louis, M., Skovrind, M., Garde, E., Heide-Jørgensen, M. P., Szpak, P., & Lorenzen, E. D. (2021). Population-specific sex and size variation in long-term foraging ecology of belugas and narwhals. *Royal Society Open Science*, *8*(2), rsos.202226, 202226. https://doi.org/10.1098/rsos.202226

Lowry, L., Laidre, K. L., & Reeves, R. (2017). *Monodon monoceros. The IUCN Red List of Threatened Species 2017: e.T13704A50367651* [Dataset]. https://doi.org/10.2305/IUCN.UK.2017-3.RLTS.T13704A50367651.en

Lydersen, C., Vaquie-Garcia, J., Lydersen, E., Christensen, G. N., & Kovacs, K. M. (2017). Novel terrestrial haul-out behaviour by ringed seals (*Pusa hispida*) in Svalbard, in association with harbour seals (*Phoca vitulina*). *Polar Research*, *36*(1), 1374124. https://doi.org/10.1080/17518369.2017.1374124

Maccali, J., Hillaire-Marcel, C., & Not, C. (2018). Radiogenic isotope (Nd, Pb, Sr) signatures of surface and sea ice-transported sediments from the Arctic Ocean under the present interglacial conditions. *Polar Research*, *37*(1), 1442982. https://doi.org/10.1080/17518369.2018.1442982

Macdonald, R. W., Harner, T., & Fyfe, J. (2005). Recent climate change in the Arctic and its impact on contaminant pathways and interpretation of temporal trend data. *Science of The Total Environment*, *342*(1–3), 5–86. https://doi.org/10.1016/j.scitotenv.2004.12.059

Macdonald, R. W., Kuzyk, Z. Z. A., & Johannessen, S. C. (2015). The vulnerability of Arctic shelf sediments to climate change. *Environmental Reviews*, *23*(4), 461–479. https://doi.org/10.1139/er-2015-0040

Mahajan, S., Zhang, R., & Delworth, T. L. (2011). Impact of the Atlantic Meridional Overturning Circulation (AMOC) on Arctic Surface Air Temperature and Sea Ice Variability. *Journal of Climate*, *24*(24), 6573–6581. https://doi.org/10.1175/2011JCLI4002.1

Mansfield, A. W., Smith, T. G., & Beck, B. (1975). The Narwhal, Monodon monoceros, in Eastern Canadian Waters. *Journal of the Fisheries Research Board of Canada*, *32*(7), 1041–1046. https://doi.org/10.1139/f75-122

Marcoux, M., Auger-Méthé, M., & Humphries, M. M. (2012). Variability and context specificity of narwhal (Monodon monoceros) whistles and pulsed calls. *Marine Mammal Science*, *28*(4), 649–665. https://doi.org/10.1111/j.1748-7692.2011.00514.x

Markus, T., Stroeve, J. C., & Miller, J. (2009). Recent changes in Arctic sea ice melt onset, freezeup, and melt season length. *Journal of Geophysical Research: Oceans*, *114*(C12), 2009JC005436. https://doi.org/10.1029/2009JC005436

Matthes, L. C., Ehn, J. K., Dalman, L. A., Babb, D. G., Peeken, I., Harasyn, M., Kirillov, S., Lee, J., Bélanger, S., Tremblay, J.-É., Barber, D. G., & Mundy, C. J. (2021). Environmental drivers of spring primary production in Hudson Bay. *Elementa: Science of the Anthropocene*, *9*(1), 00160. https://doi.org/10.1525/elementa.2020.00160

Matthews, C. J. D., & Ferguson, S. H. (2014). Validation of dentine deposition rates in beluga whales by interspecies cross dating of temporal δ13C trends in teeth. *NAMMCO Scientific Publications*, *8*. https://doi.org/10.7557/3.3196

Matthews, C. J. D., & Ferguson, S. H. (2015). Weaning age variation in beluga whales (Delphinapterus leucas). *Journal of Mammalogy*, *96*(2), 425–437. https://doi.org/10.1093/jmammal/gyv046

Matthews, C. J. D., Longstaffe, F. J., & Ferguson, S. H. (2016). Dentine oxygen isotopes (δ18O) as a proxy for odontocete distributions and movements. *Ecology and Evolution*, *6*(14), 4643–4653. https://doi.org/10.1002/ece3.2238

May, W. E., & Rumble, J. (2004). *Certificate of Analysis Standard Reference Material 1646a*. National Institute of Standards & Technology. https://tsapps.nist.gov/srmext/certificates/1646a.pdf

McLeish, T. (2013). *Narwhals: Arctic whales in a melting world.* University of Washington Press.

McMahon, K. W., & McCarthy, M. D. (2016). Embracing variability in amino acid δ15N fractionation: Mechanisms, implications, and applications for trophic ecology. *Ecosphere*, *7*(12), e01511. https://doi.org/10.1002/ecs2.1511

Michel, C., Bluhm, B., Gallucci, V., Gaston, A. J., Gordillo, F. J. L., Gradinger, R., Hopcroft, R., Jensen, N., Mustonen, T., Niemi, A., & Nielsen, T. G. (2012). Biodiversity of Arctic

marine ecosystems and responses to climate change. *Biodiversity*, *13*(3–4), 200–214. https://doi.org/10.1080/14888386.2012.724048

Miles, M. W., Divine, D. V., Furevik, T., Jansen, E., Moros, M., & Ogilvie, A. E. J. (2014). A signal of persistent Atlantic multidecadal variability in Arctic sea ice. *Geophysical Research Letters*, *41*(2), 463–469. https://doi.org/10.1002/2013GL058084

Moore, S. E., & Huntington, H. P. (2008). Arctic Marine Mammals and Climate Change: Impacts and Resilience. *Ecological Applications*, *18*(sp2), S157–S165. https://doi.org/10.1890/06-0571.1

Nakano, T. (2016). Potential uses of stable isotope ratios of Sr, Nd, and Pb in geological materials for environmental studies. *Proceedings of the Japan Academy, Series B*, *92*(6), 167–184. https://doi.org/10.2183/pjab.92.167

Neve, P. B. (1995). Life history of narwhals (Monodon monoceros) in West Greenland, Part II. *Specialeafhandling Ved Københavns Universitet*, 1–12.

Newsome, S. D., Clementz, M. T., & Koch, P. L. (2010). Using stable isotope biogeochemistry to study marine mammal ecology. *Marine Mammal Science*, *26*(3), 509–572. https://doi.org/10.1111/j.1748-7692.2009.00354.x

Newsome, S. D., Etnier, M. A., Monson, D. H., & Fogel, M. L. (2009). Retrospective characterization of ontogenetic shifts in killer whale diets via δ13C and δ15N analysis of teeth. *Marine Ecology Progress Series*, *374*, 229–242. https://doi.org/10.3354/meps07747

Nweeia, M. T., Eichmiller, F. C., Hauschka, P. V., Donahue, G. A., Orr, J. R., Ferguson, S. H., Watt, C. A., Mead, J. G., Potter, C. W., Dietz, R., Giuseppetti, A. A., Black, S. R., Trachtenberg, A. J., & Kuo, W. P. (2014). Sensory ability in the narwhal tooth organ system. *The Anatomical Record*, *297*(4), 599–617. https://doi.org/10.1002/ar.22886

Nweeia, M. T., Eichmiller, F. C., Hauschka, P. V., Tyler, E., Mead, J. G., Potter, C. W., Angnatsiak, D. P., Richard, P. R., Orr, J. R., & Black, S. R. (2012). Vestigial Tooth Anatomy and Tusk Nomenclature for Monodon Monoceros. *The Anatomical Record*, *295*(6), 1006–1016. https://doi.org/10.1002/ar.22449

Ocean North Canada. (2014). *Baffin Island and West Greenland Currents* [Map]. https://www.pew.org/en/research-and-analysis/fact-sheets/0001/01/01/from-the-north-water-polynya-to-lancaster-sound

Olivelli, A., Arcucci, R., Rehkämper, M., & Van De Flierdt, T. (2025). Mapping the global distribution of lead and its isotopes in seawater with explainable machine learning. *Earth System Science Data*, *17*(7), 3679–3699. https://doi.org/10.5194/essd-17-3679-2025

Outridge, P. M., Hobson, K. A., & Savelle, J. M. (2005). Changes in mercury and cadmium concentrations and the feeding behaviour of beluga (Delphinapterus leucas) near Somerset Island, Canada, during the 20th century. *Science of The Total Environment*, *350*(1–3), 106–118. https://doi.org/10.1016/j.scitotenv.2004.12.081

Outridge, P. M., & Stewart, R. E. (1999). Stock discrimination of Atlantic walrus (Odobenus rosmarus rosmarus) in the eastern Canadian Arctic using lead isotope and element signatures in teeth. *Canadian Journal of Fisheries and Aquatic Sciences*, *56*(1), 105–112. https://doi.org/10.1139/f98-155

Pagano, A. M., & Williams, T. M. (2021). Physiological consequences of Arctic sea ice loss on large marine carnivores: Unique responses by polar bears and narwhals. *Journal of Experimental Biology*, *224*(Suppl_1), jeb228049. https://doi.org/10.1242/jeb.228049

Parmentier, F.-J. W., Christensen, T. R., Rysgaard, S., Bendtsen, J., Glud, R. N., Else, B., Van Huissteden, J., Sachs, T., Vonk, J. E., & Sejr, M. K. (2017). A synthesis of the arctic terrestrial and marine carbon cycles under pressure from a dwindling cryosphere. *Ambio*, *46*(S1), 53–69. https://doi.org/10.1007/s13280-016-0872-8

Peek, S., & Clementz, M. T. (2012). Sr/Ca and Ba/Ca variations in environmental and biological sources: A survey of marine and terrestrial systems. *Geochimica et Cosmochimica Acta*, *95*, 36–52. https://doi.org/10.1016/j.gca.2012.07.026

Perovich, D., Meier, W., Tschudi, M., Hendricks, S., Petty, A. A., Divine, D., Farrell, S., Gerland, S., Haas, C., Kaleschke, L., Pavlova, O., Ricker, R., Tian-Kunze, X., Wood, K., & Webster, M. (2020). Arctic Report Card 2020: Sea Ice. *Arctic Report Card*. https://doi.org/10.25923/N170-9H57

Perryman, C. R., Wirsing, J., Bennett, K. A., Brennick, O., Perry, A. L., Williamson, N., & Ernakovich, J. G. (2020). Heavy metals in the Arctic: Distribution and enrichment of five metals in Alaskan soils. *PLOS ONE*, *15*(6), e0233297. https://doi.org/10.1371/journal.pone.0233297

Pilfold, N. W., McCall, A., Derocher, A. E., Lunn, N. J., & Richardson, E. (2017). Migratory response of polar bears to sea ice loss: To swim or not to swim. *Ecography*, *40*(1), 189–199. https://doi.org/10.1111/ecog.02109

Pin, C., Gannoun, A., & Dupont, A. (2014). Rapid, simultaneous separation of Sr, Pb, and Nd by extraction chromatography prior to isotope ratios determination by TIMS and MC-ICP-MS. *J. Anal. At. Spectrom.*, *29*(1), 1858–1870. https://doi.org/10.1039/C4JA00169A

Polyakov, I. V., Pnyushkov, A. V., Alkire, M. B., Ashik, I. M., Baumann, T. M., Carmack, E. C., Goszczko, I., Guthrie, J., Ivanov, V. V., Kanzow, T., Krishfield, R., Kwok, R., Sundfjord,

A., Morison, J., Rember, R., & Yulin, A. (2017). Greater role for Atlantic inflows on sea-ice loss in the Eurasian Basin of the Arctic Ocean. *Science*, *356*(6335), 285–291. https://doi.org/10.1126/science.aai8204

Pomerleau, C., Stern, G. A., Pućko, M., Foster, K. L., Macdonald, R. W., & Fortier, L. (2016). Pan-Arctic concentrations of mercury and stable isotope ratios of carbon (δ13C) and nitrogen (δ15N) in marine zooplankton. *Science of The Total Environment*, *551–552*, 92–100. https://doi.org/10.1016/j.scitotenv.2016.01.172

Post, D. M. (2002). Using Stable Isotopes To Estimate Trophic Position: Models, Methods, And Assumptions. *Ecology*, *83*(3), 703–718. https://doi.org/10.1890/0012-9658(2002)083%255B0703:USITET%255D2.0.CO;2

Post, E., Bhatt, U. S., Bitz, C. M., Brodie, J. F., Fulton, T. L., Hebblewhite, M., Kerby, J., Kutz, S. J., Stirling, I., & Walker, D. A. (2013). Ecological Consequences of Sea-Ice Decline. *Science*, *341*(6145), 519–524. https://doi.org/10.1126/science.1235225

Pradel, A., Hufenus, R., Schneebeli, M., & Mitrano, D. M. (2025). Impact of contaminant size and density on their incorporation into sea ice. *Nature Communications*, *16*(1), 4375. https://doi.org/10.1038/s41467-025-59608-2

Pućko, M., Stern, G. A., Macdonald, R. W., Jantunen, L. M., Bidleman, T. F., Wong, F., Barber, D. G., & Rysgaard, S. (2015). The delivery of organic contaminants to the Arctic food web: Why sea ice matters. *Science of The Total Environment*, *506–507*, 444–452. https://doi.org/10.1016/j.scitotenv.2014.11.040

Qi, H., Coplen, T. B., Geilmann, H., Brand, W. A., & Böhlke, J. K. (2003). Two new organic reference materials for δ13C and δ15N measurements and a new value for the δ13C of NBS 22 oil. *Rapid Communications in Mass Spectrometry*, *17*(22), 2483–2487. https://doi.org/10.1002/rcm.1219

Rantanen, M., Karpechko, A. Yu., Lipponen, A., Nordling, K., Hyvärinen, O., Ruosteenoja, K., Vihma, T., & Laaksonen, A. (2022). The Arctic has warmed nearly four times faster than the globe since 1979. *Communications Earth & Environment*, *3*(1), 168. https://doi.org/10.1038/s43247-022-00498-3

Rau, G. H., Takahashi, T., Des Marais, D. J., Repeta, D. J., & Martin, J. H. (1992). The relationship between δ13C of organic matter and [CO2(aq)] in ocean surface water: Data from a JGOFS site in the northeast Atlantic Ocean and a model. *Geochimica et Cosmochimica Acta*, *56*(3), 1413–1419. https://doi.org/10.1016/0016-7037(92)90073-R

Read, C. J., & Stephansson, S. E. (1976). Distribution and migration routes of marine mammals in the central Arctic region. *Fisheries and Marine Service Technical Report 667*.

Reed, A. J., Tuerena, R. E., Archambault, P., & Solan, M. (2021). Editorial: Biogeochemical Consequences of Climate-Driven Changes in the Arctic. *Frontiers in Environmental Science*, *9*, 696909. https://doi.org/10.3389/fenvs.2021.696909

Reeves, R. R., Ewins, P. J., Agbayani, S., Heide-Jørgensen, M. P., Kovacs, K. M., Lydersen, C., Suydam, R., Elliott, W., Polet, G., Van Dijk, Y., & Blijleven, R. (2014). Distribution of endemic cetaceans in relation to hydrocarbon development and commercial shipping in a warming Arctic. *Marine Policy*, *44*, 375–389. https://doi.org/10.1016/j.marpol.2013.10.005

Rey-Iglesia, A., Wilson, T., Routledge, J., Skovrind, M., Garde, E., Heide-Jørgensen, M. P., Szpak, P., & Lorenzen, E. D. (2023). Combining δ13C and δ15N from bone and dentine in marine mammal palaeoecological research: Insights from toothed whales. *Isotopes in Environmental and Health Studies*, *59*(1), 66–77. https://doi.org/10.1080/10256016.2022.2145285

Richard, P. R. (1991). Abundance and Distribution of Narwhals (Monodon monoceros) in Northern Hudson Bay. *Canadian Journal of Fisheries and Aquatic Sciences*, *48*(2), 276–283. https://doi.org/10.1139/f91-038

Richard, P., Weaver, P., Dueck, L., & Barber, D. (1994). Distribution and numbers of Canadian High Arctic narwhals (Monodon monoceros) in August 1984. *Meddelelser Om Grønland. Bioscience*, *39*, 41–50. https://doi.org/10.7146/mogbiosci.v39.142533

Robicheau, B. M., Tolman, J., Rose, S., Desai, D., & LaRoche, J. (2023). Marine nitrogen-fixers in the Canadian Arctic Gateway are dominated by biogeographically distinct noncyanobacterial communities. *FEMS Microbiology Ecology*, *99*(12), fiad122. https://doi.org/10.1093/femsec/fiad122

Rogalla, B., Allen, S. E., Colombo, M., Myers, P. G., & Orians, K. J. (2025). Modeling Dissolved Pb Concentrations in the Western Arctic Ocean: The Continued Legacy of Anthropogenic Pollution. *Journal of Geophysical Research: Oceans*, *130*(4), e2025JC022415. https://doi.org/10.1029/2025JC022415

Rohonczy, J., Chételat, J., Robinson, S. A., Arragutainaq, L., Heath, J. P., McClelland, C., Mickpegak, R., & Forbes, M. R. (2024). Contrasting trophic transfer patterns of cadmium and mercury in the Arctic marine food web of east Hudson Bay, Canada. *Environmental Science and Pollution Research*, *31*(13), 20586–20600. https://doi.org/10.1007/s11356-024-32268-3

Ruiz-Barradas, A., Nigam, S., & Kavvada, A. (2013). The Atlantic Multidecadal Oscillation in twentieth century climate simulations: Uneven progress from CMIP3 to CMIP5. *Climate Dynamics*, *41*(11–12), 3301–3315. https://doi.org/10.1007/s00382-013-1810-0

Ruiz-Cooley, R. I., Koch, P. L., Fiedler, P. C., & McCarthy, M. D. (2014). Carbon and Nitrogen Isotopes from Top Predator Amino Acids Reveal Rapidly Shifting Ocean Biochemistry in the Outer California Current. *PLoS ONE*, *9*(10), e110355. https://doi.org/10.1371/journal.pone.0110355

Schmidt, G. A., Bigg, G. R., & Rohling, E. J. (1999). *Global Seawater Oxygen-18 Database – v1.21* [Dataset]. http://data.giss.nasa.gov/o18data/

Sharma, S. D., Patil, D. J., & Gopalan, K. (2002). Temperature dependence of oxygen isotope fractionation of CO2 from magnesite-phosphoric acid reaction. *Geochimica et Cosmochimica Acta*, *66*(4), 589–593. https://doi.org/10.1016/S0016-7037(01)00833-X

Sherwood, O. A., Davin, S. H., Lehmann, N., Buchwald, C., Edinger, E. N., Lehmann, M. F., & Kienast, M. (2021). Stable isotope ratios in seawater nitrate reflect the influence of Pacific water along the northwest Atlantic margin. *Biogeosciences*, *18*(15), 4491–4510. https://doi.org/10.5194/bg-18-4491-2021

Shiozaki, T., Fujiwara, A., Inomura, K., Hirose, Y., Hashihama, F., & Harada, N. (2020). Biological nitrogen fixation detected under Antarctic sea ice. *Nature Geoscience*, *13*(11), 729–732. https://doi.org/10.1038/s41561-020-00651-7

Shuert, C. R., Marcoux, M., Hussey, N. E., Heide-Jørgensen, M. P., Dietz, R., & Auger-Méthé, M. (2022). Decadal migration phenology of a long-lived Arctic icon keeps pace with climate change. *Proceedings of the National Academy of Sciences*, *119*(45), e2121092119. https://doi.org/10.1073/pnas.2121092119

Slagstad, D., Wassmann, P. F. J., & Ellingsen, I. (2015). Physical constrains and productivity in the future Arctic Ocean. *Frontiers in Marine Science*, *2*. https://doi.org/10.3389/fmars.2015.00085

Soerensen, A. L., Jacob, D. J., Schartup, A. T., Fisher, J. A., Lehnherr, I., St. Louis, V. L., Heimbürger, L., Sonke, J. E., Krabbenhoft, D. P., & Sunderland, E. M. (2016). A mass budget for mercury and methylmercury in the Arctic Ocean. *Global Biogeochemical Cycles*, *30*(4), 560–575. https://doi.org/10.1002/2015GB005280

Sohm, J. A., Webb, E. A., & Capone, D. G. (2011). Emerging patterns of marine nitrogen fixation. *Nature Reviews Microbiology*, *9*(7), 499–508. https://doi.org/10.1038/nrmicro2594

Solan, M., Ward, E. R., Wood, C. L., Reed, A. J., Grange, L. J., & Godbold, J. A. (2021). Correction to 'Climate-driven benthic invertebrate activity and biogeochemical functioning across the Barents Sea polar front.' *Philosophical Transactions of the Royal Society A: Mathematical, Physical and Engineering Sciences*, *379*(2195), 20200438. https://doi.org/10.1098/rsta.2020.0438

Søreide, J. E., Leu, E., Berge, J., Graeve, M., & Falk-Petersen, S. (2010). Timing of blooms, algal food quality and *Calanus glacialis* reproduction and growth in a changing Arctic. *Global Change Biology*, *16*(11), 3154–3163. https://doi.org/10.1111/j.1365-2486.2010.02175.x

Stern, G. A., Macdonald, R. W., Outridge, P. M., Wilson, S., Chételat, J., Cole, A., Hintelmann, H., Loseto, L. L., Steffen, A., Wang, F., & Zdanowicz, C. (2012). How does climate change influence arctic mercury? *Science of The Total Environment*, *414*, 22–42. https://doi.org/10.1016/j.scitotenv.2011.10.039

Stevenson, M. A., & Abbott, G. D. (2019). Exploring the composition of macromolecular organic matter in Arctic Ocean sediments under a changing sea ice gradient. *Journal of Analytical and Applied Pyrolysis*, *140*, 102–111. https://doi.org/10.1016/j.jaap.2019.02.006

Stroeve, J., & Notz, D. (2018). Changing state of Arctic sea ice across all seasons. *Environmental Research Letters*, *13*(10), 103001. https://doi.org/10.1088/1748-9326/aade56

Sunda, W. G. (2012). Feedback Interactions between Trace Metal Nutrients and Phytoplankton in the Ocean. *Frontiers in Microbiology*, *3*. https://doi.org/10.3389/fmicb.2012.00204

Sutton, R. T., & Hodson, D. L. R. (2005). Atlantic Ocean Forcing of North American and European Summer Climate. *Science*, *309*(5731), 115–118. https://doi.org/10.1126/science.1109496

Tamelander, T., Kivimäe, C., Bellerby, R. G. J., Renaud, P. E., & Kristiansen, S. (2009). Baseline variations in stable isotope values in an Arctic marine ecosystem: Effects of carbon and nitrogen uptake by phytoplankton. *Hydrobiologia*, *630*(1), 63–73. https://doi.org/10.1007/s10750-009-9780-2

Tang, W., Wang, S., Fonseca-Batista, D., Dehairs, F., Gifford, S., Gonzalez, A. G., Gallinari, M., Planquette, H., Sarthou, G., & Cassar, N. (2019). Revisiting the distribution of oceanic N2 fixation and estimating diazotrophic contribution to marine production. *Nature Communications*, *10*(1), 831. https://doi.org/10.1038/s41467-019-08640-0

Thévenod, F., & Lee, W.-K. (2013). Toxicology of Cadmium and Its Damage to Mammalian Organs. In A. Sigel, H. Sigel, & R. K. Sigel (Eds.), *Cadmium: From Toxicity to*

Essentiality (Vol. 11, pp. 415–490). Springer Netherlands. https://doi.org/10.1007/978-94-007-5179-8_14

Thibodeau, B., Migon, C., Dufour, A., Poirier, A., Mari, X., Ghaleb, B., & Legendre, L. (2017). Low sedimentary accumulation of lead caused by weak downward export of organic matter in Hudson Bay, northern Canada. *Biogeochemistry*, *136*(3), 279–291. https://doi.org/10.1007/s10533-017-0395-9

Trenberth, K., & Zhang, R. (2025). *The Climate Data Guide: Atlantic Multi-decadal Oscillation (AMO) and Atlantic Multidecadal Variability (AMV)* [Dataset].

Ventresca Miller, A., Fernandes, R., Janzen, A., Nayak, A., Swift, J., Zech, J., Boivin, N., & Roberts, P. (2018). Sampling and Pretreatment of Tooth Enamel Carbonate for Stable Carbon and Oxygen Isotope Analysis. *Journal of Visualized Experiments*, *138*, 58002. https://doi.org/10.3791/58002-v

Verkouteren, R. M., & Klinedinst, D. B. (2003). *Standard Reference Materials: Value Assignment and Uncertainty Estimation of Selected Light Stable Isotope Reference Materials: RMs 8543-8545, RMs 8562-8564, and RM 8566* (No. NIST SP 260-149; 0 ed., p. NIST SP 260-149). National Institute of Standards and Technology. https://doi.org/10.6028/NIST.SP.260-149

Von Friesen, L. W., Farnelid, H., Von Appen, W.-J., Benavides, M., Grosso, O., Laber, C. P., Schüttler, J., Sundbom, M., Torres-Valdés, S., Bertilsson, S., Peeken, I., Snoeijs-Leijonmalm, P., & Riemann, L. (2025). Nitrogen fixation under declining Arctic sea ice. *Communications Earth & Environment*, *6*(1), 811. https://doi.org/10.1038/s43247-025-02782-4

Walker, J. L., & Macko, S. A. (1999). Dietary Studies of Marine Mammals Using Stable Carbon and Nitrogen Isotopic Rratios of Teeth. *Marine Mammal Science*, *15*(2), 314–334. https://doi.org/10.1111/j.1748-7692.1999.tb00804.x

Wassmann, P., Duarte, C. M., Agustí, S., & Sejr, M. K. (2011). Footprints of climate change in the Arctic marine ecosystem. *Global Change Biology*, *17*(2), 1235–1249. https://doi.org/10.1111/j.1365-2486.2010.02311.x

Watt, C. A., & Ferguson, S. H. (2015). Fatty acids and stable isotopes (δ13C and δ15N) reveal temporal changes in narwhal (Monodon monoceros) diet linked to migration patterns. *Marine Mammal Science*, *31*(1), 21–44. https://doi.org/10.1111/mms.12131

Watt, C. A., Heide-Jørgensen, M. P., & Ferguson, S. H. (2013). How adaptable are narwhal? A comparison of foraging patterns among the world's three narwhal populations. *Ecosphere*, *4*(6), 1–15. https://doi.org/10.1890/ES13-00137.1

Watt, C. A., Orr, J. R., & Ferguson, S. H. (2017). Spatial distribution of narwhal (Monodon monoceros) diving for Canadian populations helps identify important seasonal foraging areas. *Canadian Journal of Zoology*, *95*(1), 41–50. https://doi.org/10.1139/cjz-2016-0178

Westbrook, H. C., Bourbonnais, A., Manning, C. C. M., Tremblay, J. -É., Ahmed, M. M. M., Else, B., & Granger, J. (2024). Dissolved Nitrogen Cycling in the Eastern Canadian Arctic Archipelago and Baffin Bay From Stable Isotopic Data. *Global Biogeochemical Cycles*, *38*(12), e2023GB007926. https://doi.org/10.1029/2023GB007926

Whiteman, J. P., Elliott Smith, E. A., Besser, A. C., & Newsome, S. D. (2019). A Guide to Using Compound-Specific Stable Isotope Analysis to Study the Fates of Molecules in Organisms and Ecosystems. *Diversity*, *11*(1), 8. https://doi.org/10.3390/d11010008

Willie, S., Pihillagawa Gedara, I., Maxwell, P., Meija, J., Grinberg, P., Mester, Z., Palmer, C., Gajdosechova, Z., Le, P. M., Kubachka, K., Wolle, M., Raab, A., Feldmann, J., Sim, R., Pétursdóttir, Á. H., Matoušek, T., Musil, S., Wozniak, B., Springer, S., … Yang, L. (2013). *TORT-3: Lobster hepatopancreas reference material for trace metals*. National Research Council Canada. https://doi.org/10.4224/CRM.2013.TORT-3

Yeager, S. G., Karspeck, A. R., & Danabasoglu, G. (2015). Predicted slowdown in the rate of Atlantic sea ice loss. *Geophysical Research Letters*, *42*(24). https://doi.org/10.1002/2015GL065364

Yunda-Guarin, G., Brown, T. A., Michel, L. N., Saint-Béat, B., Amiraux, R., Nozais, C., & Archambault, P. (2020). Reliance of deep-sea benthic macrofauna on ice-derived organic matter highlighted by multiple trophic markers during spring in Baffin Bay, Canadian Arctic. *Elementa: Science of the Anthropocene*, *8*(1), 047. https://doi.org/10.1525/elementa.2020.047

Yurkowski, D. J., Hussey, N. E., Ferguson, S. H., & Fisk, A. T. (2018). A temporal shift in trophic diversity among a predator assemblage in a warming Arctic. *Royal Society Open Science*, *5*(10), 180259. https://doi.org/10.1098/rsos.180259

Zhang, R. (2015). Mechanisms for low-frequency variability of summer Arctic sea ice extent. *Proceedings of the National Academy of Sciences*, *112*(15), 4570–4575. https://doi.org/10.1073/pnas.1422296112

Zhang, R., Jensen, L. T., Fitzsimmons, J. N., Sherrell, R. M., & John, S. (2019). Dissolved cadmium and cadmium stable isotopes in the western Arctic Ocean. *Geochimica et Cosmochimica Acta*, *258*, 258–273. https://doi.org/10.1016/j.gca.2019.05.028

Zhang, X., Sigman, D. M., Morel, F. M. M., & Kraepiel, A. M. L. (2014). Nitrogen isotope fractionation by alternative nitrogenases and past ocean anoxia. *Proceedings of the*

National Academy of Sciences, *111*(13), 4782–4787. https://doi.org/10.1073/pnas.1402976111

Zhang, Y., Soerensen, A. L., Schartup, A. T., & Sunderland, E. M. (2020). A Global Model for Methylmercury Formation and Uptake at the Base of Marine Food Webs. *Global Biogeochemical Cycles*, *34*(2), e2019GB006348. https://doi.org/10.1029/2019GB006348

Zhao, S. T., Matthews, C., Davoren, G., Ferguson, S., & Watt, C. (2021). Ontogenetic profiles of dentine isotopes (δ15N and δ13C) reveal variable narwhal Monodon monoceros nursing duration. *Marine Ecology Progress Series*, *668*, 163–175. https://doi.org/10.3354/meps13738

Zhao, S. T., Matthews, C. J. D., & Watt, C. A. (2025). δ15N and δ13C cycles in narwhal (Monodon monoceros) embedded teeth reveal seasonal variation in ecology and/or physiology. *Royal Society Open Science*, *12*(3), 242237. https://doi.org/10.1098/rsos.242237

SUPPLEMENTAL MATERIAL

Table 1. Linear temporal trends and associated *p*-values for isotopic and elemental variables in annual growth layers of Baffin Bay (Tusk 1) and Hudson Bay (Tusk 2). Trends are estimated using ordinary least-squares regression of each variable on GLG year. Slopes represent the average annual change per year. Statistically significant trends are indicated by * for *p*-value ≤ 0.05 and ** for *p*-value ≤ 0.01.

Tusk	Variable	Slope	*p*-value
Tusk 1	$\delta^{13}C_{collagen}$	0.003	0.635
Tusk 1	$\delta^{15}N_{collagen}$	-0.055	< 0.001 **
Tusk 1	$\delta^{13}C_{CO3}$	-0.060	< 0.001 **
Tusk 1	$\delta^{18}O_{CO3}$	-0.009	0.480
Tusk 1	$\Delta^{13}C_{carb\text{-}coll}$	-0.063	< 0.001 **
Tusk 1	Hg	0.481	0.010 *
Tusk 1	$^{206}Pb/^{204}Pb$	0.020	< 0.001 **
Tusk 1	$^{208}Pb/^{206}Pb$	5.32e-05	0.821
Tusk 1	$^{206}Pb/^{207}Pb$	0.001	< 0.001 **
Tusk 1	Mn:Ca	2.46e-07	0.575
Tusk 1	Fe:Ca	2.91e-06	0.570
Tusk 1	As:Ca	3.99e-10	0.518
Tusk 1	Cd:Ca	-2.26e-09	0.002 **
Tusk 1	Pb:Ca	-1.01e-08	< 0.001 **
Tusk 1	Mg:Ca	-5.43e-04	< 0.001 **
Tusk 1	Cr:Ca	-3.99e-07	0.127
Tusk 1	Co:Ca	-7.49e-08	0.480
Tusk 1	Zn:Ca	3.85e-06	0.010 **
Tusk 1	Sr:Ca	-7.54e-06	0.002 **
Tusk 1	Ba:Ca	-1.76e-07	0.002 **
Tusk 2	$\delta^{13}C_{collagen}$	-0.003	0.741
Tusk 2	$\delta^{15}N_{collagen}$	0.001	0.862
Tusk 2	$\delta^{13}C_{CO3}$	-0.034	0.022 *
Tusk 2	$\delta^{18}O_{CO3}$	-9.26e-04	0.974
Tusk 2	$\Delta^{13}C_{carb\text{-}coll}$	-0.031	0.002 **
Tusk 2	Hg	0.072	0.257
Tusk 2	$^{206}Pb/^{204}Pb$	0.004	0.079
Tusk 2	$^{208}Pb/^{206}Pb$	6.43e-05	0.380
Tusk 2	$^{206}Pb/^{207}Pb$	1.91e-04	0.183
Tusk 2	Mn:Ca	-3.08e-07	0.028 *

Tusk 2	Fe:Ca	1.20e-06	0.010 **
Tusk 2	As:Ca	-8.26e-10	0.024 *
Tusk 2	Cd:Ca	-1.84e-09	0.007 **
Tusk 2	Pb:Ca	-1.86e-08	< 0.001 **
Tusk 2	Mg:Ca	-0.001	< 0.001 **
Tusk 2	Cr:Ca	-7.23e-08	0.693
Tusk 2	Co:Ca	-2.71e-07	0.085
Tusk 2	Zn:Ca	-5.68e-07	0.622
Tusk 2	Sr:Ca	-1.87e-05	< 0.001 **
Tusk 2	Ba:Ca	-4.16e-07	< 0.001 **

Table 2. Shapiro-Wilk test statistics (W) and associated *p*-values for isotopic and elemental variables in annual growth layers of Baffin Bay Tusk (Tusk 1). Variables that significantly deviate from a normal distribution are marked with * for $p \leq 0.05$ and ** for $p \leq 0.01$.

Variable	W	*p*-value	Normality
$\delta^{13}C_{collagen}$	0.898	0.023 *	Non-normal
$\delta^{15}N_{collagen}$	0.872	0.007 **	Non-normal
$\delta^{13}C_{CO3}$	0.968	0.650	Normal
$\delta^{18}O_{CO3}$	0.958	0.431	Normal
$\Delta^{13}C_{carb\text{-}coll}$	0.943	0.211	Normal
Hg	0.664	< 0.001 **	Non-normal
$^{206}Pb/^{204}Pb$	0.892	0.017 *	Non-normal
$^{208}Pb/^{206}Pb$	0.889	0.015 *	Non-normal
$^{206}Pb/^{207}Pb$	0.881	0.011 *	Non-normal
Mn:Ca	0.355	< 0.001 **	Non-normal
Fe:Ca	0.459	< 0.001 **	Non-normal
As:Ca	0.935	0.141	Normal
Cd:Ca	0.860	0.004 **	Non-normal
Pb:Ca	0.838	0.002 **	Non-normal
Mg:Ca	0.895	0.020 *	Non-normal
Cr:Ca	0.853	0.003 **	Non-normal
Co:Ca	0.925	0.086	Normal
Zn:Ca	0.919	0.064	Normal
Sr:Ca	0.849	0.003 **	Non-normal
Ba:Ca	0.813	< 0.001 **	Non-normal

Table 3. Shapiro-Wilk test statistics (W) and associated *p*-values for isotopic and elemental variables in annual growth layers of Hudson Bay Tusk (Tusk 2). Variables that significantly deviate from a normal distribution are marked with * for $p \leq 0.05$ and ** for $p \leq 0.01$.

Variable	W	*p*-value	Normality
$\delta^{13}C_{collagen}$	0.919	0.072	Normal
$\delta^{15}N_{collagen}$	0.949	0.308	Normal
$\delta^{13}C_{CO3}$	0.915	0.060	Normal
$\delta^{18}O_{CO3}$	0.919	0.073	Normal
$\Delta^{13}C_{carb\text{-}coll}$	0.964	0.577	Normal
Hg	0.974	0.801	Normal
$^{206}Pb/^{204}Pb$	0.920	0.075	Normal
$^{208}Pb/^{206}Pb$	0.947	0.270	Normal
$^{206}Pb/^{207}Pb$	0.894	0.023 *	Non-normal
Mn:Ca	0.605	< 0.001 **	Non-normal
Fe:Ca	0.912	0.053	Normal
As:Ca	0.731	< 0.001 **	Non-normal
Cd:Ca	0.928	0.113	Normal
Pb:Ca	0.869	0.007 **	Non-normal
Mg:Ca	0.795	< 0.001 **	Non-normal
Cr:Ca	0.961	0.504	Normal
Co:Ca	0.831	0.002 **	Non-normal
Zn:Ca	0.881	0.013 *	Non-normal
Sr:Ca	0.775	< 0.001 **	Non-normal
Ba:Ca	0.727	< 0.001 **	Non-normal

Table 4. Spearman correlation coefficients (ρ) and associated *p*-values for isotopic and elemental variables in annual growth layers of Baffin Bay Tusk (Tusk 1) and Hudson Bay Tusk (Tusk 2). Statistically significant correlations are indicated by * for *p*-value ≤ 0.05 and ** for *p*-value ≤ 0.01.

Variable 1	Variable 2	rho (ρ)	*p*-value
$\delta^{13}C_{collagen}$	$\delta^{15}N_{collagen}$	-0.39	0.008 **
$\delta^{13}C_{collagen}$	$\delta^{13}C_{CO3}$	0.75	< 0.001 **
$\delta^{13}C_{collagen}$	$\delta^{18}O_{CO3}$	-0.60	< 0.001 **
$\delta^{13}C_{collagen}$	$\Delta^{13}C_{carb\text{-}coll}$	0.08	0.610
$\delta^{13}C_{collagen}$	Hg	-0.22	0.148
$\delta^{13}C_{collagen}$	$^{206}Pb/^{204}Pb$	-0.26	0.089
$\delta^{13}C_{collagen}$	$^{208}Pb/^{206}Pb$	-0.18	0.242
$\delta^{13}C_{collagen}$	$^{206}Pb/^{207}Pb$	-0.29	0.052
$\delta^{13}C_{collagen}$	Mn:Ca	0.46	0.002 **
$\delta^{13}C_{collagen}$	Fe:Ca	-0.06	0.703
$\delta^{13}C_{collagen}$	As:Ca	-0.72	< 0.001 **
$\delta^{13}C_{collagen}$	Cd:Ca	-0.42	0.005 **
$\delta^{13}C_{collagen}$	Pb:Ca	0.13	0.401
$\delta^{13}C_{collagen}$	Mg:Ca	-0.27	0.072
$\delta^{13}C_{collagen}$	Cr:Ca	-0.20	0.178
$\delta^{13}C_{collagen}$	Co:Ca	0.08	0.623
$\delta^{13}C_{collagen}$	Zn:Ca	-0.33	0.026 *
$\delta^{13}C_{collagen}$	Sr:Ca	0.12	0.440
$\delta^{13}C_{collagen}$	Ba:Ca	-0.13	0.379
$\delta^{15}N_{collagen}$	$\delta^{13}C_{CO3}$	-0.11	0.466
$\delta^{15}N_{collagen}$	$\delta^{18}O_{CO3}$	0.33	0.029 *
$\delta^{15}N_{collagen}$	$\Delta^{13}C_{carb\text{-}coll}$	0.38	0.011 *
$\delta^{15}N_{collagen}$	Hg	0.06	0.678
$\delta^{15}N_{collagen}$	$^{206}Pb/^{204}Pb$	0.12	0.434
$\delta^{15}N_{collagen}$	$^{208}Pb/^{206}Pb$	0.11	0.459
$\delta^{15}N_{collagen}$	$^{206}Pb/^{207}Pb$	0.14	0.356
$\delta^{15}N_{collagen}$	Mn:Ca	-0.32	0.032 *
$\delta^{15}N_{collagen}$	Fe:Ca	-0.38	0.009 **
$\delta^{15}N_{collagen}$	As:Ca	0.43	0.004 **
$\delta^{15}N_{collagen}$	Cd:Ca	0.43	0.003 **
$\delta^{15}N_{collagen}$	Pb:Ca	0.03	0.836
$\delta^{15}N_{collagen}$	Mg:Ca	0.34	0.022 *
$\delta^{15}N_{collagen}$	Cr:Ca	0.35	0.017 *

$\delta^{15}N_{collagen}$	Co:Ca	0.34	0.022 *
$\delta^{15}N_{collagen}$	Zn:Ca	-0.46	0.001 **
$\delta^{15}N_{collagen}$	Sr:Ca	-0.03	0.821
$\delta^{15}N_{collagen}$	Ba:Ca	0.41	0.005 **
$\delta^{13}C_{CO3}$	$\delta^{18}O_{CO3}$	-0.37	0.011 *
$\delta^{13}C_{CO3}$	$\Delta^{13}C_{carb\text{-}coll}$	0.63	< 0.001 **
$\delta^{13}C_{CO3}$	Hg	-0.33	0.028 *
$\delta^{13}C_{CO3}$	$^{206}Pb/^{204}Pb$	-0.51	< 0.001 **
$\delta^{13}C_{CO3}$	$^{208}Pb/^{206}Pb$	-0.15	0.325
$\delta^{13}C_{CO3}$	$^{206}Pb/^{207}Pb$	-0.53	< 0.001 **
$\delta^{13}C_{CO3}$	Mn:Ca	0.31	0.040 *
$\delta^{13}C_{CO3}$	Fe:Ca	-0.21	0.157
$\delta^{13}C_{CO3}$	As:Ca	-0.49	< 0.001 **
$\delta^{13}C_{CO3}$	Cd:Ca	0.02	0.903
$\delta^{13}C_{CO3}$	Pb:Ca	0.53	< 0.001 **
$\delta^{13}C_{CO3}$	Mg:Ca	0.17	0.271
$\delta^{13}C_{CO3}$	Cr:Ca	-0.15	0.338
$\delta^{13}C_{CO3}$	Co:Ca	0.05	0.728
$\delta^{13}C_{CO3}$	Zn:Ca	-0.52	< 0.001 **
$\delta^{13}C_{CO3}$	Sr:Ca	0.38	0.010 *
$\delta^{13}C_{CO3}$	Ba:Ca	0.19	0.210
$\delta^{18}O_{CO3}$	$\Delta^{13}C_{carb\text{-}coll}$	0.13	0.406
$\delta^{18}O_{CO3}$	Hg	0.14	0.373
$\delta^{18}O_{CO3}$	$^{206}Pb/^{204}Pb$	0.22	0.137
$\delta^{18}O_{CO3}$	$^{208}Pb/^{206}Pb$	0.29	0.050 *
$\delta^{18}O_{CO3}$	$^{206}Pb/^{207}Pb$	0.25	0.104
$\delta^{18}O_{CO3}$	Mn:Ca	-0.38	0.011 *
$\delta^{18}O_{CO3}$	Fe:Ca	-0.03	0.840
$\delta^{18}O_{CO3}$	As:Ca	0.54	< 0.001 **
$\delta^{18}O_{CO3}$	Cd:Ca	0.38	0.010 *
$\delta^{18}O_{CO3}$	Pb:Ca	-0.13	0.393
$\delta^{18}O_{CO3}$	Mg:Ca	0.18	0.241
$\delta^{18}O_{CO3}$	Cr:Ca	0.30	0.047 *
$\delta^{18}O_{CO3}$	Co:Ca	-0.04	0.813
$\delta^{18}O_{CO3}$	Zn:Ca	0.17	0.269
$\delta^{18}O_{CO3}$	Sr:Ca	-0.42	0.004 **
$\delta^{18}O_{CO3}$	Ba:Ca	-0.06	0.695
$\Delta^{13}C_{carb\text{-}coll}$	Hg	-0.19	0.221

$\Delta^{13}C_{carb\text{-}coll}$	$^{206}Pb/^{204}Pb$	-0.45	0.002 **
$\Delta^{13}C_{carb\text{-}coll}$	$^{208}Pb/^{206}Pb$	0.11	0.469
$\Delta^{13}C_{carb\text{-}coll}$	$^{206}Pb/^{207}Pb$	-0.43	0.003 **
$\Delta^{13}C_{carb\text{-}coll}$	Mn:Ca	-0.13	0.396
$\Delta^{13}C_{carb\text{-}coll}$	Fe:Ca	-0.40	0.007 **
$\Delta^{13}C_{carb\text{-}coll}$	As:Ca	0.13	0.407
$\Delta^{13}C_{carb\text{-}coll}$	Cd:Ca	0.55	< 0.001 **
$\Delta^{13}C_{carb\text{-}coll}$	Pb:Ca	0.61	< 0.001 **
$\Delta^{13}C_{carb\text{-}coll}$	Mg:Ca	0.59	< 0.001 **
$\Delta^{13}C_{carb\text{-}coll}$	Cr:Ca	0.04	0.772
$\Delta^{13}C_{carb\text{-}coll}$	Co:Ca	0.20	0.197
$\Delta^{13}C_{carb\text{-}coll}$	Zn:Ca	-0.51	< 0.001 **
$\Delta^{13}C_{carb\text{-}coll}$	Sr:Ca	0.36	0.016 *
$\Delta^{13}C_{carb\text{-}coll}$	Ba:Ca	0.48	< 0.001 **
Hg	$^{206}Pb/^{204}Pb$	0.27	0.076
Hg	$^{208}Pb/^{206}Pb$	0.10	0.499
Hg	$^{206}Pb/^{207}Pb$	0.27	0.076
Hg	Mn:Ca	-0.44	0.002 **
Hg	Fe:Ca	0.05	0.733
Hg	As:Ca	0.20	0.195
Hg	Cd:Ca	-0.15	0.311
Hg	Pb:Ca	-0.43	0.003 **
Hg	Mg:Ca	-0.31	0.039 *
Hg	Cr:Ca	-0.15	0.338
Hg	Co:Ca	-0.06	0.685
Hg	Zn:Ca	0.09	0.565
Hg	Sr:Ca	-0.21	0.160
Hg	Ba:Ca	-0.20	0.178
$^{206}Pb/^{204}Pb$	$^{208}Pb/^{206}Pb$	-0.28	0.065
$^{206}Pb/^{204}Pb$	$^{206}Pb/^{207}Pb$	1.00	< 0.001 **
$^{206}Pb/^{204}Pb$	Mn:Ca	-0.06	0.719
$^{206}Pb/^{204}Pb$	Fe:Ca	0.07	0.630
$^{206}Pb/^{204}Pb$	As:Ca	0.06	0.690
$^{206}Pb/^{204}Pb$	Cd:Ca	-0.11	0.483
$^{206}Pb/^{204}Pb$	Pb:Ca	-0.47	0.001 **
$^{206}Pb/^{204}Pb$	Mg:Ca	-0.32	0.034 *
$^{206}Pb/^{204}Pb$	Cr:Ca	0.04	0.776
$^{206}Pb/^{204}Pb$	Co:Ca	-0.07	0.654

$^{206}Pb/^{204}Pb$	Zn:Ca	0.33	0.027 *
$^{206}Pb/^{204}Pb$	Sr:Ca	-0.45	0.002 **
$^{206}Pb/^{204}Pb$	Ba:Ca	-0.28	0.062
$^{208}Pb/^{206}Pb$	$^{206}Pb/^{207}Pb$	-0.24	0.106
$^{208}Pb/^{206}Pb$	Mn:Ca	-0.34	0.022 *
$^{208}Pb/^{206}Pb$	Fe:Ca	-0.33	0.025 *
$^{208}Pb/^{206}Pb$	As:Ca	0.26	0.091
$^{208}Pb/^{206}Pb$	Cd:Ca	0.26	0.090
$^{208}Pb/^{206}Pb$	Pb:Ca	-0.16	0.287
$^{208}Pb/^{206}Pb$	Mg:Ca	0.05	0.754
$^{208}Pb/^{206}Pb$	Cr:Ca	0.20	0.180
$^{208}Pb/^{206}Pb$	Co:Ca	0.33	0.027 *
$^{208}Pb/^{206}Pb$	Zn:Ca	-0.18	0.238
$^{208}Pb/^{206}Pb$	Sr:Ca	-0.31	0.040 *
$^{208}Pb/^{206}Pb$	Ba:Ca	0.03	0.846
$^{206}Pb/^{207}Pb$	Mn:Ca	-0.09	0.552
$^{206}Pb/^{207}Pb$	Fe:Ca	0.03	0.846
$^{206}Pb/^{207}Pb$	As:Ca	0.10	0.512
$^{206}Pb/^{207}Pb$	Cd:Ca	-0.07	0.653
$^{206}Pb/^{207}Pb$	Pb:Ca	-0.47	0.001 **
$^{206}Pb/^{207}Pb$	Mg:Ca	-0.28	0.061
$^{206}Pb/^{207}Pb$	Cr:Ca	0.04	0.817
$^{206}Pb/^{207}Pb$	Co:Ca	-0.04	0.786
$^{206}Pb/^{207}Pb$	Zn:Ca	0.32	0.035 *
$^{206}Pb/^{207}Pb$	Sr:Ca	-0.44	0.003 **
$^{206}Pb/^{207}Pb$	Ba:Ca	-0.24	0.105
Mn:Ca	Fe:Ca	0.52	< 0.001 **
Mn:Ca	As:Ca	-0.46	0.002 **
Mn:Ca	Cd:Ca	-0.31	0.040 *
Mn:Ca	Pb:Ca	0.20	0.190
Mn:Ca	Mg:Ca	-0.03	0.824
Mn:Ca	Cr:Ca	0.04	0.772
Mn:Ca	Co:Ca	-0.05	0.766
Mn:Ca	Zn:Ca	0.05	0.766
Mn:Ca	Sr:Ca	0.23	0.129
Mn:Ca	Ba:Ca	0.02	0.901
Fe:Ca	As:Ca	-0.16	0.298
Fe:Ca	Cd:Ca	-0.37	0.013 *

Fe:Ca	Pb:Ca	-0.10	0.509
Fe:Ca	Mg:Ca	-0.33	0.029 *
Fe:Ca	Cr:Ca	-0.08	0.608
Fe:Ca	Co:Ca	-0.40	0.007 **
Fe:Ca	Zn:Ca	0.49	< 0.001 **
Fe:Ca	Sr:Ca	-0.04	0.817
Fe:Ca	Ba:Ca	-0.30	0.044 *
As:Ca	Cd:Ca	0.46	0.002 **
As:Ca	Pb:Ca	0.05	0.724
As:Ca	Mg:Ca	0.54	< 0.001 **
As:Ca	Cr:Ca	0.44	0.003 **
As:Ca	Co:Ca	0.19	0.207
As:Ca	Zn:Ca	0.21	0.173
As:Ca	Sr:Ca	-0.01	0.970
As:Ca	Ba:Ca	0.40	0.007 **
Cd:Ca	Pb:Ca	0.46	0.002 **
Cd:Ca	Mg:Ca	0.61	< 0.001 **
Cd:Ca	Cr:Ca	0.25	0.103
Cd:Ca	Co:Ca	0.18	0.233
Cd:Ca	Zn:Ca	-0.16	0.283
Cd:Ca	Sr:Ca	0.22	0.151
Cd:Ca	Ba:Ca	0.49	< 0.001 **
Pb:Ca	Mg:Ca	0.68	< 0.001 **
Pb:Ca	Cr:Ca	0.07	0.630
Pb:Ca	Co:Ca	-0.05	0.749
Pb:Ca	Zn:Ca	-0.15	0.337
Pb:Ca	Sr:Ca	0.58	< 0.001 **
Pb:Ca	Ba:Ca	0.51	< 0.001 **
Mg:Ca	Cr:Ca	0.31	0.036 *
Mg:Ca	Co:Ca	0.24	0.120
Mg:Ca	Zn:Ca	-0.04	0.789
Mg:Ca	Sr:Ca	0.46	0.002 **
Mg:Ca	Ba:Ca	0.71	< 0.001 **
Cr:Ca	Co:Ca	0.38	0.010 **
Cr:Ca	Zn:Ca	-0.01	0.963
Cr:Ca	Sr:Ca	-0.06	0.689
Cr:Ca	Ba:Ca	0.25	0.094
Co:Ca	Zn:Ca	-0.31	0.040 *

Co:Ca	Sr:Ca	-0.06	0.697
Co:Ca	Ba:Ca	0.42	0.004 **
Zn:Ca	Sr:Ca	-0.16	0.308
Zn:Ca	Ba:Ca	-0.28	0.065
Sr:Ca	Ba:Ca	0.52	< 0.001 **

Table 5. Spearman correlation coefficients (ρ) and associated *p*-values for isotopic and elemental variables in annual growth layers of Baffin Bay Tusk (Tusk 1). Statistically significant correlations are indicated by * for *p*-value ≤ 0.05 and ** for *p*-value ≤ 0.01.

Variable 1	Variable 2	rho (ρ)	*p*-value
$\delta^{13}C_{collagen}$	$\delta^{15}N_{collagen}$	-0.04	0.867
$\delta^{13}C_{collagen}$	$\delta^{13}C_{CO3}$	0.49	0.019 *
$\delta^{13}C_{collagen}$	$\delta^{18}O_{CO3}$	0.03	0.900
$\delta^{13}C_{collagen}$	$\Delta^{13}C_{carb\text{-}coll}$	0.20	0.368
$\delta^{13}C_{collagen}$	Hg	-0.05	0.833
$\delta^{13}C_{collagen}$	$^{206}Pb/^{204}Pb$	-0.13	0.561
$\delta^{13}C_{collagen}$	$^{208}Pb/^{206}Pb$	0.38	0.071
$\delta^{13}C_{collagen}$	$^{206}Pb/^{207}Pb$	-0.10	0.656
$\delta^{13}C_{collagen}$	Mn:Ca	-0.56	0.007 **
$\delta^{13}C_{collagen}$	Fe:Ca	-0.59	0.003 **
$\delta^{13}C_{collagen}$	As:Ca	-0.28	0.194
$\delta^{13}C_{collagen}$	Cd:Ca	0.07	0.757
$\delta^{13}C_{collagen}$	Pb:Ca	-0.18	0.412
$\delta^{13}C_{collagen}$	Mg:Ca	-0.15	0.498
$\delta^{13}C_{collagen}$	Cr:Ca	-0.16	0.478
$\delta^{13}C_{collagen}$	Co:Ca	0.50	0.017 *
$\delta^{13}C_{collagen}$	Zn:Ca	-0.32	0.135
$\delta^{13}C_{collagen}$	Sr:Ca	-0.40	0.063
$\delta^{13}C_{collagen}$	Ba:Ca	-0.09	0.672
$\delta^{15}N_{collagen}$	$\delta^{13}C_{CO3}$	0.56	0.005 **
$\delta^{15}N_{collagen}$	$\delta^{18}O_{CO3}$	-0.00	0.987
$\delta^{15}N_{collagen}$	$\Delta^{13}C_{carb\text{-}coll}$	0.64	0.001 **
$\delta^{15}N_{collagen}$	Hg	-0.11	0.620
$\delta^{15}N_{collagen}$	$^{206}Pb/^{204}Pb$	-0.28	0.199
$\delta^{15}N_{collagen}$	$^{208}Pb/^{206}Pb$	-0.22	0.323
$\delta^{15}N_{collagen}$	$^{206}Pb/^{207}Pb$	-0.28	0.189
$\delta^{15}N_{collagen}$	Mn:Ca	-0.30	0.159
$\delta^{15}N_{collagen}$	Fe:Ca	-0.35	0.102
$\delta^{15}N_{collagen}$	As:Ca	0.22	0.305
$\delta^{15}N_{collagen}$	Cd:Ca	0.48	0.021 *
$\delta^{15}N_{collagen}$	Pb:Ca	0.47	0.023 *
$\delta^{15}N_{collagen}$	Mg:Ca	0.58	0.004 **
$\delta^{15}N_{collagen}$	Cr:Ca	0.35	0.099

$\delta^{15}N_{collagen}$	Co:Ca	0.29	0.177
$\delta^{15}N_{collagen}$	Zn:Ca	-0.64	0.001 **
$\delta^{15}N_{collagen}$	Sr:Ca	0.53	0.009 **
$\delta^{15}N_{collagen}$	Ba:Ca	0.58	0.004 **
$\delta^{13}C_{CO3}$	$\delta^{18}O_{CO3}$	0.25	0.255
$\delta^{13}C_{CO3}$	$\Delta^{13}C_{carb\text{-}coll}$	0.92	< 0.001 **
$\delta^{13}C_{CO3}$	Hg	-0.41	0.052
$\delta^{13}C_{CO3}$	$^{206}Pb/^{204}Pb$	-0.60	0.003 **
$\delta^{13}C_{CO3}$	$^{208}Pb/^{206}Pb$	0.21	0.329
$\delta^{13}C_{CO3}$	$^{206}Pb/^{207}Pb$	-0.58	0.004 **
$\delta^{13}C_{CO3}$	Mn:Ca	-0.60	0.003 **
$\delta^{13}C_{CO3}$	Fe:Ca	-0.65	0.001 **
$\delta^{13}C_{CO3}$	As:Ca	-0.07	0.764
$\delta^{13}C_{CO3}$	Cd:Ca	0.57	0.006 **
$\delta^{13}C_{CO3}$	Pb:Ca	0.46	0.029 *
$\delta^{13}C_{CO3}$	Mg:Ca	0.52	0.013 *
$\delta^{13}C_{CO3}$	Cr:Ca	-0.09	0.696
$\delta^{13}C_{CO3}$	Co:Ca	0.33	0.122
$\delta^{13}C_{CO3}$	Zn:Ca	-0.70	< 0.001 **
$\delta^{13}C_{CO3}$	Sr:Ca	0.16	0.453
$\delta^{13}C_{CO3}$	Ba:Ca	0.40	0.061
$\delta^{18}O_{CO3}$	$\Delta^{13}C_{carb\text{-}coll}$	0.19	0.392
$\delta^{18}O_{CO3}$	Hg	-0.37	0.085
$\delta^{18}O_{CO3}$	$^{206}Pb/^{204}Pb$	-0.08	0.727
$\delta^{18}O_{CO3}$	$^{208}Pb/^{206}Pb$	-0.08	0.730
$\delta^{18}O_{CO3}$	$^{206}Pb/^{207}Pb$	-0.10	0.637
$\delta^{18}O_{CO3}$	Mn:Ca	0.09	0.668
$\delta^{18}O_{CO3}$	Fe:Ca	0.12	0.599
$\delta^{18}O_{CO3}$	As:Ca	-0.37	0.084
$\delta^{18}O_{CO3}$	Cd:Ca	0.18	0.413
$\delta^{18}O_{CO3}$	Pb:Ca	0.05	0.816
$\delta^{18}O_{CO3}$	Mg:Ca	0.04	0.854
$\delta^{18}O_{CO3}$	Cr:Ca	0.01	0.977
$\delta^{18}O_{CO3}$	Co:Ca	0.15	0.498
$\delta^{18}O_{CO3}$	Zn:Ca	-0.01	0.963
$\delta^{18}O_{CO3}$	Sr:Ca	-0.29	0.187
$\delta^{18}O_{CO3}$	Ba:Ca	-0.22	0.312
$\Delta^{13}C_{carb\text{-}coll}$	Hg	-0.44	0.038 *

$\Delta^{13}C_{carb\text{-}coll}$	$^{206}Pb/^{204}Pb$	-0.62	0.001 **
$\Delta^{13}C_{carb\text{-}coll}$	$^{208}Pb/^{206}Pb$	0.17	0.446
$\Delta^{13}C_{carb\text{-}coll}$	$^{206}Pb/^{207}Pb$	-0.60	0.002 **
$\Delta^{13}C_{carb\text{-}coll}$	Mn:Ca	-0.41	0.050 *
$\Delta^{13}C_{carb\text{-}coll}$	Fe:Ca	-0.44	0.035 *
$\Delta^{13}C_{carb\text{-}coll}$	As:Ca	-0.01	0.952
$\Delta^{13}C_{carb\text{-}coll}$	Cd:Ca	0.58	0.004 **
$\Delta^{13}C_{carb\text{-}coll}$	Pb:Ca	0.58	0.004 **
$\Delta^{13}C_{carb\text{-}coll}$	Mg:Ca	0.61	0.002 **
$\Delta^{13}C_{carb\text{-}coll}$	Cr:Ca	-0.06	0.779
$\Delta^{13}C_{carb\text{-}coll}$	Co:Ca	0.23	0.289
$\Delta^{13}C_{carb\text{-}coll}$	Zn:Ca	-0.69	< 0.001 **
$\Delta^{13}C_{carb\text{-}coll}$	Sr:Ca	0.33	0.126
$\Delta^{13}C_{carb\text{-}coll}$	Ba:Ca	0.48	0.019 *
Hg	$^{206}Pb/^{204}Pb$	0.35	0.101
Hg	$^{208}Pb/^{206}Pb$	0.06	0.773
Hg	$^{206}Pb/^{207}Pb$	0.37	0.083
Hg	Mn:Ca	-0.09	0.698
Hg	Fe:Ca	-0.02	0.941
Hg	As:Ca	0.17	0.445
Hg	Cd:Ca	-0.60	0.002 **
Hg	Pb:Ca	-0.63	0.001 **
Hg	Mg:Ca	-0.51	0.013 *
Hg	Cr:Ca	-0.23	0.295
Hg	Co:Ca	0.09	0.667
Hg	Zn:Ca	-0.10	0.665
Hg	Sr:Ca	-0.07	0.745
Hg	Ba:Ca	-0.06	0.790
$^{206}Pb/^{204}Pb$	$^{208}Pb/^{206}Pb$	-0.36	0.090
$^{206}Pb/^{204}Pb$	$^{206}Pb/^{207}Pb$	1.00	< 0.001 **
$^{206}Pb/^{204}Pb$	Mn:Ca	0.19	0.379
$^{206}Pb/^{204}Pb$	Fe:Ca	0.25	0.241
$^{206}Pb/^{204}Pb$	As:Ca	-0.25	0.251
$^{206}Pb/^{204}Pb$	Cd:Ca	-0.57	0.005 **
$^{206}Pb/^{204}Pb$	Pb:Ca	-0.45	0.034 *
$^{206}Pb/^{204}Pb$	Mg:Ca	-0.65	0.001 **
$^{206}Pb/^{204}Pb$	Cr:Ca	0.05	0.834
$^{206}Pb/^{204}Pb$	Co:Ca	-0.03	0.883

$^{206}Pb/^{204}Pb$	Zn:Ca	0.46	0.029 *
$^{206}Pb/^{204}Pb$	Sr:Ca	-0.44	0.038 *
$^{206}Pb/^{204}Pb$	Ba:Ca	-0.58	0.004 **
$^{208}Pb/^{206}Pb$	$^{206}Pb/^{207}Pb$	-0.31	0.154
$^{208}Pb/^{206}Pb$	Mn:Ca	-0.20	0.348
$^{208}Pb/^{206}Pb$	Fe:Ca	-0.30	0.159
$^{208}Pb/^{206}Pb$	As:Ca	-0.13	0.548
$^{208}Pb/^{206}Pb$	Cd:Ca	0.18	0.402
$^{208}Pb/^{206}Pb$	Pb:Ca	-0.17	0.426
$^{208}Pb/^{206}Pb$	Mg:Ca	-0.05	0.806
$^{208}Pb/^{206}Pb$	Cr:Ca	-0.09	0.666
$^{208}Pb/^{206}Pb$	Co:Ca	0.39	0.065
$^{208}Pb/^{206}Pb$	Zn:Ca	-0.41	0.051
$^{208}Pb/^{206}Pb$	Sr:Ca	-0.22	0.306
$^{208}Pb/^{206}Pb$	Ba:Ca	0.13	0.555
$^{206}Pb/^{207}Pb$	Mn:Ca	0.16	0.461
$^{206}Pb/^{207}Pb$	Fe:Ca	0.22	0.313
$^{206}Pb/^{207}Pb$	As:Ca	-0.26	0.232
$^{206}Pb/^{207}Pb$	Cd:Ca	-0.56	0.007 **
$^{206}Pb/^{207}Pb$	Pb:Ca	-0.48	0.021 *
$^{206}Pb/^{207}Pb$	Mg:Ca	-0.68	< 0.001 **
$^{206}Pb/^{207}Pb$	Cr:Ca	0.04	0.851
$^{206}Pb/^{207}Pb$	Co:Ca	0.00	0.984
$^{206}Pb/^{207}Pb$	Zn:Ca	0.41	0.052
$^{206}Pb/^{207}Pb$	Sr:Ca	-0.46	0.029 *
$^{206}Pb/^{207}Pb$	Ba:Ca	-0.57	0.005 **
Mn:Ca	Fe:Ca	0.90	< 0.001 **
Mn:Ca	As:Ca	0.11	0.630
Mn:Ca	Cd:Ca	-0.08	0.706
Mn:Ca	Pb:Ca	-0.01	0.966
Mn:Ca	Mg:Ca	-0.03	0.905
Mn:Ca	Cr:Ca	0.27	0.206
Mn:Ca	Co:Ca	-0.35	0.102
Mn:Ca	Zn:Ca	0.66	< 0.001 **
Mn:Ca	Sr:Ca	-0.11	0.630
Mn:Ca	Ba:Ca	-0.17	0.447
Fe:Ca	As:Ca	0.01	0.959
Fe:Ca	Cd:Ca	-0.28	0.191

Fe:Ca	Pb:Ca	-0.10	0.663
Fe:Ca	Mg:Ca	-0.18	0.420
Fe:Ca	Cr:Ca	0.14	0.513
Fe:Ca	Co:Ca	-0.43	0.042 *
Fe:Ca	Zn:Ca	0.70	< 0.001 **
Fe:Ca	Sr:Ca	-0.06	0.781
Fe:Ca	Ba:Ca	-0.20	0.357
As:Ca	Cd:Ca	0.13	0.552
As:Ca	Pb:Ca	0.26	0.227
As:Ca	Mg:Ca	0.40	0.057
As:Ca	Cr:Ca	0.05	0.830
As:Ca	Co:Ca	-0.09	0.679
As:Ca	Zn:Ca	0.03	0.883
As:Ca	Sr:Ca	0.45	0.031 *
As:Ca	Ba:Ca	0.49	0.019 *
Cd:Ca	Pb:Ca	0.60	0.003 **
Cd:Ca	Mg:Ca	0.61	0.002 **
Cd:Ca	Cr:Ca	0.40	0.059
Cd:Ca	Co:Ca	0.09	0.682
Cd:Ca	Zn:Ca	-0.39	0.066
Cd:Ca	Sr:Ca	0.34	0.107
Cd:Ca	Ba:Ca	0.41	0.054
Pb:Ca	Mg:Ca	0.80	< 0.001 **
Pb:Ca	Cr:Ca	0.16	0.456
Pb:Ca	Co:Ca	-0.27	0.214
Pb:Ca	Zn:Ca	-0.13	0.552
Pb:Ca	Sr:Ca	0.43	0.043 *
Pb:Ca	Ba:Ca	0.40	0.062
Mg:Ca	Cr:Ca	0.16	0.472
Mg:Ca	Co:Ca	-0.04	0.866
Mg:Ca	Zn:Ca	-0.23	0.281
Mg:Ca	Sr:Ca	0.57	0.005 **
Mg:Ca	Ba:Ca	0.48	0.023 *
Cr:Ca	Co:Ca	0.26	0.228
Cr:Ca	Zn:Ca	-0.07	0.747
Cr:Ca	Sr:Ca	0.18	0.397
Cr:Ca	Ba:Ca	0.20	0.352
Co:Ca	Zn:Ca	-0.54	0.009 **

Co:Ca	Sr:Ca	-0.25	0.257
Co:Ca	Ba:Ca	0.10	0.633
Zn:Ca	Sr:Ca	-0.21	0.343
Zn:Ca	Ba:Ca	-0.53	0.010 *
Sr:Ca	Ba:Ca	0.61	0.002 **

Table 6. Spearman correlation coefficients (ρ) and associated *p*-values for isotopic and elemental variables in annual growth layers of Hudson Bay Tusk (Tusk 2). Statistically significant correlations are indicated by * for *p*-value ≤ 0.05 and ** for *p*-value ≤ 0.01.

Variable 1	Variable 2	rho (ρ)	*p*-value
$\delta^{13}C_{collagen}$	$\delta^{15}N_{collagen}$	0.34	0.120
$\delta^{13}C_{collagen}$	$\delta^{13}C_{CO3}$	0.63	0.002 **
$\delta^{13}C_{collagen}$	$\delta^{18}O_{CO3}$	0.16	0.479
$\delta^{13}C_{collagen}$	$\Delta^{13}C_{carb\text{-}coll}$	0.25	0.263
$\delta^{13}C_{collagen}$	Hg	0.18	0.412
$\delta^{13}C_{collagen}$	$^{206}Pb/^{204}Pb$	0.09	0.705
$\delta^{13}C_{collagen}$	$^{208}Pb/^{206}Pb$	0.09	0.683
$\delta^{13}C_{collagen}$	$^{206}Pb/^{207}Pb$	0.07	0.755
$\delta^{13}C_{collagen}$	Mn:Ca	0.04	0.868
$\delta^{13}C_{collagen}$	Fe:Ca	-0.05	0.809
$\delta^{13}C_{collagen}$	As:Ca	0.29	0.190
$\delta^{13}C_{collagen}$	Cd:Ca	0.02	0.920
$\delta^{13}C_{collagen}$	Pb:Ca	0.22	0.319
$\delta^{13}C_{collagen}$	Mg:Ca	0.12	0.603
$\delta^{13}C_{collagen}$	Cr:Ca	0.38	0.084
$\delta^{13}C_{collagen}$	Co:Ca	0.03	0.888
$\delta^{13}C_{collagen}$	Zn:Ca	-0.41	0.057
$\delta^{13}C_{collagen}$	Sr:Ca	-0.30	0.175
$\delta^{13}C_{collagen}$	Ba:Ca	0.08	0.724
$\delta^{15}N_{collagen}$	$\delta^{13}C_{CO3}$	0.16	0.468
$\delta^{15}N_{collagen}$	$\delta^{18}O_{CO3}$	-0.31	0.158
$\delta^{15}N_{collagen}$	$\Delta^{13}C_{carb\text{-}coll}$	0.16	0.483
$\delta^{15}N_{collagen}$	Hg	-0.11	0.636
$\delta^{15}N_{collagen}$	$^{206}Pb/^{204}Pb$	0.44	0.042 *
$\delta^{15}N_{collagen}$	$^{208}Pb/^{206}Pb$	-0.07	0.770
$\delta^{15}N_{collagen}$	$^{206}Pb/^{207}Pb$	0.45	0.036 *
$\delta^{15}N_{collagen}$	Mn:Ca	0.20	0.364
$\delta^{15}N_{collagen}$	Fe:Ca	-0.41	0.060
$\delta^{15}N_{collagen}$	As:Ca	0.04	0.873
$\delta^{15}N_{collagen}$	Cd:Ca	0.05	0.813
$\delta^{15}N_{collagen}$	Pb:Ca	-0.12	0.590
$\delta^{15}N_{collagen}$	Mg:Ca	-0.04	0.850
$\delta^{15}N_{collagen}$	Cr:Ca	0.16	0.473

$\delta^{15}N_{collagen}$	Co:Ca	0.34	0.122
$\delta^{15}N_{collagen}$	Zn:Ca	-0.78	< 0.001 **
$\delta^{15}N_{collagen}$	Sr:Ca	-0.14	0.544
$\delta^{15}N_{collagen}$	Ba:Ca	0.26	0.241
$\delta^{13}C_{CO3}$	$\delta^{18}O_{CO3}$	0.20	0.381
$\delta^{13}C_{CO3}$	$\Delta^{13}C_{carb\text{-}coll}$	0.89	< 0.001 **
$\delta^{13}C_{CO3}$	Hg	0.17	0.445
$\delta^{13}C_{CO3}$	$^{206}Pb/^{204}Pb$	-0.05	0.821
$\delta^{13}C_{CO3}$	$^{208}Pb/^{206}Pb$	-0.20	0.378
$\delta^{13}C_{CO3}$	$^{206}Pb/^{207}Pb$	-0.02	0.920
$\delta^{13}C_{CO3}$	Mn:Ca	0.18	0.412
$\delta^{13}C_{CO3}$	Fe:Ca	-0.25	0.252
$\delta^{13}C_{CO3}$	As:Ca	0.48	0.026 *
$\delta^{13}C_{CO3}$	Cd:Ca	0.53	0.012 *
$\delta^{13}C_{CO3}$	Pb:Ca	0.69	< 0.001 **
$\delta^{13}C_{CO3}$	Mg:Ca	0.61	0.003 **
$\delta^{13}C_{CO3}$	Cr:Ca	0.18	0.427
$\delta^{13}C_{CO3}$	Co:Ca	0.03	0.884
$\delta^{13}C_{CO3}$	Zn:Ca	-0.29	0.192
$\delta^{13}C_{CO3}$	Sr:Ca	0.23	0.295
$\delta^{13}C_{CO3}$	Ba:Ca	0.41	0.058
$\delta^{18}O_{CO3}$	$\Delta^{13}C_{carb\text{-}coll}$	0.10	0.665
$\delta^{18}O_{CO3}$	Hg	0.06	0.791
$\delta^{18}O_{CO3}$	$^{206}Pb/^{204}Pb$	-0.03	0.893
$\delta^{18}O_{CO3}$	$^{208}Pb/^{206}Pb$	0.24	0.288
$\delta^{18}O_{CO3}$	$^{206}Pb/^{207}Pb$	-0.04	0.867
$\delta^{18}O_{CO3}$	Mn:Ca	0.05	0.814
$\delta^{18}O_{CO3}$	Fe:Ca	0.06	0.807
$\delta^{18}O_{CO3}$	As:Ca	0.13	0.570
$\delta^{18}O_{CO3}$	Cd:Ca	0.15	0.508
$\delta^{18}O_{CO3}$	Pb:Ca	0.02	0.944
$\delta^{18}O_{CO3}$	Mg:Ca	0.04	0.863
$\delta^{18}O_{CO3}$	Cr:Ca	0.20	0.382
$\delta^{18}O_{CO3}$	Co:Ca	-0.31	0.159
$\delta^{18}O_{CO3}$	Zn:Ca	0.03	0.881
$\delta^{18}O_{CO3}$	Sr:Ca	-0.24	0.274
$\delta^{18}O_{CO3}$	Ba:Ca	-0.36	0.100
$\Delta^{13}C_{carb\text{-}coll}$	Hg	0.04	0.853

$\Delta^{13}C_{carb\text{-}coll}$	$^{206}Pb/^{204}Pb$	-0.02	0.934
$\Delta^{13}C_{carb\text{-}coll}$	$^{208}Pb/^{206}Pb$	-0.28	0.205
$\Delta^{13}C_{carb\text{-}coll}$	$^{206}Pb/^{207}Pb$	0.03	0.895
$\Delta^{13}C_{carb\text{-}coll}$	Mn:Ca	0.32	0.150
$\Delta^{13}C_{carb\text{-}coll}$	Fe:Ca	-0.33	0.140
$\Delta^{13}C_{carb\text{-}coll}$	As:Ca	0.49	0.019 *
$\Delta^{13}C_{carb\text{-}coll}$	Cd:Ca	0.66	< 0.001 **
$\Delta^{13}C_{carb\text{-}coll}$	Pb:Ca	0.68	< 0.001 **
$\Delta^{13}C_{carb\text{-}coll}$	Mg:Ca	0.69	< 0.001 **
$\Delta^{13}C_{carb\text{-}coll}$	Cr:Ca	0.02	0.946
$\Delta^{13}C_{carb\text{-}coll}$	Co:Ca	0.10	0.673
$\Delta^{13}C_{carb\text{-}coll}$	Zn:Ca	-0.25	0.255
$\Delta^{13}C_{carb\text{-}coll}$	Sr:Ca	0.46	0.030 *
$\Delta^{13}C_{carb\text{-}coll}$	Ba:Ca	0.52	0.013 *
Hg	$^{206}Pb/^{204}Pb$	-0.21	0.356
Hg	$^{208}Pb/^{206}Pb$	0.06	0.799
Hg	$^{206}Pb/^{207}Pb$	-0.25	0.272
Hg	Mn:Ca	-0.63	0.002 **
Hg	Fe:Ca	0.35	0.107
Hg	As:Ca	-0.14	0.521
Hg	Cd:Ca	-0.12	0.589
Hg	Pb:Ca	-0.24	0.284
Hg	Mg:Ca	-0.28	0.202
Hg	Cr:Ca	-0.22	0.326
Hg	Co:Ca	-0.26	0.246
Hg	Zn:Ca	0.13	0.563
Hg	Sr:Ca	-0.28	0.203
Hg	Ba:Ca	-0.40	0.068
$^{206}Pb/^{204}Pb$	$^{208}Pb/^{206}Pb$	-0.38	0.078
$^{206}Pb/^{204}Pb$	$^{206}Pb/^{207}Pb$	0.99	< 0.001 **
$^{206}Pb/^{204}Pb$	Mn:Ca	0.04	0.876
$^{206}Pb/^{204}Pb$	Fe:Ca	-0.13	0.572
$^{206}Pb/^{204}Pb$	As:Ca	-0.41	0.062
$^{206}Pb/^{204}Pb$	Cd:Ca	-0.11	0.625
$^{206}Pb/^{204}Pb$	Pb:Ca	-0.33	0.139
$^{206}Pb/^{204}Pb$	Mg:Ca	-0.34	0.121
$^{206}Pb/^{204}Pb$	Cr:Ca	-0.13	0.568
$^{206}Pb/^{204}Pb$	Co:Ca	-0.23	0.295

$^{206}Pb/^{204}Pb$	Zn:Ca	-0.28	0.213
$^{206}Pb/^{204}Pb$	Sr:Ca	-0.22	0.314
$^{206}Pb/^{204}Pb$	Ba:Ca	-0.16	0.466
$^{208}Pb/^{206}Pb$	$^{206}Pb/^{207}Pb$	-0.43	0.046 *
$^{208}Pb/^{206}Pb$	Mn:Ca	0.07	0.755
$^{208}Pb/^{206}Pb$	Fe:Ca	-0.04	0.848
$^{208}Pb/^{206}Pb$	As:Ca	0.04	0.856
$^{208}Pb/^{206}Pb$	Cd:Ca	0.01	0.980
$^{208}Pb/^{206}Pb$	Pb:Ca	-0.15	0.514
$^{208}Pb/^{206}Pb$	Mg:Ca	-0.12	0.607
$^{208}Pb/^{206}Pb$	Cr:Ca	0.29	0.189
$^{208}Pb/^{206}Pb$	Co:Ca	0.12	0.596
$^{208}Pb/^{206}Pb$	Zn:Ca	0.02	0.948
$^{208}Pb/^{206}Pb$	Sr:Ca	-0.36	0.103
$^{208}Pb/^{206}Pb$	Ba:Ca	-0.28	0.211
$^{206}Pb/^{207}Pb$	Mn:Ca	0.06	0.778
$^{206}Pb/^{207}Pb$	Fe:Ca	-0.19	0.406
$^{206}Pb/^{207}Pb$	As:Ca	-0.37	0.094
$^{206}Pb/^{207}Pb$	Cd:Ca	-0.06	0.774
$^{206}Pb/^{207}Pb$	Pb:Ca	-0.26	0.237
$^{206}Pb/^{207}Pb$	Mg:Ca	-0.27	0.217
$^{206}Pb/^{207}Pb$	Cr:Ca	-0.15	0.501
$^{206}Pb/^{207}Pb$	Co:Ca	-0.21	0.340
$^{206}Pb/^{207}Pb$	Zn:Ca	-0.28	0.200
$^{206}Pb/^{207}Pb$	Sr:Ca	-0.13	0.572
$^{206}Pb/^{207}Pb$	Ba:Ca	-0.08	0.728
Mn:Ca	Fe:Ca	-0.11	0.639
Mn:Ca	As:Ca	0.43	0.046 *
Mn:Ca	Cd:Ca	0.15	0.518
Mn:Ca	Pb:Ca	0.29	0.183
Mn:Ca	Mg:Ca	0.50	0.020 *
Mn:Ca	Cr:Ca	0.40	0.067
Mn:Ca	Co:Ca	0.36	0.099
Mn:Ca	Zn:Ca	-0.28	0.201
Mn:Ca	Sr:Ca	0.30	0.180
Mn:Ca	Ba:Ca	0.45	0.037 *
Fe:Ca	As:Ca	-0.13	0.568
Fe:Ca	Cd:Ca	-0.48	0.025 *

Fe:Ca	Pb:Ca	-0.39	0.075
Fe:Ca	Mg:Ca	-0.52	0.015 *
Fe:Ca	Cr:Ca	-0.07	0.766
Fe:Ca	Co:Ca	-0.16	0.489
Fe:Ca	Zn:Ca	0.38	0.085
Fe:Ca	Sr:Ca	-0.34	0.119
Fe:Ca	Ba:Ca	-0.42	0.051
As:Ca	Cd:Ca	0.21	0.340
As:Ca	Pb:Ca	0.44	0.041 *
As:Ca	Mg:Ca	0.62	0.002 **
As:Ca	Cr:Ca	0.50	0.019 *
As:Ca	Co:Ca	0.45	0.038 *
As:Ca	Zn:Ca	-0.21	0.356
As:Ca	Sr:Ca	0.41	0.061
As:Ca	Ba:Ca	0.40	0.065
Cd:Ca	Pb:Ca	0.60	0.004 **
Cd:Ca	Mg:Ca	0.43	0.045 *
Cd:Ca	Cr:Ca	-0.24	0.281
Cd:Ca	Co:Ca	0.14	0.544
Cd:Ca	Zn:Ca	-0.28	0.211
Cd:Ca	Sr:Ca	0.44	0.041 *
Cd:Ca	Ba:Ca	0.34	0.124
Pb:Ca	Mg:Ca	0.79	< 0.001 **
Pb:Ca	Cr:Ca	0.02	0.924
Pb:Ca	Co:Ca	0.17	0.448
Pb:Ca	Zn:Ca	-0.01	0.956
Pb:Ca	Sr:Ca	0.60	0.003 **
Pb:Ca	Ba:Ca	0.61	0.003 **
Mg:Ca	Cr:Ca	0.27	0.215
Mg:Ca	Co:Ca	0.28	0.205
Mg:Ca	Zn:Ca	-0.02	0.940
Mg:Ca	Sr:Ca	0.67	< 0.001 **
Mg:Ca	Ba:Ca	0.67	< 0.001 **
Cr:Ca	Co:Ca	0.46	0.033 *
Cr:Ca	Zn:Ca	-0.16	0.482
Cr:Ca	Sr:Ca	-0.19	0.395
Cr:Ca	Ba:Ca	0.12	0.596
Co:Ca	Zn:Ca	-0.26	0.235

Co:Ca	Sr:Ca	0.24	0.278
Co:Ca	Ba:Ca	0.56	0.007 **
Zn:Ca	Sr:Ca	0.17	0.448
Zn:Ca	Ba:Ca	-0.17	0.460
Sr:Ca	Ba:Ca	0.68	< 0.001 **

Table 7. Annual growth layer, year of deposition, calculated Suess effect correction (‰), measured $\delta^{13}C_{collagen}$ (‰), associated analytical uncertainty (±1 SD, ‰), and Suess effect-corrected $\delta^{13}C_{collagen}$ (‰) from the Baffin Bay narwhal tusk (Tusk 1).

Sample ID	Year	Suess Effect	$\delta^{13}C_{collagen}$	±1 SD	Corrected $\delta^{13}C_{collagen}$
BB-01	1997	-0.58	-16.22	0.08	-15.64
BB-02	1998	-0.60	-15.57	0.08	-14.97
BB-03	1999	-0.61	-15.69	0.08	-15.08
BB-04	2000	-0.63	-15.61	0.08	-14.98
BB-05	2001	-0.65	-15.53	0.08	-14.88
BB-06	2002	-0.67	-15.51	0.08	-14.84
BB-07	2003	-0.68	-15.76	0.08	-15.08
BB-08	2004	-0.70	-15.56	0.08	-14.86
BB-09	2005	-0.72	-15.48	0.08	-14.76
BB-10	2006	-0.74	-15.52	0.08	-14.78
BB-11	2007	-0.76	-15.58	0.08	-14.82
BB-12	2008	-0.78	-15.59	0.08	-14.81
BB-13	2009	-0.81	-15.41	0.08	-14.60
BB-14	2010	-0.83	-15.74	0.08	-14.91
BB-15	2011	-0.85	-15.80	0.08	-14.95
BB-16	2012	-0.87	-16.02	0.08	-15.15
BB-17	2013	-0.90	-15.98	0.08	-15.08
BB-18	2014	-0.92	-16.18	0.08	-15.26
BB-19	2015	-0.95	-16.04	0.08	-15.09
BB-20	2016	-0.97	-16.02	0.08	-15.05
BB-21	2017	-1.00	-15.89	0.08	-14.89
BB-22	2018	-1.03	-15.93	0.08	-14.90
BB-23	2019	-1.05	-15.95	0.08	-14.90
BB-24	2020	-1.08	-16.12	0.08	-15.04

Table 8. Annual growth layer, year of deposition, measured $\delta^{15}N_{collagen}$ (‰), and associated analytical uncertainty (±1 SD, ‰), from the Baffin Bay narwhal tusk (Tusk 1).

Sample ID	Year	$\delta^{15}N_{collagen}$	±1 SD
BB-01	1997	19.02	0.23
BB-02	1998	19.34	0.23
BB-03	1999	18.58	0.23
BB-04	2000	18.50	0.23
BB-05	2001	18.78	0.23
BB-06	2002	19.09	0.23
BB-07	2003	18.18	0.23
BB-08	2004	17.73	0.23
BB-09	2005	18.08	0.23
BB-10	2006	17.55	0.23
BB-11	2007	17.69	0.23
BB-12	2008	17.88	0.23
BB-13	2009	17.97	0.23
BB-14	2010	17.67	0.23
BB-15	2011	17.75	0.23
BB-16	2012	18.06	0.23
BB-17	2013	17.45	0.23
BB-18	2014	17.88	0.23
BB-19	2015	17.59	0.23
BB-20	2016	17.67	0.23
BB-21	2017	17.82	0.23
BB-22	2018	17.53	0.23
BB-23	2019	17.97	0.23
BB-24	2020	17.90	0.23

Table 9. Annual growth layer, year of deposition, calculated Suess effect correction (‰), measured $\delta^{13}C_{CO3}$ (‰), associated analytical uncertainty (±1 SD, ‰), and Suess effect-corrected $\delta^{13}C_{CO3}$ (‰) from the Baffin Bay narwhal tusk (Tusk 1).

Sample ID	Year	Suess Effect	$\delta^{13}C_{CO3}$	±1 SD	Corrected $\delta^{13}C_{CO3}$
BB-01	1997	-0.58	-13.30	0.09	-12.72
BB-02	1998	-0.60	-12.49	0.09	-11.89
BB-03	1999	-0.61	-12.66	0.09	-12.05
BB-04	2000	-0.63	-12.39	0.09	-11.76
BB-05	2001	-0.65	-12.99	0.09	-12.34
BB-06	2002	-0.67	-13.05	0.09	-12.38
BB-07	2003	-0.68	-13.03	0.09	-12.35
BB-08	2004	-0.70	-12.93	0.09	-12.23
BB-09	2005	-0.72	-12.87	0.09	-12.15
BB-10	2006	-0.74	-13.32	0.09	-12.58
BB-11	2007	-0.76	-13.48	0.09	-12.72
BB-12	2008	-0.78	-13.39	0.09	-12.61
BB-13	2009	-0.81	-13.38	0.09	-12.57
BB-14	2010	-0.83	-13.62	0.09	-12.79
BB-15	2011	-0.85	-13.88	0.09	-13.03
BB-16	2012	-0.87	-14.23	0.09	-13.36
BB-17	2013	-0.90	-14.45	0.09	-13.55
BB-18	2014	-0.92	-14.46	0.09	-13.54
BB-19	2015	-0.95	-14.51	0.09	-13.56
BB-20	2016	-0.97	-14.28	0.09	-13.31
BB-21	2017	-1.00	-14.20	0.09	-13.20
BB-22	2018	-1.03	-14.07	0.09	-13.04
BB-23	2019	-1.05	-14.19	0.09	-13.14
BB-24	2020	-1.08	-13.93	0.09	-12.85

Table 10. Annual growth layer, year of deposition, measured $\delta^{18}O_{CO3}$ (‰), associated analytical uncertainty (±1 SD, ‰), and $\delta^{18}O_{CO3}$ values converted from the VPDB to the VSMOW scale (‰) from the Baffin Bay narwhal tusk (Tusk 1).

Sample ID	Year	$\delta^{18}O_{CO3}$ (*VPDB*)	±1 SD	$\delta^{18}O_{CO3}$ (*VSMOW*)
BB-01	1997	-4.74	0.09	26.03
BB-02	1998	-4.07	0.09	26.72
BB-03	1999	-3.90	0.09	26.90
BB-04	2000	-4.47	0.09	26.31
BB-05	2001	-5.02	0.09	25.74
BB-06	2002	-4.94	0.09	25.83
BB-07	2003	-4.18	0.09	26.61
BB-08	2004	-3.85	0.09	26.95
BB-09	2005	-4.11	0.09	26.68
BB-10	2006	-4.59	0.09	26.19
BB-11	2007	-4.39	0.09	26.39
BB-12	2008	-5.64	0.09	25.11
BB-13	2009	-4.35	0.09	26.44
BB-14	2010	-4.11	0.09	26.68
BB-15	2011	-3.85	0.09	26.95
BB-16	2012	-4.07	0.09	26.72
BB-17	2013	-4.40	0.09	26.38
BB-18	2014	-4.83	0.09	25.94
BB-19	2015	-5.09	0.09	25.67
BB-20	2016	-4.88	0.09	25.89
BB-21	2017	-4.48	0.09	26.30
BB-22	2018	-4.50	0.09	26.28
BB-23	2019	-4.46	0.09	26.32
BB-24	2020	-4.57	0.09	26.21

Table 11. Annual growth layer, year of deposition, $\Delta^{13}C_{carb\text{-}coll}$ (‰), and associated analytical uncertainty (±1 SD, ‰) from the Baffin Bay narwhal tusk (Tusk 1).

Sample ID	Year	$\Delta^{13}C_{carb\text{-}coll}$	±1 SD
BB-01	1997	2.92	0.12
BB-02	1998	3.08	0.12
BB-03	1999	3.03	0.12
BB-04	2000	3.22	0.12
BB-05	2001	2.54	0.12
BB-06	2002	2.46	0.12
BB-07	2003	2.73	0.12
BB-08	2004	2.63	0.12
BB-09	2005	2.61	0.12
BB-10	2006	2.20	0.12
BB-11	2007	2.10	0.12
BB-12	2008	2.20	0.12
BB-13	2009	2.03	0.12
BB-14	2010	2.12	0.12
BB-15	2011	1.92	0.12
BB-16	2012	1.79	0.12
BB-17	2013	1.53	0.12
BB-18	2014	1.72	0.12
BB-19	2015	1.53	0.12
BB-20	2016	1.74	0.12
BB-21	2017	1.69	0.12
BB-22	2018	1.86	0.12
BB-23	2019	1.76	0.12
BB-24	2020	2.19	0.12

Table 12. Annual growth layer, year of deposition, Hg concentrations (μg/g), and associated analytical uncertainty (±1 SD, μg/g) from the Baffin Bay narwhal tusk (Tusk 1).

Sample ID	Year	[Hg]	±1 SD
BB-01	1997	5.00	1.35
BB-02	1998	-	-
BB-03	1999	3.93	1.35
BB-04	2000	3.33	1.35
BB-05	2001	8.75	1.35
BB-06	2002	7.22	1.35
BB-07	2003	7.50	1.35
BB-08	2004	5.76	1.35
BB-09	2005	5.44	1.35
BB-10	2006	4.71	1.35
BB-11	2007	7.14	1.35
BB-12	2008	5.46	1.35
BB-13	2009	5.19	1.35
BB-14	2010	7.08	1.35
BB-15	2011	6.14	1.35
BB-16	2012	5.00	1.35
BB-17	2013	4.29	1.35
BB-18	2014	30.00	1.35
BB-19	2015	7.30	1.35
BB-20	2016	9.39	1.35
BB-21	2017	9.50	1.35
BB-22	2018	8.49	1.35
BB-23	2019	15.39	1.35
BB-24	2020	22.86	1.35

Table 13. Annual growth layer, year of deposition, $^{206}Pb/^{204}Pb$, $^{208}Pb/^{206}Pb$, $^{206}Pb/^{207}Pb$, and associated analytical uncertainty (±1 SD) from the Baffin Bay narwhal tusk (Tusk 1).

Sample ID	Year	$^{206}Pb/^{204}Pb$	±1 SD	$^{208}Pb/^{206}Pb$	±1 SD	$^{206}Pb/^{207}Pb$	±1 SD
BB-01	1997	18.931	0.022	2.071	0.003	1.210	0.002
BB-02	1998	19.006	0.022	2.069	0.003	1.214	0.002
BB-03	1999	18.944	0.022	2.074	0.003	1.211	0.002
BB-04	2000	18.945	0.022	2.073	0.003	1.212	0.002
BB-05	2001	18.912	0.022	2.075	0.003	1.210	0.002
BB-06	2002	19.014	0.022	2.073	0.003	1.216	0.002
BB-07	2003	19.070	0.022	2.074	0.003	1.218	0.002
BB-08	2004	19.003	0.022	2.078	0.003	1.215	0.002
BB-09	2005	19.172	0.022	2.071	0.003	1.224	0.002
BB-10	2006	18.572	0.022	2.100	0.003	1.189	0.002
BB-11	2007	19.312	0.022	2.080	0.003	1.232	0.002
BB-12	2008	19.409	0.022	2.078	0.003	1.237	0.002
BB-13	2009	19.365	0.022	2.069	0.003	1.236	0.002
BB-14	2010	19.322	0.022	2.068	0.003	1.233	0.002
BB-15	2011	19.229	0.022	2.072	0.003	1.227	0.002
BB-16	2012	19.410	0.022	2.062	0.003	1.237	0.002
BB-17	2013	19.201	0.022	2.075	0.003	1.226	0.002
BB-18	2014	19.388	0.022	2.066	0.003	1.236	0.002
BB-19	2015	19.362	0.022	2.069	0.003	1.235	0.002
BB-20	2016	19.325	0.022	2.065	0.003	1.234	0.002
BB-21	2017	19.295	0.022	2.075	0.003	1.231	0.002
BB-22	2018	19.108	0.022	2.083	0.003	1.221	0.002
BB-23	2019	19.255	0.022	2.079	0.003	1.229	0.002
BB-24	2020	19.372	0.022	2.083	0.003	1.237	0.002

Table 14. Annual growth layer, year of deposition, major elements (Ca, Mg, Cr; ppm), and associated analytical uncertainty (±1 SD; ppm) from the Baffin Bay narwhal tusk (Tusk 1).

Sample ID	Year	Ca	±1 SD	Mg	±1 SD	Cr	±1 SD
BB-01	1997	211142.31	0.07	11779.713	0.002	9.491	0.004
BB-02	1998	205173.28	0.07	10683.226	0.002	4.270	0.004
BB-03	1999	204011.63	0.07	9603.811	0.002	4.873	0.004
BB-04	2000	207288.33	0.07	9899.034	0.002	2.458	0.004
BB-05	2001	212572.02	0.07	9926.552	0.002	2.875	0.004
BB-06	2002	202804.37	0.07	9181.500	0.002	2.416	0.004
BB-07	2003	196726.34	0.07	8524.570	0.002	1.407	0.004
BB-08	2004	207755.56	0.07	8746.424	0.002	0.873	0.004
BB-09	2005	209785.27	0.07	9006.555	0.002	2.860	0.004
BB-10	2006	205268.08	0.07	8727.958	0.002	2.068	0.004
BB-11	2007	181928.04	0.07	7716.968	0.002	3.031	0.004
BB-12	2008	204961.12	0.07	8259.859	0.002	1.915	0.004
BB-13	2009	205113.05	0.07	8229.325	0.002	3.865	0.004
BB-14	2010	211732.28	0.02	8274.473	0.03	-	-
BB-15	2011	203246.39	0.07	8190.690	0.002	2.416	0.004
BB-16	2012	216772.33	0.03	9250.140	0.004	3.880	0.001
BB-17	2013	218277.45	0.03	9293.556	0.004	2.975	0.001
BB-18	2014	222203.49	0.03	9374.814	0.004	1.320	0.001
BB-19	2015	220124.75	0.03	8629.658	0.004	4.799	0.001
BB-20	2016	222870.07	0.03	8969.348	0.004	1.792	0.001
BB-21	2017	194333.70	0.07	8155.327	0.002	3.267	0.004
BB-22	2018	212784.39	0.07	8769.417	0.002	1.245	0.004
BB-23	2019	213378.16	0.07	7520.158	0.002	3.509	0.004
BB-24	2020	214326.28	0.07	7505.036	0.002	3.271	0.004

Table 15. Annual growth layer, year of deposition, major elements (Ca, Co, Zn; ppm), and associated analytical uncertainty (±1 SD; ppm) from the Baffin Bay narwhal tusk (Tusk 1).

Sample ID	Year	Ca	±1 SD	Co	±1 SD	Zn	±1 SD
BB-01	1997	211142.31	0.07	2.315	0.004	89.306	0.005
BB-02	1998	205173.28	0.07	2.383	0.004	76.341	0.005
BB-03	1999	204011.63	0.07	1.981	0.004	87.128	0.005
BB-04	2000	207288.33	0.07	1.920	0.004	86.088	0.005
BB-05	2001	212572.02	0.07	1.646	0.004	83.825	0.005
BB-06	2002	202804.37	0.07	2.303	0.004	83.273	0.005
BB-07	2003	196726.34	0.07	2.619	0.004	80.198	0.005
BB-08	2004	207755.56	0.07	2.133	0.004	84.204	0.005
BB-09	2005	209785.27	0.07	2.474	0.004	93.466	0.005
BB-10	2006	205268.08	0.07	1.790	0.004	102.534	0.005
BB-11	2007	181928.04	0.07	2.819	0.004	83.930	0.005
BB-12	2008	204961.12	0.07	2.466	0.004	93.266	0.005
BB-13	2009	205113.05	0.07	2.686	0.004	90.496	0.005
BB-14	2010	211732.28	0.02	-	-	109.452	0.017
BB-15	2011	203246.39	0.07	2.141	0.004	98.812	0.005
BB-16	2012	216772.33	0.03	1.525	0.004	116.537	0.005
BB-17	2013	218277.45	0.03	1.741	0.004	119.454	0.005
BB-18	2014	222203.49	0.03	0.470	0.004	122.021	0.005
BB-19	2015	220124.75	0.03	1.396	0.004	113.893	0.005
BB-20	2016	222870.07	0.03	1.850	0.004	113.333	0.005
BB-21	2017	194333.70	0.07	2.343	0.004	90.149	0.005
BB-22	2018	212784.39	0.07	2.060	0.004	101.681	0.005
BB-23	2019	213378.16	0.07	2.951	0.004	88.095	0.005
BB-24	2020	214326.28	0.07	2.392	0.004	86.381	0.005

Table 16. Annual growth layer, year of deposition, major elements (Ca, Ba, Sr; ppm), and associated analytical uncertainty (±1 SD; ppm) from the Baffin Bay narwhal tusk (Tusk 1).

Sample ID	Year	Ca	±1 SD	Ba	±1 SD	Sr	±1 SD
BB-01	1997	211142.31	0.07	2.755	0.003	240.766	0.005
BB-02	1998	205173.28	0.07	2.314	0.003	211.341	0.005
BB-03	1999	204011.63	0.07	1.891	0.003	185.620	0.005
BB-04	2000	207288.33	0.07	1.867	0.003	190.320	0.005
BB-05	2001	212572.02	0.07	1.558	0.003	209.215	0.005
BB-06	2002	202804.37	0.07	1.382	0.003	190.852	0.005
BB-07	2003	196726.34	0.07	1.144	0.003	173.598	0.005
BB-08	2004	207755.56	0.07	1.271	0.003	162.048	0.005
BB-09	2005	209785.27	0.07	1.334	0.003	169.261	0.005
BB-10	2006	205268.08	0.07	1.319	0.003	177.283	0.005
BB-11	2007	181928.04	0.07	1.017	0.003	148.000	0.005
BB-12	2008	204961.12	0.07	0.978	0.003	160.505	0.005
BB-13	2009	205113.05	0.07	1.010	0.003	163.204	0.005
BB-14	2010	211732.28	0.02	0.879	0.066	184.616	0.068
BB-15	2011	203246.39	0.07	1.118	0.003	152.335	0.005
BB-16	2012	216772.33	0.03	1.188	0.007	189.848	0.005
BB-17	2013	218277.45	0.03	0.968	0.007	180.472	0.005
BB-18	2014	222203.49	0.03	1.399	0.007	184.578	0.005
BB-19	2015	220124.75	0.03	1.082	0.007	184.131	0.005
BB-20	2016	222870.07	0.03	1.587	0.007	195.750	0.005
BB-21	2017	194333.70	0.07	1.242	0.003	163.341	0.005
BB-22	2018	212784.39	0.07	1.263	0.003	173.068	0.005
BB-23	2019	213378.16	0.07	1.439	0.003	181.225	0.005
BB-24	2020	214326.28	0.07	1.402	0.003	175.466	0.005

Table 17. Annual growth layer, year of deposition, trace metals (Ca, Mn, Fe; ppb), and associated analytical uncertainty (±1 SD; ppb) from the Baffin Bay narwhal tusk (Tusk 1).

Sample ID	Year	Ca	±1 SD	Mn	±1 SD	Fe	±1 SD
BB-01	1997	72353561.15	3.71	1977.80	0.80	27717.43	1.68
BB-02	1998	33496395.54	3.71	577.89	0.80	2771.49	1.68
BB-03	1999	53047690.94	3.71	1171.08	0.80	8674.01	1.68
BB-04	2000	51129795.75	3.71	903.75	0.80	1028.85	1.68
BB-05	2001	52979776.76	3.71	868.44	0.80	829.49	1.68
BB-06	2002	57204752.86	3.71	770.95	0.80	1154.05	1.68
BB-07	2003	50689285.49	3.71	909.09	0.80	1984.02	1.68
BB-08	2004	43370770.76	3.71	705.69	0.80	1076.15	1.68
BB-09	2005	66704506.09	3.71	1241.78	0.80	2407.07	1.68
BB-10	2006	54005761.68	3.71	1276.36	0.80	7131.27	1.68
BB-11	2007	60087376.81	3.71	1011.83	0.80	1981.04	1.68
BB-12	2008	53565342.94	3.71	868.47	0.80	2187.46	1.68
BB-13	2009	52053675.86	3.71	854.02	0.80	1343.31	1.68
BB-14	2010	63730746.74	3.71	1173.45	0.80	10276.17	1.68
BB-15	2011	67986418.07	3.71	15160.46	0.80	155622.58	1.68
BB-16	2012	156903504.21	3.21	4758.34	0.32	88589.20	0.56
BB-17	2013	152318992.97	3.21	1380.00	0.32	7358.21	0.56
BB-18	2014	149784562.02	3.21	1685.11	0.32	17633.45	0.56
BB-19	2015	140863654.53	3.21	1429.25	0.32	11708.34	0.56
BB-20	2016	141614165.59	3.21	1225.64	0.32	7191.02	0.56
BB-21	2017	68679276.36	3.71	1122.16	0.80	4440.28	1.68
BB-22	2018	72992726.84	3.71	1320.26	0.80	11878.96	1.68
BB-23	2019	80472806.74	3.71	1074.99	0.80	3412.73	1.68
BB-24	2020	83928525.23	3.71	1238.11	0.80	4660.93	1.68

Table 18. Annual growth layer, year of deposition, trace metals (As, Cd, Pb; ppb), and associated analytical uncertainty (±1 SD; ppb) from the Baffin Bay narwhal tusk (Tusk 1).

Sample ID	Year	As	±1 SD	Cd	±1 SD	Pb	±1 SD
BB-01	1997	23.37	1.78	20.33	1.79	103.60	1.86
BB-02	1998	13.34	1.78	11.66	1.79	28.65	1.86
BB-03	1999	23.38	1.78	28.94	1.79	76.99	1.86
BB-04	2000	18.93	1.78	28.36	1.79	67.46	1.86
BB-05	2001	22.42	1.78	22.64	1.79	49.26	1.86
BB-06	2002	24.62	1.78	15.33	1.79	33.52	1.86
BB-07	2003	23.31	1.78	11.98	1.79	22.64	1.86
BB-08	2004	17.33	1.78	12.57	1.79	49.62	1.86
BB-09	2005	26.88	1.78	18.51	1.79	35.09	1.86
BB-10	2006	22.11	1.78	15.64	1.79	42.87	1.86
BB-11	2007	15.33	1.78	15.48	1.79	23.05	1.86
BB-12	2008	17.41	1.78	11.08	1.79	26.55	1.86
BB-13	2009	16.87	1.78	13.39	1.79	20.92	1.86
BB-14	2010	16.97	1.78	12.39	1.79	18.19	1.86
BB-15	2011	16.62	1.78	13.11	1.79	19.51	1.86
BB-16	2012	19.20	0.71	13.31	0.73	77.81	0.41
BB-17	2013	26.40	0.71	23.12	0.73	31.21	0.41
BB-18	2014	29.41	0.71	10.90	0.73	36.33	0.41
BB-19	2015	22.42	0.71	11.42	0.73	24.62	0.41
BB-20	2016	34.24	0.71	11.27	0.73	26.16	0.41
BB-21	2017	20.32	1.78	8.58	1.79	11.79	1.86
BB-22	2018	20.42	1.78	9.50	1.79	14.77	1.86
BB-23	2019	22.43	1.78	13.25	1.79	14.82	1.86
BB-24	2020	20.63	1.78	14.05	1.79	17.95	1.86

Table 19. Annual growth layer, year of deposition, calculated Suess effect correction (‰), measured $\delta^{13}C_{collagen}$ (‰), associated analytical uncertainty (±1 SD, ‰), and Suess effect-corrected $\delta^{13}C_{collagen}$ (‰) from the Hudson Bay narwhal tusk (Tusk 2).

Sample ID	Year	Suess Effect	$\delta^{13}C_{collagen}$	±1 SD	Corrected $\delta^{13}C_{collagen}$
HB-01	1998	-0.60	-15.03	0.08	-14.43
HB-02	1999	-0.61	-14.99	0.08	-14.38
HB-03	2000	-0.63	-14.38	0.08	-13.75
HB-04	2001	-0.65	-14.35	0.08	-13.70
HB-05	2002	-0.67	-14.72	0.08	-14.05
HB-06	2003	-0.68	-14.75	0.08	-14.07
HB-07	2004	-0.70	-14.37	0.08	-13.67
HB-08	2005	-0.72	-14.48	0.08	-13.76
HB-09	2006	-0.74	-14.35	0.08	-13.61
HB-10	2007	-0.76	-14.30	0.08	-13.54
HB-11	2008	-0.78	-14.48	0.08	-13.70
HB-12	2009	-0.81	-14.93	0.08	-14.12
HB-13	2010	-0.83	-15.15	0.08	-14.32
HB-14	2011	-0.85	-15.07	0.08	-14.22
HB-15	2012	-0.87	-14.93	0.08	-14.06
HB-16	2013	-0.90	-15.03	0.08	-14.13
HB-17	2014	-0.92	-15.29	0.08	-14.37
HB-18	2015	-0.95	-15.11	0.08	-14.16
HB-19	2016	-0.97	-15.24	0.08	-14.27
HB-20	2017	-1.00	-15.16	0.08	-14.16
HB-21	2018	-1.03	-15.11	0.08	-14.08
HB-22	2019	-1.05	-14.90	0.08	-13.85
HB-23	2020	-1.08	-15.14	0.08	-14.06
HB-24	2021	-1.11	-14.74	0.08	-13.63

Table 20. Annual growth layer, year of deposition, measured $\delta^{15}N_{collagen}$ (‰), and associated analytical uncertainty (±1 SD, ‰) from the Hudson Bay narwhal tusk (Tusk 2).

Sample ID	Year	$\delta^{15}N_{collagen}$	±1 SD
HB-01	1998	17.26	0.23
HB-02	1999	17.37	0.23
HB-03	2000	17.75	0.23
HB-04	2001	17.70	0.23
HB-05	2002	17.89	0.23
HB-06	2003	17.67	0.23
HB-07	2004	17.72	0.23
HB-08	2005	17.99	0.23
HB-09	2006	17.49	0.23
HB-10	2007	17.89	0.23
HB-11	2008	17.50	0.23
HB-12	2009	17.40	0.23
HB-13	2010	17.06	0.23
HB-14	2011	17.30	0.23
HB-15	2012	17.15	0.23
HB-16	2013	17.19	0.23
HB-17	2014	18.01	0.23
HB-18	2015	17.21	0.23
HB-19	2016	17.69	0.23
HB-20	2017	17.67	0.23
HB-21	2018	17.74	0.23
HB-22	2019	17.81	0.23
HB-23	2020	17.73	0.23
HB-24	2021	17.66	0.23

Table 21. Annual growth layer, year of deposition, calculated Suess effect correction (‰), measured $\delta^{13}C_{CO3}$ (‰), associated analytical uncertainty (±1 SD, ‰), and Suess effect-corrected $\delta^{13}C_{CO3}$ (‰) from the Hudson Bay narwhal tusk (Tusk 2).

Sample ID	Year	Suess Effect	$\delta^{13}C_{CO3}$	±1 SD	Corrected $\delta^{13}C_{CO3}$
HB-01	1998	-0.60	-13.14	0.09	-12.54
HB-02	1999	-0.61	-12.49	0.09	-11.88
HB-03	2000	-0.63	-11.87	0.09	-11.24
HB-04	2001	-0.65	-12.11	0.09	-11.46
HB-05	2002	-0.67	-11.78	0.09	-11.11
HB-06	2003	-0.68	-12.27	0.09	-11.59
HB-07	2004	-0.70	-12.00	0.09	-11.30
HB-08	2005	-0.72	-11.57	0.09	-10.85
HB-09	2006	-0.74	-12.34	0.09	-11.60
HB-10	2007	-0.76	-12.22	0.09	-11.46
HB-11	2008	-0.78	-12.28	0.09	-11.50
HB-12	2009	-0.81	-12.89	0.09	-12.08
HB-13	2010	-0.83	-12.97	0.09	-12.14
HB-14	2011	-0.85	-12.97	0.09	-12.12
HB-15	2012	-0.87	-12.98	0.09	-12.11
HB-16	2013	-0.90	-13.05	0.09	-12.15
HB-17	2014	-0.92	-13.17	0.09	-12.25
HB-18	2015	-0.95	-13.34	0.09	-12.39
HB-19	2016	-0.97	-13.53	0.09	-12.56
HB-20	2017	-1.00	-13.17	0.09	-12.17
HB-21	2018	-1.03	-13.30	0.09	-12.27
HB-22	2019	-1.05	-13.51	0.09	-12.46
HB-23	2020	-1.08	-13.46	0.09	-12.38
HB-24	2021	-1.11	-12.26	0.10	-11.15

Table 22. Annual growth layer, year of deposition, measured $\delta^{18}O_{CO3}$ (‰), associated analytical uncertainty (±1 SD, ‰), and $\delta^{18}O_{CO3}$ values converted from the VPDB to the VSMOW scale (‰) from the Hudson Bay narwhal tusk (Tusk 2).

Sample ID	Year	$\delta^{18}O_{CO3}$ (*VPDB*)	±1 SD	$\delta^{18}O_{CO3}$ (*VSMOW*)
HB-01	1998	-6.61	0.09	24.11
HB-02	1999	-6.79	0.09	23.92
HB-03	2000	-5.87	0.09	24.87
HB-04	2001	-5.66	0.09	25.09
HB-05	2002	-5.38	0.09	25.37
HB-06	2003	-5.94	0.09	24.80
HB-07	2004	-5.54	0.09	25.21
HB-08	2005	-5.70	0.09	25.04
HB-09	2006	-5.07	0.09	25.69
HB-10	2007	-5.05	0.09	25.71
HB-11	2008	-5.90	0.09	24.84
HB-12	2009	-5.69	0.09	25.05
HB-13	2010	-5.67	0.09	25.07
HB-14	2011	-5.40	0.09	25.35
HB-15	2012	-5.49	0.09	25.26
HB-16	2013	-4.95	0.09	25.82
HB-17	2014	-6.00	0.09	24.73
HB-18	2015	-5.18	0.09	25.58
HB-19	2016	-4.85	0.09	25.92
HB-20	2017	-4.95	0.09	25.82
HB-21	2018	-8.09	0.09	22.58
HB-22	2019	-7.90	0.09	22.78
HB-23	2020	-6.93	0.09	23.78
HB-24	2021	-4.06	0.05	26.73

Table 23. Annual growth layer, year of deposition, $\Delta^{13}C_{carb\text{-}coll}$ (‰), and associated analytical uncertainty (±1 SD, ‰) from the Hudson Bay narwhal tusk (Tusk 2).

Sample ID	Year	$\Delta^{13}C_{carb\text{-}coll}$	±1 SD
HB-01	1998	1.89	0.12
HB-02	1999	2.50	0.12
HB-03	2000	2.51	0.12
HB-04	2001	2.24	0.12
HB-05	2002	2.94	0.12
HB-06	2003	2.48	0.12
HB-07	2004	2.37	0.12
HB-08	2005	2.91	0.12
HB-09	2006	2.01	0.12
HB-10	2007	2.08	0.12
HB-11	2008	2.20	0.12
HB-12	2009	2.04	0.12
HB-13	2010	2.18	0.12
HB-14	2011	2.10	0.12
HB-15	2012	1.95	0.12
HB-16	2013	1.98	0.12
HB-17	2014	2.12	0.12
HB-18	2015	1.77	0.12
HB-19	2016	1.71	0.12
HB-20	2017	1.99	0.12
HB-21	2018	1.81	0.12
HB-22	2019	1.39	0.12
HB-23	2020	1.68	0.12
HB-24	2021	2.48	0.12

Table 24. Annual growth layer, year of deposition, Hg concentrations (μg/g), and associated analytical uncertainty (±1 SD, μg/g) from the Hudson Bay narwhal tusk (Tusk 2).

Sample ID	Year	[Hg]	±1 SD
HB-01	1998	3.57	1.35
HB-02	1999	1.11	1.35
HB-03	2000	-	-
HB-04	2001	3.85	1.35
HB-05	2002	5.00	1.35
HB-06	2003	4.69	1.35
HB-07	2004	4.23	1.35
HB-08	2005	7.69	1.35
HB-09	2006	4.17	1.35
HB-10	2007	-	-
HB-11	2008	9.41	1.35
HB-12	2009	7.69	1.35
HB-13	2010	7.37	1.35
HB-14	2011	5.42	1.35
HB-15	2012	7.50	1.35
HB-16	2013	4.74	1.35
HB-17	2014	5.17	1.35
HB-18	2015	7.22	1.35
HB-19	2016	4.05	1.35
HB-20	2017	5.46	1.35
HB-21	2018	5.71	1.35
HB-22	2019	6.90	1.35
HB-23	2020	1.82	1.35
HB-24	2021	6.36	1.35

Table 25. Annual growth layer, year of deposition, $^{206}Pb/^{204}Pb$, $^{208}Pb/^{206}Pb$, $^{206}Pb/^{207}Pb$, and associated analytical uncertainty (±1 SD) from the Hudson Bay narwhal tusk (Tusk 2).

Sample ID	Year	$^{206}Pb/^{204}Pb$	±1 SD	$^{208}Pb/^{206}Pb$	±1 SD	$^{206}Pb/^{207}Pb$	±1 SD
HB-01	1998	18.869	0.022	2.072	0.003	1.206	0.002
HB-02	1999	19.106	0.022	2.069	0.003	1.220	0.002
HB-03	2000	19.120	0.022	2.068	0.003	1.220	0.002
HB-04	2001	19.131	0.022	2.068	0.003	1.221	0.002
HB-05	2002	19.091	0.022	2.069	0.003	1.219	0.002
HB-06	2003	19.095	0.022	2.070	0.003	1.219	0.002
HB-07	2004	19.074	0.022	2.072	0.003	1.218	0.002
HB-08	2005	19.042	0.022	2.072	0.003	1.216	0.002
HB-09	2006	19.016	0.022	2.073	0.003	1.215	0.002
HB-10	2007	19.044	0.022	2.072	0.003	1.216	0.002
HB-11	2008	19.071	0.022	2.071	0.003	1.218	0.002
HB-12	2009	18.973	0.022	2.066	0.003	1.212	0.002
HB-13	2010	19.069	0.022	2.071	0.003	1.217	0.002
HB-14	2011	19.113	0.022	2.071	0.003	1.220	0.002
HB-15	2012	19.112	0.022	2.070	0.003	1.220	0.002
HB-16	2013	18.880	0.022	2.078	0.003	1.206	0.002
HB-17	2014	19.211	0.022	2.068	0.003	1.225	0.002
HB-18	2015	19.011	0.022	2.071	0.003	1.213	0.002
HB-19	2016	19.150	0.022	2.072	0.003	1.222	0.002
HB-20	2017	19.102	0.022	2.074	0.003	1.219	0.002
HB-21	2018	19.088	0.022	2.072	0.003	1.218	0.002
HB-22	2019	19.139	0.022	2.072	0.003	1.221	0.002
HB-23	2020	19.163	0.022	2.069	0.003	1.222	0.002
HB-24	2021	19.214	0.022	2.069	0.003	1.237	0.002

Table 26. Annual growth layer, year of deposition, major elements (Ca, Mg, Cr; ppm), and associated analytical uncertainty (±1 SD; ppm) from the Hudson Bay narwhal tusk (Tusk 2).

Sample ID	Year	Ca	±1 SD	Mg	±1 SD	Cr	±1 SD
HB-01	1998	200593.16	0.07	15641.475	0.002	4.429	0.004
HB-02	1999	209062.53	0.07	13087.381	0.002	0.874	0.004
HB-03	2000	218132.45	0.07	11641.725	0.002	0.833	0.004
HB-04	2001	210797.54	0.07	10283.354	0.002	1.863	0.004
HB-05	2002	216973.88	0.07	10104.113	0.002	4.517	0.004
HB-06	2003	269811.61	0.07	11561.834	0.002	1.046	0.004
HB-07	2004	217895.67	0.07	9500.127	0.002	4.191	0.004
HB-08	2005	214905.85	0.07	9290.498	0.002	1.916	0.004
HB-09	2006	207663.55	0.07	8328.316	0.002	2.517	0.004
HB-10	2007	222487.35	0.07	8750.462	0.002	1.399	0.004
HB-11	2008	222541.46	0.03	8765.135	0.004	1.540	0.001
HB-12	2009	221906.58	0.03	8398.027	0.004	0.274	0.001
HB-13	2010	223394.90	0.03	7838.085	0.004	0.000	0.001
HB-14	2011	222885.81	0.03	8340.879	0.004	1.475	0.001
HB-15	2012	220720.19	0.03	8055.760	0.004	2.467	0.001
HB-16	2013	224548.83	0.07	8219.939	0.002	2.500	0.004
HB-17	2014	217306.12	0.07	7831.330	0.002	0.931	0.004
HB-18	2015	211203.15	0.07	7512.459	0.002	1.850	0.004
HB-19	2016	211799.65	0.07	7387.634	0.002	0.549	0.004
HB-20	2017	211307.62	0.07	7761.861	0.002	3.314	0.004
HB-21	2018	223253.46	0.07	6420.762	0.002	2.626	0.004
HB-22	2019	219773.47	0.07	6236.367	0.002	1.296	0.004
HB-23	2020	218307.26	0.07	5639.168	0.002	2.547	0.004
HB-24	2021	209297.63	0.07	7671.145	0.002	3.007	0.004

Table 27. Annual growth layer, year of deposition, major elements (Ca, Co, Zn; ppm), and associated analytical uncertainty (±1 SD; ppm) from the Hudson Bay narwhal tusk (Tusk 2).

Sample ID	Year	Ca	±1 SD	Co	±1 SD	Zn	±1 SD
HB-01	1998	200593.16	0.07	5.750	0.004	112.535	0.005
HB-02	1999	209062.53	0.07	1.835	0.004	94.179	0.005
HB-03	2000	218132.45	0.07	1.627	0.004	89.988	0.005
HB-04	2001	210797.54	0.07	2.889	0.004	83.881	0.005
HB-05	2002	216973.88	0.07	2.181	0.004	79.616	0.005
HB-06	2003	269811.61	0.07	2.266	0.004	103.578	0.005
HB-07	2004	217895.67	0.07	2.797	0.004	94.149	0.005
HB-08	2005	214905.85	0.07	3.090	0.004	89.774	0.005
HB-09	2006	207663.55	0.07	1.901	0.004	87.775	0.005
HB-10	2007	222487.35	0.07	1.933	0.004	91.653	0.005
HB-11	2008	222541.46	0.03	2.104	0.004	100.230	0.005
HB-12	2009	221906.58	0.03	0.081	0.004	97.214	0.005
HB-13	2010	223394.90	0.03	2.132	0.004	103.333	0.005
HB-14	2011	222885.81	0.03	1.658	0.004	103.867	0.005
HB-15	2012	220720.19	0.03	0.111	0.004	107.206	0.005
HB-16	2013	224548.83	0.07	1.882	0.004	97.865	0.005
HB-17	2014	217306.12	0.07	2.218	0.004	88.693	0.005
HB-18	2015	211203.15	0.07	2.479	0.004	91.589	0.005
HB-19	2016	211799.65	0.07	0.819	0.004	91.290	0.005
HB-20	2017	211307.62	0.07	2.233	0.004	89.528	0.005
HB-21	2018	223253.46	0.07	2.425	0.004	88.896	0.005
HB-22	2019	219773.47	0.07	1.827	0.004	93.759	0.005
HB-23	2020	218307.26	0.07	2.627	0.004	93.624	0.005
HB-24	2021	209297.63	0.07	1.317	0.004	89.641	0.005

Table 28. Annual growth layer, year of deposition, major elements (Ca, Ba, Sr; ppm), and associated analytical uncertainty (±1 SD; ppm) from the Hudson Bay narwhal tusk (Tusk 2).

Sample ID	Year	Ca	±1 SD	Ba	±1 SD	Sr	±1 SD
HB-01	1998	200593.16	0.07	3.167	0.003	281.966	0.005
HB-02	1999	209062.53	0.07	3.295	0.003	285.194	0.005
HB-03	2000	218132.45	0.07	2.445	0.003	278.138	0.005
HB-04	2001	210797.54	0.07	2.041	0.003	228.371	0.005
HB-05	2002	216973.88	0.07	1.765	0.003	203.852	0.005
HB-06	2003	269811.61	0.07	2.078	0.003	258.969	0.005
HB-07	2004	217895.67	0.07	1.692	0.003	210.737	0.005
HB-08	2005	214905.85	0.07	4.033	0.003	192.305	0.005
HB-09	2006	207663.55	0.07	1.191	0.003	188.996	0.005
HB-10	2007	222487.35	0.07	1.243	0.003	204.478	0.005
HB-11	2008	222541.46	0.03	1.225	0.007	210.571	0.005
HB-12	2009	221906.58	0.03	1.075	0.007	212.895	0.005
HB-13	2010	223394.90	0.03	1.211	0.007	224.549	0.005
HB-14	2011	222885.81	0.03	0.921	0.007	189.502	0.005
HB-15	2012	220720.19	0.03	0.972	0.007	206.871	0.005
HB-16	2013	224548.83	0.07	0.819	0.003	184.668	0.005
HB-17	2014	217306.12	0.07	1.103	0.003	224.295	0.005
HB-18	2015	211203.15	0.07	0.926	0.003	173.685	0.005
HB-19	2016	211799.65	0.07	1.072	0.003	184.486	0.005
HB-20	2017	211307.62	0.07	0.866	0.003	174.430	0.005
HB-21	2018	223253.46	0.07	1.000	0.003	181.024	0.005
HB-22	2019	219773.47	0.07	0.827	0.003	177.737	0.005
HB-23	2020	218307.26	0.07	1.516	0.003	177.804	0.005
HB-24	2021	209297.63	0.07	0.906	0.003	166.296	0.005

Table 29. Annual growth layer, year of deposition, trace metals (Ca, Mn, Fe; ppb), and associated analytical uncertainty (±1 SD; ppb) from the Hudson Bay narwhal tusk (Tusk 2).

Sample ID	Year	Ca	±1 SD	Mn	±1 SD	Fe	±1 SD
HB-01	1998	88893774.95	3.71	6443.19	0.80	5423.78	1.68
HB-02	1999	90034291.54	3.71	2921.59	0.80	5302.88	1.68
HB-03	2000	98592537.50	3.71	2688.77	0.80	7496.64	1.68
HB-04	2001	106366970.13	3.71	2507.11	0.80	3337.03	1.68
HB-05	2002	105699475.90	3.71	2370.83	0.80	3235.44	1.68
HB-06	2003	138596984.11	3.71	2877.26	0.80	5021.63	1.68
HB-07	2004	113248327.85	3.71	2424.65	0.80	4175.98	1.68
HB-08	2005	122722376.55	3.71	2464.91	0.80	5550.84	1.68
HB-09	2006	119132136.34	3.71	2807.01	0.80	7718.08	1.68
HB-10	2007	122437977.07	3.71	2309.70	0.80	5288.72	1.68
HB-11	2008	126759741.01	3.21	1870.61	0.32	10286.39	0.56
HB-12	2009	124561485.13	3.21	1236.50	0.32	7595.57	0.56
HB-13	2010	123461207.67	3.21	1910.83	0.32	12731.65	0.56
HB-14	2011	125216491.94	3.21	1842.04	0.32	5402.13	0.56
HB-15	2012	123951179.82	3.21	1855.83	0.32	9916.10	0.56
HB-16	2013	130244258.98	3.71	2591.43	0.80	15039.13	1.68
HB-17	2014	118974908.37	3.71	2693.95	0.80	10780.23	1.68
HB-18	2015	101527946.64	3.71	1850.23	0.80	12052.62	1.68
HB-19	2016	125467201.76	3.71	2051.20	0.80	4747.17	1.68
HB-20	2017	131744140.36	3.71	2072.04	0.80	4924.07	1.68
HB-21	2018	140430518.28	3.71	1987.66	0.80	6929.67	1.68
HB-22	2019	147699161.41	3.71	1979.38	0.80	5898.18	1.68
HB-23	2020	141471227.23	3.71	2106.94	0.80	10905.32	1.68
HB-24	2021	142045219.94	3.71	2753.75	0.80	15285.41	1.68

Table 30. Annual growth layer, year of deposition, trace metals (As, Cd, Pb; ppb), and associated analytical uncertainty (±1 SD; ppb) from the Hudson Bay narwhal tusk (Tusk 2).

Sample ID	Year	As	±1 SD	Cd	±1 SD	Pb	±1 SD
HB-01	1998	24.41	1.78	0.96	1.79	30.06	1.86
HB-02	1999	13.50	1.78	13.77	1.79	116.32	1.86
HB-03	2000	15.31	1.78	17.63	1.79	130.16	1.86
HB-04	2001	16.41	1.78	16.11	1.79	113.11	1.86
HB-05	2002	17.27	1.78	13.75	1.79	80.99	1.86
HB-06	2003	20.32	1.78	19.18	1.79	103.98	1.86
HB-07	2004	17.28	1.78	17.98	1.79	91.32	1.86
HB-08	2005	15.04	1.78	14.01	1.79	80.82	1.86
HB-09	2006	15.31	1.78	9.14	1.79	54.12	1.86
HB-10	2007	12.28	1.78	7.22	1.79	43.42	1.86
HB-11	2008	17.43	0.71	4.27	0.73	51.21	0.41
HB-12	2009	15.53	0.71	7.50	0.73	37.57	0.41
HB-13	2010	16.07	0.71	20.02	0.73	29.69	0.41
HB-14	2011	14.37	0.71	10.94	0.73	36.92	0.41
HB-15	2012	13.70	0.71	4.27	0.73	47.75	0.41
HB-16	2013	17.32	1.78	7.03	1.79	75.69	1.86
HB-17	2014	15.38	1.78	7.11	1.79	18.91	1.86
HB-18	2015	14.37	1.78	6.41	1.79	23.56	1.86
HB-19	2016	11.81	1.78	6.15	1.79	17.15	1.86
HB-20	2017	15.36	1.78	7.69	1.79	18.15	1.86
HB-21	2018	15.28	1.78	6.33	1.79	15.41	1.86
HB-22	2019	12.93	1.78	5.95	1.79	16.21	1.86
HB-23	2020	14.25	1.78	2.95	1.79	21.35	1.86
HB-24	2021	15.62	1.78	5.90	1.79	17.96	1.86

Table 31. Pairwise overlap (%) of $^{206}Pb/^{207}Pb$ and $^{208}Pb/^{206}Pb$ with 95% confidence ellipses for Tusk 1 (Baffin Bay), Tusk 2 (Hudson Bay), Marine Shelf Sediments, Canadian Basin Water, Canadian Arctic Archipelago Water, and Baffin Bay Water.

Variable 1	Variable 2	Overlap (%)
Baffin Bay Tusk	Hudson Bay Tusk	17.9
Baffin Bay Tusk	Marine Shelf Sediments	6.2
Baffin Bay Tusk	Canadian Basin Water	0
Baffin Bay Tusk	Canadian Arctic Archipelago Water	16.5
Baffin Bay Tusk	Baffin Bay Water	3.8
Hudson Bay Tusk	Marine Shelf Sediments	11.8
Hudson Bay Tusk	Canadian Basin Water	0
Hudson Bay Tusk	Canadian Arctic Archipelago Water	3.6
Hudson Bay Tusk	Baffin Bay Water	0.3

Table 32. Linear temporal trends and associated *p*-values for environmental variables in Baffin Bay and Hudson Bay. Slopes represent the average annual change in million km^2 yr^{-1} for ice extent, in °C yr^{-1} for water temperature and in psu yr^{-1} for salinity. AMV/AMO index anomalies are reported in °C yr^{-1} for the periods 1870-2020 and 1997-2020. Statistically significant trends are indicated by * for *p*-value ≤ 0.05 and ** for *p*-value ≤ 0.01.

Variable	Slope	*p*-value
Baffin Bay Ice Extent	-0.0058	< 0.001 **
Arctic Bay Water Temperature	0.0119	0.022 *
Arctic Bay Water Salinity	-0.0078	0.060
Hudson Bay Ice Extent	-0.0034	< 0.001 **
Naujaat Water Temperature	0.0017	0.748
Naujaat Water Salinity	-0.0017	0.465
AMV/AMO Index Anomaly (1870-2020)	2.79×10^{-5}	0.917
AMV/AMO Index Anomaly (1997-2020)	-0.0017	0.632

Table 33. Spearman correlation coefficients (ρ) and associated *p*-values between isotopic and elemental variables in annual growth layers of Baffin Bay narwhal tusk (Tusk 1) and environmental variables. Environmental variables include Baffin Bay (BB) ice extent (million km^2), Arctic Bay salinity (psu) and Arctic Bay sea surface temperature (SST; °C). Statistically significant correlations are indicated by * for *p*-value ≤ 0.05 and ** for *p*-value ≤ 0.01.

Variable 1	Variable 2	rho (ρ)	*p*-value
BB Ice Extent	$\delta^{13}C_{collagen}$	-0.25	0.243
BB Ice Extent	$\delta^{15}N_{collagen}$	0.15	0.477
BB Ice Extent	$\delta^{13}C_{CO3}$	-0.05	0.824
BB Ice Extent	$\delta^{18}O_{CO3}$	-0.39	0.063
BB Ice Extent	$\Delta^{13}C_{carb\text{-}coll}$	-0.01	0.950
BB Ice Extent	Hg	-0.11	0.626
BB Ice Extent	$^{206}Pb/^{204}Pb$	0.05	0.815
BB Ice Extent	$^{208}Pb/^{206}Pb$	-0.17	0.419
BB Ice Extent	$^{206}Pb/^{207}Pb$	0.03	0.872
BB Ice Extent	Mn:Ca	0.03	0.900
BB Ice Extent	Fe:Ca	0.06	0.767
BB Ice Extent	As:Ca	0.05	0.834
BB Ice Extent	Cd:Ca	-0.15	0.473
BB Ice Extent	Pb:Ca	0.15	0.492
BB Ice Extent	Mg:Ca	0.26	0.221
BB Ice Extent	Cr:Ca	0.38	0.067
BB Ice Extent	Co:Ca	-0.02	0.915
BB Ice Extent	Zn:Ca	0.08	0.704
BB Ice Extent	Sr:Ca	0.15	0.497
BB Ice Extent	Ba:Ca	0.13	0.552
Salinity	$\delta^{13}C_{collagen}$	-0.37	0.079
Salinity	$\delta^{15}N_{collagen}$	-0.25	0.238
Salinity	$\delta^{13}C_{CO3}$	-0.46	0.023 *
Salinity	$\delta^{18}O_{CO3}$	-0.19	0.383
Salinity	$\Delta^{13}C_{carb\text{-}coll}$	-0.43	0.038 *
Salinity	Hg	-0.15	0.500
Salinity	$^{206}Pb/^{204}Pb$	0.49	0.015 *
Salinity	$^{208}Pb/^{206}Pb$	-0.52	0.009 **
Salinity	$^{206}Pb/^{207}Pb$	0.46	0.022 *
Salinity	Mn:Ca	0.33	0.110
Salinity	Fe:Ca	0.32	0.132

Salinity	As:Ca	-0.05	0.831
Salinity	Cd:Ca	-0.04	0.865
Salinity	Pb:Ca	0.07	0.741
Salinity	Mg:Ca	-0.17	0.421
Salinity	Cr:Ca	0.03	0.907
Salinity	Co:Ca	-0.55	0.005 **
Salinity	Zn:Ca	0.59	0.002 **
Salinity	Sr:Ca	-0.04	0.840
Salinity	Ba:Ca	-0.41	0.047 *
SST	$\delta^{13}C_{collagen}$	0.31	0.145
SST	$\delta^{15}N_{collagen}$	0.21	0.313
SST	$\delta^{13}C_{CO3}$	0.14	0.517
SST	$\delta^{18}O_{CO3}$	-0.31	0.146
SST	$\Delta^{13}C_{carb\text{-}coll}$	0.06	0.791
SST	Hg	-0.09	0.677
SST	$^{206}Pb/^{204}Pb$	-0.02	0.913
SST	$^{208}Pb/^{206}Pb$	0.18	0.407
SST	$^{206}Pb/^{207}Pb$	-0.01	0.958
SST	Mn:Ca	-0.16	0.443
SST	Fe:Ca	-0.24	0.257
SST	As:Ca	0.07	0.747
SST	Cd:Ca	0.29	0.174
SST	Pb:Ca	0.11	0.607
SST	Mg:Ca	0.08	0.701
SST	Cr:Ca	0.29	0.169
SST	Co:Ca	0.23	0.273
SST	Zn:Ca	-0.12	0.568
SST	Sr:Ca	0.16	0.463
SST	Ba:Ca	0.18	0.391

Table 34. Spearman correlation coefficients (ρ) and associated *p*-values between isotopic and elemental variables in annual growth layers of Hudson Bay narwhal tusk (Tusk 2) and environmental variables. Environmental variables include Hudson (HB) ice extent (million km^2), Naujaat salinity (psu) and Naujaat sea surface temperature (SST; °C). Statistically significant correlations are indicated by * for *p*-value ≤ 0.05 and ** for *p*-value ≤ 0.01.

Variable 1	Variable 2	rho (ρ)	*p*-value
HB Ice Extent	$\delta^{13}C_{collagen}$	0.1	0.643
HB Ice Extent	$\delta^{15}N_{collagen}$	0.41	0.049 *
HB Ice Extent	$\delta^{13}C_{CO3}$	0	0.982
HB Ice Extent	$\delta^{18}O_{CO3}$	-0.16	0.441
HB Ice Extent	$\Delta^{13}C_{carb\text{-}coll}$	-0.07	0.755
HB Ice Extent	Hg	0.07	0.751
HB Ice Extent	$^{206}Pb/^{204}Pb$	-0.07	0.736
HB Ice Extent	$^{208}Pb/^{206}Pb$	-0.15	0.475
HB Ice Extent	$^{206}Pb/^{207}Pb$	-0.08	0.715
HB Ice Extent	Mn:Ca	-0.21	0.314
HB Ice Extent	Fe:Ca	-0.07	0.760
HB Ice Extent	As:Ca	0.01	0.957
HB Ice Extent	Cd:Ca	-0.06	0.788
HB Ice Extent	Pb:Ca	0.02	0.910
HB Ice Extent	Mg:Ca	-0.12	0.580
HB Ice Extent	Cr:Ca	0.10	0.635
HB Ice Extent	Co:Ca	0.15	0.494
HB Ice Extent	Zn:Ca	-0.34	0.105
HB Ice Extent	Sr:Ca	-0.09	0.668
HB Ice Extent	Ba:Ca	-0.01	0.961
Salinity	$\delta^{13}C_{collagen}$	0.23	0.284
Salinity	$\delta^{15}N_{collagen}$	-0.27	0.194
Salinity	$\delta^{13}C_{CO3}$	0.16	0.465
Salinity	$\delta^{18}O_{CO3}$	0.42	0.043 *
Salinity	$\Delta^{13}C_{carb\text{-}coll}$	-0.01	0.955
Salinity	Hg	0.21	0.351
Salinity	$^{206}Pb/^{204}Pb$	-0.31	0.136
Salinity	$^{208}Pb/^{206}Pb$	-0.09	0.680
Salinity	$^{206}Pb/^{207}Pb$	-0.29	0.170
Salinity	Mn:Ca	-0.16	0.443
Salinity	Fe:Ca	0.17	0.438

Salinity	As:Ca	0.07	0.734
Salinity	Cd:Ca	-0.08	0.725
Salinity	Pb:Ca	0.17	0.414
Salinity	Mg:Ca	0.04	0.843
Salinity	Cr:Ca	-0.11	0.593
Salinity	Co:Ca	-0.26	0.214
Salinity	Zn:Ca	0.13	0.557
Salinity	Sr:Ca	0.13	0.544
Salinity	Ba:Ca	-0.15	0.493
SST	$\delta^{13}C_{collagen}$	0.51	0.010 *
SST	$\delta^{15}N_{collagen}$	0.49	0.014 *
SST	$\delta^{13}C_{CO3}$	0.48	0.017 *
SST	$\delta^{18}O_{CO3}$	-0.16	0.444
SST	$\Delta^{13}C_{carb\text{-}coll}$	0.42	0.043 *
SST	Hg	-0.14	0.521
SST	$^{206}Pb/^{204}Pb$	-0.04	0.843
SST	$^{208}Pb/^{206}Pb$	0	0.984
SST	$^{206}Pb/^{207}Pb$	-0.02	0.920
SST	Mn:Ca	0.17	0.440
SST	Fe:Ca	-0.68	< 0.001 **
SST	As:Ca	0.31	0.146
SST	Cd:Ca	0.37	0.078
SST	Pb:Ca	0.41	0.048 *
SST	Mg:Ca	0.52	0.009 **
SST	Cr:Ca	0.09	0.692
SST	Co:Ca	0.25	0.233
SST	Zn:Ca	-0.58	0.003 **
SST	Sr:Ca	0.28	0.188
SST	Ba:Ca	0.47	0.020 *

Table 35. Spearman correlation coefficients (ρ) and associated *p*-values between AMV/AMO Index Anomaly (°C; 1997-2020) and isotopic and elemental variables in annual growth layers of Baffin Bay narwhal tusk (Tusk 1). Statistically significant correlations are indicated by * for *p*-value ≤ 0.05 and ** for *p*-value ≤ 0.01.

Variable 1	Variable 2	rho (ρ)	*p*-value
AMV/AMO Index Anomaly	$\delta^{13}C_{collagen}$	0.27	0.194
AMV/AMO Index Anomaly	$\delta^{15}N_{collagen}$	-0.09	0.683
AMV/AMO Index Anomaly	$\delta^{13}C_{CO3}$	0.23	0.288
AMV/AMO Index Anomaly	$\delta^{18}O_{CO3}$	0.42	0.041 *
AMV/AMO Index Anomaly	$\Delta^{13}C_{carb\text{-}coll}$	0.19	0.367
AMV/AMO Index Anomaly	Hg	-0.30	0.160
AMV/AMO Index Anomaly	$^{206}Pb/^{204}Pb$	0.09	0.671
AMV/AMO Index Anomaly	$^{208}Pb/^{206}Pb$	0.10	0.639
AMV/AMO Index Anomaly	$^{206}Pb/^{207}Pb$	0.09	0.665
AMV/AMO Index Anomaly	Mn:Ca	0.04	0.869
AMV/AMO Index Anomaly	Fe:Ca	0.03	0.894
AMV/AMO Index Anomaly	As:Ca	-0.26	0.214
AMV/AMO Index Anomaly	Cd:Ca	0.16	0.463
AMV/AMO Index Anomaly	Pb:Ca	0.09	0.662
AMV/AMO Index Anomaly	Mg:Ca	0.02	0.923
AMV/AMO Index Anomaly	Cr:Ca	-0.13	0.560
AMV/AMO Index Anomaly	Co:Ca	0.05	0.834
AMV/AMO Index Anomaly	Zn:Ca	0.11	0.610
AMV/AMO Index Anomaly	Sr:Ca	-0.18	0.389
AMV/AMO Index Anomaly	Ba:Ca	-0.26	0.221

Table 36. Spearman correlation coefficients (ρ) and associated *p*-values between AMV/AMO Index Anomaly (°C; 1998-2020) and isotopic and elemental variables in annual growth layers of Hudson Bay narwhal tusk (Tusk 2). Statistically significant correlations are indicated by * for *p*-value ≤ 0.05 and ** for *p*-value ≤ 0.01.

Variable 1	Variable 2	rho (ρ)	*p*-value
AMV/AMO Index Anomaly	$\delta^{13}C_{collagen}$	0.15	0.488
AMV/AMO Index Anomaly	$\delta^{15}N_{collagen}$	-0.31	0.143
AMV/AMO Index Anomaly	$\delta^{13}C_{CO3}$	0.28	0.200
AMV/AMO Index Anomaly	$\delta^{18}O_{CO3}$	0.08	0.708
AMV/AMO Index Anomaly	$\Delta^{13}C_{carb\text{-}coll}$	0.22	0.319
AMV/AMO Index Anomaly	Hg	0.04	0.854
AMV/AMO Index Anomaly	$^{206}Pb/^{204}Pb$	-0.2	0.349
AMV/AMO Index Anomaly	$^{208}Pb/^{206}Pb$	0.24	0.278
AMV/AMO Index Anomaly	$^{206}Pb/^{207}Pb$	-0.20	0.349
AMV/AMO Index Anomaly	Mn:Ca	0.05	0.819
AMV/AMO Index Anomaly	Fe:Ca	0.16	0.474
AMV/AMO Index Anomaly	As:Ca	0.04	0.861
AMV/AMO Index Anomaly	Cd:Ca	0.07	0.757
AMV/AMO Index Anomaly	Pb:Ca	0.28	0.201
AMV/AMO Index Anomaly	Mg:Ca	0.20	0.359
AMV/AMO Index Anomaly	Cr:Ca	0.03	0.883
AMV/AMO Index Anomaly	Co:Ca	0.02	0.925
AMV/AMO Index Anomaly	Zn:Ca	0.42	0.047 *
AMV/AMO Index Anomaly	Sr:Ca	0.19	0.388
AMV/AMO Index Anomaly	Ba:Ca	0.24	0.270